DESIGN OPTIMIZATION OF MULTI-PLY SOFT ARMOR TARGETS BASED ON FAILURE MODES UNDER PROJECTILE NORMAL IMPACT

A Dissertation

Submitted to the Faculty

of

Purdue University

by

Zherui Guo

In Partial Fulfillment of the

Requirements for the Degree

of

Doctor of Philosophy

May 2020

Purdue University

West Lafayette, Indiana

THE PURDUE UNIVERSITY GRADUATE SCHOOL
STATEMENT OF DISSERTATION APPROVAL

Dr. Weinong W. Chen, Chair

School of Aeronautics and Astronautics

Dr. James F. Doyle

School of Aeronautics and Astronautics

Dr. Wenbin Yu

School of Aeronautics and Astronautics

Dr. Chelsea S. Davis

School of Aeronautics and Astronautics

Approved by:

Dr. Gregory A. Blaisdell

Head of the School Graduate Program

To my parents, who have been awaiting this moment for a long time coming;

To my brother, who will soon be where I am now; and

To Stephenie Martinez, who endured my long hours and short attention spans.

ACKNOWLEDGMENTS

First and foremost, none of this would have been possible without my advisor and mentor, Professor Weinong Chen, who took me under his wing more than 11 years ago. Your penchant for hard work, late nights, and dedication to seeking scientific truths have rubbed off on me. Our many talks have made me a better researcher and an even better person, and I sincerely thank you for the many opportunities that have graced my academic path. I have burdened you enough for the past years, and I hope that you get a well-deserved break soon. To my committee members, Professor Doyle, Professor Yu, and Professor Davis: thank you all for your insight and lengthy discussions. It is very humbling to be learning from people whom I hold in high esteem, and all your knowledge and wisdom will carry me through my years to come.

To the many peers who have come and gone during this graduate school stint: you have made these the best years of my life. Long after the highs of graduation will have faded, the fondest memories that remain will undoubtedly be of our whimsical late night exchanges over a pint or two, from which many exciting scientific ideas were borne (though not many have been actualised). The passion you all have for research have motivated and driven me to be a better scientist than I ever thought I could and would be. A person of my lack of ability would have found graduate school torturous were it not for you myriad people who have offered help without complaint, the full list of whom would be too extensive (and a tad disrespectful) to place in a short paragraph. Please do allow me the chance to express my sincerest gratitude to each of you individually.

And finally, to the one who suffered silently to support my selfish pursuits of science: I could not have thought of a better time or place to announce our little secret. Thank you for everything, my co-author in life, my dearest wife, Stephenie Martinez-Morales.

PREFACE

The current work comprises two parts that the author believes would best organize some of the concepts discussed herein. The first part is mainly composed of a compilation of prior published works by the author in efforts to investigate the ballistic impact response and the corresponding failure modes of soft body armor targets, and touches on some design optimization ideas and directions that may be potentially developed in future works. The second part essentially consists of a multitude of disparate ideas that have branched out from soft armor studies, though the larger theme still involves ballistic impact response of various targets. In this second part, we explore some generally interesting phenomena and observations that may have initially served as distractions, but eventually became their own developed research directions out of personal curiosity.

The ever-growing importance of personal body armor in today's world means that existing literature in the field of soft armor ballistic impact have been both extensive and intensive (often even more so than the current work is able to achieve), but it appears that some questions still remain unanswered. How do failure modes differ in the through-thickness direction of impact as the projectile perforates the system? How do the target's material properties determine its efficiency against ballistic impact, and how do projectile properties come into play? How do micro-scale impact responses and failure modes fully translate to macro-scale ballistic resistance? How do we avoid certain undesirable failure modes, or if they're inevitable, how can we take advantage of these differences in failure modes to optimize these body armor systems? The current work hopes to at least help answer some of these questions.

The main research direction in the first part looking at soft armor impact failure modes and design optimization is obviously of immediate relevance to this dissertation. We start off with an examination of the different types of failure modes that

impact on fibrous armors may yield. Subsequently, building on these concepts, we take a deeper look into how different impact parameters cause different failure modes, and we end with a discussion of how the armor panel may be designed around these different failure modes. Although some rudimentary analytical and modeling efforts have been put forth, the current work places more emphasis heavily on experimental techniques and observations, as is the nature of the work typically produced by our research group.

TABLE OF CONTENTS

Page

Page

LIST OF TABLES

LIST OF FIGURES

Figure Page

Figure Page

Figure Page

ABSTRACT

Guo, Zherui , Purdue University, May 2020. Design Optimization of Multi-ply Soft Armor Targets Based on Failure Modes Under Projectile Normal Impact. Major Professor: Weinong Chen.

At the ballistic limit velocity of a soft armor target pack, the impact response has been shown to be decoupled in the thickness direction, with the initial few plies behaving in an inelastic fashion via off-axis failure modes such as transverse shear or diametral compression. Past the initial few layers, the remaining plies dissipate energy via membrane-like responses, which only involve in-plane tensile failure modes of the constituent fibers. Since these initial plies only contribute to energy absorption via inelastic kinetic energy transfer, previous studies have shown that these plies may be replaced with another material with other desirable properties, such as lower manufacturing costs or stab-resistance.

However, the methodology of determining these parameters is still largely empirical. Armor panels are typically impacted and the shot outcomes subsequently evaluated in order to achieve a quantitative ballistic performance for the panel. Additionally, the ballistic performance is usually determined with respect to a particular projectile. Several models have been proposed to provide an efficient method of predicting ballistic limit determination, but results are sometimes difficult to translate across different projectile-target pairs.

The main research direction in the first volume looking at soft armor impact failure modes and design optimization is obviously of immediate relevance to this dissertation. We start off with an examination of the different types of failure modes that impact on fibrous armors may yield. Subsequently, building on these concepts, we take a deeper look into how different impact parameters cause different failure modes, and we end with a discussion of how the armor panel may be designed around these

different failure modes. Although some rudimentary analytical and modeling efforts have been put forth, the current work places more emphasis heavily on experimental techniques and observations, as is the nature of the work typically produced by our research group.

1. INTRODUCTION

Modern personal body armor systems have evolved greatly from the heavy plates used in days of yore, mainly because the threats faced today are completely different from before. These body armor systems are very rarely made of monolithic materials, if at all. Instead, they usually comprise several components such as a ceramic plate insert at the strike face, followed by one or two polymeric fabric system near the body for flexibility and breathability. Besides halting high velocity impinging projectiles, these armor systems are also able to dissipate energy sufficiently to mitigate the risk of internal injuries. High-performance polymeric materials are typically characterized by certain specific criteria, most notably for their excellent properties such as thermal resistance, mechanical strength, low specific density, high thermal, electrical, or sound insulation, as well as resistance to destructive conditions such as flames or chemicals [1].

While most of the earlier fiber materials were metallic, one of the first high-performance fibers was made of glass, which had a strength of about 2 GPa [2]. These glass fibers were mainly used in composites, resulting in a lightweight and yet high-strength material with many useful applications. One well-known example of a popular composite material made from glass fibers is fiberglass, which is typically made by coating woven fiberglass fabrics with a resin. Fiberglass is still in use today in many commercial products such as boats, hobby aircraft, and surfboards.

Carbon fibers were the next step in composite technology, and were first developed by Roger Bacon in 1958. Carbon fibers, by themselves, exhibit higher strength-to-weight ratio compared to glass fibers. The popularity of carbon fibers increased as carbon-fiber-reinforced composite materials became more widespread in commercial applications, such as automotive and aircraft parts. Even today, carbon-fiber composites are still widely-used, such as the recently-developed Boeing 787 Dreamliner,

which contains approximately 35 tons of carbon-fiber-reinforced polymer. Carbon fibers have been shown to be stronger and more rigid, although the disadvantage of carbon fibers is their brittleness [3].

Two commonly-used polymeric fibers in soft body armors today are aramid and polyethylene fibers. First discovered by Stephanie Kwolek from DuPont in 1965, Kevlar® is one of the more popular aramid fibers in use in the market right now, with other examples being Nomex® (also by DuPont), as well as Technora® and Twaron®, both of which are made by Teijin. In particular, Kevlar® 29 and KM2 fibers are used in ballistic applications due to their high strength-to-weight ratio, relatively high resistance to chemical and environmental exposure, and low thermal conductivity. These properties not only make it useful for protective applications such as bulletproof vests and jackets, but also for high-impact explosive conditions such as turbine engine fragmentation barriers in aircraft.

The other commonly-used polymer is ultra-high molecular weight polyethylene (UHMWPE), with two of the well-known UHMWPE products being Dyneema® from DSM and Spectra® from Honeywell. In recent decades, UHMWPE fibers have replaced aramid fibers in certain applications due to better resistance to degradation [4]. Polyethylene, in contrast to PPTA, is more flexible due to its long chains and relatively weak transverse bonds. UHMWPE derives its tensile strength from the van der Waal's forces between its extremely long chains of molecules. These van der Waal's forces, although weak individually, become significant when multiplied along the length of these polymers. The resulting structure is therefore highly-resistant to shearing between molecule chains, thereby accounting for their high longitudinal yield strength.

Despite the ubiquity of soft body armors, the methodology of predicting the ballistic performance is still largely empirical. These soft armor vests are typically impacted, and the shot outcomes subsequently evaluated to achieve a quantitative ballistic performance for the panel. Although empirical results are still very useful in guiding the design processes for optimizing these body armor systems, the underlying

principles by which these fibers are able to stop ballistic threats with such efficiency is still not well and fully understood.

1.1 Multi-Scale Testing of Soft Armor Systems

Body armors made from these fibers have proven to be extremely effective against ballistic threats, and a wide range of experimentation has been performed on these materials. However, studies on these armor systems are extensive and tend to be very complex, and may be classified (albeit very generally) into several different size scales to make the problem more tenable:

1. Micro-scale ($\sim$ 1-10 μm). Micro-scale systems typically include single polymeric fibers and filaments that measure several microns in diameter. These fibers themselves are made from bundles of even smaller fibrils ($\sim$ several nm) held together by a somewhat amorphous matrix. Experiments performed on these micro-scale mostly focus on their mechanical properties, which are then used for meso-scale and macro-scale computations.

2. Meso-scale ($\sim$ 1 mm). At one level up, we have meso-scale systems on the order of 1 to several millimeters. Meso-scale systems may include single yarns comprising bundles of single fibers, or in a computational sense, some generally repeating structure such as in-plane and through-thickness weave patterns, and representative unit cells/volumes. Although not as common, ballistic experiments have been performed on meso-scale yarns and tows.

3. Macro-scale ($\sim$ 1 m). These include 3D systems such full vests and shoot packs, and quasi-2D systems such as single plies. Impact tests are performed on these structures to evaluate the halting and energy-absorption capabilities. Computational methods exist but may be expensive due to the large amount of interactions occurring within these structures, although many simplifying

models have shown to be equally effective in predicting the performance of these systems.

The current work focuses on experiments performed to investigate the mechanical response of these armor systems at their respective scales, with special emphasis on the the through-thickness failure mode progression upon projectile normal impact.

1.2 Ballistic Evaluation of Panel Targets

One of the earliest evaluation methods of panel targets by Recht & Ipson [5] involved measuring the striking velocity V_s and the residual velocity V_r i.e. the velocity of the projectile after perforating the target Figure 1.1, giving a measure of the impact energy absorbed by the target. The critical velocity V_c (or ballistic limit) is then calculated at the point of highest striking velocity where the V_r is zero. These initial models attempted to fit this type of curve with a hyperbolic equation with the form $V_r^2 = AV_s^2 + B$ such that the fitting is more physically relevant to the kinetic energy absorption.

These early perforation models worked well for monolithic, isotropic panels where material properties were easily obtained and failure modes could be easily deduced from experimentation, but soft armor target panels are multi-layered, orthotropic (or at best, transversely isotropic), and have meso-scale weave architectures, and failure modes differ greatly in the through-thickness direction. Although similar empirical power-law curve-fits using were employed for fibrous soft armor panels [6, 7] to some degree of success, subsequent studies have shown that exponential models were more suitably employed to describe the shape of the experimental data. It was finally demonstrated by Clark *et al.* [8] that a Weibull model best described the features of the V_r-V_s plots. By this time, the concept of areal density ratio of the target/projectile as a predictive parameter was already in use. The areal density ratio is defined as

$$\eta = \frac{A_d A_p}{m_p} \tag{1.1}$$

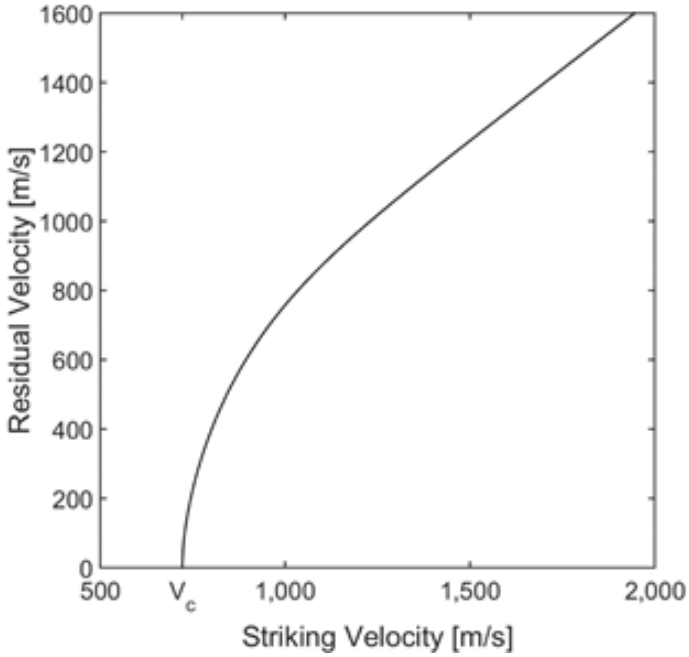

Figure 1.1. Residual velocity against striking velocity for typical soft armor/thin target impact.

where A_d is the target system areal density, A_p is the projectile's presented area, and m_p is the projectile mass. Based on prior works by Clark et al., Cunniff proposed a generalized predictive model in one of his earlier works in this field [9]: a form of Weibull predictive model for the ballistic limit and residual velocities based semi-empirically on the extensive amount of ballistic experimental data obtained, as per Equation 1.2 and 1.3 below.

$$V_c = X_8 X_5^{(sec\theta - 1)} e^{X_6 \eta^{X_7}} \tag{1.2}$$

$$V_r^2 = \frac{V_s^2 - V_c^2 e^{-X_3(\frac{V_s}{V_c} - 1)^{X_4}}}{1 + X_2 \eta} \tag{1.3}$$

In Equations 1.2 and 1.3, X_n are regression coefficients obtained from experimental data. The critical velocity V_c of a particular projectile-target pair is then predicted given a known areal density ratio η and angle of obliquity θ. However, the downside of such a method is obvious: the ballistic performance can only be predicted using regression coefficients that have to be obtained from other experiments beforehand. Nonetheless, such a design tool proved to be extremely useful, as the equations were shown to fit several different types of fabric armors and even composite panels [10,11].

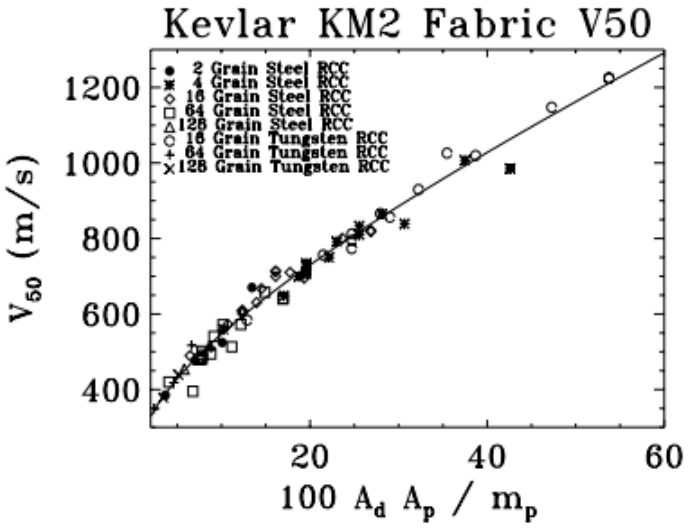

Figure 1.2. Ballistic limit V50 as a function of areal density ratio for different projectile sizes and materials. Image from Cunniff (1999) [10]

1.2.1 Cunniff Non-Dimensional Parameter

In the next iteration of the regression analysis, Cunniff proposed a non-dimensional parameter which collapsed all the ballistic limit data for soft armor panels composed of several different polymer fibers. This parameter, now informally known as the *Cunniff velocity*, effectively normalizes all the ballistic limit plots such that

$$\frac{V_{50}}{\sqrt[3]{U^*}} = f\left(\frac{A_d A_p}{m_p}\right) \tag{1.4}$$

$\sqrt[3]{U^*}$ is known as the Cunniff velocity, where U^* is given by

$$U^* = \frac{\sigma\varepsilon}{2\rho}\sqrt{\frac{E}{\rho}} = \frac{\sigma\varepsilon}{2\rho}c_0 \tag{1.5}$$

where σ and ε are the fiber failure stress and strain respectively, E is the longitudinal fiber modulus, ρ is the fiber density, and c_0 is the longitudinal wave speed. The significance of this parameter comes from the fact that the ballistic performance of the soft armor target panel can be predicted with its constituent fiber properties. Equation 1.5 then effectively provides a merit parameter for comparing the expected macro-scale performance of panels made of these micro-scale fibers.

1.2.2 Decoupled response of soft body armor

In another significant study, Cunniff proposed that the total energy absorption E_{abs} of an armor system as the sum of two main energy-absorption mechanisms [10, 12]: an elastic strain energy function Ω, typically dominant at velocities near the system's ballistic limit; and an inelastic impact function ξ, largely dominant at velocities past the ballistic limit.

$$E_{abs} = \frac{1}{2}m_p\left(V_s^2 - V_r^2\right) = \Omega + \xi \tag{1.6}$$

$$\Omega = \frac{1}{2}m_p V_c^2 e^{-X_3\left(\frac{V_s}{V_c}-1\right)^{X_4}} \quad \text{for } V_s \geq V_c \tag{1.7}$$

$$\xi = \frac{1}{2}X_2 A_d A_p V_r^2 \quad \text{for } V_s \gg V_c \tag{1.8}$$

At striking velocities below or near the ballistic limit, the major energy-dissipation mechanisms involve fiber axial strain energy and kinetic energy, as well as through-thickness kinetic energy when the fabric system is moved in the out-of-plane direction

[13,14]. Cunniff, in his various studies on soft armor impact ([9,10,12]), has described this portion of energy absorption as *elastic*. The energy absorbed by the material per unit mass may be interpreted in Equation 1.5 as being carried away from the impact site at the speed of sound in the material .

Past the ballistic limit, these elastic strain energy mechanisms start to become less significant, while localized (henceforth described as *inelastic*) failure modes start to take over. The energy does not get transferred rapidly enough away from the site of impact and is further prevented from dissipating due to localized damage to the material. In this high impact velocity regime, the amount of striking kinetic energy absorbed via the fabric strain energy mechanism is assumed to be a decreasing function of striking velocity.

More importantly, it was found experimentally that the impact response of a soft armor panel is decoupled in the through-thickness direction i.e. upon impact, the strike-face plies of a multiple-ply armor system respond as if they were not backed by the remaining plies of the system [12]. At the critical velocity V_c of the entire armor system, the impact velocity of the projectile on these initial few plies is much higher than their respective critical velocities, and therefore they fail inelastically before absorbing any significant amount of strain energy. In this regime, the main energy absorption mechanism is via kinetic energy transfer and the areal density of the target is the critical parameter. This can be demonstrated from the fact that the ballistic limit of a 24-ply target panel is extremely well-approximated with shot data for a 12-ply system. The V50 of the 24-ply system was shown to be equal to the striking velocity onto the 12-ply system that results in a residual velocity equal to the 12-ply system.

In view of the decoupled response of the target panel where the frontal strike-face portion responds inelastically, it was further shown that a portion of these frontal layers may be replaced with a material with other desirable properties such as low cost or ease of manufacturing, as long as the areal density is preserved. It should be noted, however, that when the areal density ratio is sufficiently small (i.e. larger

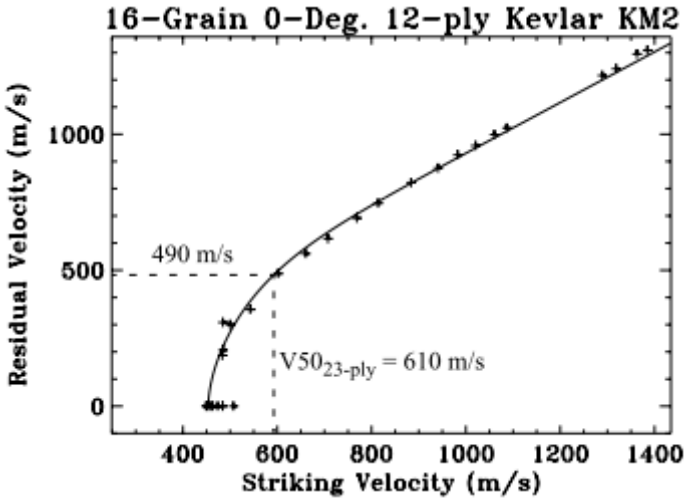

Figure 1.3. V_r-V_s curve for 12-ply system showing the decoupled response, which allows for a good estimation of the 23-ply system (24-ply data was not available according to Cunniff). Image from Cunniff [12].

projectiles or low number of plies), the response is still largely dominated by elastic mechanisms.

The experimental observation of a two-stage penetration process indicates a diphasic response, especially when impacting composite panels. In most of these composite panels, the two failure mode regimes are rather well-defined [15–20] and decoupled. The initial transverse shear mode is easily observed via sectioned views, and in this regime, they often exhibit localized failure or fiber fracture. The subsequent onset of elastic energy dissipation at the rear side is demarcated by the presence of composite delamination, where the remaining target material exhibits a pyramidal tent, and failure modes tend to be tensile. Ćwik et al. [20, 21] performed 20-mm FSP shots on Dyneema® HB26 and explicitly defined a First Major Delamination (FMD) within a composite target panel upon ballistic impact as the boundary between the frontal inelastic portion of the panel and the rear elastic membrane portion. Interestingly, at low striking velocities, the FMD occurs approximately 1/3 of the panel thickness from the strike face, but with higher striking velocities, the FMD gradually moves

to about two-thirds of the thickness. Karthikeyan & Russell [18] investigated the impact response of steel spheres on Dyneema® HB26 composite panels and proposed the idea of a proximal (or strike-face) and distal region. In the proximal strike-face region, fiber fracture (i.e. localized failure) was shown to be one of the dominant failure mechanisms; in the distal region, membrane stretching, delamination, pull-out etc. were dominant features, indicating responses related to elastic properties.

In other recent works, Heisserer et al. [22] studied the depth of penetration into thin and thick Dyneema® HB26 ultra-high molecular weight polyethylene (UHMWPE) composite panels with hardened steel spheres and demonstrated a distinct impact response behavior difference in the specific energy absorption per ply. Zhang et al. [23] provided CT-scans of post-impact HB80 panels under ballistic impact, which reveal the obvious two-stage decoupled response in the thickness direction. Yang & Chen [24, 25] investigated the energy absorption mechanism and failure mode of each constituent layer in a soft armor panel and determined the number of frontal perforated layers to be consistent regardless of panel thickness, although their impact velocities were not necessarily at the panel's ballistic limit.

Replacement of the strike-face portion with some other material may bring about some beneficial properties of the overall system as well. For example, Pyrex® borosilicate glass/KM2 fabric [12] and A-110AT titanium alloy/nylon fabric [26] hybrids have shown to improve the ballistic performance of the target panel over the full fabric panel equivalent due to the superior properties of the strike face material, but this improvement is not always sustained across different strike face ratios. In the case of Pyrex®/KM2 hybrids, their performance at larger areal density ratios is superior to a full fabric panel of equivalent areal density (Figure 1.4). However, at lower areal density ratios, the performance notably decreases and eventually the full fabric system outperforms the hybrid system.

This difference in performance was attributed to projectile deformation —at larger areal density ratios (i.e. smaller projectiles), the projectiles were hypothesized to deform upon impact with the glass, while larger projectiles tend not to deform as

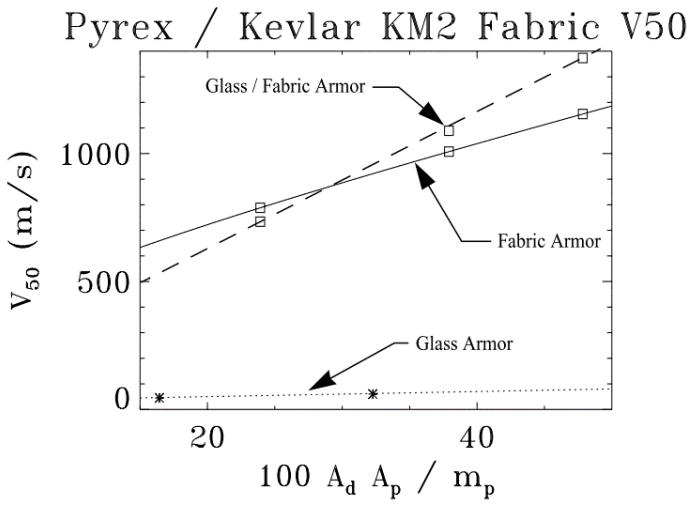

Figure 1.4. Ballistic performance comparison of bi-material hybrid Pyrex®/KM2 system vs full fabric KM2 system. Note that the superior performance of the hybrid is not sustained across all areal density ratios. Image from Cunniff [12].

significantly. The effects of projectile strength and micro-scale geometry are therefore another important aspect in the failure modes of these targets, which are not reflected in the longitudinal fiber properties utilized by the Cunniff parameter.

1.3 Research gaps

While prior works have been both extensive and intensive, it appears that some questions still remain unanswered. How do failure modes differ in the through-thickness direction of impact as the projectile perforates the system? How do the target's material properties determine its efficiency against ballistic impact? How do micro-scale properties and failure modes fully translate to macro-scale ballistic resistance? And more importantly, how do we avoid certain undesirable failure modes, or if they're inevitable, how can we take advantage of these differences in failure modes to optimize these body armor systems? Some of these research gaps are broadly highlighted as follows.

1.3.1 Failure mode progression through the layers

As this projectile perforates the soft armor target's layers at the ballistic limit, the failure modes start off being extremely localized at the strike face before gradually progressing to a more global, wave-controlled membrane deformation at the rear portion. This sort of localized failure mode was observed for ballistic impact on full soft armor packs and typically implies that the efficiency of these fibrous armor systems are greatly reduced, leading to the hypothesis that the Cunniff parameter (at the fabric and shoot pack-scale) and Smith velocities (at the yarn and fiber levels) may be further improved by considering these off-axis stress concentrations in their respective formulations. The modification and possible unification of the Cunniff parameter and the Smith velocity to reflect off-axis stress states is more major research component.

1.3.2 Strike-face material effects

If the localized failure of the target strike-face material is physically inevitable, it would be useful to examine how the material properties at the strike face affect the ballistic resistance and response, as well as the persistence of this localized failure mode in the through-thickness direction. Cunniff [12] previously stated that the frontal material may be replaced with a system of the same areal mass and still achieve similar ballistic performance, but the amount of high-performance fabric material that can be replaced and the effects on the ballistic performance has yet to be fully quantified. Moreover, while these soft armor systems show excellent resistance against ballistic impact, cut- and stab-resistance is another major requirement of these body armors [27], since these damage modes remain a viable threat to users of these armor systems. The feasibility of replacing the frontal material with a more stab-resistant material as well as knowing the fraction to which these high-performance fabrics can be replaced will no doubt be of great use in designing an efficient armor system. The systematic study of varying frontal material properties, and the amount of frontal

material that can be replaced are both equally important factors in the overall ballistic performance of the hybrid armor system.

1.3.3 Effect of projectile properties

The hardnesses of the projectiles used in previous literature are typically between Rc 28-32 [28], sufficiently hard such that they do not deform significantly upon impact with soft armor targets, if at all. However, the experiments performed by Cunniff [12] with small projectiles on Pyrex®/KM2 bi-material hybrids shows that projectile deformation may be significant under certain conditions, and existing literature is somewhat lacking in this aspect. Moreover, actual commercial bullets such as Full Metal Jackets (FMJs) and Jacketed Hollow Points (JHPs) are usually made of soft lead with a gilding copper jacket, which render them extremely deformable.

Apart from material properties, the dynamics and micro-scale geometric properties of the projectile are seldom studied in the impact of soft armor target systems. For example, the edge geometries of the impacting projectiles may initiate off-axis stress states within the impacted fibers. Additionally, in real world applications, soft armor targets may be impacted by projectiles with extremely high rates of spin and cause premature failure, which is another topic that is seldom explored by existing literature. From previous work performed within our group, it was shown that these off-axis stress-states significantly reduce the failure strength and strain of the constituent fibers [29–31], either through severe shear or torsion (Figure 1.5). At the macro-scale level, it is then of interest to determine how these geometric stress concentrations result in failure modes, and whether this has an effect on the diphasic response of the soft armor targets.

1.3.4 Diphasic armor response and design optimization

Following the principles of the progression of failure modes, a quasi-diphasic armor may be designed that instead takes advantage of the different failure modes to

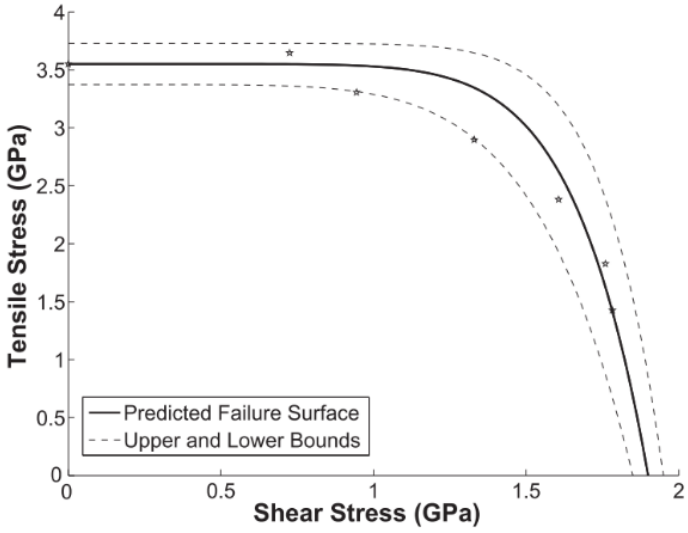

Figure 1.5. Tensile failure stresses at different torsional shear stress levels. Image from Hudspeth [31].

optimize the ballistic performance. In a recent advancement in composite technology, the X-hybrid panel architecture [32] produced by the Army Research Laboratory (ARL) consisted of a 75% by panel net weight strike face in a typical [0°/90°] cross-ply fashion. The remaining 25% of the plies comprised a quasi-isotropic layup in which every two succeeding plies are laid in a [0°/22.5°/45°/67.5°/90°] fashion. Presumably, this takes advantage of the inelastic failure modes on the panel strike face to dissipate the initial striking kinetic energy. This is followed by dissipating energy via elastic membrane strain energy, in which case the rotated plies provide a greater advantage by involving more armor material. The ratios of the two phases were obtained after several trials of testing and refinement, but a thorough knowledge of the fraction of the strike face inelastic response may give us more insight how to best design these armor systems.

The difficulties in answering these questions lie in the fact that the micro-scale material and macro-scale structural responses of these armor systems are coupled and highly nonlinear. Even with simplified models, current experimental, analytical, and computational efforts in the field of fibrous soft armor systems have not been able to

completely answer and fill some of the research gaps mentioned herein. Nonetheless, the following chapters are a compilation of the works published by the author in an attempt to answer (or at least, better understand) the underlying mechanisms of ballistic response and failure.

2. REVERSE BALLISTICS PENETRATION OF BALLISTIC FABRIC

Chapter adapted from prior published work. Z. Guo, J. Zheng, W. Chen, Reverse ballistics penetration of Kevlar® fabric with different indenters at different loading rates, Text. Res. J. 87(2017) 1165–1176.

Abstract

In this study, the mechanical load on a bullet-shaped indenter when impacted by a single-ply Kevlar fabric was experimentally investigated using a reverse ballistics method at both quasi-static and dynamic rates. Different indenter geometries, namely the 9mm Luger, .223 Remington, and .308 Winchester bullet geometries, were used. The penetration load of the stationary indenter was measured using a force transducer located behind the indenter, and the penetration load was then plotted against the impact velocity of the fabric sample. Different mechanisms of penetration were observed at different impact velocities. Penetration mechanisms were also found to be highly dependent on projectile nose geometry. A modified method to obtain an approximate ballistic limit based on the impact loads was used to compare the efficacy of different geometry types.

2.1 Introduction

The capability of a bullet-resistant ballistic fabric in stopping a projectile (typically measured using the V50 ballistic limit) during impact is dependent on several mechanisms such as fiber and fabric mechanical properties (e.g. density and tensile modulus), fabric weave structure, far-field boundary conditions, and projectile geom-

etry. The energy absorption mechanism of the fabric is dependent on the projectile striking velocity. Below the ballistic limit, there is limited to no penetration, implying that the striking velocities below that limit have zero residual velocity. Past the ballistic limit, the residual velocity is typically observed to increase rapidly for a small range of velocities before increasing relatively linearly with respect to the striking velocity at high velocities [10]. The change in residual velocity behavior across the whole range of velocities indicates a possible change in failure modes and energy-absorption mechanisms. In particular, previous studies have shown that at high velocities, the only dominant energy-dissipation mechanism is via tensile loading of the yarn [11,14]. Previous studies by Cunniff [9,14] and Hudspeth *et al.* [33] have shown that the effect of aperture size is negligible above the V50 limit, indicating that the damage done at high impact velocities tends to be localized. On the other hand, at velocities below the V50 limit, mechanisms such as inter-yarn friction and yarn-projectile friction etc. tend to play a part in dissipating energy as well, and these mechanisms involve a much larger zone of impact. The projectile geometry, in any case, accounts for differences in fabric ballistic performance [33], which is the reason that the destructive testing of bullet-resistant vests is dependent on bullet type and threat level.

The typical energy-absorption curve is characteristically μ-shaped i.e. the energy-absorption increases with striking velocity up to the V50 limit before decreasing for a range of velocities. Past the V50, the kinetic energy absorbed by the fabric system is calculated by subtracting the residual kinetic energy from the striking kinetic energy, thus the energy-absorption is dependent on the square of the striking velocity. A previous study by Cunniff [14] indicated a possible increase in energy-absorption again at extremely high striking velocities. Of interest in this study is the regime where the energy absorption decreases (when the striking velocity exceeds the V50) due to a change in absorption mechanism, and this regime is not well-studied. Insight into this regime would allow for more accurate modeling in future studies.

While normal ballistics allows us to measure the ballistic capabilities of the target fabric, the mechanics of the penetration process cannot be accurately examined.

Reverse ballistics (in which the typical target is launched at the projectile) provides us with more insight into the effects of the stopping power of the single-ply fabric on the projectile. Reverse ballistics experiments also have the advantage of removing the effects of inertia which are inherent in normal ballistics experiments when measuring the load on the projectile.

The aim of this study is to examine the resistive load on a projectile when penetrating a single layer of high-performance fabric, as well as investigating the effects of projectile nose geometry pertaining to the V50 ballistic limit by measuring the resistive load acting on the different geometries. Hockauf *et al.* [34] used a novel reverse Hopkinson bar to measure and characterize the loading profile on different indenter geometries when impacted by multiple layers of fabric. However, such a method may not be practical or feasible for a single layer of fabric, or for a wide range of velocities. Previous studies by Montgomery *et al.* [35] and Lim *et al.* [36] have also examined the effects of perforating a single-ply fabric using different projectile geometries, but the analyses were still largely fabric system-oriented rather than projectile-oriented.

2.2 Experimental procedure

The Kevlar® fabric samples were prepared from a Point Blank Pathfinder Special bulletproof vest manufactured in 2008 by Point Blank Body Armor. The fabric within the vest layers were 600d Kevlar® (specific fiber type was not provided by manufacturer), with an areal density of 175 g/m^2, weave density of 12.00×13.50 ends/picks per cm, and a fiber failure strain of 4.42±0.26%.

In order to launch the fabric sample, the fabric was fixed on a polyurethane foam sabot using a 3.2 mm (0.125 in.) thick PVC foam fixture ring, using epoxy to attach the fabric to the sabot at eight points around the circumference of the recess. Care was taken to ensure that the principal yarns themselves were not attached to the foam, only the corners located 45° from the principal directions were attached. The fabric sample and sabot are shown in Figure 2.1.

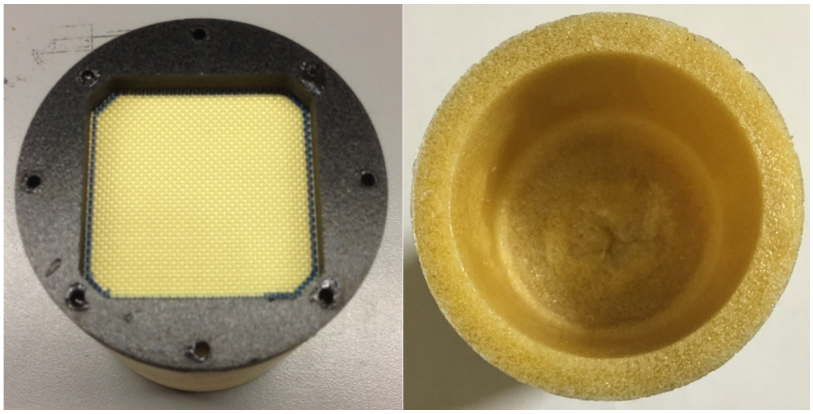

Figure 2.1. Kevlar® fabric fixed on polyurethane foam sabot using a PVC foam ring (left) and a 1.25-inch (32 mm) deep recess in the sabot (right).

Table 2.1. Bullet geometries used in the experiment.

Projectile	9mm Luger	.223 Remington	.308 Winchester
Profile	Elliptical	Ogival	Ogival
Diameter (mm)	9.01	5.70	7.85
Length (mm)	10.54	12.70	19.94

The fabric window measures 41×41 mm^2 (1.6×1.6 in^2), with a slight chamfer on the corners where the fabric is secured to the PVC ring and sabot. These dimensions were chosen to ensure maximum exposure area of the fabric within the gas gun bore without compromising the secure attachment of the ring-sabot interface with the fabric or the radial strength of the sabot. A larger window size is also desired to minimize the effects of the boundary on the load signal, especially at low striking velocities.

The indenters used in this experiment were 9-mm Luger, .223 Remington, and .308 Winchester snap caps manufactured by A-Zoom. These geometries were chosen because they represent a variety of shape profiles and presented areas, and are typically used in calibration and certification of bullet-resistant vests. These snap caps are made of hard anodized aluminum. The resultant impact force was recorded by a Kistler 5000 lb-f (22,246 N) force transducer located behind the indenter. Table 2.1 gives the dimensions of the bullet-shaped indenters.

The quasi-static experiments were performed using an MTS 810 servo-hydraulic system shown in Figure 2.2, with the crosshead speed varied between 1, 10, and 100 mm/s for one full loading-unloading cycle. An Interface 200 lb-f (890 N) force transducer located behind the indenter was used to measure the indentation load.

The dynamic experiments were performed using a high-pressure smooth-bore gas gun, with an inner bore of 63.5 mm (2.5 in.). A recess within the sabot was molded to ensure that the indenter only penetrates the fabric, which was not backed up by the polyurethane foam. A 51 mm (2 in.) thick ballistic shield was placed in front

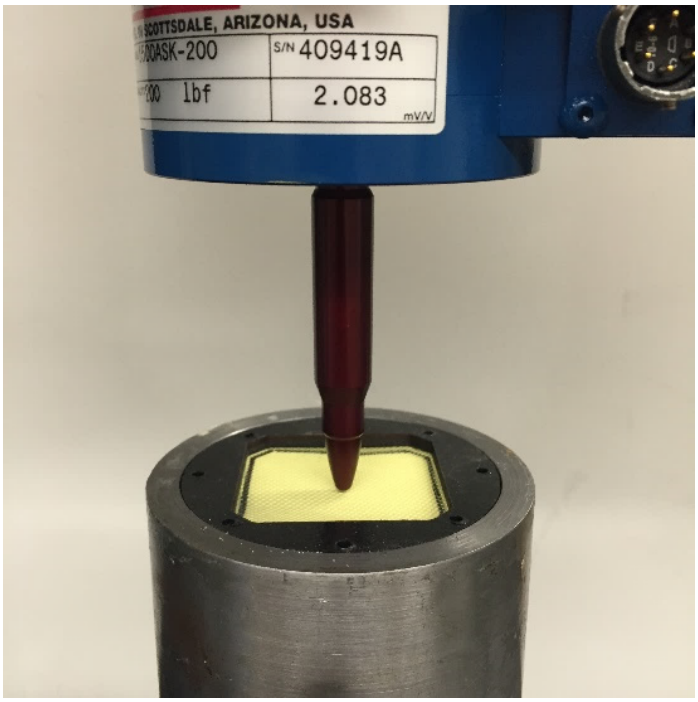

Figure 2.2. Quasi-static setup of reverse ballistics indentation experiment.

of the indenter, with the indenter tip protruding from a 0.75 in. through-hole, as in Figure 2.3. This ballistic shield serves as a protective barrier to protect the force transducer from impact damage, as well as ensure that any damage to the fabric only comes from the snap cap bullet tip and not the entire round. The corresponding striking velocities were measured using two pairs of laser diodes and sensors.

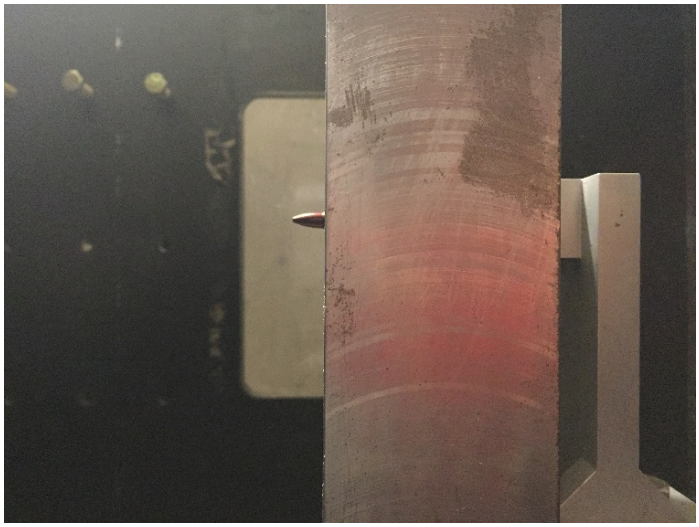

Figure 2.3. Ballistic shield with indenter protruding from through-hole.

In order to reduce the effects of the fabric sample's kinetic energy due to different masses in the dynamic experiment, the projectiles were molded and machined to have an average mass of 87.7±3.6 g. These were fired at velocities ranging from 29.5 to 245 m/s. A total of 45 samples were tested in the quasi-static experiments, with 5 samples tested per loading rate per indenter. A total of 36 samples were tested in the dynamic experiments.

2.3 Results & Discussion

2.3.1 Quasi-static experiments

At low velocities below the ballistic limit, the projectile does not penetrate the single-ply Kevlar® fabric. This implies that the main mechanism dissipating the ki-

netic energy, apart from yarn strain, is the pulling out of the principal yarns when impacted by the indenter. This yarn pull-out mechanism during quasi-static penetration of the indenter can be observed in Figure 2.4 below. Each curve represents the combined average load-displacement curve for 5 samples.

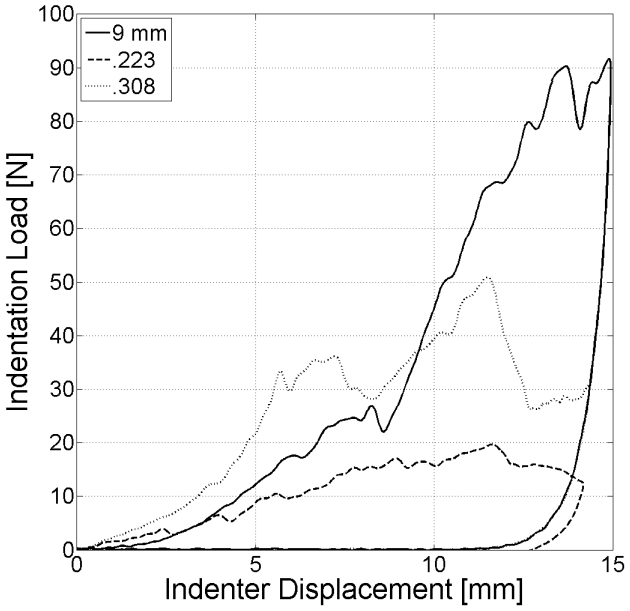

Figure 2.4. Averaged load signal for all indenters at 1 mm/s indentation rate.

The 9-mm indenter is observed to have the highest resistive load from the fabric during penetration, followed by the .308 and .223 indenters. For all three indenters, there is a slight oscillatory phenomenon occurring throughout the indentation process due to stick-slip when the yarns are uncrimping and translating. This phenomenon is reflected in Figure 2.5, which shows distinct yarn pull-out and uncrimping features along both the perpendicular warp and weft directions of the impact site.

As the indenter begins to push on the fabric during the indentation process, the initial portion is dominated by the uncrimping of the principal yarn. As the indenter moves further in, more yarns in the principal directions of the impact site begin to uncrimp. The number of yarns uncrimping and the rate at which they uncrimp

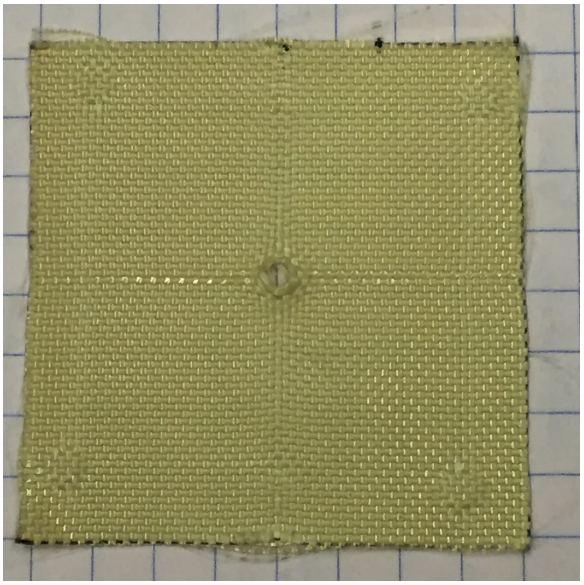

Figure 2.5. Yarn pull-out effects along both warp and weft (principal) directions in fabric impacted by .223 Remington indenter at 1 mm/s.

are dependent on the geometry of the indenter. Figure 2.6 illustrates how these geometrical differences result in their unique load histories, and a brief explanation of this mechanism is proposed. In the case of the 9-mm indenter, it has a larger radius of curvature at the nose-tip, which implies that the yarns are uncrimping and translating at a similar rate relative to each other. This results in a large peak near the end of the indentation loading cycle as all the yarns begin to translate at approximately the same time after being fully uncrimped, and this drop in yarn pull-out load signifies the start of the yarn-translating stage [37]. On the other hand, the sharper ogival indenters, while experiencing the same mechanism of yarn uncrimping/translating, cause the yarns nearer to the tip of the indenter to start translating while the remaining yarns in the impact zone are still being uncrimped with more of a "puncturing" type of movement. Instead of having the yarns uncrimp and translate at relatively the same time, the yarns take turns uncrimping (during which the pull-out load increases) and translating (during which the pull-out load decreases). A more drastic comparison would be between a flat-nosed projectile (infinite radius of curvature) compared to an extremely sharp cone (extremely small radius of curvature) and the projectile geometry effects are immediately seen.

Due to the different calibers and sharpnesses of the indenters, we propose to normalize the load signals by their respective presented areas A_p and normalized radii of curvature ρ_N, with some reference to Montgomery's previous work investigating the effect of nose geometry [35]. The normalized radius of curvature of the indenters is defined by

$$\rho_N = \frac{R^2/L}{2R} = \frac{R}{2L} \tag{2.1}$$

where R is the indenter bullet radius and L is the bullet length of the indenter. These calculated values are given in Table 2.2. By scaling and normalizing these geometries with respect to A_p and ρ_N, the indenter profiles are mathematically manipulated into one general shape (Figure 2.7). These two parameters are especially

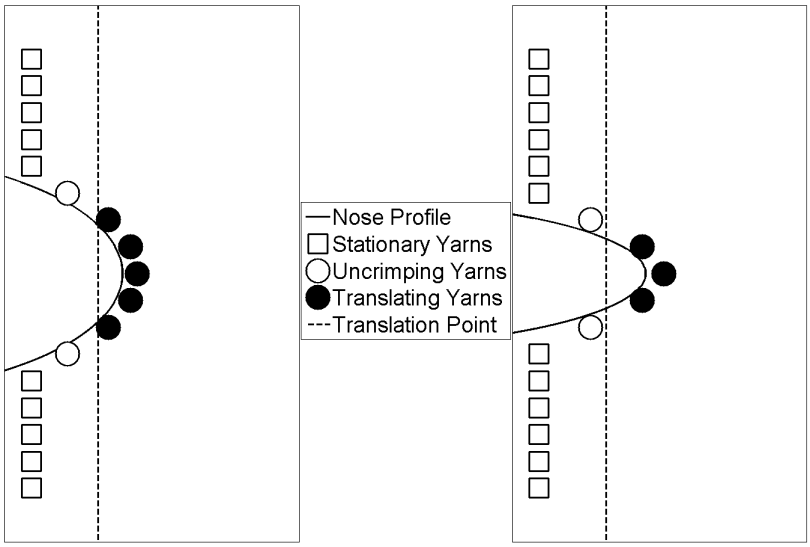

Figure 2.6. Yarn pull-out mechanism for a 9-mm Luger indenter with a larger radius of curvature (left) compared to a sharper .223 Remington indenter (right).

Table 2.2. Calculated geometric parameters.

Projectile	9mm Luger	.223 Remington	.308 Winchester
A_p (mm^2)	63.8	25.5	48.4
Radius of Curvature (mm)	1.93	0.640	0.772
ρ_N	0.214	0.112	0.098

effective since the indenter geometries can be accurately approximated with an elliptical curve. The post-normalization quasi-static indentation load for the data in Figure 2.4 is then reduced to that in Figure 2.8.

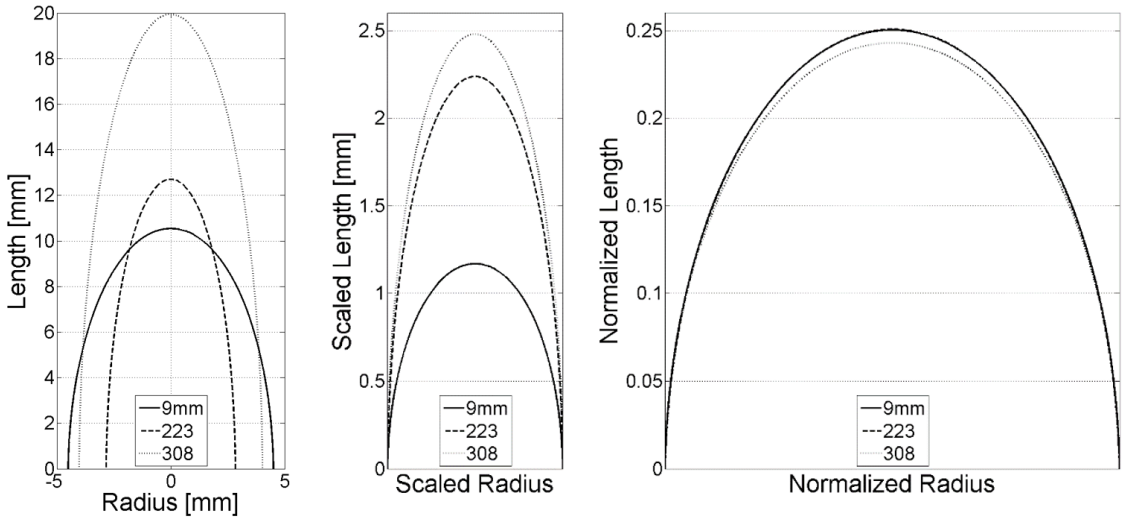

Figure 2.7. Diagram of original indenter geometries (left), geometries after scaling with respect to radius (center), and after normalizing with respect to A_p and ρ_N (right).

The quasi-static load histories at higher indentation velocities (10 and 100 mm/s) were observed to display similar trends (Figure 2.9), with the 9-mm indenter having the highest peak pre-normalization loads and the .223 having the lowest. These peak

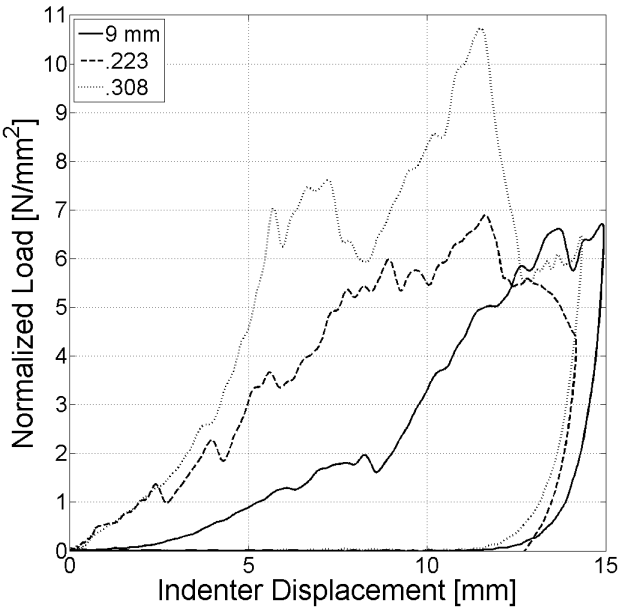

Figure 2.8. Post-normalization averaged load signal for all indenters at 1 mm/s.

load values were then plotted against loading rate as a comparison of the rate effects, demonstrating the efficacy of normalizing the load signal with respect to A_p and ρ_N.

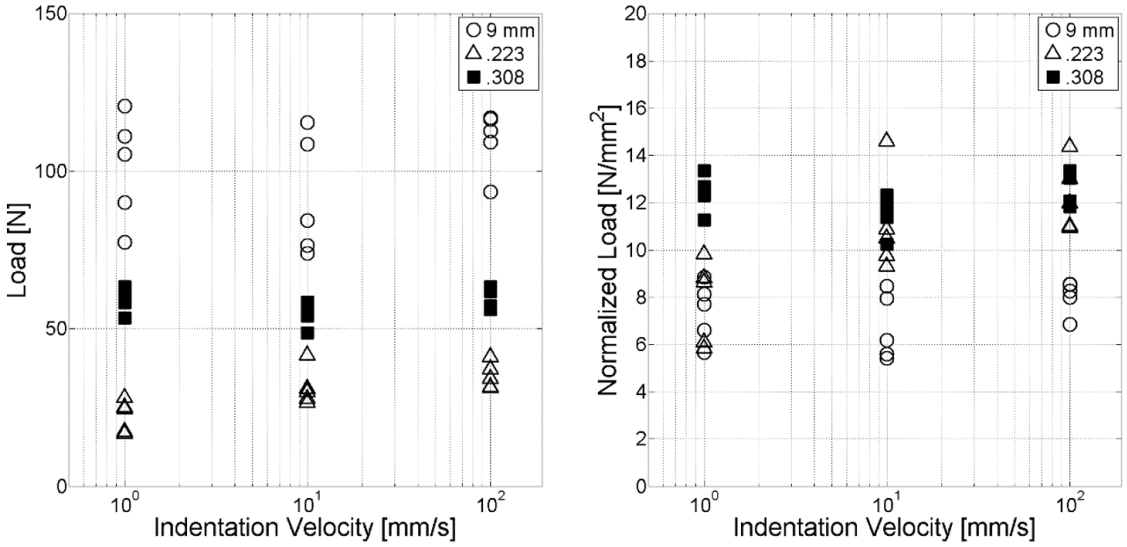

Figure 2.9. Peak indentation load vs loading rate pre-normalization (left), and post-normalization (right) with respect to presented area and normalized radius of curvature.

Within the range of quasi-static velocities tested, no significant rate effects were found, a trend reflected by a single out-of-plane yarn pull-out from the same fabric [37, 38]. Normalized peak load data is shown to have significant reduction in scatter compared to pre-normalization of the data as shown in Figure 2.9.

2.3.2 Dynamic experiments

Post-mortem qualitative analysis of the impacted fabric samples shows four main regimes of deformation mechanisms:

1. *No penetration.* At low velocities, samples only show slight dents and transverse deformation without penetration;

2. *Yarn pull-out.* Samples showing yarn pull-out effects demonstrate further transverse deformation, yarn uncrimping, and yarn translation, but without complete indenter penetration. The uncrimping and translation are visible along the principal yarn directions;

3. *Nose-through.* The fabric samples were shown to have been penetrated completely by the indenter tip, however the yarns appear to have just moved aside by the projectile 'nosing through' the fabric without fracture.

4. *Yarn rupture.* At high velocities, the yarns rupture at the impact site, and this is accompanied by nosing-through of the indenter (within the velocities tested) without significant yarn pull-out.

These four regimes are shown in Figures 2.10 to 2.12.

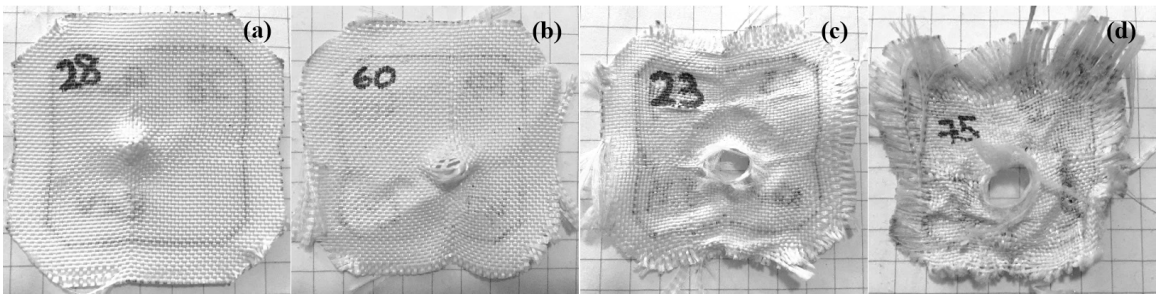

Figure 2.10. Four different regimes of impact for the 9mm Luger indenter – no penetration (a), yarn pull-out (b), projectile nose-through (c), and yarn rupture (d).

Note that these regimes are just a spectrum for qualitative analysis and there are overlaps in mechanism. In particular, any nosing through of the projectile through the fabric is typically accompanied with a certain degree of yarn pull-out, since the yarns have to be translated slightly from their original position. A typical dynamic experiment impact load signal obtained from these experiments is shown in Figure 2.13.

The dynamic load signal is within the order of 1 ms, a sufficiently long time for numerous longitudinal wave reflections, thus negating the need for longitudinal wave

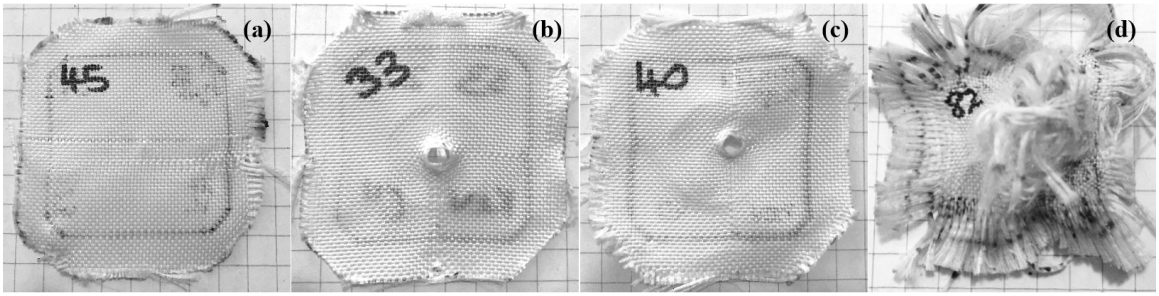

Figure 2.11. Four different regimes of impact for the .223 Remington indenter – no penetration (a), yarn pull-out (b), projectile nose-through (c), and yarn rupture (d).

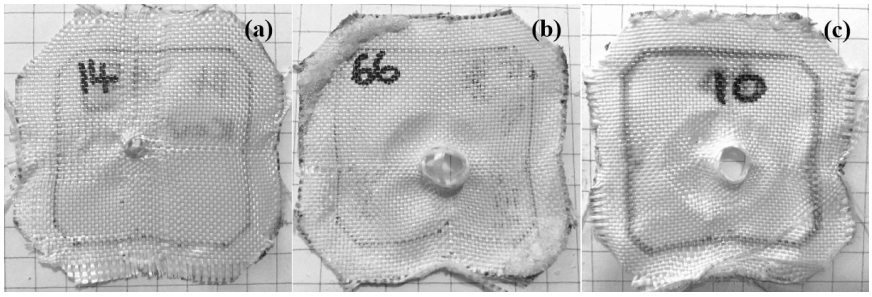

Figure 2.12. Three different regimes of impact for the .308 Winchester indenter – no penetration (a), yarn pull-out (b), and projectile nose-through (c). Yarn rupture was not observed within the samples obtained.

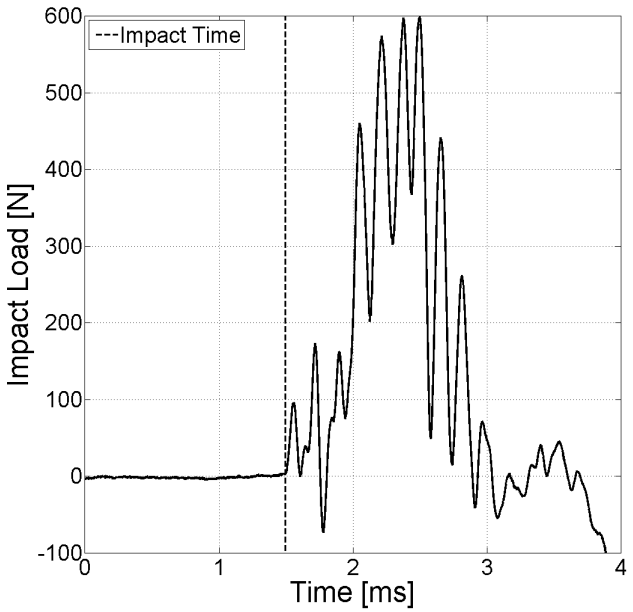

Figure 2.13. Impact load signal of dynamic reverse ballistics test with respect to time.

analysis. With the calculated striking velocity and the known distance between the laser diode and the indenter tip, the impact load can be verified as the first signal peak by calculating the time delay between the velocity trigger and the load signal data. Subsequent peaks are due to further crushing of the sabot and failure of the

epoxy, as well as any residual air pressure behind the projectile. Further discussion of impact loads is assumed to be about this initial peak unless stated otherwise. The impact loads were then plotted against the striking velocity for each indenter geometry, differentiating between the deformation mechanism regimes. These plots are shown in Figures 2.14-2.16.

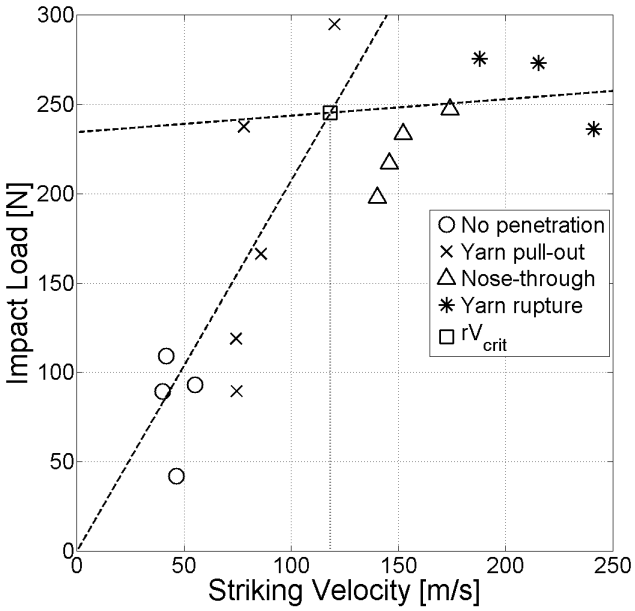

Figure 2.14. Plot of impact load vs striking velocity categorized by deformation mechanism regime for 9-mm Luger indenter.

Post-shot analysis of the indenter tips showed no visible deformation, thus the energy absorbed during impact due to tip deformation can be neglected. It can be observed from the impact load vs striking velocity plots that at lower velocities, the main mechanism resisting bullet penetration is the pulling out of yarns in the principal directions. In this low-velocity regime, the impact load increases due to yarn uncrimping and pull-out, and increases with striking velocity. As the striking velocity increases further, the deformation mechanism begins to shift towards the projectile nosing through the fabric or even yarn rupture. At these velocities, there

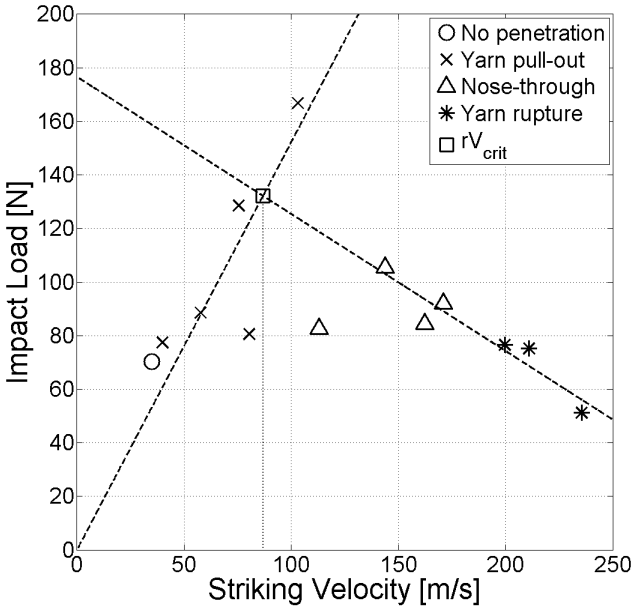

Figure 2.15. Plot of impact load vs striking velocity categorized by deformation mechanism regime for .223 Remington indenter.

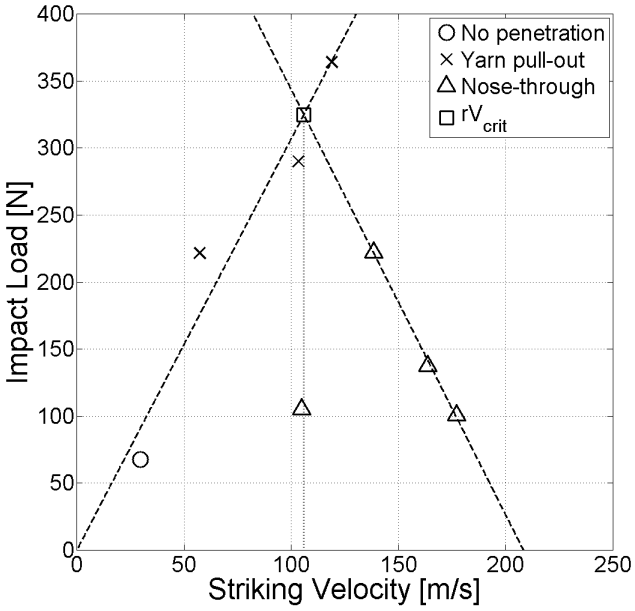

Figure 2.16. Plot of impact load vs striking velocity categorized by deformation mechanism regime for .308 Winchester indenter.

appears to be minimal yarn pull-out and the resistive impact load is observed to begin levelling out or even decreasing with respect to striking velocity. Due to its rounded geometry, the resistive load for the 9-mm indenter appears more scattered near the critical velocity, where any nosing-through of the projectile is also accompanied with more yarn pull-out compared to the ogive geometries of the .223 and .308 indenters.

From previous extensive studies by Cunniff [9–11], the ballistic limit is largely dependent on the areal density ratio of the armor system to the projectile in a forward ballistics setting. However, in a reverse ballistics frame of reference, the "projectile" is the indenter, and since the indenter is stationary in this study, the indenter mass in this case does not serve any practical meaning. Moreover, the residual velocity of the indenter or the fabric cannot be obtained practically in order to determine the fabric ballistic limit value. A modified method to quantitatively estimate the efficacy of the indenter geometry in penetrating the fabric system is therefore proposed.

In a typical normal ballistics experiment, the residual velocity is observed to increase sharply at the ballistic limit, indicating a sudden drop in resistive load acting on the projectile by the fabric. Similarly, from the impact load vs striking velocity curves, the load decreases sharply. However, there is no certain way of knowing where exactly the load would decrease. Compare Figure 2.15, where the load decrement is observed after the peak yarn pull-out load, to Figure 2.16, where the decrement is observed before the peak pull-out load. This suggests that there is a cross-over zone in which either mechanism could be in place. Near this zone of uncertainty, the projectile is either held back by the yarns pulling out, or it manages to nose through the fabric. There is a large peak load value due to the yarn pull-out mechanism (without full indenter penetration) as well as a local impact load minimum due to the indenter nosing through the fabric. This may explain the fact that in a normal forward ballistics test, the V50 is the point where statistically, the projectile has 50% chance of penetration.

Two linear fits were therefore performed on both the non-penetration (*No penetration* and *Yarn pull-out*) and the penetration regimes (*Nose-through* and *Yarn*

rupture) to obtain an estimate of the ballistic limit. From here on, this estimated ballistic limit lower-bound value will be termed the rV_{crit} so as not to confuse the term with the proper technical definition. Due to the crossover zone near the ballistic limit, when the projectile only has a finite probability of penetrating the fabric, penetration from the projectile nosing through causes the local load minimum, and therefore these significantly outlying points were excluded in order to obtain a proper R^2 value for the linear fits. The rV_{crit} values for the 9-mm Luger, .223 Remington, and .308 Winchester are 118.3, 86.8, and 105.8 m/s respectively.

2.3.3 Comparison between different mechanisms

The load histories during the impact process were examined. The impact time was determined as in Figure 2.13, while the time of complete penetration is estimated using the indenter nose length and the measured velocity. As the load histories for different indenters at different mechanisms look relatively similar, only the 9-mm Luger load histories are presented here for brevity. These plots have been time-adjusted. The *No penetration* phase is essentially just the yarn pull-out mechanism at low velocities and therefore not included below.

For the yarn pull-out mechanism, the load histories display two distinct peaks, similar to the quasi-static load histories in Figures 2.4 and 2.8. The first peak value appears to increase with an increase in striking velocity. As the velocity increases further past the rV_{crit}, the projectile begins to nose through the fabric, at which point the load history appears to smooth out over the impact duration. Increasing striking velocity results in a distinct single peak when the yarns rupture at the impact site. Similar to the reverse ballistics study by Hockauf *et al.* [34], an analysis of the impact energy was subsequently performed by integrating the area under the load-displacement curve, with the indenter displacement approximated using the striking velocity and the impact time. Figure 2.18 shows the integrated load-displacement energy curves.

The general trend of the impact energy appears to increase with striking velocity up to the rV_{crit}, after which the integrated load-displacement energy decreases as the striking velocity increases further. This curve is similar to the energy-absorption curve obtained from the residual velocities [14], as well as in comparison with the calculated missile kinetic energy loss versus striking velocity as performed explicitly investigated by Wilde [39] and Termonia [40]. The energies for the 9-mm Luger appear to be more scattered near the rV_{crit} because of the larger projectile presented area and radius of curvature resulting in a larger range of velocities where both yarn pull-out and nosing-through might occur. The ogival indenter energies are considerably much sharper at the peak near the rV_{crit}.

2.3.4 Comparison between different indenter geometries

In a forward ballistics scenario, the V50 limit is dependent on the areal density ratio of the fabric to the projectile, given by Cunniff [14] as $A_d A_p/m_p$, where A_d is the areal density of the armor system, A_p is the projectile presented area, and m_p is the projectile mass. In general, it appears that the change in V50 is relatively linear within a small areal density ratio range. However, there is a need to modify the equations with certain assumptions based on the differences in reverse ballistics experiments.

It can be assumed that within a small areal density range, the V50 varies linearly as a function of the areal density of the projectile [10]. The areal density of the fabric system is not necessary in this study as the same fabric is being used, and therefore reduces to a constant. Furthermore, in order to compare the effects of indenter geometry and not the striking kinetic energy, we require the mass to be the same in all cases, therefore the rV_{crit} is proportional to the presented area (in this reverse ballistics case, of the indenter).

With a blunter nose profile, the radius of curvature is larger and the rV_{crit} is expected to be higher, implying that the rV_{crit} is somewhat proportional to ρ_N. Since

the rV_{crit} is proportional to both A_p and ρ_N, the rV_{crit} value is plotted against the parameter $A_p\rho_N A_p\rho_N$. This parameter is also used in normalizing the quasi-static peak load values.

The linear regression has an R^2 value of 0.7894, which is a considerably good fit given the assumptions made in the analysis. While the data appears to vary relatively linearly with respect to $A_p\rho_N$, there are still insufficient data points for a conclusive fit. Further studies would provide further insight into the effects of the parameter $A_p\rho_N$ on the predicted rV_{crit} values.

2.4 Conclusions

A reverse ballistics method of investigating the effects of geometry on the penetration of a single-ply bullet-resistant fabric was developed, with the bullet as the indenter and the fabric as the projectile. At quasi-static loading rates of 1, 10, and 100 mm/s, yarn pull-out was the dominant mechanism in resisting the indenter. Load histories exhibit characteristics of yarn pull-out behavior that appear to be geometry-dependent. Normalization of the peak indentation loads with respect to the parameter $A_p\rho_N$ showed significant reduction in scatter across all indenter geometries and all loading rates.

Dynamic impact experiments of the indenters were performed with a smooth bore gas gun. Over the whole range of striking velocities, different mechanisms of indentation and penetration were experienced by the fabric, as evidenced by post-mortem analysis of the impacted fabric samples. At low velocities, yarn pull-out was the dominant mechanism in the resultant resistive force acting against the indenter; at high velocities, projectiles either nosed through the fabric or the yarns were ruptured.

Impact loads were shown to level off or decrease past a certain critical velocity, which coincides with the change in mechanism of penetration from yarn pull-out and no penetration to the projectile nosing through. The restrictions of the reverse ballistics method necessitated a modification to the usual method of determining the

V50 ballistic limit of a system by taking advantage of the distinct drop in energy absorbed by the fabric over the range of striking velocities to assume a change in gradient of the impact load vs striking velocity plot. Linear regressions for both regimes were performed to estimate a lower-bound of the V50, named in this study as the 'rV_{crit}'. Near this value, either the yarn pull-out mechanism dominates in preventing the indenter from penetrating, or the indenter manages to nose through the fabric, resulting in a drop in impact load. In a forward ballistics sense, this explains the statistical significance of the V50, where 50% of projectiles fired would penetrate the system.

Normalization of the rV_{crit} with respect to the parameter $A_p\rho_N$ again showed a good linear fit, suggesting one possible quantitative factor in determining the rV_{crit} (and indirectly, the ballistic limit for normal ballistics) is the sharpness. Further studies are recommended to investigate deeper into this phenomenon.

2.5 Acknowledgments

The authors would like to thank the U.S. Army, P.M. Soldier Protection and Individual Equipment, Technical Management Directorate for their support in this work. The authors would also like to thank Stephenie Martinez-Morales and Niranjan Parab for their help and contribution with the equipment and experiments.

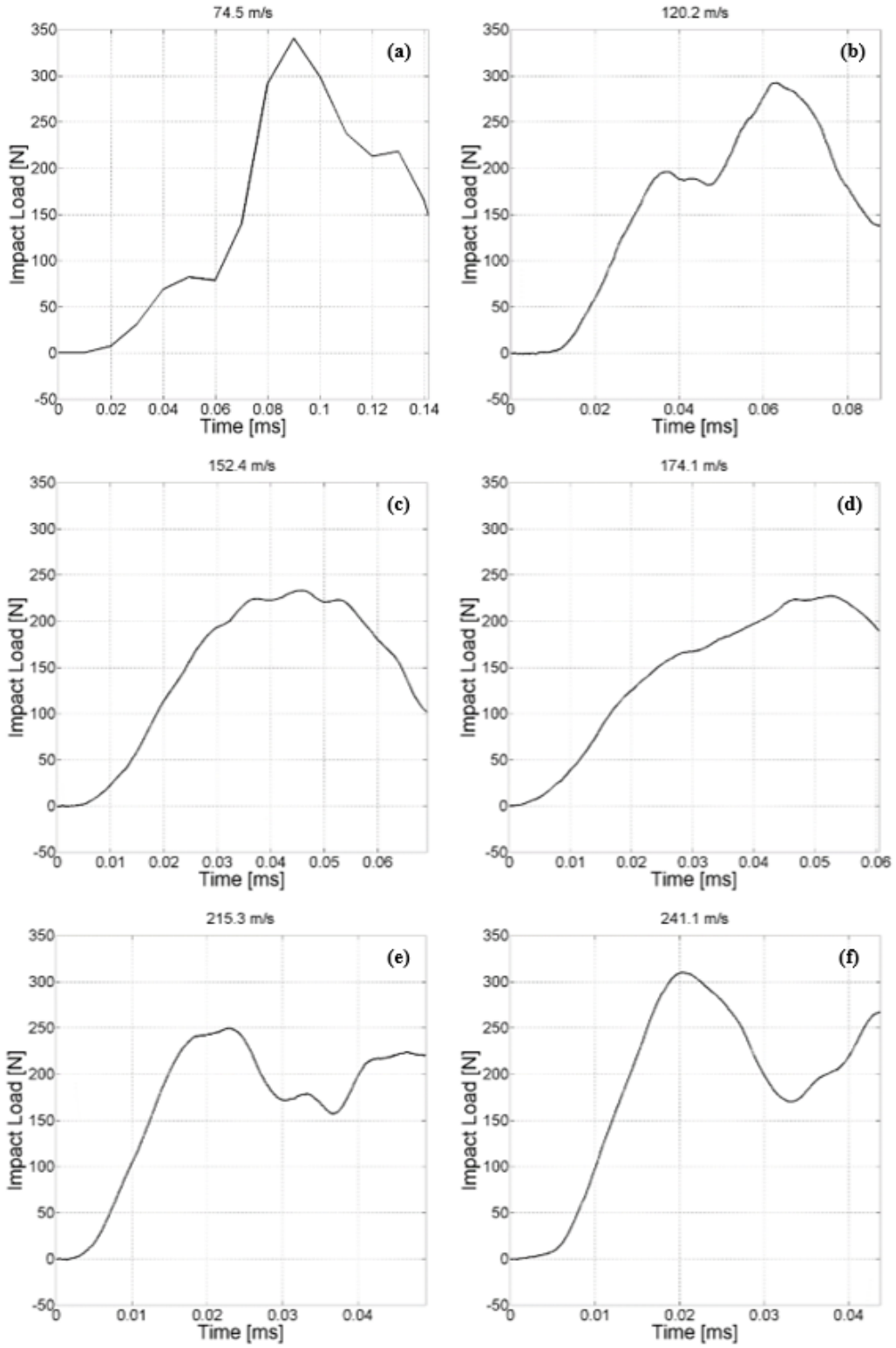

Figure 2.17. Load histories for the 9-mm Luger indenter arranged by increasing velocity for different mechanisms: yarn pull-out (a)-(b), nose-through (c)-(d), and yarn rupture (e)-(f).

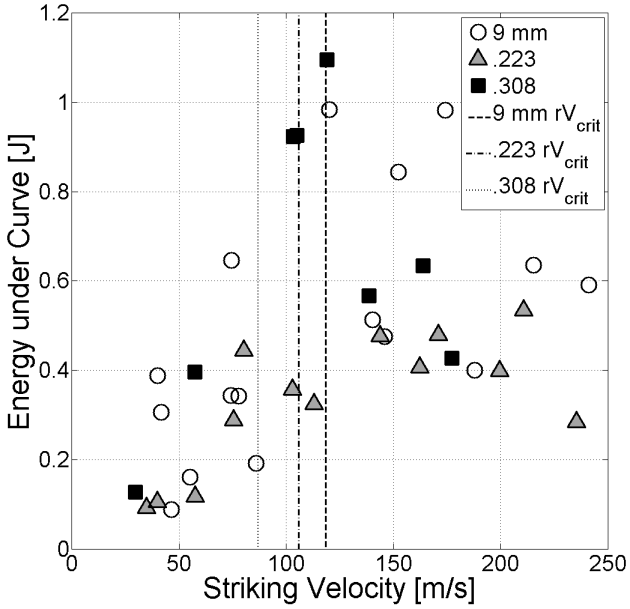

Figure 2.18. Energy vs striking velocity for all indenter geometries.

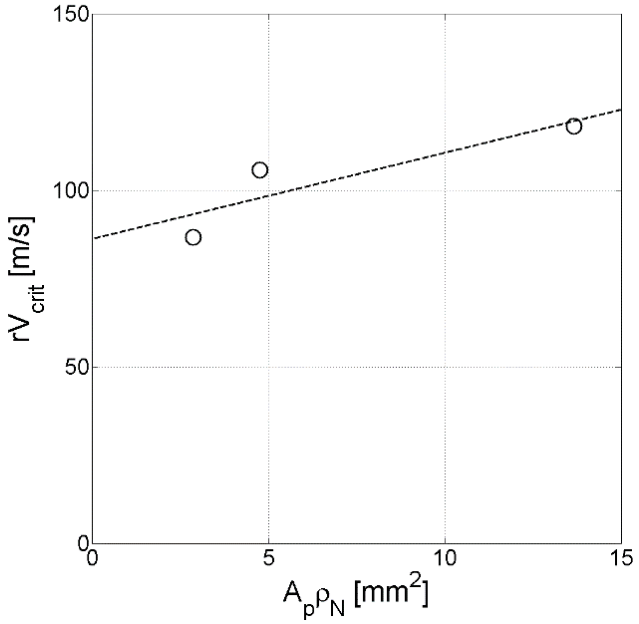

Figure 2.19. Plot of rV_{crit} against $A_p\rho_N$.

3. IMPROVED TWIN-FIBER TRANSVERSE COMPRESSION

Chapter adapted from prior published work. Z. Guo, W. Chen, J. Zheng, Improved quasi-static twin-fiber transverse compression of several high-performance fibers, (2018). doi:10.1177/0040517518775927.

Abstract

The method of determining the quasi-static transverse compressive response of several high-performance polymer fibers was improved upon from a previous twin-fiber transverse compression setup in order to detect small initial high compliance signals while maintaining consistent diametral compression. Two fibers were laid parallel between two polished tool steel platens, and the fibers were subsequently compressed using a piezo-electric actuator at quasi-static rates. The new experimental setup ensures that the compression cycle begins when extremely small load signals are detected so that initial elastic transverse moduli may be more accurately measured. Nominal stress-strain curves were obtained for several types of high-performance fibers. Results show good agreement with previously-obtained measurements. S-glass fibers exhibited a vastly different mechanical response compared to the polymer fibers.

3.1 Introduction

The excellent mechanical properties of high-performance fibers such as para-aramids (e.g. Kevlar®, Twaron®) and ultra-high molecular weight polyethylene (UHMWPE, e.g. Dyneema®, Spectra®), are the main reason why they are so widely employed in various fields. Extensive research has been done on real-world ballistic-

resistant applications such as engine fragmentation barriers and panels, and a large portion is especially devoted to studying their effectiveness as ballistic armor against projectile impact. Due to the way these fibers are typically manufactured and drawn, they tend to be highly-anisotropic, with their longitudinal and transverse properties varying by as much as one to two orders of magnitude apart [41–46]. It is surprising that while their longitudinal properties have been extensively researched and published, the transverse properties of these fibers have not been as extensively quantified in existing literature, despite the fact that nearly all impact on the fabric structures are from transverse/radial directions. Besides being a useful property for modeling ballistic impact into soft armor targets, knowing mechanical behavior is also useful for designing more efficient and effective manufacturing processes for textiles. Examples of such commercial applications may include fabric cutting, stamping, or pressing, all of which involve some form of diametral compression of the constituent fibers.

One of the earliest studies on anisotropic fibers was performed by Ward *et al.* as early as 1965 [41]. In this study, a single fiber was sandwiched between two parallel glass plates, and the load on the fiber was applied via weights on a lever arm. The corresponding contact width of the fiber with the glass platen at different load levels during compression was monitored under a microscope using interference fringe patterns. Kawabata [45] performed similar transverse compression experiments on aramid fibers using an electromagnetic power driver to indent the fiber and a force transducer to detect the applied load. Simultaneously, a linear differential transformer connected to the driver rod detects the displacement of the indenter plane. The setup was able to directly measure extremely small changes in initial elastic deformation. Recent fiber transverse compression experiments [46–49] were mostly based on slight modifications of Kawabata's experimental setup.

From these experiments, the load and displacement values may be obtained, and the nominal stress and strain values are calculated from there. Nominal rather than true stress/strain values are used since they require the experimental determination of contact width, which may not be easily-measurable.

$$\sigma_{nom} = \frac{F}{L \times d} \tag{3.1}$$

$$\varepsilon_{nom} = \frac{\Delta d}{d} \tag{3.2}$$

In the above equations, F is the applied load, L is the total gage length, d is the fiber diameter, and Δd is the compressed distance. Using Hertzian contact theory for diametral compression, the transverse elastic modulus is calculated via the equation first formulated by Jawad & Ward [50]

$$\varepsilon_{nom} \approx \frac{4\sigma_{nom}}{\pi E_t}\left(0.19 + sinh^{-1}\sqrt{\frac{\pi E_t}{8\sigma_{nom}}}\right) \tag{3.3}$$

The complexity of the equation means that curve-fitting is often used to estimate the transverse modulus E_t. The form of contact analysis in Equation 3.3 requires that the fiber be compressed in plane strain and assumes that the longitudinal modulus E_{11} is sufficiently large compared to E_t. Therefore, the reciprocal (i.e. compliance s_{11}) is sufficiently small and can be neglected. Hertzian analysis also requires that the contact width between the fiber and the platen be small (and hence within the elastic regime), which may not be an easily-measurable quantity. This initial elastic response is extremely sensitive to any platen surface roughness, non-parallel compression, or any variations in fiber diameters [41]. In this regard, previous setups dealing with the transverse compression of a single fiber have presented several difficulties due to the small initial elastic deformation range. Phoenix and Skelton [44] experimented on the transverse compression of multiple fibers (one to four fibers). However, the methodology presents its own set of issues, as the tallest fiber is compressed first before the others, resulting in spuriously low values of calculated fiber moduli.

To address these problems, a twin-fiber experimental setup was built in a previous study by the authors [51]. The twin-fiber compression system ensures complete

initial contact with the compression platen, and that the loading state on both fibers is diametral by way of a load splitter. Verification of experimental accuracy was performed with gold fibers and then compared with numerical simulation results using ABAQUS. Transverse moduli values of Kevlar® KM2 and Dyneema® SK76 were given as 1.270 and 0.985 GPa respectively. However, the previous study aimed to achieve higher compressive stresses and mechanical responses of the fibers, at the expense of measuring the small initial applied loads with higher measurement resolution.

The aim of the current study is therefore to present an improved automated twin-fiber compression setup for more accurate initial load measurements and a more repeatable experimental procedure. A multitude of fibers typically used in ballistic applications were tested using this new setup: Kevlar® KM2, Kevlar® 29, Kevlar® 129, and Twaron® CT2040 (p-phenylene terephthalamide, or PPTA), Dyneema® SK75 and SK76 (ultra-high molecular weight polyethylene, or UHMWPE), AuTx (Russian aramid co-polymer, also known in some earlier literature as A265), Zylon® AS and Zylon® HM (p-phenylene-2,6-benzobisoxazole, or PBO), and 758 ZenTron® S-glass fibers. It is hoped that the transverse moduli values and experimental methodologies provided in this study would be useful for future modelling efforts.

3.2 Experimental procedure

3.2.1 Samples

The fibers and their respective fiber properties are given in Table 3.1. Fibers were kept in a cool, dark environment (approx. 15-27°C), except when taken out for sample preparation. Recorded relative humidity levels were between 15-35%. It is known that the mechanical properties of Zylon® fibers may degrade over time in certain conditions [52, 53]. To our best knowledge, the tested PBO fibers were not subjected to these conditions detailed in previous literature. Scanning electron microscopy (FEI Nova NanoSEM 450) was performed on a large section of yarn, and

Table 3.1. Fibers used in study. Plus/minus values indicate one standard deviation.

Fiber	Fiber Type	Diam. [μm]	No. of Samples
AuTx (A265)	RUSAR	9.28±0.17 [49]	25
Dyneema® SK75	UHMWPE	22.73±1.12	23
Dyneema® SK76	UHMWPE	15.94±0.27 [51]	41
Kevlar® KM2	PPTA	12.02±0.32 [51]	29
Kevlar® 29	PPTA	12.78±0.46	20
Kevlar® 129	PPTA	12.29±0.43	21
758 ZenTron®	S-Glass	14.26±0.10	22
Twaron® CT2040	PPTA	10.62±0.46	21
Zylon® AS	PBO	11.40±0.17 [54]	22
Zylon® HM	PBO	11.18±0.19	24

the pre-compressed diameter measurements were performed on random filaments at 20 different locations. Scanned fibers appeared to be uniform over lengths of at least 1 cm. Unless referenced from existing literature, the nominal diameters listed below were averaged over 20 measurements from the micrographs.

At least 20 samples of each fiber were tested, with certain fibers repeated more times for a statistically meaningful result due to larger errors. Erratic displacement signals were occasionally recorded, usually due to slightly off-axis placement of fibers on the platens — these tests were voided. Fibers were tested in batches of approximately 6-7 samples, and as much as possible, each batch was prepared from one single filament to reduce the effects of differing diameters.

3.2.2 Experimental setup

Fig. 3.1 presents a full schematic of the improved quasi-static transverse compression setup, as shown in Fig. 3.2. A Kistler load cell (Kistler 9712B50) measures

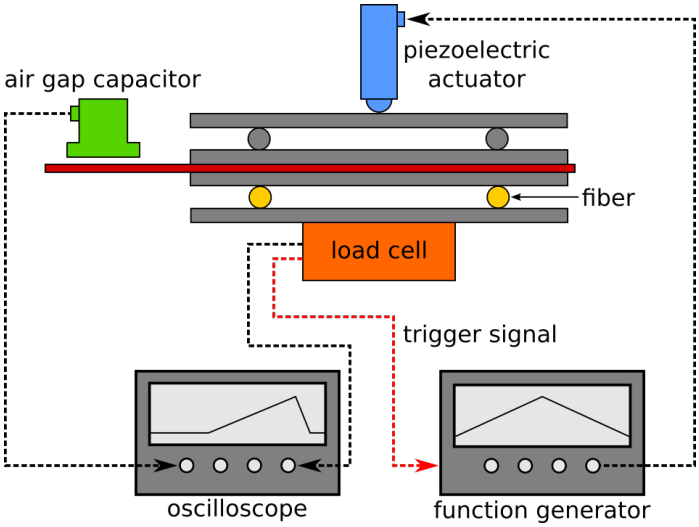

Figure 3.1. Schematic of twin-fiber transverse compression experimental setup. Dashed lines and arrows indicate input/output signals and signal directions, respectively.

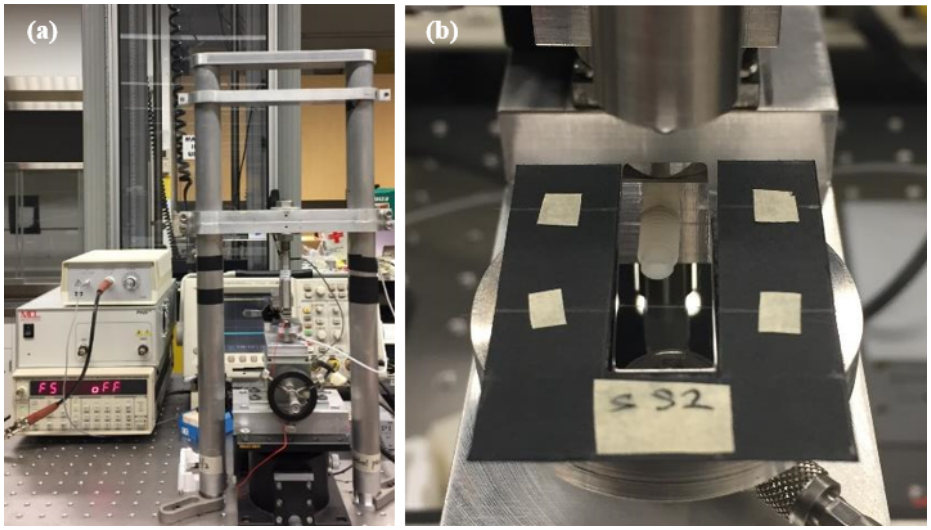

Figure 3.2. Full experimental setup (a), with sample fibers mounted on cardboard substrate on a tool steel gage block polished to a mirror finish (b).

the compressive load applied by the ball-tipped piezoelectric actuator (Physik Instrumente P-840.30, maximum uniaxial travel 45 μ m). As the fibers get compressed, the air-gap capacitive displacement sensor (Physik Instrumente D-510.050, maximum

resolution 2 nm) measures the displacement of the gage strip. The load splitter was designed using a Mitutoyo® tool steel gage block, with two 1 mm-diameter stainless steel dowel pins attached to the gage block using steel epoxy (J-B Weld). This ensures that the loads are applied directly and evenly above the two fibers. Although this setup eliminates the risk of the tallest fiber being contacted first, the fibers will inherently experience a slight pre-stress/pre-strain from the top platen. The total weight of the top platen, load splitter, and gage strip piece is 25 g, and for transverse moduli values on the order of about 1 GPa, the nominal pre-stress/pre-strain is on the order of 1-2 MPa and 3-5 mε respectively. The fibers had a gage length of 8.89 mm (0.35") and mounted on to a thin cardboard substrate using adhesive tape. Slight pre-tension was necessary to ensure kinks in the fibers were removed – this slight pre-tension was achieved with just the weight of the cardboard substrate alone (¡ 0.1 g). The transverse compression experiments were performed at a displacement rate of 0.45 μm/s for a total duration of 100 s. System compliance varied linearly up to approximately 1.1 μm for a 77 N load, or 0.014 μm/N. This was subtracted from the post-processed displacement curves.

Since the small initial elastic compression regime is of interest in this study, it was necessary to start the compression sequence upon a very small initial preload. The dilemma therefore lies with deciding the voltage measurement scale, because measuring small voltage changes (on the order of 1 mV) is usually done at the expense of measuring large overall load voltage signals, which is on the order of 1-10 V. To overcome this issue, the Kistler force transducer signal is first output to a Kistler (Type 5010) charge amplifier, which then outputs to two separate signal channels on a Tektronix MDO3014 oscilloscope: a large voltage scale signal to measure the overall compressive load voltage (typically 5-6 V), and a much smaller voltage scale to detect the small initial loads. A trigger level is then set for the small load voltage, which is typically set to a trigger load of 100 mN. Although lower trigger levels are possible, it becomes more susceptible to false-triggering via noise or voltage drift.

By raising the vertical stage upwards carefully, a small load is detected when contact is first made with the piezo-actuator. Upon detecting this initial load, a trigger out TTL (transistor–transistor logic) voltage is then output to a function generator (Stanford Research Systems DS335). This function generator provides an input voltage profile to drive the piezo-actuator. By using frequency-shift keying with the appropriate frequency levels on the function generator, a triangular pulse of 5 mHz frequency is started when the TTL level is 'high' (i.e. above trigger load) and zero frequency when the TTL level is 'low' (i.e. no load). The advantage of this setup lies in its self-sustenance: when the compressive load signal is above the trigger load of 100 mN, the TTL signal remains 'high' and the piezo-actuator continues pushing. When the piezo-actuator starts retracting due to the triangular pulse, contact is immediately broken and the compressive load quickly drops to zero, thus interrupting any further input from the function generator.

3.3 Results & Discussion

The nominal stress-strain curve for a single Kevlar® KM2 transverse compression test is given in Fig. 3 below. An initial curved portion is observed during the initial elastic compression regime, which is where the Hertzian contact equation is used to curve-fit the data and obtain a transverse modulus value. Past the initial elastic point, the fiber starts to yield plastically to give a somewhat plateau-like shape, where mechanisms such as softening and fibrillation tend to occur [55]. Subsequently, as the fiber yields further, the nominal stress increases rapidly due to both material stiffening and geometric effects, which is similar to the densification response in cellular solids. Depending on the fiber, the nominal strain typically reaches a limit, which is where it geometrically resembles a flat ribbon. Much higher stresses are required to compress them to higher nominal strains past this point. Apart from glass fibers, the general shapes of the stress-strain curves for all other polymer fibers do not differ significantly.

Variations in stress-strain curves arise due to several main factors: slightly different initial loading states when placing them between the platens, slight differences in initial diameters (even if the samples were prepared from the same fiber) resulting in different loading profiles across the cross-section, and to some extent, transverse yielding modes, which tends to affect curve at high strain values. Care has been taken to ensure proper and uniform loading of the fibers, and the effect of different diameters was minimized by extracting the samples from the same filament. However, the large difference in length scales between the fibers and the testing platform mean that these problems are somewhat unavoidable, but may be mitigated via rigorous statistical analysis.

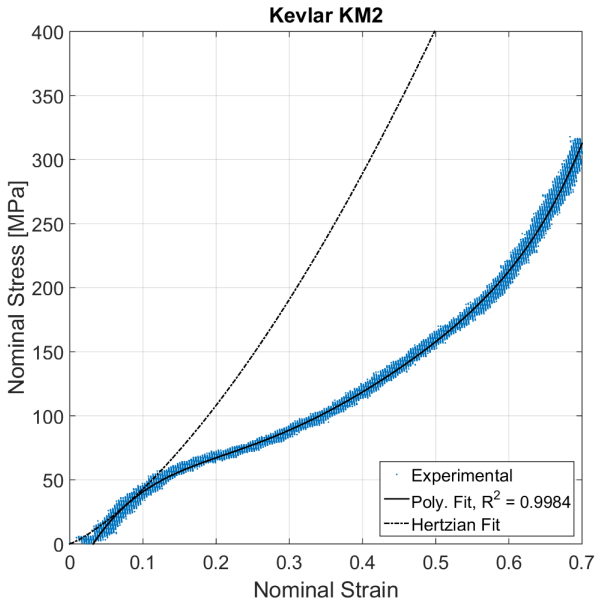

Figure 3.3. Nominal stress-strain curve for a Kevlar® KM2 twin-fiber compression test. A polynomial was used to fit the data for the full strain range, while a Hertzian fit (Equation 3.3) was used to find the transverse elastic modulus.

Proper data was first selected by removing 'bad' data samples that either produced nominal strains of larger than 1.0 or exhibited a reversal in nominal strain during the

loading process. These atypical results are usually indicative of tilting due to improper or unbalanced compression, and are therefore not included in the sample size listed in Table 3.1. Compression tilt was further verified via scanning electron microscopy, since the post-compression widths would be vastly different. With a complete dataset of at least 20 samples, each nominal stress-strain curve was subsequently fitted with a suitable cubic/quintic polynomial (except in the case of S-glass fibers where quadratic fits were used, which will be discussed later). As much as possible, quintic polynomials were used as they provide a better fit of strain values. Polynomial fits were sufficiently accurate as the R^2 values for a large majority of the fits were between 0.95-0.99. The mean nominal stress curves and 95% prediction bounds were then calculated using the curve-fitted polynomials and experimental standard deviations. It should be noted that the polynomial curves do not pass through the origin of the axes, as is expected of an ideal stress-strain curve. Forcing the polynomial through the origin point resulted in much poorer fits at larger strain values. Consequently, this constraint was relaxed and a separate Hertzian fit for the initial elastic portion was performed.

Due to the high sensitivity of the displacement capacitor, the signal-to-noise ratio of the initial small displacement portion renders it difficult to curve-fit the elastic portion without subjective judgment. In view of this issue, a method of estimating the transverse modulus and elastic limit was done via curve-fitting such that the Hertzian contact stress-strain given in Eq. 3.3 intersects the mean stress-strain curve tangentially. This assumes that the initial elastic Hertzian portion at small strains and the subsequent polynomial curve-fit at larger strains form a combined smooth spline. Physically, this method also appears to follow the experimental data well, as can be observed in Fig. 3.3 above. The fitted moduli and elastic limit values are given in Table 3.2. For comparison, the transverse moduli and elastic limits of similar fibers in existing literature are given as well. Average curves for each fiber type are presented in the subsequent sections.

Notably, there appears to be somewhat of a large deviation between reported and current experimental values for certain fibers such as AuTx, Dyneema® SK76, and

Kevlar® 29, although the values still lie within the same order of magnitude. In the case of Dyneema® SK76 and AuTx, this deviation can be attributed to the higher sensitivity of the current setup compared to the previously published experimental results, meaning that a smaller load resolution could be measured with our current setup. The same may be true for the results published for Kevlar® 29, however it is more likely that such an experiment lends itself to more variability. In fact, Singletary [46] reported an average value of 2.4 GPa, but single tests reported fitted values as low as 0.88 GPa.

Except for the ZenTron® S-glass fibers, the morphologies of the other polymer fibers are typically well-described as axially-oriented crystalline fibrils within a somewhat amorphous matrix. This unique structure lends to their highly-anisotropic nature. In the axial direction, the tensile strength and modulus of the fibers is dependent mostly on the fibrils; in the transverse direction, however, the response is dependent on the cross-sectional bulk properties. Factors such as the mechanical response of the crystalline and amorphous structures, and the packing arrangement, van der Waals interactions etc. play a role in the transverse stiffness. The degree of anisotropy is given in Table 3.2 as the ratio of longitudinal to transverse moduli (E_L/E_t). It should also be noted that the values for ZenTron® are reported as a range. This will be further discussed in its respective section.

Table 3.2. Reported and measured transverse moduli, elastic limits, and tensile moduli for comparison.

	E_t [GPa]		Elastic Limit [%]			
Fiber	Reported	Current	Reported	Current	E_L [GPa]	E_L/E_t
AuTx (A265)	1.83 [49]	0.905	-	7.90	140.51±2.32 [49]	155
Dyneema® SK75	-	0.666	-	2.73	113 [56]	170
Dyneema® SK76	0.985 [51]	0.483	2 [51]	8.48	132 [31]	273
Kevlar® KM2	1.270 [51]	1.251	5 [51]	4.07	84.62±4.18 [57]	67.6
	1.34 [57]					
Kevlar® 29	2.45±0.40 [46]	1.411	6.1±1.1 [46]	6.43	99.1 [11]	70.2
	0.77 [44]				101±6 [58]	71.6
Kevlar® 129	-	1.007	-	8.78	108.98±3.40 [59]	108
758 ZenTron®	-	0.221	-	N/A	93.8 [60]	0.997-1.05
		89.2-94.1				
Twaron® CT2040	-	1.168	-	5.25	90 [61]	77
Zylon® AS	-	0.574	-	7.49	180 [62]	314
					149.51 [54]	
Zylon® HM	0.91 [63]	1.290	-	6.25	270 [62]	209
					315.2 [63]	244

Table 3.3. Measured post-compression fiber widths with relevant statistics. Calculated theoretical nominal strains are included.

	Width [μm]				
Fiber	Average	Median	1 Std. Dev.	CV (%)	ε_{calc}
AuTx (A265)	15.77	15.88	1.06	7	0.53±0.06
Dyneema® SK75	47.76	47.19	3.63	8	0.62±0.09
Dyneema® SK76	41.68	47.19	3.42	8	0.70±0.27
Kevlar® KM2	20.43	20.71	1.34	7	0.53±0.07
Kevlar® 29	20.67	20.70	1.76	9	0.50±0.10
Kevlar® 129	20.82	20.83	1.60	8	0.53±0.09
758 ZenTron®	15.00	14.97	1.58	11	0.24±0.10
					0.16[1]
Twaron® CT2040	18.18	18.04	1.29	7	0.53±0.09
Zylon® AS	24.83	24.89	1.81	7	0.64±0.04
Zylon® HM	22.39	22.81	1.93	9	0.60±0.05

As a comparative estimate of the accuracy of the curve-fit approximation and of the improved compression setup, cursory statistical analysis was performed. The post-compression widths were measured using scanning electron microscopy (Nova NanoSEM 2000), and deformation processes were examined at the same time. The mean, median, one standard deviation, and the coefficient of variation (i.e. standard deviation divided by mean) are tabulated in Table 3.3 below. Arithmetic means and medians lie very close to each other, indicating rather closely bunched data points about a true central tendency, although larger differences are observed for the UHMWPE fibers.

Included in the table above is a calculated maximum nominal strain as a quick method of verifying that the compression results are reliable without relying heavily

[1]calculated using elliptical cross-section approximation

on other methods such as finite element simulations. Since the compression gage length is orders of magnitude larger than the fiber diameters, the fibers can be safely assumed to be compressed in plane strain. Assuming an initial cross-sectional circular area and a final quasi-rectangular cross-sectional area of the fibers, the final thickness of the compressed fibers can be estimated using mass conservation via the equation

$$t = \frac{\pi d^2}{4w} \tag{3.4}$$

where w is the final post-compression width as measured via scanning electron microscopy. However, due to the low compliance of S-glass fibers, the rectangular approximation overestimates the amount of compression as the final area is closer to an ellipse of width w, giving a final height that is more closely approximated by d^2/w. The theoretical maximum nominal strain as calculated using the measured dimensions is then given by

$$\varepsilon_{calc} = 1 - \frac{t}{d} \tag{3.5}$$

Due to variations in pre- and post-compression dimensions, the theoretical strains were calculated using extrema values of one standard deviation i.e. minimum and maximum diameters and widths within one standard deviation. The calculated strain for the S-Glass fibers using a rectangular and elliptical cross-sectional area are also given in Table 3.3. In general, the theoretical strain values approximate the experimental strain maxima reliably, and the final widths correlate inversely to the approximated transverse elastic moduli, which is to be expected. Although post-compression micrographs for each fiber type are presented in the subsequent sections, the current study is not focused on the deformed microstructure of the fibers.

3.3.1 PPTA – Kevlar® KM2, Kevlar® 29, Kevlar® 129, and Twaron® CT2040 fibers

Kevlar®, a para-aramid fiber, was first discovered and manufactured by DuPont in the mid-1970s, and is currently one of the oldest and most well-known high-performance fibers. As such, studies on their properties and microstructures are numerous. Twaron®, a similar para-aramid, is currently manufactured by Teijin. Due to their similarities in chemical structure and manufacturing process, their mechanical properties are not expected to vary significantly. In a previous study, KM2 was compressed using the same twin-fiber setup [51], although previous stress-strain signals may not have reflected the initial elastic regime accurately. Slight modifications in the setup are expected to improve the accuracy and reproducibility of previous results. The current Kevlar® KM2 transverse modulus and elastic limit values of 1.251 GPa and 4.07% are extremely close to the previously-obtained values of 1.270 GPa and 5%, indicating consistency and repeatability between experiments. The nominal stress-strain curve for KM2 is similar to the previously-obtained curve [51], though slight deviations are noted (Fig. 3.4). The stress-strain curves for Kevlar® 29, Kevlar® 129, and Twaron® CT2040 are also given in Figs. 3.4-3.7.

Using reference strain values of 20% and 40% for comparison, the current study gives nominal stress values of 75 and 170 MPa respectively, which is comparably close to the previous values of approximately 80 and 200 MPa respectively. The lower stress-strain values in this study are presumably due to more accurate initial load-displacement measurements. Sockalingam et al. [55] obtained quasi-static KM2 compression results of similar orders of magnitude, with an experimental maximum nominal stress of approximately 450 MPa at a corresponding nominal strain of 65%.

These PPTA fibers typically have a skin-core structure [46, 47, 64], and tend to deform in a ductile fashion. Previous studies have suggested a dependence of the transverse mechanical response on the thickness of the skin [46, 65]. Dobb & Robson [65] showed that Twaron® had a slightly thinner skin than the Kevlar® variants

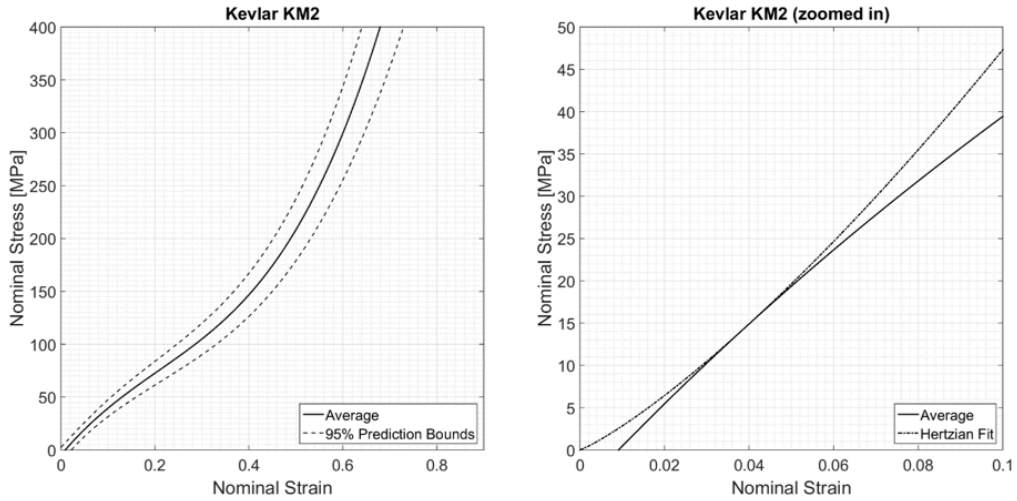

Figure 3.4. Nominal stress-strain curve of Kevlar® KM2 using cubic polynomial fit (left) and zoomed-in initial portion with Hertzian fit (right).

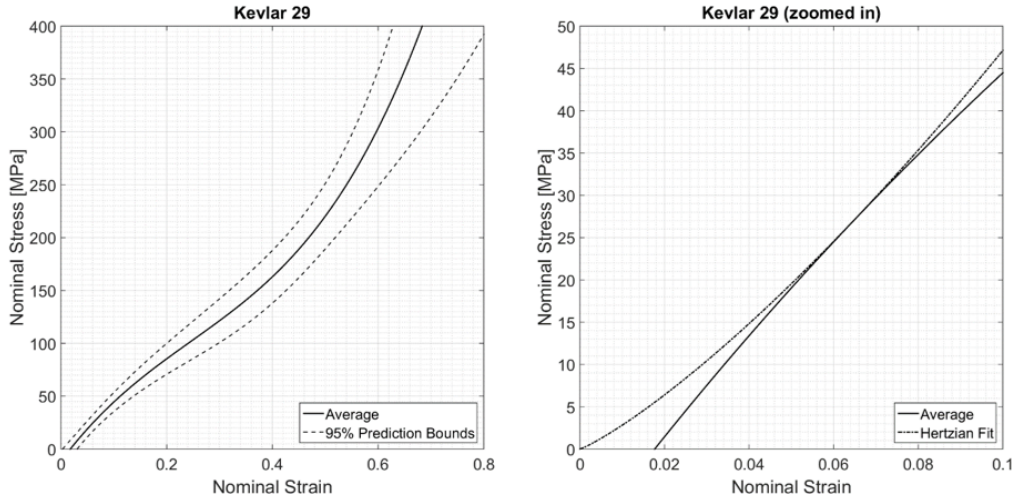

Figure 3.5. Nominal stress-strain curve of Kevlar® 29 using cubic polynomial fit (left) and zoomed-in initial portion with Hertzian fit (right).

tested (0.15 μm for Twaron® compared to 0.3-1.0 μm for Kevlar® 29). More core defects were also observed in Twaron®, which may explain the slightly lower transverse modulus of CT2040 compared to KM2 and Kevlar® 29. Post-compression micro-

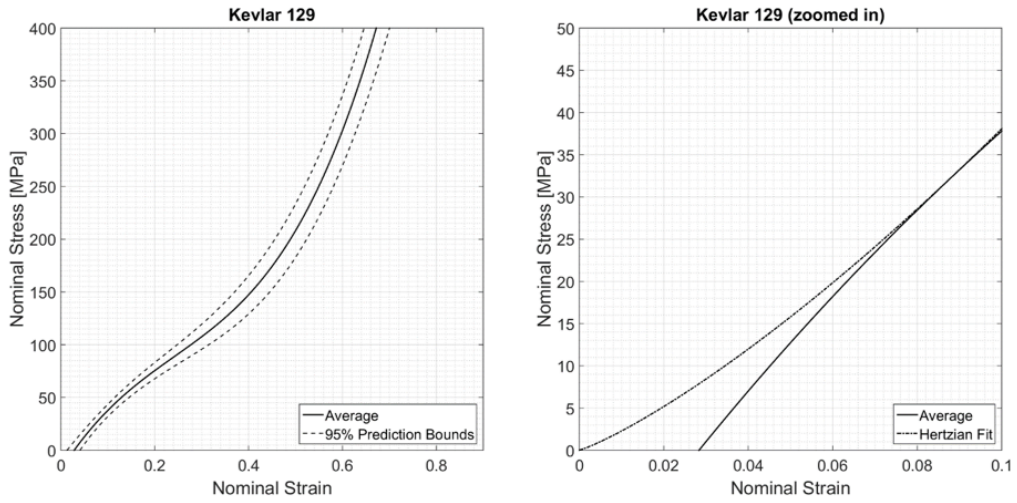

Figure 3.6. Nominal stress-strain curve of Kevlar® 129 using cubic polynomial fit (left) and zoomed-in initial portion with Hertzian fit (right).

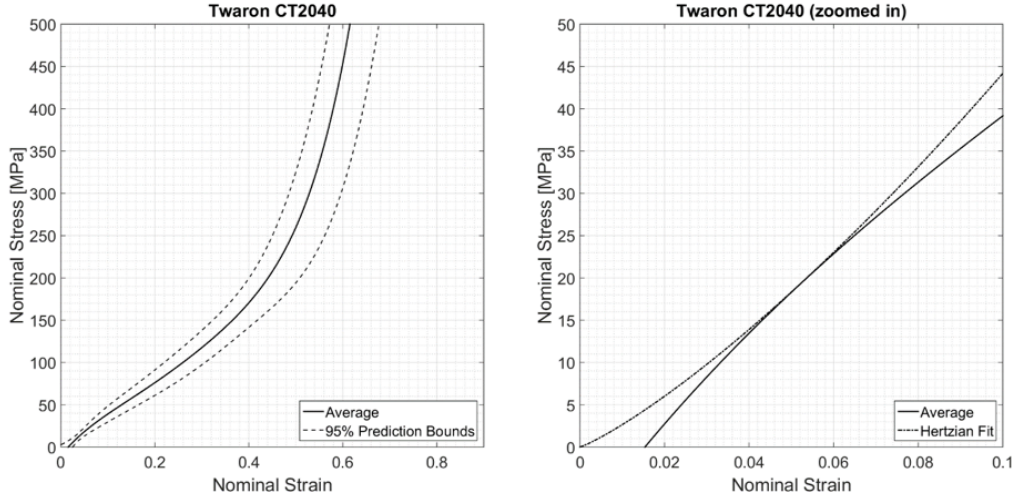

Figure 3.7. Nominal stress-strain curve of Twaron® CT2040 using quintic polynomial fit (left) and zoomed-in initial portion with Hertzian fit (right).

graphs of all variations of PPTA fibers did not exhibit significant features of interest. Fibers were compressed evenly along the whole gage length without any significant zones of fibrillation within the range of tested nominal strains. This is somewhat con-

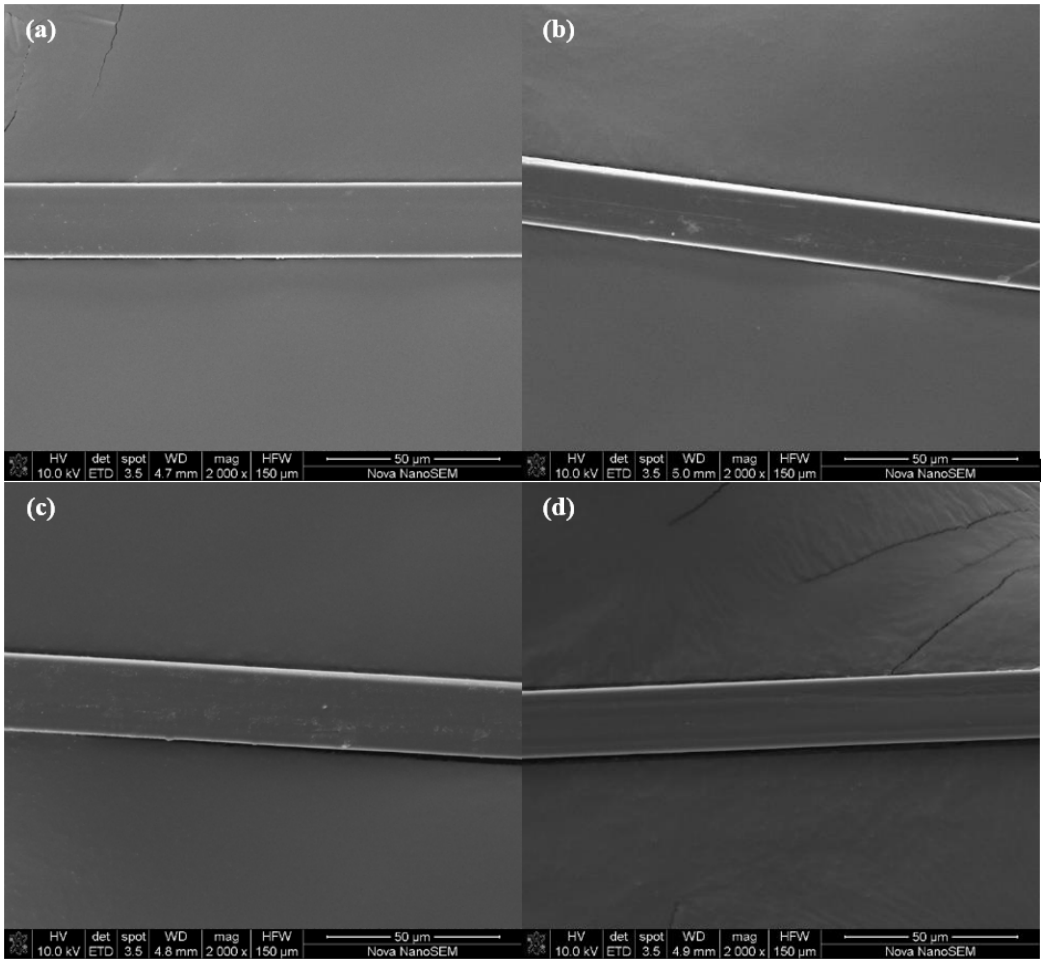

Figure 3.8. Micrographs of (a) Kevlar® KM2, (b) Kevlar® 29, (c) Kevlar® 129, and (d) Twaron® CT2040.

trary to the model of PPTA transverse compression response proposed by Singletary et al. [46], where major fibrillation is expected to occur at nominal strains of about 40% and beyond. Some visible lines can be observed running longitudinally down the axis of the fiber in Fig. 3.8 for Kevlar® 29 and Twaron® CT2040, which may suggest the onset of fibrillation.

3.3.2 UHMWPE – Dyneema® SK75 and Dyneema® SK76 fibers

Dyneema® SK75 is a multi-purpose grade fiber typically used in commercial marine applications such as ropes, nets, and mooring lines [56], while Dyneema® SK76 is ballistic-grade fiber most commonly-used in military applications. These polymer fibers are therefore engineered for their specific purposes, leading to slightly different mechanical responses as deemed suitable. The UHMWPE fibers tend to exhibit large experimental deviation compared to the PPTA fibers discussed previously, especially for Dyneema® SK76. The large variation can be attributed to their larger diameters compared to the other fibers tested in the study (approx. 16-24 μm), and their transverse moduli are known to be lower as well [2, 66].

Polyethylene is the simplest possible polymer that consists purely of carbon covalent bonds and hydrogen atom side groups, which also leads to very weak van der Waals' forces between chains. As such, the fibrils spread out much more easily under compressive load, leading to low values of initial elastic moduli of UHMWPE fibers. Post-compression micrographs exhibit behavior similar to previous observations by Marissen [2], who noted that Dyneema® filaments are able to deform and spread out transversely to a very large extent. In two extreme curvature cases, the Dyneema® filament was tied in a knot and stretched over a blade edge, only to result in transverse spreading rather than tensile failure.

Therefore, in contrast to the PPTA fibers, Dyneema® SK75 and SK76 exhibited obvious signs of fibrillation and fibril bunch spreading, as seen from the micrographs in Figs. 3.11 and 3.12. The degree of splitting and spreading did not seem to be related

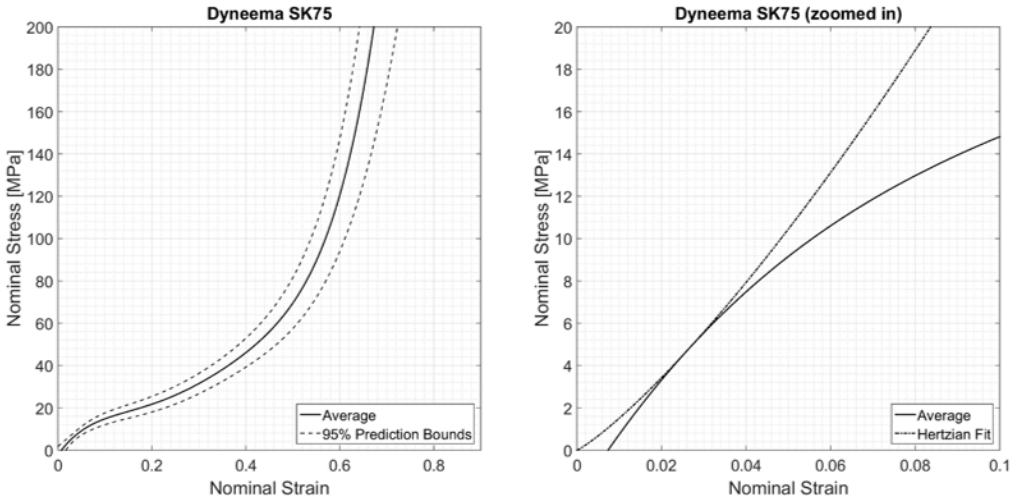

Figure 3.9. Nominal stress-strain curve of Dyneema® SK75 using quintic polynomial fit (left) and zoomed-in initial portion with Hertzian fit (right).

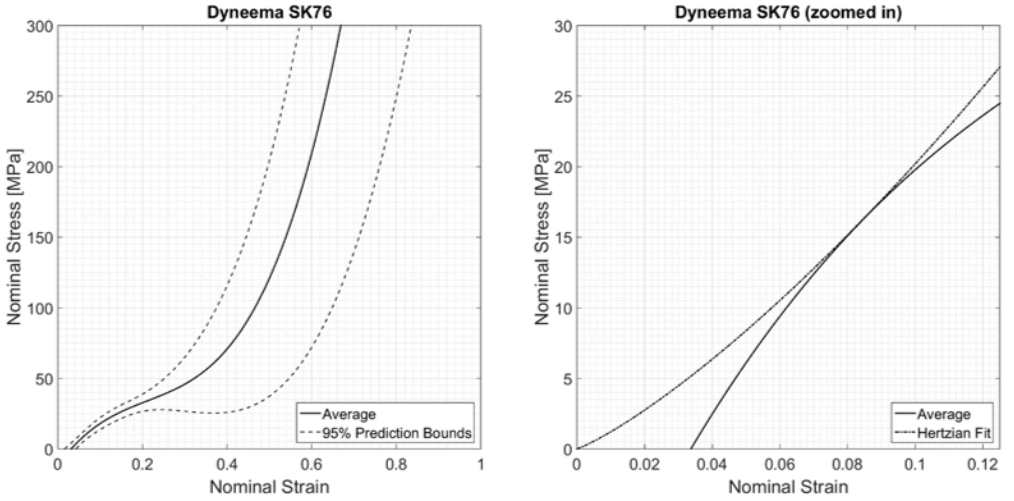

Figure 3.10. Nominal stress-strain curve of Dyneema® SK76 using cubic polynomial fit (left) and zoomed-in initial portion with Hertzian fit (right).

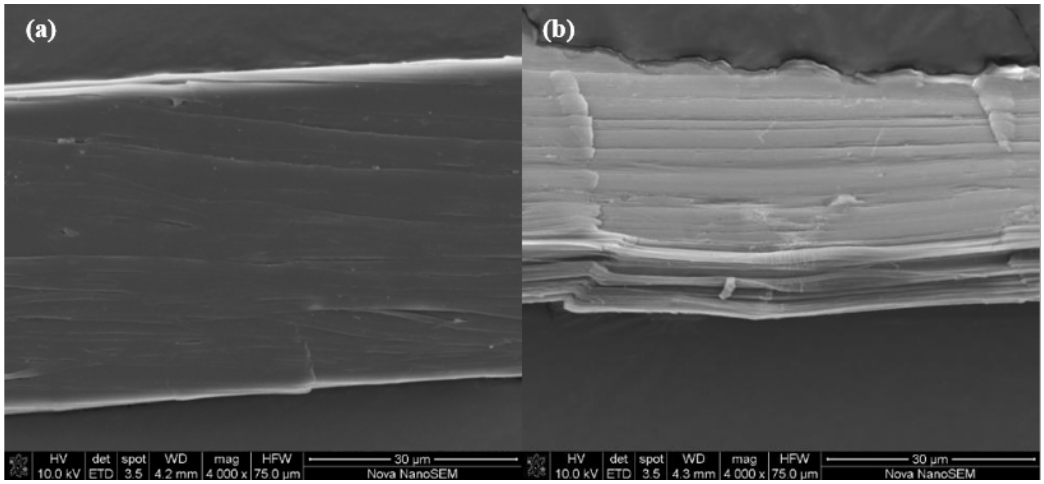

Figure 3.11. Different degrees of severe fibrillation and fibril spreading in SK75 after compression.

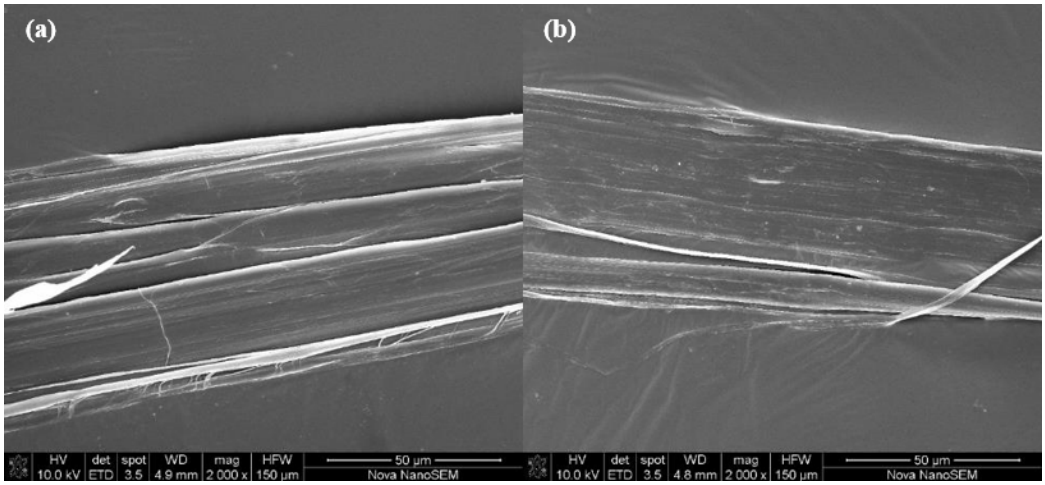

Figure 3.12. Zones of severe fibrillation of SK76 fibers after compression.

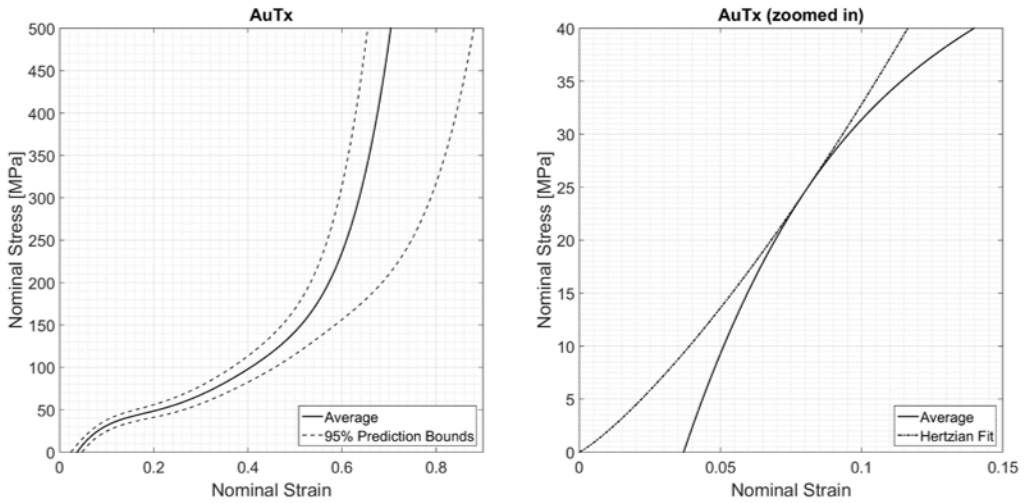

Figure 3.13. Nominal stress-strain curve of AuTx using quintic polynomial fit (left) and zoomed-in initial portion with Hertzian fit (right).

to the magnitude of nominal stress, as all the fibers were compressed to similar loads, and the fiber damage was not the same in both fibers for a single test. Some kink band-like structures were observed for SK75, although such observations were rare and possibly related to slightly uneven loading due to the much larger diameters.

3.3.3 RUSAR – AuTx fibers

AuTx is a high-performance Russian aramid (RUSAR) fiber, and is a co-polymer made up partially of PPTA, 5-amino-2-(p-amino phenyl)-benzimidazole, and other monomers [49]. The internal structure of AuTx consists mostly of large corrugated fibril bundles rather than single fibrils, with a typically cylindrical fiber shape [67].

At lower strains, the experimental results were consistent; at larger strains past approximately 40%, stress deviations become significantly larger (Fig. 3.13). This may be attributed to the sudden failure and fibrillation of the fibers past the 40% strain mark, as described by Singletary *et al.* for PPTA fibers [47]. The different degrees of fibrillation at about 60-65% maximum strain can be observed in the post-compression micrographs.

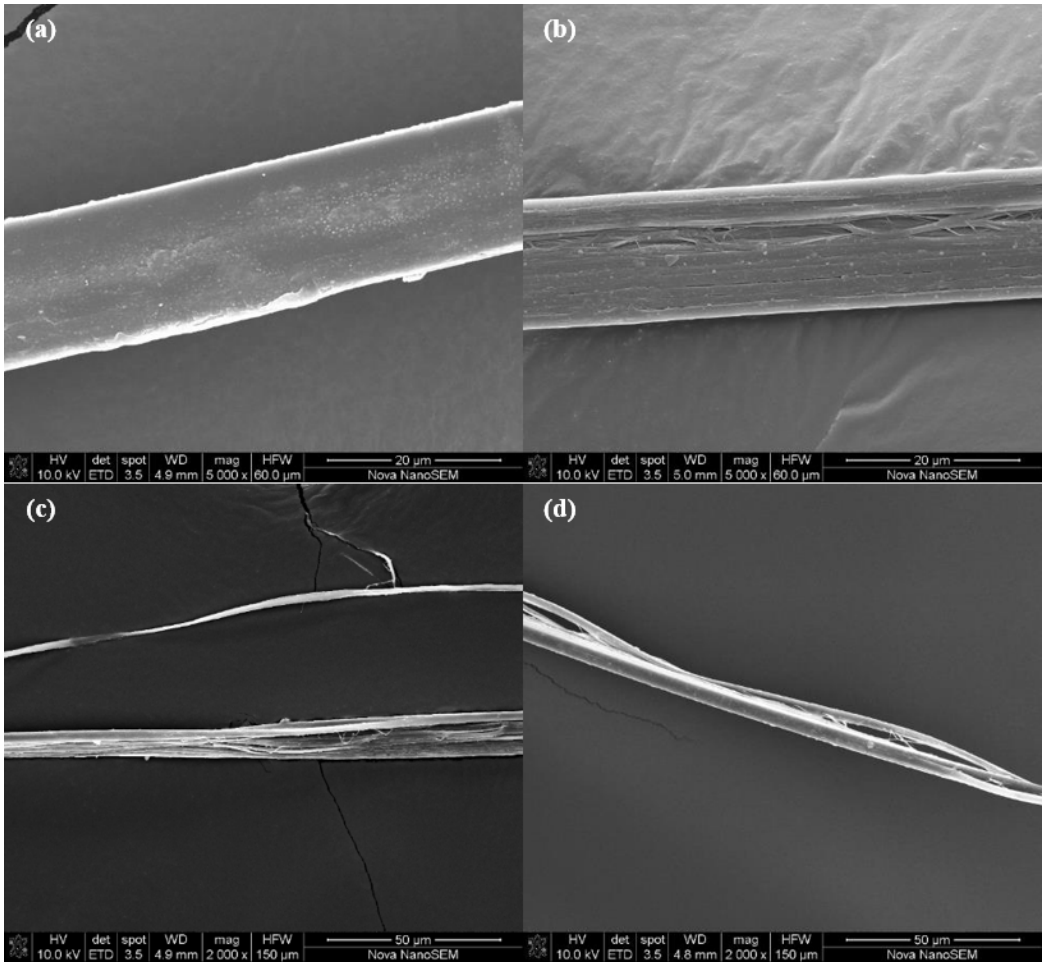

Figure 3.14. Uniform compression zone of AuTx fibers (a), with occasional zones of splitting (b). Severe fibrillation after transverse compression was sometimes observed (c,d).

The AuTx fibers were difficult to separate from a single yarn as they often became entangled. Although care has been exercised to minimize fiber damage during sample preparation and the atypical datasets were removed, localized fiber damage may have resulted in large deviations and different degrees of fibrillation, as seen in the micrographs. Assuming no pre-compression damage to the fibers occurred during sample preparation, the AuTx fibers appear to be more susceptible to axial splitting under compression to high transverse nominal strains, compared to pure PPTA fibers such as Kevlar® or Twaron®.

3.3.4 PBO – Zylon® AS and Zylon® HM fibers

PBO fibers are known for their superior strength-to-weight ratios compared to some of the other polymer fibers in use [11, 62]. Similar to PPTA fibers, these PBO fibers exhibit a skin-core structure that is highly-oriented along the fiber axis [68, 69]. The PBO fibers have a much thinner, void-free skin structure of approximately 0.2 μm thickness. The measured Zylon® AS (As Spun) fibers had a much lower transverse elastic modulus than the Zylon® HM (High Modulus) fibers. While the latter has a higher longitudinal modulus than the AS fibers, there have been no reports of their variation in transverse moduli. The respective microvoid structures of the two variants may have led to the differences in transverse moduli [69]. The nominal stress-strain curves for Zylon® AS and HM are given in Figs. 3.15 and 3.16.

Post-compression micrographs of both Zylon® AS and Zylon® HM show uniform compression over the gage lengths. Zylon® AS was relatively featureless (Fig. 3.17) compared to Zylon® HM (Fig. 3.18), as the latter exhibited some degree of fibrillation in irregularly-spaced locations along the fiber axis, although this form of fiber damage was not a common occurrence. While PBO fibers do have excellent mechanical properties, the detrimental effects of environmental and chemical degradation on their longitudinal mechanical properties have been well-documented [52, 53], to the extent that soft armor vests made from PBO have been recalled and new ballistic

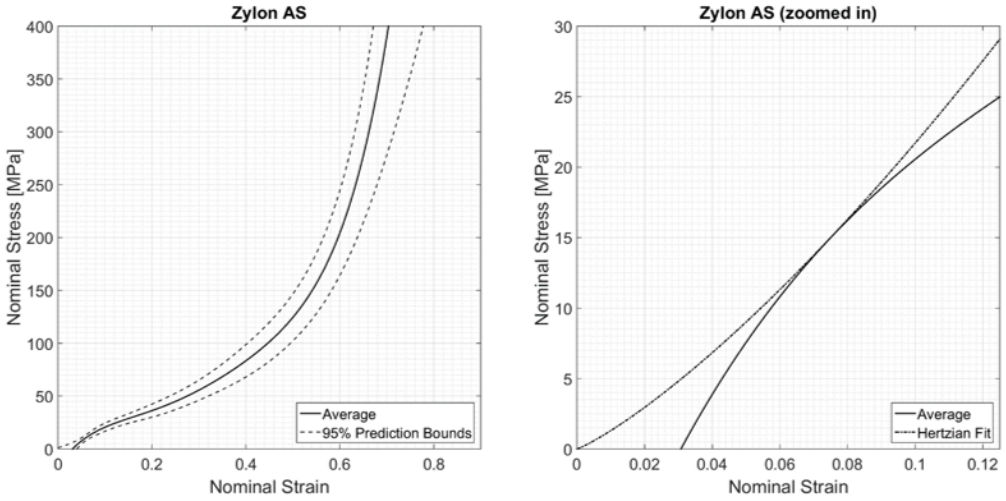

Figure 3.15. Nominal stress-strain curve of Zylon® AS using quintic polynomial fit (left), and zoomed-in initial portion with Hertzian fit (right).

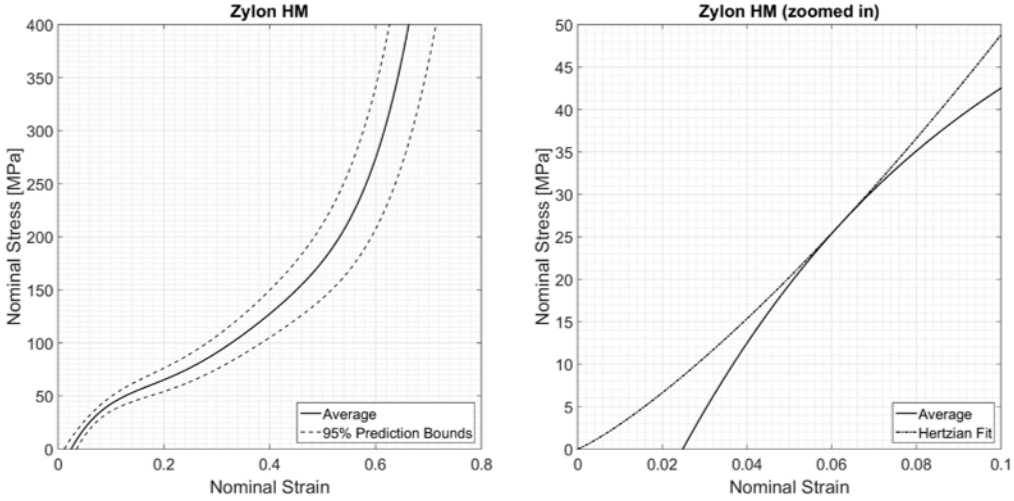

Figure 3.16. Nominal stress-strain curve of Zylon® HM using quintic polynomial fit (left), and zoomed-in initial portion with Hertzian fit (right).

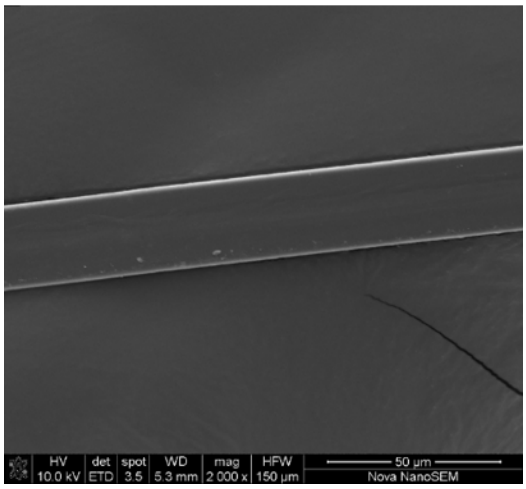

Figure 3.17. Typical post-compression Zylon® AS fiber. Fibers were well- and uniformly-compressed over the gage length, with relatively featureless compression zones.

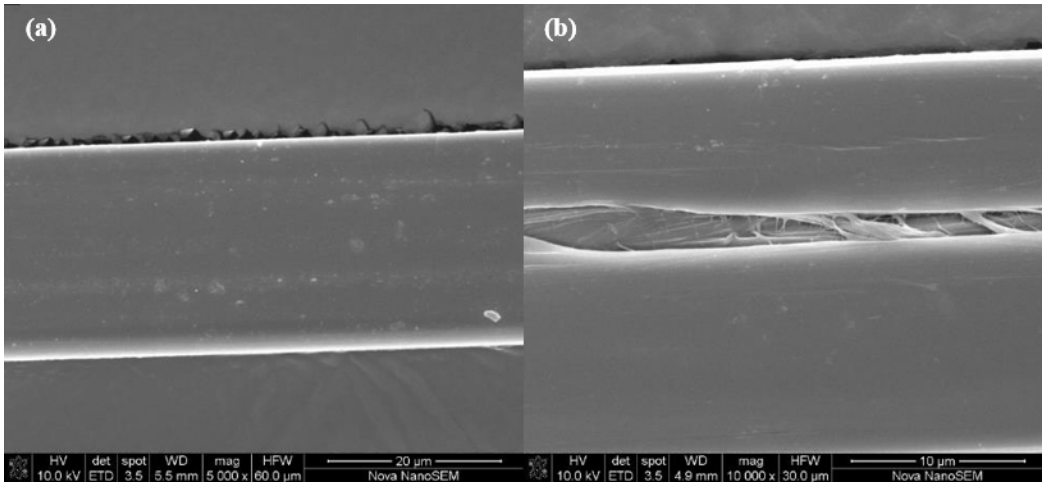

Figure 3.18. Different degrees of fibrillation of Zylon® HM fibers after transverse compression, with (a) no visible damage, and (b) occasional axial splitting and separation of fibrils.

standards were established [70]. Although care has been taken to ensure that these tested fibers were not exposed to such conditions, it is unknown if the transverse mechanical properties are similarly affected by other unstudied mechanisms. The reader is advised to consider these factors when using our results.

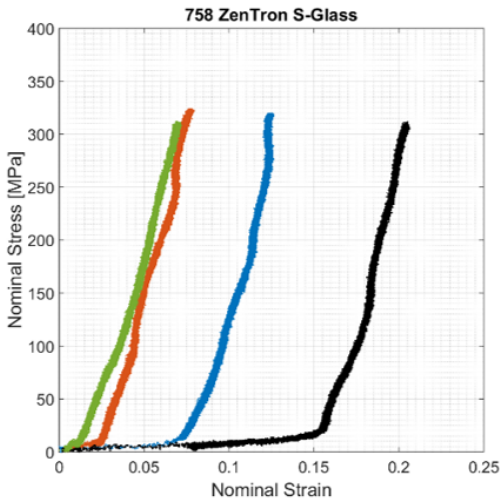

Figure 3.19. Nominal stress-strain curves of several 758 ZenTron® S-glass compression tests, exhibiting two distinct regimes of compressive response.

3.3.5 S-Glass – 758 ZenTron® fibers

The S-glass fiber compression experiments were unexpectedly difficult to perform, as they tend to fail during sample preparation under slight tension due to their brittle nature. They also exhibit high stiffness during compression, leading to low signal-to-noise ratios throughout the whole compression cycle. The combination of the above properties mean that the compression load-displacement signal is atypical compared to the other fibers in this study, as shown in Fig. 3.19 for a few representative tests. The compressive response of these fibers typically exhibits two distinct regimes: an initial high compliance regime, which appears to be similar across all fibers, followed by a stiffening regime. The stiffening response appears to be strain-shifted.

Due to the amorphous structure of glass fibers, the longitudinal and transverse properties were expected to be the same. That is, they are more isotropic rather than transversely isotropic. However, this atypical response is most likely due to the effects of a low stiffness protective sizing on the glass fibers [71, 72], which is usually applied to reduce the detrimental effects of mechanical abrasion between fibers (Fig. 3.20). A

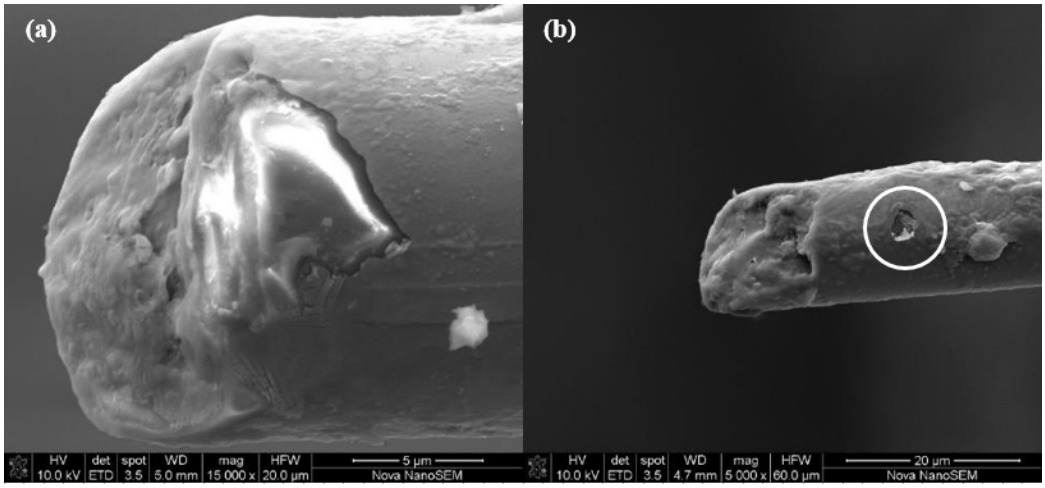

Figure 3.20. Micrographs of broken ends of S-glass fibers showing (a) sizing on the fibers, and (b) cracking in sizing layer shown in circle.

Hertzian fit of the initial compliance gives a transverse modulus value in this regime of about 221 MPa. Once this initial sizing is compressed to a limit, the mechanical response is then dependent on the high stiffness glass fibers within, which explains the sudden stiffening. However, the elastic limit of this initial regime does not appear to be consistent across the fibers, although an experimental maximum of about 16% was achieved for some samples.

To measure the transverse moduli of the actual glass material, the initial high compliance portion was truncated. The high strength portion had minimal scatter in load-displacement measurements across different samples. The stress-strain data was smoothed using a 100-point moving average algorithm to remove noise, which was especially important due to the low displacement voltage signals within this regime. This data-smoothing did not affect the stress-strain results due to the high sampling rate used for the S-glass tests. The resultant stress-strain curve exhibits an extremely subtle change in compressive response within a very narrow range of strain values, as per Fig. 3.21. The initial portion was then fitted using Eq. 3.3 to give a fitted value of 98 GPa. However, the current form of Eq. 3.3 assumes that the longitudinal stiffness E_L is much larger than the transverse stiffness E_t, which is not the case for

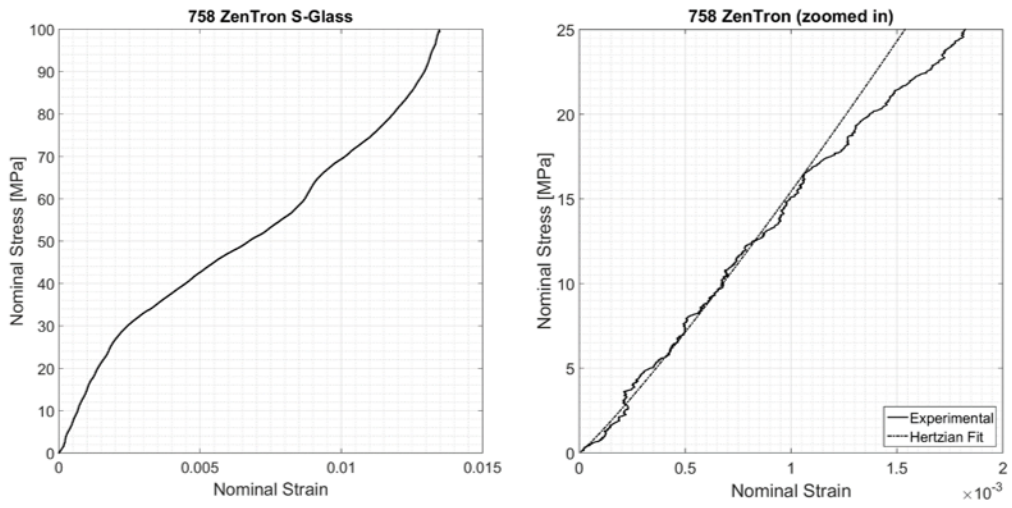

Figure 3.21. Nominal stress-strain curve of a typical ZenTron® compression test for high stiffness portion with initial low stiffness portion removed (left), and zoomed-in initial portion with Hertzian fit (right).

glass fibers since they are isotropic. The following set of equations for the transverse stiffness are used instead [46, 50]

$$s_{11} = \frac{1}{E_{fit}} = \frac{1}{E_t} - \frac{\nu_{lt}^2}{E_L} = \frac{1-\nu^2}{E} \tag{3.6}$$

where E_{fit} is obtained as 98 GPa and ν is the Poisson's ratio assumed to be between 0.2-0.3. This give the transverse modulus a range of values between 89.2-94.1 GPa. Compared to the longitudinal modulus of 93.8 GPa provided by the manufacturer, this provides certainty that the glass fibers are indeed isotropic, and again proves the accuracy of the transverse compression setup.

The measured post-compression diameters of the glass fibers showed negligible to no deformation (Fig. 3.22). Some of the brittle glass fibers fractured during sample preparation for the SEM -– a closer look at these broken ends revealed that the internal morphology of these glass fibers is relatively uniform. Some striations were observed to run longitudinally down the axis of the fibers at certain irregularly-spaced

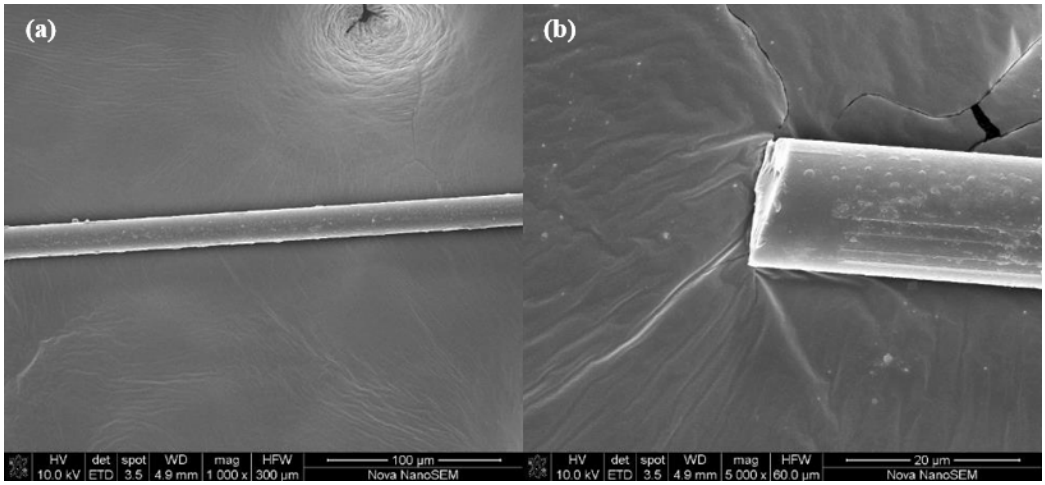

Figure 3.22. Post-compression micrographs of ZenTron® fibers showing negligible flattening (a). Uniform horizontal striations are observed on the surface of the glass fibers (b).

locations, which may possibly indicate the axial splitting failure mode of the sizing layer when compressed.

3.4 Conclusions

The twin-fiber transverse compression setup of several anisotropic high performance ballistic fibers was improved upon from a previous setup in order to more accurately measure the small initial elastic loads. The current setup was improved over previous setups by increasing the initial load resolution by a whole order of magnitude, allowing the compressive cycle to be triggered using its own initial preload. This setup then provides more accurate and repeatable data for fitting to Hertzian contact equations in order to determine the elastic moduli more reliably. Measured transverse moduli and elastic limits compared well with previously-obtained results. Post-compression micrographs showed different transverse failure and damage mechanisms between the different polymer fibers. Using post-compression widths measured using scanning electron microscopy, the final nominal strain was estimated using plane strain and mass conservation assumptions. S-glass fibers demonstrated vastly

different behavior compared to the other ballistic fibers due to their isotropic structure and sizing layer. Failure modes and mechanisms of these fibers under transverse compression may be left to a future work.

4. LOCALIZED IMPACT STRESS CONCENTRATIONS IN SOFT ARMORS DUE TO MICRO-SCALE PROJECTILE EDGE GEOMETRIES

Chapter adapted from prior published work. Z. Guo, S. Martinez-Morales, W. Chen, Projectile strength effects on the ballistic impact response of soft armor targets, Text. Res. J. (2019) 004051751986288. doi:10.1177/0040517519862882.

Abstract

Although extensive focus has been put on the ballistic performance of projectiles with certain macro-scale geometries and dimensions, the micro-scale geometries are not as rigorously-standardized. The localized stress concentrations arising from micro-scale geometries introduce multi-axial and locally concentrated stress states within the constituent material of the soft armor target, which can result in premature failure that is not predicted with existing models. In this study, the micro-scale edge/corner geometries of RCC projectiles are varied, and their respective ballistic performance was determined via experiments to examine the effects of the localized stress concentrations. Target panels were examined post-mortem and the effects of these localized stress concentrations on the failure modes were quantified. Experiments results indicate that stress concentrations drastically reduce the ballistic performance of the soft armor targets, and the fabric targets appear to fail without significant strain energy absorption.

4.1 Introduction

The significance and importance of soft body armors for personnel protection has increased multiple-fold over the decades since their first conception. The impact and energy absorption mechanisms during the ballistic penetration of soft armor systems have long been a subject of extensive studies. The exact underlying physics behind the impact and failure phenomena is still not fully understood, and still largely depends on empirical data from extensive ballistic tests. In typical analyses of soft armor ballistic performance, several types of projectiles are used, namely spheres, right circular cylinders (or RCCs), and fragment-simulating projectiles (FSPs). RCCs have proven to be a popular choice of projectile geometry because of their relative ease of machining, testing, analysis, and modeling. For these reasons, existing literature investigating the ballistic performance of soft armor targets under RCC impact are too numerous to count.

In order to standardize the method of obtaining a ballistic limit velocity, design guidelines such as the MIL-DTL-46593B [73] detail exact dimensions and tolerances of FSPs required for testing of the soft armor targets. However, the micro-scale dimensions have not been as rigorously specified for other types of projectiles. Cunniff examined the effects of variations in RCC projectile physical properties and dimension tolerances [28], but did not look further into the effects of edge sharpness on the ballistic performance. The importance of these micro-scale dimensions should not be understated, as one would typically expect a target material to fail more easily when impacted by a sharper edge geometry than a blunt one. In fact, Hertzian contact analysis of a cylindrical punch on a plane shows that an idealized sharp corner results in a contact stress that is theoretically infinite at the boundary of the impact face, as in Figure 4.1.

A similar Hertzian pressure analysis was performed by Attwood *et al.* for a cubical punch on an ultra-high molecular weight polyethylene composite beam [74] to give

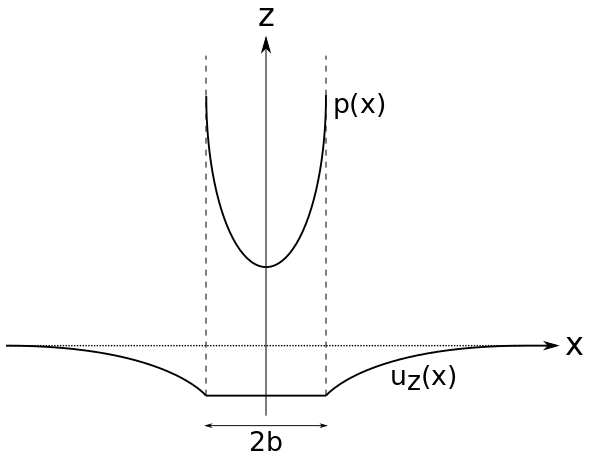

Figure 4.1. Pressure profile $p(x)$ and indentation displacement profile $u_z(x)$ of an elastic half-space indenter by a planar punch of width $2b$.

an idea of the stress states beneath the contact zone. For a flat 2D planar punch indenting an elastic half-space,

$$\sigma_{zz}(x) = p(x) = p_0 \left[1 - \left(\frac{x}{b}\right)^2\right]^{-1/2}, \quad p_0 = \frac{2F_L}{\pi b} \tag{4.1}$$

where F_L is the normal force per unit length. From Equation 4.1, the Hertzian contact pressure becomes infinite at the edge of the cylinder for an ideally sharp corner. It is evident that, while these ideally sharp corners make it much simpler for analysis, the Hertzian case of an ideal flat indenter is unrealistic and modifications must be introduced to account for the micro-scale curvature geometries at the corners. The corners of a physical object are always finitely sharp, and the radii of curvature can be easily measured via microscopy. These corner stress concentrations then become analytically-finite, which are more realistic, and may be quantified for comparison.

The localized stress concentrations due to micro-scale geometries have been previously-shown to reduce the effectiveness of polymer fibers by introducing off-axis stresses that result in premature fiber failure. Mayo & Wetzel [61] demonstrated that by indenting certain polymer fibers with a razor blade, the fiber consequently fails in a

transverse shear-like cutting manner, which drastically reduces the effective failure strain as stresses are concentrated at the blade tip. Hudspeth *et al.* [29, 30] took it a step further and showed that the failure modes transition from fibrillation under pure axial tension when using large round indenters to a more shear-like cutting mode similar to the results of Mayo & Wetzel when using razor blades. Interestingly, the failure modes of a polymer fiber using an FSP indenter transitions from axial tensile failure at low subtended angles of the fiber to an off-axis cutting-mode failure which occurs near the edges of the FSP face. These exact same result and findings were further simulated by Sockalingam *et al.* [55] to show effects of multi-axial stress states numerically. Hudspeth *et al.* later transversely-impacted high-performance polymer yarns with the same round, FSP, and razor blade projectiles [75] in order to demonstrate the same detrimental effects of localized stress concentrations. In the same manner as the fibers under quasi-static indentation, the razor blade projectiles initiated stress states that reduced the overall ballistic performance of the yarn compared to a round indenter, which tend to initiate axial tensile failure in the yarns. These same stress concentrations are undoubtedly introduced in a similar manner during projectile impact on a soft armor target, which may result in similar premature failure response.

In this study, the effects of localized stress concentrations that occur at the corners of projectiles are analyzed with respect to their influence on ballistic performance using both experimental and analytical methods, with a focus on RCC projectiles. Experimentally, high-rigidity projectiles with different corner radii of curvature were used to impact a Twaron® soft armor fabric panel, and the ballistic performance was then determined to compare the effects of these localized stress concentrations. Post-mortem analysis was performed to examine the difference and progression of failure modes in the through-thickness direction when RCCs of different edge radii are used to impact these panels.

4.2 Experimental procedure

4.2.1 Gas gun setup

Projectiles were shot with a single-stage smooth-bore light-gas gun with an inner bore diameter of 9.80 mm and barrel length of 3.66 m. In order to improve accuracy and reduce trajectory instability due to drag on the RCC projectiles, the target is located approximately 0.4 m from the tip of the barrel. Alignment was performed to ensure perpendicularity of the target panel to the shot axis. A steel safety chamber was placed behind the target panel mount to retrieve any exiting projectiles using either terry cloth rags or 10% by weight porcine skin ballistic gelatin (ambient temperatures permitting).

Target panels were clamped on all four corners using L-brackets with inner Neoprene rubber linings (50A Durometer) of 25.4 mm (1 in.) width to grip the target panel firmly, leaving an exposed surface area of 0.254 $\times$ 0.254 m^2 (10 in. $\times$ 10 in.). The L-brackets were secured using 12 flanged screws equally-spaced on all corners, and then tightened using a torque wrench to a maximum torque of 2.8 N-m (25 in-lb). Velocity measurements were made using in-house laser diode instrumentation to measure velocities accurate to within 3.05 m/s (10 ft/s).

4.2.2 Target material

The base Twaron® balanced plain-weave fabric samples (840 denier yarns, 27 $\times$ 27 ends/picks per inch) were obtained from Barrday and manufactured in 2015, with an areal density of 0.215 kg/m^2 (0.044 lb/ft^2) per ply, 3.011 kg/m^2 (0.617 lb/ft2) for 14 plies, and 4.732 kg/m^2 (0.969 lb/ft2) for 22 plies. The number of plies was chosen in order to calibrate the ballistic test results with the ones provided by the manufacturer and with a previous study performed by the authors [76]. Fabric materials were cut to sample sizes of 0.305 $\times$ 0.305 m^2 (12 in. $\times$ 12 in.), and subsequently edge-stitched three times together with a 25.4 mm (1 in.) margin from the edges for easier

handling. The edge-stitching does not significantly alter the ballistic performance. Panels were kept in storage in an air-tight container with clay desiccant packets for at least 24 hours prior to shooting to absorb any moisture that may be present due to transportation.

4.2.3 Projectile material and geometries

Steel right circular cylinders (RCCs) were cut and faced out of 7 mm rod stock, and have diameters and lengths measured to be within 7.00±0.02 mm. In accordance with MIL-DTL-46593B [73], the projectiles were verified to have hardnesses of at least Rc 31±1 using a spot hardness tester. Edge geometries were varied to various radii of curvature. Sharpened corners were achieved by cutting and facing, while blunt corners were obtained by edge filleting after cutting and facing. To achieve somewhat intermediate radii of curvature, a batch of projectiles were tumbled with suitable ceramic media for 5 hours. Projectile edge geometries were measured using scanning electron microscopy (Nova NanoSEM 200). Typical radii of curvature were approximately 120-150 μm for the blunt projectiles, 100-120 μm for the tumbled projectiles, and 35-75 μm for the sharpened projectiles, as shown in the micrograph in Figure 4.2 (Figure 4.2 shows diameters rather than radii of curvature due to the microscope software). It should be noted that exact radii of curvature are difficult to achieve at the micro-scale when machining macro-scale dimensions, but the different processes nonetheless provide three relatively distinct regimes of edge radii, as per Table 4.1. As a comparison, 7-mm spheres were also tested – these represent the extreme case of projectile "bluntness". The parameter η in Table 4.1 refers to the areal density ratio of the target to the projectile.

4.2.4 Shooting procedure

A total of 12 shots per panel were performed to determine the ballistic limit using the bracketing method as detailed in NIJ-0101.06 [70]. Shot locations were

Table 4.1. Projectile and target materials with respective properties.

Panel No.	Projectile geom.	Edge	Corner radius [μm]	Mass [g]	Target	η $\times 100$
22T-S-46	RCC	sharp	35-75	2.11	22 Twaron	8.63
22T-T-54	RCC	tumbled	100-120	2.11	22 Twaron	8.63
22T-B-45	RCC	blunt	120-150	2.11	22 Twaron	8.63
14T-S-52	RCC	sharp	35-75	2.11	14 Twaron	1.82
14T-T-49	RCC	tumbled	100-120	2.11	14 Twaron	1.82
14T-B-53	RCC	blunt	120-150	2.11	14 Twaron	1.82
14T-R-51	Sphere	round	3500	1.37	14 Twaron	2.81

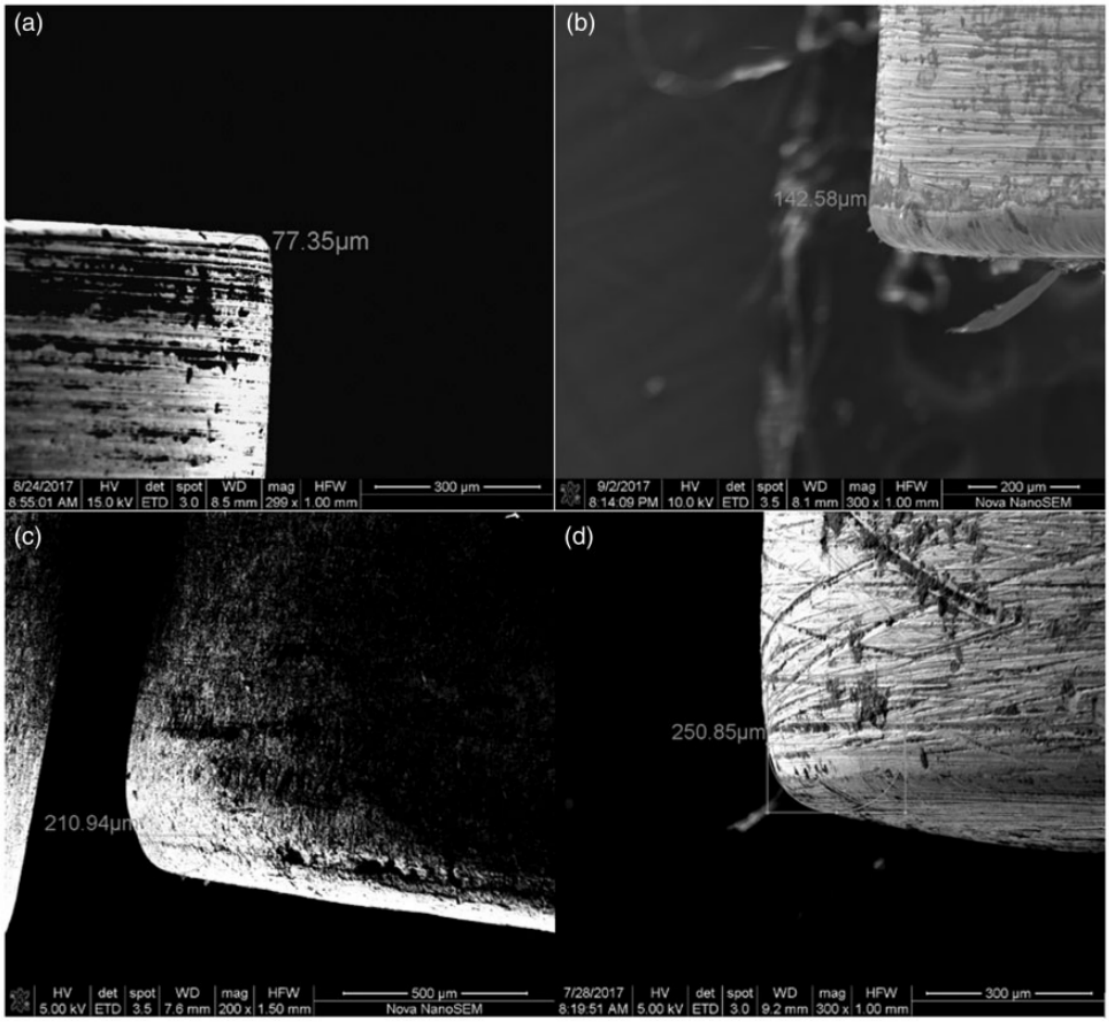

Figure 4.2. Micrographs of typical RCC projectiles prior to shooting with (a,b) sharp corners, (c) tumbled corners, and (d) blunted corners.

pre-determined and marked using a template such that the shots were located 25.4 mm (1 inch) from the panel stitching, at least 50.8 mm (2 in.) apart from each other, and (as much as possible) that the principal yarns do not overlap. For uniformity in testing, pre-and post-test temperatures and humidity levels were also recorded to ensure that testing conditions do not vary significantly.

As the test chamber and targets are not exactly the same as detailed in the NIJ-0101.06 [10] standard, the methodology was slightly modified. The first shot is fired at a desired velocity of 304.8 m/s (1000 ft/s) – this velocity was referenced and estimated with respect to the manufacturer's datasheet for a 9 mm FMJ projectile impact. If the shot outcome is a partial penetration, a shot outcome of '0' is assigned to the shot number and the subsequent desired shot velocity is increased by 30.5 m/s (100 ft/s); if the shot outcome is a complete penetration, a shot outcome of '1' is assigned to the shot number and the subsequent desired shot velocity is decreased by 304.8 m/s (1000 ft/s). In the case of an unacceptable shot e.g. inaccurate shot location or large deviation of actual striking velocity from desired shot velocity of more than 3.05 m/s (10 ft/s), the shot is repeated.

The process is repeated till the first shot outcome "reversal", i.e., from partial to complete penetration or vice versa. At this point, the change in desired velocity is lowered to 22.9 m/s (75 ft/s). Similarly, if the shot outcome is a partial penetration, a shot outcome of '0' is assigned to the shot number and the subsequent desired shot velocity is increased by 22.9 m/s (75 ft/s); if the shot outcome is a complete penetration, a shot outcome of '1' is assigned to the shot number and the subsequent desired shot velocity is decreased by 22.9 m/s (75 ft/s).

Again, this process is repeated till the next shot outcome "reversal", where desired velocity step is further lowered to 15.2 m/s (50 ft/s). If the shot outcome is a partial penetration, a shot outcome of '0' is assigned to the shot number and the subsequent desired shot velocity is increased by 15.2 m/s (50 ft/s); if the shot outcome is a complete penetration, a shot outcome of '1' is assigned to the shot number and the subsequent desired shot velocity is decreased by 15.2 m/s (50 ft/s). The procedure is then repeated till a total of 12 acceptable shots are completed, up to a total of 16 possible shots per target panel if necessary in the case of unacceptable shots.

4.3 Results & Discussion

Recorded pre- and post-testing temperatures and relative humidity levels were between 17.0-26.0°C and 34-49% respectively. Tests were completed within 5 hours of test commencement.

4.3.1 Ballistic limit results

The outcome of each shot was assigned a value of '0' for partially-penetrated shots, and a value of '1' for complete penetration shots. Perforation of the panel was verified visually during the test, and via post-mortem for confirmation. Two different methods of calculating the V_{50} ballistic limit, the NIJ-0101.06 [70] and MIL-STD-662F [77] standard methods, were compared and averaged (Table 4.2). NIJ-0101.06 uses a logistical S-curve regression while MIL-STD-662F uses the arithmetic mean of the lowest complete penetration velocities and highest partial penetration velocities. The full details of the calculation methods are given in their respective references. An improvement in ballistic performance of the RCC projectiles was observed for the sharper-edged projectiles (Panels 46 and 52), while the blunt and tumbled RCCs produced rather similar ballistic limit results. The steel spheres produced only one single complete perforation result within the pressure limits of the gas gun, and the ballistic limit was assumed to be at or above 462.0 m/s.

Table 4.2. Results of ballistic limit tests.

Panel No.	Proj. Geom	Edge	Rc [µm]	Rc/Rp [× 100]	[η×100]	Ave. V_{50} [m/s]	KEabs [J]
22T-S-46	RCC	sharp	35-75	1.00-2.14	8.63	341.0	122.7
22T-T-54	RCC	tumbled	100-120	2.86-3.43	8.63	426.0	191.5
22T-B-45	RCC	blunt	120-150	3.43-4.29	8.63	412.5	179.9
14T-S-52	RCC	sharp	35-75	1.00-2.14	1.82	303.4	97.11
14T-T-49	RCC	tumbled	100-120	2.86-3.43	1.82	372.4	146.3
14T-B-53	RCC	blunt	120-150	3.43-4.29	1.82	377.1	150.0
14T-R-51	Sphere	sphere	3500	1	2.81	$\geq$ 462.0*	$\geq$ 225.2

*Maximum possible velocities of 462.0 m/s were achieved with the gun without sufficient complete penetration results. The ballistic limit is assumed to be at or above this velocity.

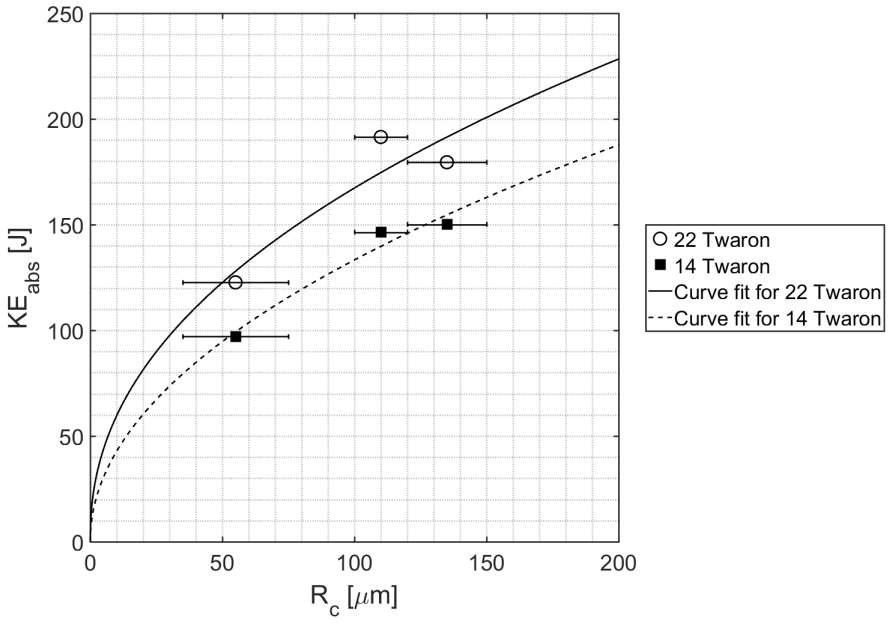

Figure 4.3. Plot of kinetic energy absorption at V_{50} ballistic limit for 22- and 14-ply Twaron® panels, along with power-law curve-fits.

The kinetic energy absorbed at the ballistic limit KE_{abs} was observed to decrease with the corner radius Rc, which is expected. These results were fitted with a power-law fit to approximate the relationship (Figure 4.3).

$$KE_{abs} = \begin{cases} 13.71\,(R_c[\mu m])^{0.4939} \approx 13.32\sqrt{R_c[\mu m]}, & \text{14 Twaron} \\ 21.19\,(R_c[\mu m])^{0.4487} \approx 16.68\sqrt{R_c[\mu m]}, & \text{22 Twaron} \end{cases} \tag{4.2}$$

The fits in Equation 4.2 did not include the V_{50} kinetic energy absorbed for the spherical projectile, since an actual V_{50} was not determined. The exponents of both are exceedingly close to a value of 0.5, so the data points were forced to a square-root function fit for a simpler approximation without significant decrease in the corresponding R^2 values.

4.3.2 Target post-mortem analysis

Post-mortem analysis was performed on the individual impacted fabric plies to investigate the effects of edge sharpness of the failure modes of these plies during impact. Visual inspection of the target plies was performed and the failure mode of each shot location through the plies was categorized into three main types of failure using the same methodology detailed in a previous work [78]:

1. *Rupture.* In this mode, the edges of the shot hole appear to be punched out and fail in a very localized manner. Hole is often large and clean with minimal transverse fabric movement around the shot location (Figure 4.4). Yarn rupture modes typically occur at the strike face of the target panel.

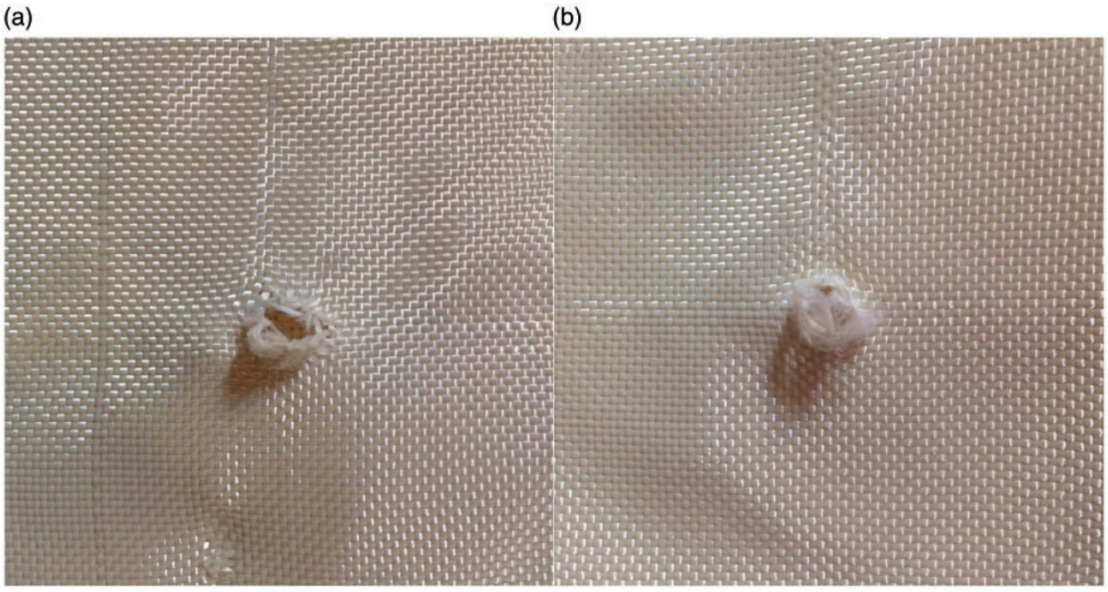

Figure 4.4. Post-mortem images showing (a) front side of shot exhibiting localized yarn rupture, and (b) rear side of shot exhibiting severe yarn rupture and entanglement.

2. *Mixed mode.* Once the projectile has ruptured the initial few layers, the subsequent layers may either show ply damage via yarn pull-out (Figure 4.5a) or via

nosing-through as the yarns slide around the projectile (Figure 4.5b). These defeat mechanisms are collectively termed 'mixed mode' as the differences between them may be hard to distinguish, since these modes typically occur in the middle to end plies. In mixed mode failure, broken yarns may be observed, though not as frequently as in rupture mode. Principal yarn translation and the characteristic tetrahedral transverse wavefront of fabric plies are more prominent.

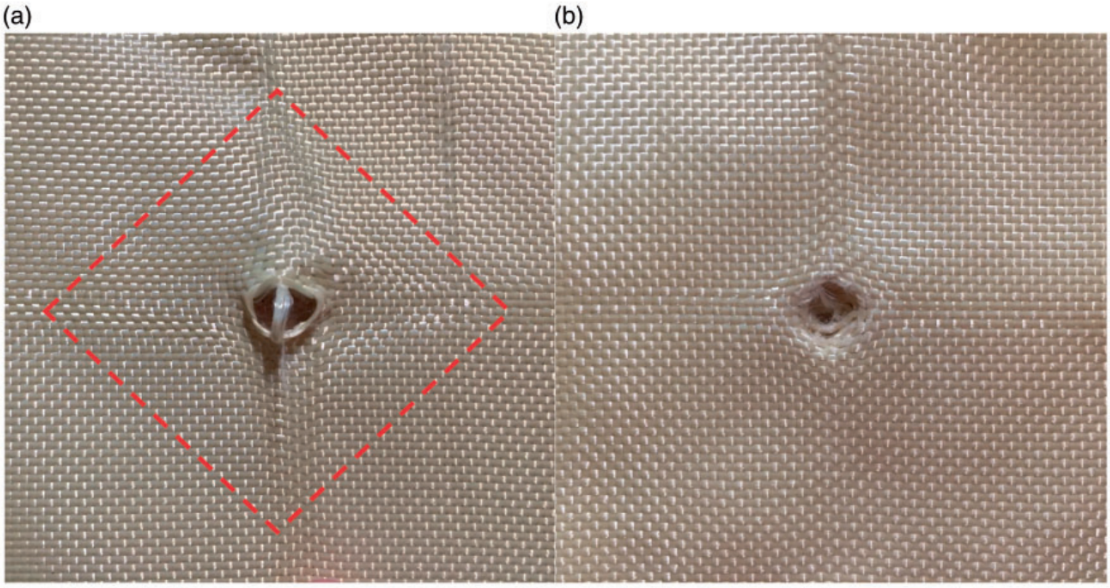

Figure 4.5. Post-mortem images showing (a) rear side of shot exhibiting significant yarn pull-out with principal yarn translation, and (b) front side of show exhibiting nosing-through of projectile. Red dashed parallelogram highlights evidence of transverse wavefront propagation.

3. *Intact.* At low velocities, the projectile does not fully penetrate the target panel, occasionally resulting in layers that show slight indentation and minimal yarn pull-out but exhibit no means of projectile perforation (Figure 4.6). Since the focus is on the defeat mechanisms and failure modes of the fabric plies, we

consider this form of response to be “intact”, even though the fabric ply shows obvious signs of being impacted.

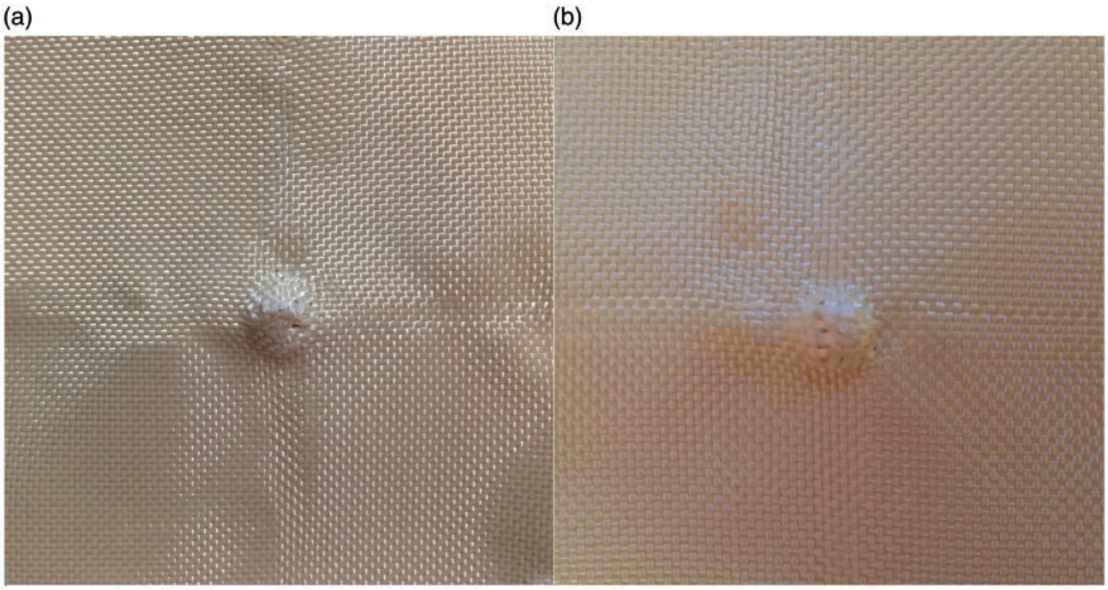

Figure 4.6. Post-mortem image showing indentation imprint by (a) an RCC, and (b) a sphere. Both exhibit yarn translation at impact site but no signs of projectile perforation.

Since the visual inspection method is highly qualitative, the results and observations gleamed from the post-mortem data merely presents a trend study for comparison. For each target panel, the total number of rupture/mixed mode/intact layers were first determined and then calculated as a percentage of number of shots multiplied by the number of layers. These results are given in Table 4.3. Rupture modes observed at shot locations of the steel spheres exhibited severe damage at a small point of contact at the tip of the sphere, and while the yarns are indeed ruptured, they should not be considered the same form of rupture mode as induced by an RCC, since the yarns impacted by a sphere can rupture without significant aperture formation for the steel sphere to perforate. Nonetheless, the steel sphere results are

Table 4.3. Results of post-mortem analysis on target panels.

Panel No.	R_c [μm]	Target	% Rupt.	% Mixed	% Intact	KE_{abs} [J]
22T-S-46	35-75	22 Twaron	59.5	1.5	32.6	122.7
22T-T-54	100-120	22 Twaron	52.7	11.4	36.0	191.5
22T-B-45	120-150	22 Twaron	50.4	6.8	42.8	179.9
14T-S-52	35-75	14 Twaron	62.5	14.9	22.6	97.11
14T-T-49	100-120	14 Twaron	57.7	11.3	31.0	146.3
14T-B-53	120-150	14 Twaron	42.3	15.5	42.3	150.0
14T-R-51	3500	14 Twaron	48.6	21.4	30	$\geq$ 225.2

included as a reference. The data from Table 4.3 is plotted in Figure 4.7 for a more visual comparison.

It should be noted that the velocities impacting the target panels for each shot are different as per the 12-shot method detailed previously. However, these percentage occurrences reflect the distribution of failure modes at or near the V_{50} ballistic limit. The sharp-edged projectiles tend to result in a higher percentage of rupture modes at the strike face and the lowest percentage of intact plies at the rear face of the target panel. On the other hand, blunt projectiles result in the lowest percentage of rupture modes and highest percentage of rear-face intact plies. A general trend may be noted where a larger degree of rupturing results in a lowered energy absorption. This trend is also more distinct for the thinner 14-ply target panels compared to the 22-ply target panels, where the rupturing mechanism may not persist far enough in the through-thickness direction during perforation (at least when impacted at the ballistic limit velocity). These results further support the hypothesis that off-axis stress states within the constituent polymer fiber material tend to result in premature failure.

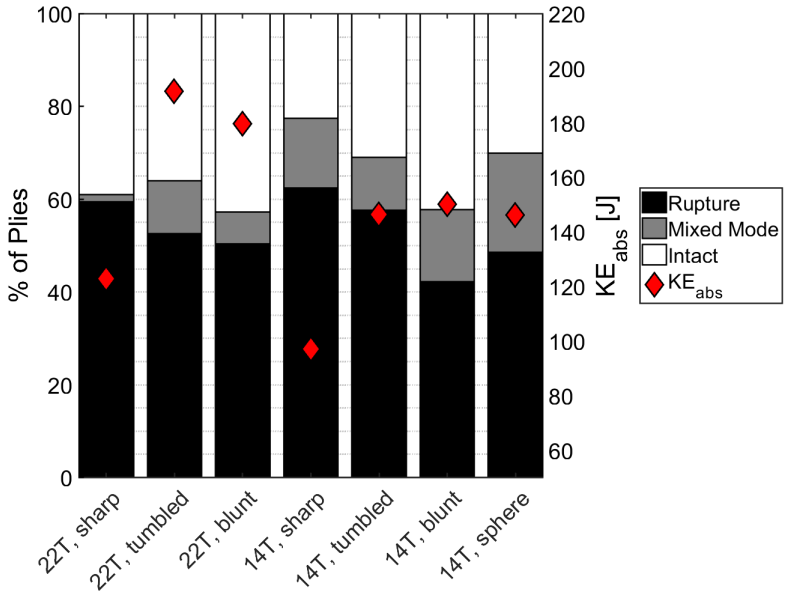

Figure 4.7. Stacked bar graph of different failure modes and percentage occurrence per target panel, along with KE_{abs} kinetic energy absorption trend.

4.3.3 Projectile post-mortem analysis

Post-impact projectile diameters and lengths were also measured to quantify the amount of deformation or damage occurring to the projectiles during impact. Post-impact projectiles were caught with a catch chamber lined with cotton jersey cloth rags and soft rubber sheets to prevent deformation of the perforated projectiles upon impact with the chamber walls. On occasion, partially-penetrated projectiles were trapped within the fabric target layers, and subsequent shots may impact these trapped projectiles, resulting in extreme deformation. These projectiles were not considered for post-mortem analysis. For all projectiles, the post-impact diameters and lengths were 7.01±0.005 mm and 7.01±0.016 mm respectively, indicating no statistically-significant macro-scale deformation. Larger deviations in post-impact lengths were most likely due to residue from impact at the strike face, which was not

removed to preserve the condition of the projectiles as-retrieved. A closer inspection of these projectiles using scanning electron microscopy revealed that projectile damage tends to occur at the edges of the RCCs (Figure 4.8). The degree of deformation appears to be somewhat related to the impact velocity and the outcome of the shot (i.e. partial or complete penetration). However, completely-penetrated projectiles were not examined as the method of projectile retrieval behind the target may have resulted in further deformation.

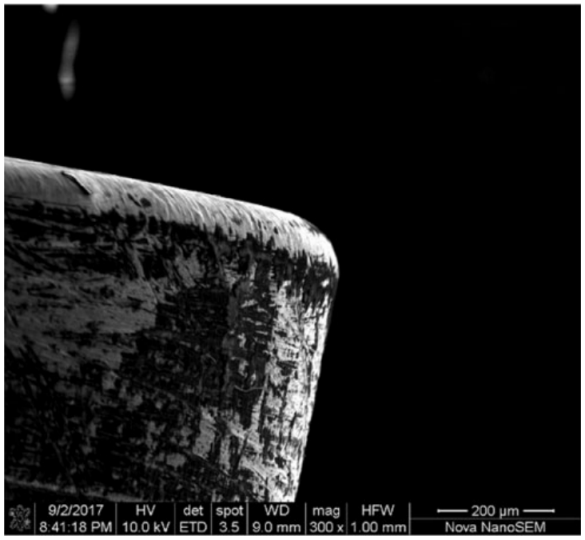

Figure 4.8. Micro-scale projectile mushrooming deformation can be observed at the RCC edges.

In Figure 4.9, partially-penetrated projectiles for blunt- and sharp-edged RCCs were examined to see if the edge radius of curvature changed significantly. In Figure 4.9a, the blunt-edged RCC exhibited moderate localized damage after penetrating 20 layers (17 rupture, 3 mixed-mode, 2 intact). In Figure 4.9b, the sharp-edged RCC, on the other hand, showed some degree of projectile edge blunting after penetrating 18 layers (18 rupture, 0 mixed-mode, 4 intact). It may be possible that the larger stress concentrations result in a much more premature failure of the material directly in front of the projectile, resulting in less micro-scale damage. These results war-

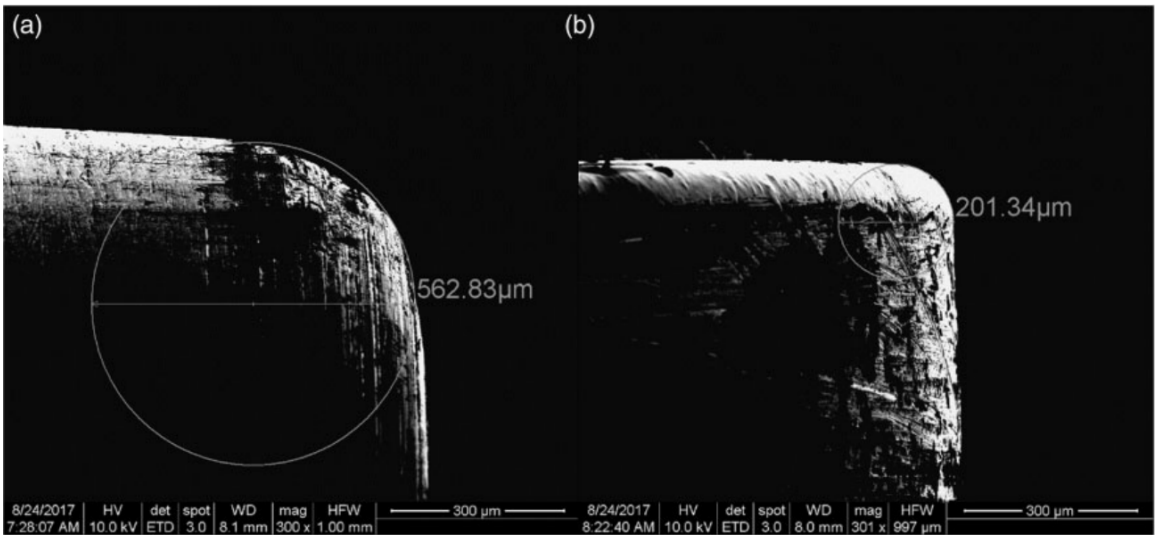

Figure 4.9. Micrographs of (a) blunt RCC edge for 22T-B-45 projectile shot at velocity of 340 m/s, and (b) sharp RCC edge for 22T-S-46 projectile shot at velocity of 296.3 m/s. Both striking velocities were sub-ballistic limit and resulted in partially-penetrated projectiles.

rant further investigation into the micro-scale damage to the projectile as a means of improving ballistic performance.

4.4 Conclusions

The micro-scale stress concentrations occurring at the edges of projectiles were examined for their effects on the ballistic performance on soft armor targets. Steel right circular cylinder of various edge radii of curvature and spherical projectiles were used to impact Twaron® panels to obtain the ballistic limit. Sharper edges were shown to initiate more off-axis stress states in the constituent fiber material, resulting in premature failure, as is expected of a sharper geometry. Post-mortem analysis of the panels revealed that three main regimes of target material response were observed, namely via yarn rupture, mixed mode defeat via yarn pull-out or windowing, and exhibiting no projectile perforation. Sharper edge radii of the RCC

projectiles were shown to result in more yarn rupture due to off-axis stress states. Results of this study indicate that multi-axial stress states and stress concentrations also result in reduced performance of the fabric armor target panels. In view of this, care should be taken in ensuring that physical dimensions and tolerances of RCC projectiles are rigorously defined as they are for FSP dimensions.

5. PROJECTILE STRENGTH EFFECTS

Chapter adapted from prior published work. Z. Guo, S. Martinez-Morales, W. Chen, Projectile strength effects on the ballistic impact response of soft armor targets, Text. Res. J. (2019) 004051751986288. doi:10.1177/0040517519862882.

5.1 Abstract

Upon impact with a target panel, a portion of the projectile's striking kinetic energy is dissipated via heat loss or deformation. Typical ballistic performance determination standards require strict projectile hardnesses values of Rc 29±2 for consistency and repeatability, but it is of interest to examine if these required hardness values give a lower bound where the ballistic performance determination is independent of the projectile's strength. In this study, a large range of yield strengths of metallic right circular cylinders were used to test the effects on the ballistic response of a multi-ply soft body armor. Results show that with an increase in projectile yield strength, the ballistic limit velocity decreases. This degradation in ballistic performance of the soft armor target levels off at higher yield strengths to about 75% of the expected ballistic performance for Rc 29, indicating that there may be a minimum projectile strength after which the influence of strength is no longer significant. The degree of deformation of projectiles during impact is related to the striking velocity and the off-axis failure of the soft armor target material.

5.2 Introduction

The significance and importance of soft body armors for personnel protection has only increased multiple-fold over the decades since their first conception. The

impact and energy absorption mechanisms during the ballistic penetration of soft armor systems have long been a subject of extensive studies. The exact underlying physics behind the impact and failure phenomena is still not fully understood, and still largely depends on empirical data from extensive ballistic tests. One of the earlier analytical models was proposed by Recht and Ipson [5], who formulated a model to predict the ballistic limit velocity of a monolithic target panel. The set of equations presented first modeled the perforation process as an inelastic rigid body impact of the impacting projectile cylinder and the target shear plug. Using the conservation of linear momentum and energy, the full energy balance equation of a cylinder impacting a target panel is given by

$$\frac{1}{2}m_p V_s^2 = \frac{1}{2}(m_p + m_f)V_r^2 + E_s + E_i \tag{5.1}$$

where m_p is the projectile mass, m_f is the assumed fabric plug mass, V_s is the projectile striking velocity, and V_r is the residual velocity after perforation. E_s is the work done during formation of a target shear plug. In their formulation, E_i is the energy dissipated via projectile deformation and heat generation when the cylindrical projectile impacts a hypothetical free-standing target shear plug. Recht & Ipson expressed this via the equation [5]

$$E_i = \left(\frac{m_f}{m_p + m_f}\right)\frac{1}{2}m_p V_s^2 \tag{5.2}$$

During ballistic impact, two possible damage and deformation scenarios may occur: loss of projectile mass due to erosion, or an increase in presented area due to mushrooming. The former scenario is relatively straightforward, as projectiles have been known to experience mass loss from erosion when impacting a target at high velocities, especially for hard targets [79]. The projectile gradually loses both mass and velocity during the perforation process, and therefore, some portion of kinetic energy. The latter scenario results in 'mushrooming' of the impacted end. This mechanism

dissipates striking kinetic energy via plastic work done by deforming the impact end of the cylinder. Consequently, this increased presented area due to mushrooming further results in a higher ballistic limit of the remaining plies in the target by involving more material during perforation. A more detailed energy balance equation which included these other mechanisms was further expressed by Corran, Shadbolt, and Ruiz for projectile impact onto a plate [80]. In their analysis, the projectile's striking kinetic energy was partitioned into target elastic energy, target plastic energy due to permanent plate bending, work done due to shear plug formation, and projectile mushrooming at the impact end.

For soft armor targets, Cunniff proposed a semi-empirical energy balance that may be similarly expressed as per Equation 5.1 by rearranging the equations provided in Ref. [10]

$$\frac{1}{2}m_p V_s^2 = \frac{1}{2}(m_p + X_2 m_f)V_r^2 + \frac{1}{2}m_p V_c^2 exp\left[- X_3 \left(\frac{V_s}{V_c} - 1 \right)^{X_4} \right] \tag{5.3}$$

$$V_c = X_5 exp(X_6 \eta^{X_7}), \quad \eta = \frac{m_f}{m_p} = \frac{A_d A_p}{m_p} \tag{5.4}$$

In Equations 5.3 and 5.4, X_2 to X_7 are regression coefficients, and V_c is the critical ballistic limit velocity. The dimensionless parameter η is the mass ratio of the target plug to the projectile, A_d is the areal density of the target, and A_p is the projectile's presented area. The second exponential term in Equation 5.3 implicitly includes the work terms E_i and E_s from Equation 5.1, and possibly other mechanisms that may exist. For the particular case of soft armor targets, the work done E_s due to the formation of a hypothetical shear plug has been shown to be somewhat independent of striking velocity [81], and is almost purely a function of projectile diameter, target thickness, and target through-thickness shear strength. Similar effects of projectile plastic deformation on the ballistic performance of the soft armor targets have not been of particular focus in existing literature.

Experimentally, the interactions between these mechanisms may be complex and hard to isolate, and for this reason soft armor target impact studies have been largely focused on the strength and material properties of the target [9, 10, 12]. However, the significance of the projectile strength on the ballistic performance should not be ignored, since commercial bullets (such as full metal jacket FMJ rounds or semi-jacketed hollow point SJHP rounds) are typically made of softer metals and thus deform easily upon ballistic impact (Fig. 5.1). Ballistic limit determination tests are often based on specified standard hardnesses of Rc 27-31 [8, 28, 73], and while these hardness values are higher than commercial bullets, higher impact velocities will also result in projectile deformation.

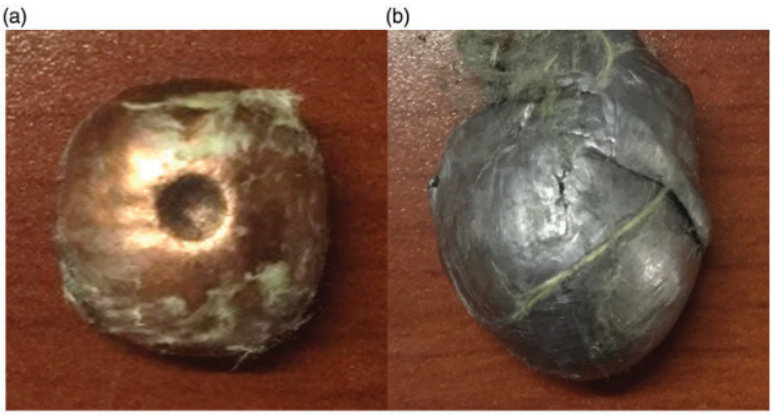

Figure 5.1. Post-impact 9 mm FMJ (left) and .44 Magnum SJHP (right) rounds after impacting a soft armor ballistic vest. Both show extreme deformation due to the low strengths of the lead core and copper jacket.

An earlier study that reflects these mechanisms [12] was performed by Cunniff using 2-, 4-, and 16-grain right-circular cylinders (RCCs) and consequently, different target/projectile areal density ratios, on a Pyrex glass/Kevlar® KM2 fabric hybrid target system. Results showed that at lower areal density ratios i.e. larger projectile areal density for the same target system, the full Kevlar® KM2 fabric system outperformed the Pyrex/Kevlar® KM2 hybrid panel (Fig. 5.2). At higher areal density

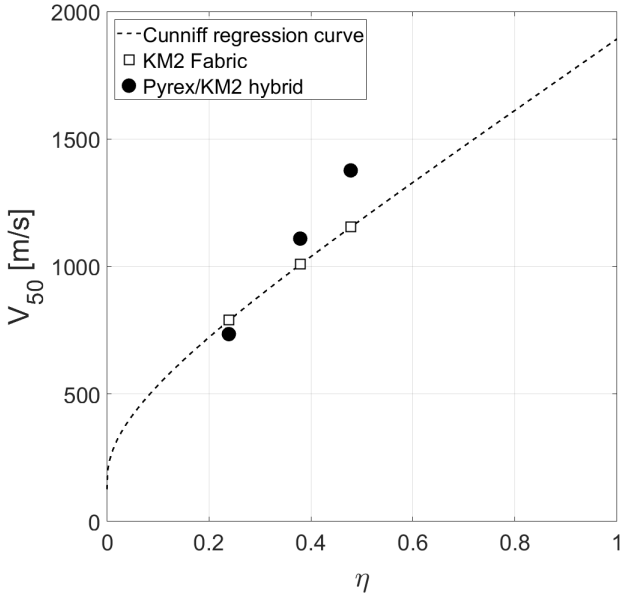

Figure 5.2. Ballistic limits of full Kevlar® KM2 fabric and Pyrex®/Kevlar® KM2 hybrid, with the latter exhibiting superior ballistic performance when projectiles are small [12].

ratios, the Pyrex/Kevlar® KM2 hybrid outperformed the full KM2 fabric system. One mechanism may be due to the hard/brittle Pyrex® layer in a hybrid system that help resist the projectile at the strike-face more efficiently at higher impact velocities (since higher areal density ratios lead to higher ballistic limit velocities). Cunniff attributed this superior performance of the hybrid to the deformation of the smaller 2- and 4-grain projectiles during impact, whereas the larger 16-grain projectiles do not typically deform within the range of striking velocities tested near the respective ballistic limit. Although further examination on the recovered projectiles was not performed, projectile erosion and plastic mushrooming scenarios nonetheless remain distinct possibilities as well, which is ultimately related to the strength of the impacting projectile and the interaction with the target panel.

In recent studies directly examining the effects of projectile strength, Ćwik et al. [20,21] impacted Dyneema® HB26 and Spectra® 3124 ultra-high molecular weight

polyethylene (UHMWPE) composites using steel and copper 20-mm fragment-simulating projectiles (FSPs). The masses of these FSPs are 53.1 and 60.25 g respectively, which indicate relatively similar areal density ratios in their study. The ballistic performance of the copper FSPs were reduced in comparison to the steel FSPs, as the ballistic limit velocity of the target panel was much higher for the copper FSP than the steel FSP. Mass losses were insignificant for both projectile materials (up to 4%) even at high striking velocities, but the copper projectiles were observed to deform substantially via mushrooming. The larger effective projectile presented area due to mushrooming resulted in a larger contact area during impact, and thus a larger target area that failed via tearing or melting. In this study, we further investigate the effects of projectile deformation and mass loss on the ballistic performance of these projectiles. Metal projectiles of various materials and strengths are used to impact and perforate Twaron® soft armor targets.

5.3 Experimental procedure

5.3.1 Gas gun setup

Projectiles were shot with a single-stage smooth-bore light-gas gun. The target is located approximately 0.4 m from the tip of the barrel to improve accuracy and reduce trajectory instability and tumbling of the RCC projectiles. Alignment was performed to ensure perpendicularity of the target panel to the shot axis. A steel soft-catch safety chamber was placed behind the target panel mount to retrieve any perforated projectiles. Target panels were clamped with L-brackets and 25.4 mm-width Neoprene rubber linings (50A Durometer) for added grip, leaving an exposed surface area of 0.254×0.254 m^2 (10 in.$\times$10 in.). L-brackets were secured using 12 flanged screws equally-spaced on all corners and torqued to 2.8 N-m (25 in-lb). Laser diodes were used to measure velocities accurate to within 3.1 m/s (10 ft/s).

5.3.2 Target material

Base Twaron® CT709 balanced plain-weave fabric samples were made from 930 dtex yarns (27 × 27 ends/picks per 25.4 mm). Fabric samples had an areal density of 4.354 kg/m^2 for 22 plies. Target panels were cut to 0.305×0.305 m^2 (12 in.×12 in.) sizes and edge-stitched three times together with a 25.4 mm (1 in.) margin from the edges for easier handling. Panels were kept in a cool, dry area at room temperature for at least 24 hours prior to shooting.

5.3.3 Projectiles

To study the effect of material strength on the deformation of the impacting projectile, right circular cylinders (RCCs) of different materials were chosen based on different hardnesses and densities, with their respective properties given in Table 5.1. Rockwell C hardness values for O1 steel RCCs were tested and averaged over several measurements using a spot hardness tester on the impact end. To obtain physically meaningful values for comparison, O1 steel Rockwell C hardness values were first converted to Vickers diamond pyramid hardness values [82]. The hardened O1 steel yield strengths were then calculated from the Vickers hardness H_v via known correlations provided by Pavlina & van Tyne [83] (5.5). The calculated yield strength was compared with existing studies for Rc 60 O1 steel [84] and AISI M2 steel [85] and shown to be accurate. Equation 5.5 also gives an approximate yield strength of 755 MPa for standard Rc 29 projectiles.

$$\sigma_y = -90.7 + 2.876H_v \tag{5.5}$$

RCC pieces had nominal diameters and lengths of 9 mm. RCCs were tumbled with ceramic media for five hours prior to testing to reduce the edge sharpness, as a previous study by the authors showed that localized edge geometries demonstrably reduced ballistic performance of the fabric due to off-axis failure [86]. Tumbled projectiles had micro-scale edge radii of curvature of at least 125 μm, where the ballistic limits

Table 5.1. Projectile materials and properties used in study.

Material	RCC/Total mass [g]	Rockwell	Vickers	σ_y [MPa]
O1 steel	4.48/4.88	HRC 61	720	2200 [84]
O1 steel	4.48/4.88	HRC 42	412	1100
M2 steel	4.60/5.00	HRC 62	746	2700 [85]
360 brass	4.83/5.23	HRB 75	N/A	159
7075-T6 Al	1.60/2.00	HRB 72	N/A	427
6061-T6 Al	1.49/1.89	HRB 60	N/A	241

are less dependent on these micro-scale stress concentrations. Instead of using sabots which require stripping before impact, light copper gas checks were lightly-attached on the non-impact end using petroleum jelly to form a better gas seal for higher gun efficiency and to achieve higher velocities. These gas checks weigh 0.4 g and have been added to the total mass in Table 5.1.

5.3.4 Shooting procedure

Twelve shots per panel were performed to determine the ballistic limit using the bracketing method as detailed in NIJ-0101.06 [70], with the first shot targeted at 305 m/s (1000 ft/s). The shot locations were located 25.4 mm (1 inch) from the panel stitching and at least 50.8 mm (2 inches) apart from each other, and as far as possible, shots were located such that the principal yarns do not overlap. For uniformity in testing, pre-and post-test temperatures and humidity levels were also recorded to ensure that testing conditions do not vary significantly.

5.4 Results & Discussion

Recorded pre- and post-testing temperatures and relative humidity levels were between 17.0-26.0 °C and 34-49% respectively. Tests were completed within 5 hours of test commencement. High-speed images were taking using a Shimadzu HyperVision HPV-X2 to ensure normal impact of the projectile without any significant yaw or pitch in the flight trajectory (Fig. 5.3).

5.4.1 Impact flash phenomena

The image sequences revealed a phenomenon whereby a transient flash of light occurred at the time and site of impact, and only occurs very briefly for a maximum duration of about 5 µs. A similar flashing phenomenon was previously observed by Chocron et al. [87] when impacting Dyneema® HB80 laminates with a polyurethane

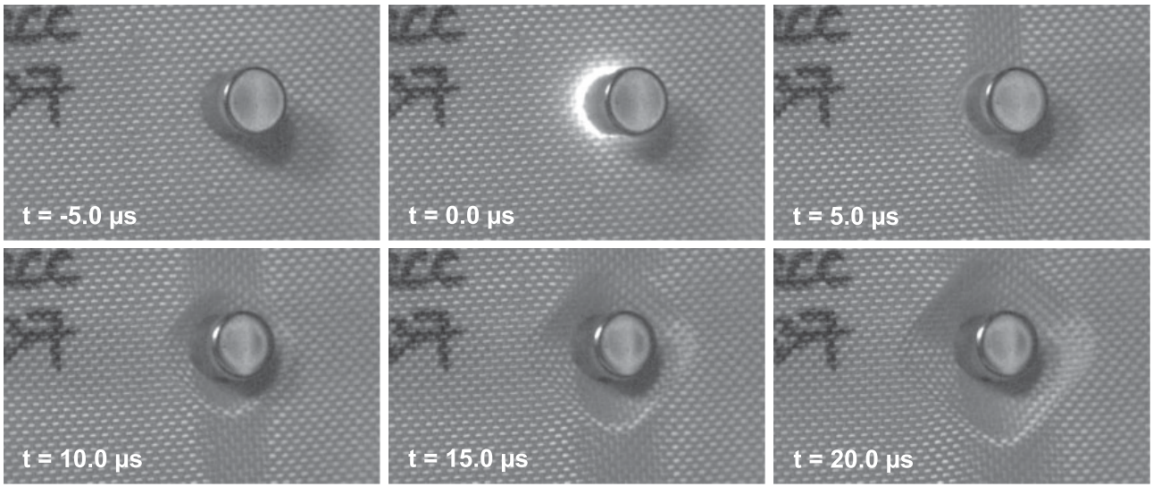

Figure 5.3. High-speed image sequence of 6061-T6 RCC impacting fabric target at 339 m/s, with a frame rate of 400 kHz and 200 ns exposure. A brief flash occurs at the time and site of impact ($t = 0$). Principal yarns in the vertical direction appear to be strained first before a square pyramidal tent propagates from impact site.

matrix, and recently by Ćwik et al. and Yang & Chen [20, 88] on Dyneema® SB71 laminates. Chocron et al. and Ćwik et al. attribute this to isentropic shock loading of the polyurethane matrix upon impact [20, 87], and the flash is a result of an "autoignition effect" from the shock, resulting in localized melting of either the UHMWPE fibers or the polyurethane matrix, or both.

The same phenomenon was observed in previous studies [76, 86] when firing O1 steel projectiles on 22-ply Twaron® CT709 fabric, indicating that this phenomenon may be projectile-independent i.e. a flash occurs in the fabric under certain conditions regardless of projectile material. As far as the authors are aware, there are currently no prior reports of similar phenomena occurring for aluminum projectiles impacting aramid fibers.

Table 5.2. Experimental and predicted ballistic limit velocities and ratios.

		V_{50} [m/s]				
Material	100η	NIJ	662F	Exp. Ave.	Predicted	Ratio
O1 steel	5.68	345	349	347	388	0.895
O1 steel	5.68	337	339	338	388	0.871
M2 steel	5.54	316	316	316	393	0.804
360 brass[a]	5.30	411	410	>411	381	1.078
7075-T6 Al	13.85	606	599	603	533	1.131
6061-T6 Al[b]	14.65	N/A	N/A	>601	548	1.096

[a]Tests were performed for 12 shots up to a maximum of 410 m/s with only 1 complete penetration. Ballistic limit is assumed to be at or above this velocity.

[b]Tests were performed for only 4 shots. Maximum possible velocities of 601 m/s were achieved without complete penetration. Ballistic limit is assumed to be at or above this velocity.

5.4.2 Ballistic limit results

The outcome of each shot was assigned a value of '0' for partially-perforated shots and '1' for completely-perforated shots. Perforation of the panel was verified visually during the test, and via post-mortem for confirmation. Two different methods of calculating the V_{50} ballistic limit, the NIJ-0101.06 [70] and MIL-STD-662F [77] methods, were compared and averaged (Table 5.2). NIJ-0101.06 uses a logistical S-curve regression while MIL-STD-662F uses the arithmetic mean of the lowest complete penetration velocities and highest partial penetration velocities. The full details of the calculation methods are given in their respective references.

In a previous study [10], Cunniff demonstrated that the V_{50} ballistic limit velocities of soft armor targets may be collapsed onto a single curve when the V_{50} velocities are non-dimensionalized with respect to the Cunniff velocity i.e. the cube root of the

product of the fiber specific toughness and the longitudinal sound speed within the fiber, given as

$$\Omega^{1/3} = \left(\frac{\sigma\varepsilon}{2\rho} \sqrt{\frac{E}{\rho}} \right)^{1/3} \tag{5.6}$$

where σ is the longitudinal failure strength, ε is the longitudinal failure strain, ρ is the fiber density, and E is the longitudinal modulus. The normalized ballistic limits for several different armor materials and constituent fibers were shown to collapse onto a single normalized regression curve for Kevlar® 29 [11] ($\Omega^{1/3} = 624$). For Twaron® CT2040, the fiber properties are obtained from Mayo & Wetzel [61]: failure strength $\sigma = 3.3$ GPa, failure strain $\varepsilon = 3.3\%$, density $\rho = 1440$ kg/m^3, and longitudinal modulus $E = 90$ GPa, giving $\Omega^{1/3} = 668$. The V_{50} velocities for Twaron® CT709 are then predicted using the equation

$$V_{50} = \left(\frac{\Omega_{Twaron}}{\Omega_{Kevlar29}} \right)^{1/3} \left[X_5 exp(X_6 \eta^{X_7}) \right] \tag{5.7}$$

X_5, X_6, and X_7 are the regression coefficients given in Ref. [10] as 269.32, 2.9068, and 0.7586 respectively. Since the ballistic data is typically based on a standardized projectile Rockwell C hardness of 27-31, these predicted V_{50} values provide a baseline comparison for the experimentally-obtained V_{50} in our experiments to account for different areal density ratios. The experimental and predicted V_{50} velocities and the experimental to predicted ratios are also tabulated in Table 5.2. Experimental data for Twaron® CT709 was plotted along with the regression curve in Fig. 5.4 calculated using Equation 5.7, as well as with data from previous studies [86] using 7-mm O1 steel RCCs for comparison.

The brass and aluminum projectiles lie above the master curve, indicating subpar performance of these projectile materials in comparison to a baseline Rc 29 steel projectile. On the other hand, the stronger projectiles lie at or below the predicted

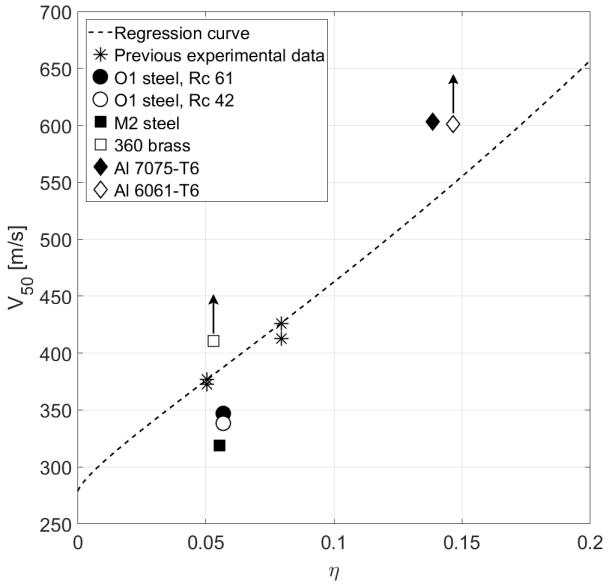

Figure 5.4. Plot of Twaron® CT709 V_{50} against areal density ratio η, with regression curve calculated using Equation 5.7 for comparison.

V_{50}, indicating similar or superior performance. By plotting the experimental to predicted V_{50} ratios from Table 5.2, the influence of the areal density ratio η on the target performance results is eliminated, and the effects of strength on the ballistic performance may be isolated – these results are plotted in Fig. 5.5. The figure also includes the predicted point for an RCC with hardness Rc 29 (yield strength 755 MPa) and using Equation 5.7.

As expected, the general trend of the ballistic limit velocity ratio decreases with an increase in projectile yield strength. Although the somewhat linear data appears to indicate that a hypothetical infinitely-high strength projectile impacting the target would yield a near-zero V_{50}, it is more likely that the influence of projectile strength would level off, closer to what the power-law fit in Fig. 5.5 would suggest. Note that this fit is merely included to visualize trends and should not be taken to be predictive.

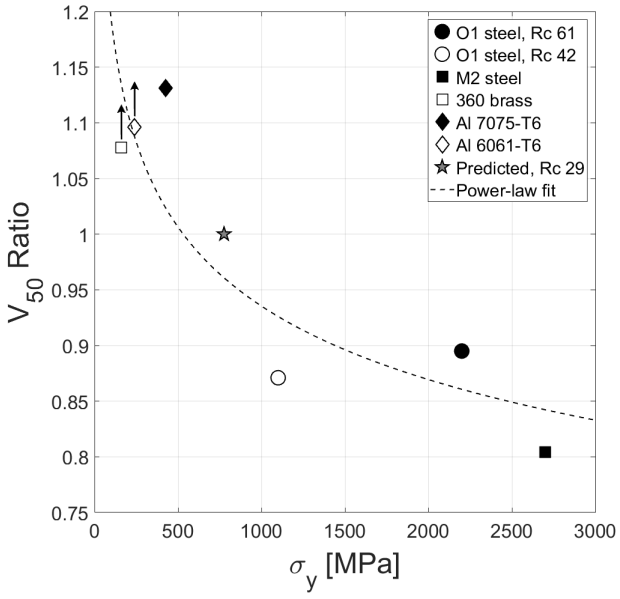

Figure 5.5. Plot of V_{50} ratios against yield strengths of projectiles.

The effects of inelastic impact deformation are further investigated via post-mortem analysis of the projectiles.

5.4.3 Projectile deformation

Post-impact projectiles were caught with a catch chamber lined with cotton jersey cloth rags and soft rubber sheets to prevent deformation of the projectiles upon impact with the chamber walls. On occasion, partially-penetrated projectiles were trapped within the fabric target layers, and subsequent shots may impact these trapped projectiles, resulting in extreme deformation and damage. These projectiles were not considered for post-mortem analysis. Post-impact diameters, lengths, and masses were measured to quantify the amount of deformation or damage occurring to the projectiles during impact (Table 5.3). Note that the average values for each material type in Table 5.3 are taken across a range of impact velocities.

Table 5.3. Post-impact measurements of RCCs.

		Post-Impact Diam.		Post-Impact Length		Post-Impact Mass	
Material	No. of points	Meas. [mm]	% Change	Meas. [mm]	% Change	Meas. [g]	% Change
O1 steel, Rc 61	13	8.99±0.01	-0.11	8.99±0.01	-0.11	4.48±0.01	0.00
O1 steel, Rc 42	10	9.00±0.01	0.00	9.00±0.01	0.00	4.48±0.01	0.00
M2 steel	12	9.00±0.00	0.00	8.99±0.02	-0.11	4.59±0.01	-0.22
360 brass	12	9.05±0.09	0.56	9.00±0.02	0.00	4.82±0.01	-0.21
7075-T6 Al	9	9.05±0.04	0.56	9.00±0.02	0.00	1.60±0.00	0.00
6061-T6 Al	4	9.81±0.42	9.00	8.85±0.20	-1.67	1.49±0.00	0.00

From Table 5.3, the mass loss during ballistic impact is practically negligible, implying that the projectiles, even the high hardness Rc 61 RCCs, do not fail in a brittle fashion, but rather they deform in a ductile fashion if at all. The post-impact diameters are noticeably larger for softer materials i.e. brass, 7075-T6, and 6061-T6. An explicit analytical expression for the projectile mushrooming energy has been previously given by Johnson [89] and included in Corran *et al.*'s analysis for projectile impact on ductile steel plates [80].

$$E_m = \frac{2\sigma_y A_p H}{9(\sqrt{A_{p,d}/A_p} - 1)} \left\{ 3 \left(\sqrt{\frac{A_{p,d}}{A_p}} \right)^3 ln \left[\sqrt{\frac{A_{p,d}}{A_p}} - \left(\sqrt{\frac{A_{p,d}}{A_p}} \right)^3 + 1 \right] \right\} \tag{5.8}$$

In Equation 5.8, $A_{p,d}$ is the projectile's mushroomed presented area and H is the length of the deformed section. While A_p and $A_{p,d}$ can be easily calculated from measurements in Table 5.3, the difficulty lies in measuring and determining the deformed section length H as the perforation process typically results in non-ideally axisymmetric impact for these soft armor targets. Equation 5.2 and Equation 5.8 together suggest that the trends of plastic work done is related to the striking kinetic energy, and therefore the post-impact percentage change in A_p for each shot and each material are plotted against the striking kinetic energy in Figs. 5.6(a)-(d). Since all the steel projectiles did not exhibit significant deformation, only the Rc 42 O1 steel RCC data is plotted for comparison.

Slight negative changes in A_p are due to deviations in measured diameters. The soft metals exhibited much larger degrees of deformation as the inelastic impact energy increases. For the aluminum RCCs, the areal density of the fabric target is relatively higher compared to their respective projectile masses, which resulted in larger degrees of deformation. However, 7075-T6 displayed less yielding compared to 6061-T6 due to the higher strength of the former. Post-impact projectiles were examined for micro-scale damage or deformation via scanning electron microscopy (Nova NanoSEM 200, Thermo Fisher Scientific, USA) in Figs. 5.7 to 5.9.

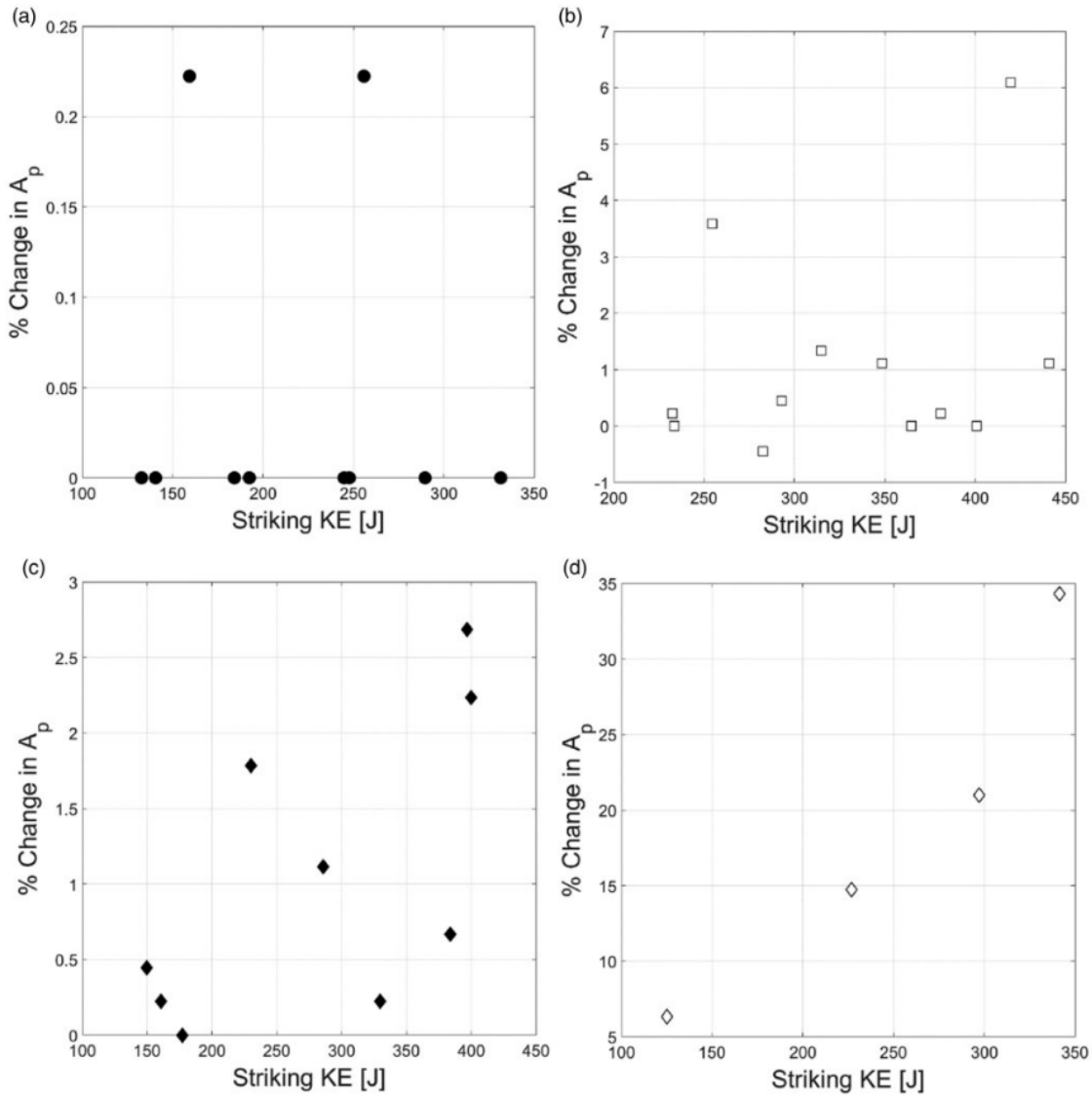

Figure 5.6. Percentage change in projectile presented area A_p against striking kinetic for (a) Rc 42 O1 steel; (b) 360 brass; (c) 7075-T6; and (d) 6061-T6.

Micrographs of steel projectiles showed minimal damage/deformation at the corners, which is reflected in the post-impact measurements in Fig. 5.7. For the brass and 7075 projectiles (Figs. 5.8 and 5.9 respectively), micro-scale plastic deformation was observed even though the 7075 projectiles are much stronger than the brass projec-

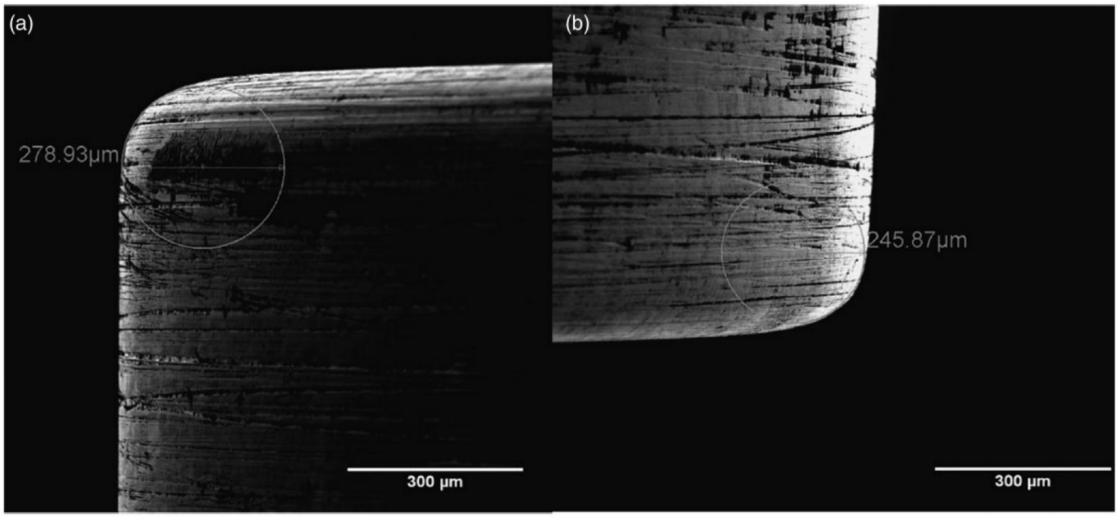

Figure 5.7. Post-impact micrographs of M2 tool steel RCC projectile shot at (a) 306 m/s (sub-V_{50}), striking KE 234 J, and (b) 387 m/s (above V_{50}), striking KE 374 J. Negligible to no deformation is observed at either velocity.

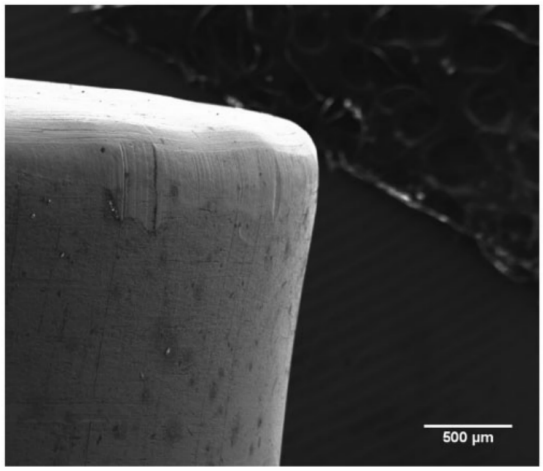

Figure 5.8. Post-impact micrograph of 360 brass RCC projectile shot at 298 m/s (sub-V_{50}), striking KE 232 J. Slight mushrooming deformation is observed at the impact end. Yarn imprints may be observed as well.

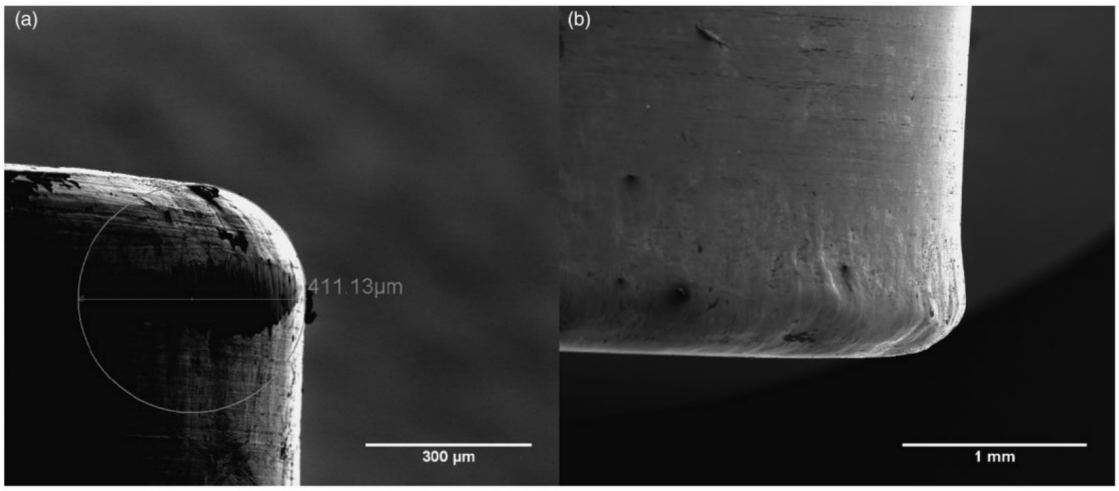

Figure 5.9. Post-impact micrographs of 7075-T6 aluminum RCC projectiles shot at (a) 387 m/s (sub-V_{50}), striking KE 150 J, and (b) 620 m/s (above V_{50}, complete penetration), striking KE 384 J. Deformation may be observed for both velocities, although larger degrees of mushrooming are observed at above V_{50} velocities.

tiles. The micro-scale deformation for these softer projectiles (in comparison with the much stronger steel) is related to the striking kinetic energies, as suggested by Equation 5.2. In general, where the projectile hardness exceeds the standardized values of Rc 29±2, the projectiles do not appear to exhibit any large-scale deformation, even at velocities higher than the ballistic limit. For softer projectiles, the impact ends generally deform via mushrooming. The deformation is obvious when examining the post-impact 6061-T6 projectiles, where the impact end severely mushroomed out and the fabric weave pattern became imprinted. Although not to such a severe degree as the 6061-T6 projectiles, the brass projectiles showed similar weave-pattern imprinting and mushrooming. This is likely due to the range of striking kinetic energies for brass being relatively low compared to the 6061-T6, as seen in Fig. 5.6.

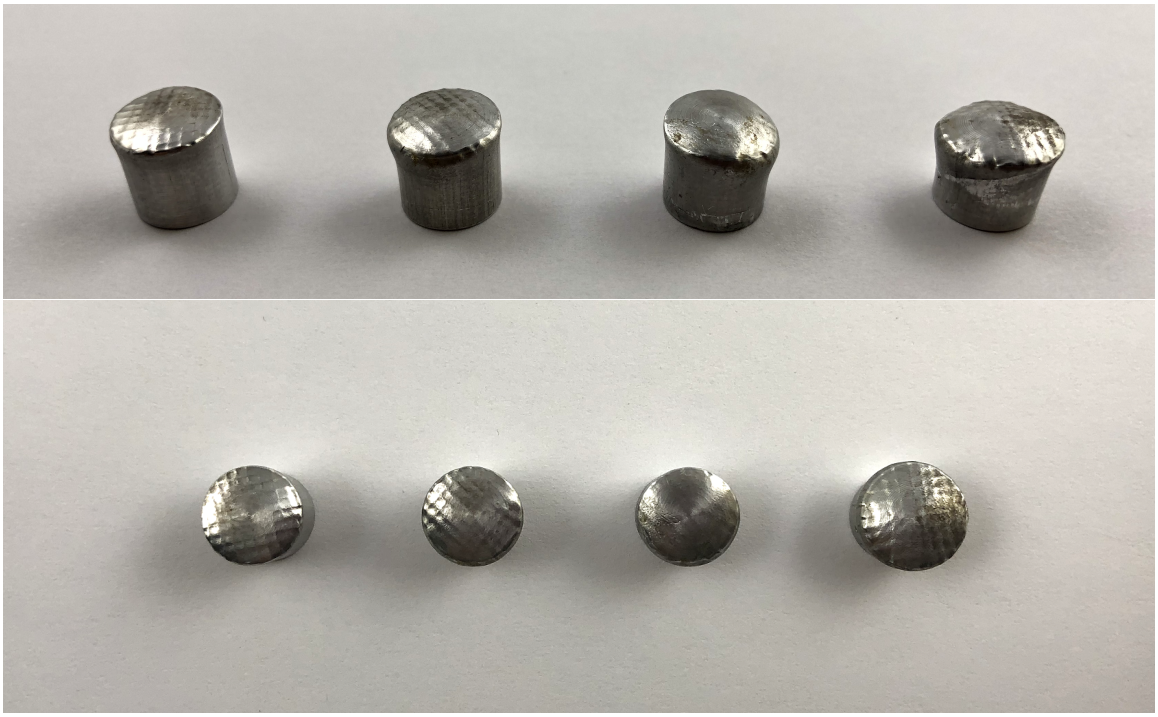

Figure 5.10. Photographs of (a) top and (b) elevated side profiles of post-impact 6061-T6 aluminum RCCs. Striking velocities of RCCs were (left to right) 364, 490, 561, and 601 m/s respectively. Progressively severe degrees of mushrooming deformation are shown with increasing striking velocities.

5.4.4 Discussion of energy dissipation due to damage or deformation

Target post-mortem analysis

It was also observed that the degree of deformation appears to be somewhat related to the impact velocity and the outcome of the shot (i.e. partial or complete perforation). These data points are shown in Fig. 5.6(b) and (c), where some of the high impact kinetic energies yielded minimal deformation. To explain this behavior, post-mortem inspection was also performed on the impacted targets. An examination of the fabric target's failure modes using prior methods for all shots reveals that the constituent plies of woven fabric targets typically respond in three broad ways: via

yarn rupture, nosing-through (also known as "windowing"), or no failure [78, 86], as shown in Fig. 5.11. At high velocities with respect to the individual ply, the yarns fail and rupture locally without significant yarn pull-out (Fig. 5.11a). This type of failure mode typically occurs for the frontal few plies closer to the strike face. When the velocity is sufficiently low, the yarns do not fail, but slip through the weave structure instead. A certain degree of yarn pull-out is often observed along with the characteristic diamond-shaped region of fabric strain (Fig. 5.11b). This defeat mode typically occurs in the middle of the pack after the regime of yarn rupture, and for shots that completely perforate at or near the critical velocity, this form of ply failure may be found at the rear of the pack. When the projectile is finally too slow to initiate sufficient yarn pull-out to slip through the weave structure, only minor dents and deformation are observed (Fig. 5.11c). The degree of deformation is difficult to quantify, but in this mode, it is obvious that the projectile does not perforate the fabric. Since this inspection method is purely visual, it should be noted that large scatter in determining actual failures modes is to be expected.

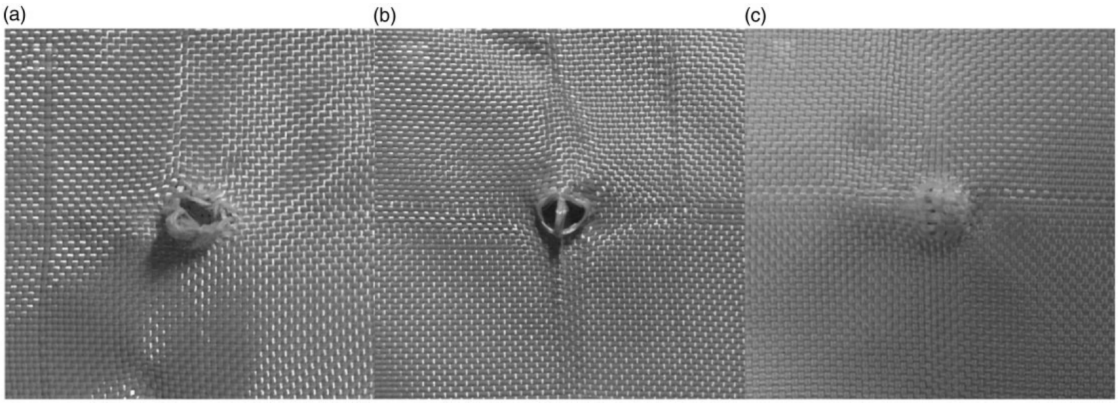

Figure 5.11. Broad categories of failure modes as observed in post-mortem: (a) localized yarn rupture, (b) windowing/nosing-through, and (c) no failure.

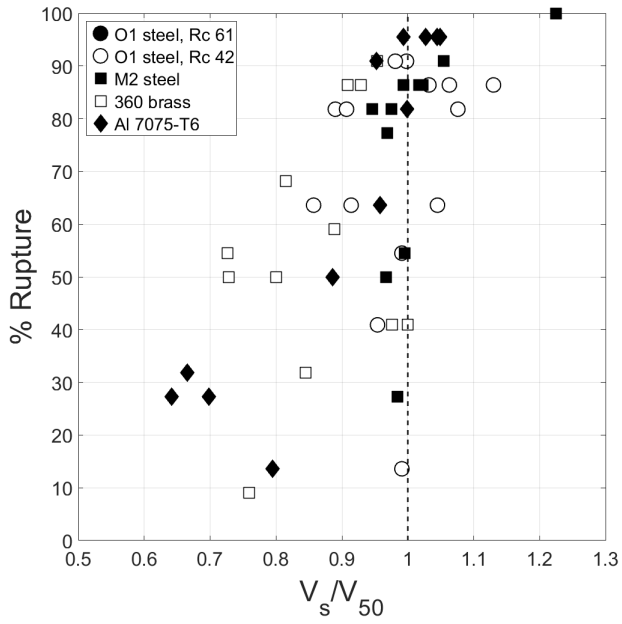

Figure 5.12. Plot of percentage ruptured plies against normalized striking velocities.

Fig. 5.12 shows that, generally speaking, the percentage of ruptured plies increases with V_s, with practically all the plies failing via rupture (i.e. off-axis modes) at velocities past the V_{50}. 6061-T6 aluminum was not included in Fig. 5.12 as the V_{50} velocity is expected to be much higher, since practically no yarn rupture was observed even at the maximum velocity of 601 m/s. The failure mode trends suggest that at high velocities, the localized failure of the contacted target material results in less projectile edge damage/deformation. Near or below V_{50} velocity regimes, the yarns of the individual plies are more likely to survive the impact for a longer time. This sustained contact time of the target and the projectile results in larger degrees of deformation of the projectile before the target material strains to failure. In cases where localized off-axis failure occurs and the target is defeated, energy dissipation via projectile deformation is lower compared to cases where the projectile is halted by the fabric. For example, a brass RCC with $V_s = 391$ m/s completely perforated the 22-ply Twaron® panel and ruptured approximately 91% of the plies but exhibited

no significant post-impact change in diameter; for another partially-perforated shot with $V_s = 401$ m/s, the brass RCC ruptured 41% of the plies but had a post-impact diameter of 9.27 mm (3% change). Presently, the dependence of the degree of yarn rupture on the projectile strength is inconclusive with the current set of post-mortem data and should be examined via in-situ methods.

5.5 Conclusions

The material yield strengths of RCC projectiles were varied to investigate the role of projectile deformation as an energy-dissipation mechanism during soft armor target impact. Target thicknesses were kept constant to isolate and exclude the effects of through-thickness shearing. The ballistic performance of the target panel generally decreases with an increase in projectile yield strength, although the marginal improvement in projectile performance is observed to diminish at higher yield strengths. The measured post-impact degrees of deformation of the RCCs correlate well with the inelastic impact energy dissipation using Recht & Ipson's formulation, especially for lower strength projectiles. At velocities near the V_{50}, localized failure of the target material resulted in less severe deformation of the impinging projectiles compared to similar velocities where the projectile was stopped. This effect is more pronounced for softer projectile materials where yielding is more likely to occur at these ballistic velocities.

Optimizing the design of soft armor target panels based on progression of failure modes under ballistic impact

In prior chapters, the failure modes and of these soft armors under ballistic impact were investigated. The different types of failure modes occurring in single-ply fabrics were investigated and broadly categorized via reverse ballistics experiments. The effects of different projectile parameters on the response of soft armor targets were further looked into, and the corresponding failure modes were categorized in the same fashion.

In the next part, the design optimization of these soft body armor systems is discussed from the perspective of utilizing our knowledge gained so far on these failure modes. We start off by looking at the two 'phases' of soft armor failure – inelastic and elastic. Inelastic failure involves localized, premature (i.e. fails before significant strain energy is dissipated) failure that is often associated with high velocity impact with respect to the system's ballistic limit velocity while elastic failure modes involve significant membrane strain energy absorption before failure.

The degree of inelastic failure is first experimentally determined by replacing the frontal soft armor fabric with a different material of varying types and ratios, and then semi-empirically analyzed using Cunniff's energy-absorption analysis to generate various curves that may help guide soft armor designs. The stacking order is then examined in terms of existing non-dimensional ballistic performance merit parameters, before all the concepts are brought together in the final section through experimentation and analysis of actual body armors impacted by commercial bullets.

6. REPLACING THE STRIKE-FACE MATERIAL OF MULTI-PLY SOFT ARMOR TARGETS

Chapter adapted from prior published work. Z. Guo, W. Chen, J. Zheng, Effect of replacement strike-face material on the ballistic performance of multi-ply soft armor targets, Text. Res. J. 89 (2018) 711–725.

Abstract

In this study, the impact-face material of a multi-ply soft armor system was varied to different ratios and tested for the effects on the ballistic performance. It is known that the first few layers of multi-ply soft armor material typically fail inelastically near the system ballistic limit and can be replaced with a "sacrificial" material with other more desirable properties. Previous studies have determined that the ballistic performance of these hybrid systems is largely dependent on the amount of high-performance backing material. However, the extent to which the high-performance fabric can be replaced has yet to be fully quantified and examined. Materials of different properties, namely stainless-steel mesh, Makrolon® polycarbonate sheets, and cotton were used as replacement frontal material for 840d Twaron® panels, and the hybrid panels were impacted by O1 tool steel RCC projectiles fired using a single stage smooth-bore gas gun. Results show that the ballistic performance is maintained up to a frontal material ratio of about 40%, and off-axis material properties play a role in energy dissipation.

6.1 Introduction

High-performance ballistic fibers are used in a multitude of different fields due to their unparalleled strength-to-weight ratios. These fibers have been utilized in commercial and industrial applications such as tow ropes, fishing nets and lines, and turbine fragmentation containment systems in aircraft. More importantly, these fibers have proven to be extremely effective against ballistic threats, and a wide range of experimentation has been performed on these materials. However, the underlying principles by which these fibers are able to stop ballistic threats with such efficiency is still not well and fully understood. The ballistic limit is a metric by which these fabric armor systems are evaluated and compared, and is most commonly defined using the V50, the velocity at which a projectile has a statistical 50% chance of penetrating the target system.

At striking velocities below or near the ballistic limit, the major energy-dissipation mechanisms involve fiber axial strain energy and kinetic energy, as well as through-thickness kinetic energy when the fabric system is moved in the out-of-plane direction [10, 13, 14]. Cunniff, in his various seminal studies on soft armor impact [9, 10, 12], has described this portion of energy absorption as "elastic". The energy absorbed by the material per unit mass is carried away from the impact site at the speed of sound in the material. Past the ballistic limit, these elastic strain energy mechanisms start to become less significant, while localized (henceforth described as "inelastic") failure modes start to take over. The energy does not get transferred rapidly enough away from the site of impact, and is further prevented from dissipating due to localized damage to the material.

The ballistic limit of a multiple-ply fabric system can be predicted given the target system/projectile areal density ratio [9, 10, 12]. The relationship between the ballistic performance and the areal density ratio has been empirically verified for a broad range of ballistic materials to a rather high degree of accuracy, and thus provides an excellent design basis for soft armor structures. An analytical membrane model was

developed by Phoenix & Porwal [90] to explain this relationship. The areal density ratio parameter is given by

$$\eta = \frac{A_d A_p}{m_p} \tag{6.1}$$

where A_d is the target system areal density, A_p is the projectile's presented area, and m_p is the projectile mass. In addition, the ballistic response of such a multiple-ply target system is typically decoupled through the system's layers [12]. In other words, "the first few plies of a multiple-ply armor system respond as if they were free-standing, not backed by the remaining plies of the system." At the V_{50} velocity for the whole target system, the velocity is sufficiently high with respect to the frontal layers for them to behave inelastically. These initial layers may then be swapped with a different material to result in a similar or possibly even improved ballistic limit, along with other desirable characteristics such as low cost or comfort. The caveat to using this "low-cost" frontal material is that the impacting projectile should not yield a sufficiently low ballistic limit for the rear high-performance material portion of the hybrid system. In such scenarios, for the same areal density ratio η, the hybrid system will perform worse than a full high-performance fabric system.

6.1.1 "Shear plug" failure mode

The formation of a shear plug typically occurs for continuum targets such as ductile metals, bulk polymers, or certain stiffened composite targets [19, 91]. As its name suggests, an actual plug of material is sheared off during impact on a target plate at sufficiently high velocities. In high-performance ballistic fabrics, however, the term "shear plug" is likely to be a misnomer, as there has been little to no direct evidence of shear plugs forming, even at high impact velocities. Most of the analysis in existing literature refer more to a localized inelastic failure mode than an actual plug. Regardless, various authors have suggested an analytical shear plug-

type localized deformation mechanism which occurs as a significant failure mode [9, 81,92–94], through either explicit analysis in their respective literature or by inference from their equations of motion. Most recently, Nguyen *et al.* [19] and Hudspeth [81] derived equations for this shear-plugging mechanism to describe the through-thickness energy absorption. Equations 6.2 to 6.4 below are a rearrangement of both authors' formulations to provide clarity.

$$E_{shear} = \int_0^t \tau_{max} \left(\pi \kappa D_p\right) t dt = \frac{1}{2} \tau_{max} \pi \kappa D_p t^2 \tag{6.2}$$

$$KE_{plug} = \frac{1}{2} \kappa^2 A_d A_p V_r^2 \tag{6.3}$$

$$E_{absorbed} = \frac{1}{2} m_p \left(V_s^2 - V_r^2\right) = E_{shear} + KE_{plug} \tag{6.4}$$

In the equations, E_{shear} is the amount of energy required to shear a fabric plug of mass, t is the through-panel thickness, τ_{max} is the shear strength in the through-thickness direction, D_p is the projectile diameter, V_s is the striking velocity, V_r is the residual velocity, and κ is a non-dimensional scaling coefficient (given as 1.6 in Ref. [19]). It is seen from Equation 6.2 and Ref. [81] that this inelastic energy is minimally-dependent on the impact velocity, and consequently the energy absorption fraction via this mechanism decreases with increasing striking energy. In fact, at high striking velocities way past the ballistic limit of a certain system, the "shear energy" contribution is negligible and the Cunniff derivation for inelastic energy [10] is recovered. Nonetheless, near the ballistic limit, a higher shear strength material may contribute more to the overall energy absorption than a weaker material.

A set of experiments performed by Alesi [26] in 1957 investigated the synergistic effects of frontal layers on the armor system as a whole. Specifically, Alesi tested hybrid panels of window glass/Nylon fabric, A-110AT titanium alloy/Nylon fabric, and polymethyl methacrylate (PMMA)/polyvinyl butyral (PVB) under impact from

0.22-caliber fragment-simulating projectiles (FSPs). The three panels exhibited synergistic effects, meaning that the hybrid system performed similar to or even better than a target panel of purely nylon fabric. However, many factors appear to be involved, such as the ratio of frontal material areal density to the whole target system areal density, target/projectile areal density ratios, as well as the amount of high performance backing material. As a conclusion, Alesi states that at lower velocities, the difference between the hybrid and fabric target diminishes quickly, and eventually, the nylon fabric system becomes superior.

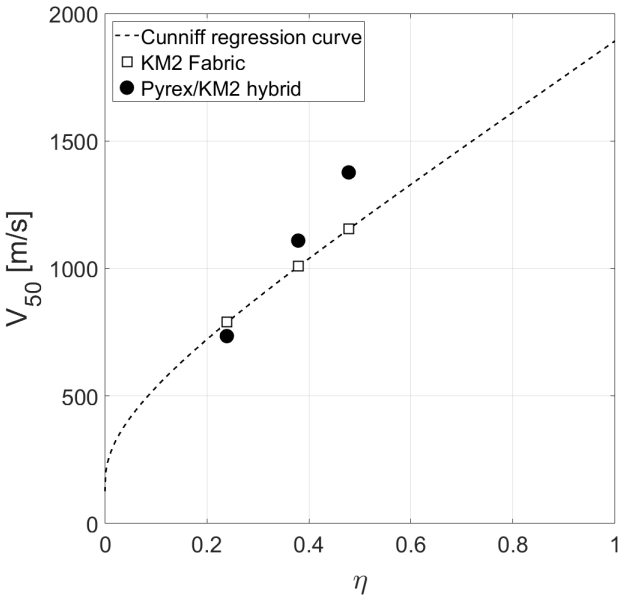

Figure 6.1. Hybrid Pyrex/KM2 and full KM2 fabric panel ballistic performance, as performed by Cunniff [12]

A subsequent experiment [12] was performed by Cunniff using 2-, 4-, and 16-grain RCCs (and consequently, different target/projectile areal density ratios) on a Pyrex glass/Kevlar® KM2 fabric hybrid panel target system to help narrow down these factors (Fig. 6.1). In particular, the target areal density was kept constant while changing the projectile areal density. It was found that at lower areal density ratios i.e.

larger projectile areal density for the same target system, the full KM2 fabric system will outperform the Pyrex/KM2 hybrid panel. At higher areal density ratios (smaller projectile mass), the Pyrex/KM2 hybrid outperforms the full KM2 fabric system – the transition areal density ratio seems to occur at $\eta \approx 0.294$ based on linear fits. This has been attributed to the deformation of the smaller 2- and 4-grain projectiles during impact, whereas the same mass projectiles "do not typically deform during impact onto fabric armor at this areal density" [12]. Deformation during impact increases the overall presented area, resulting in better ballistic performance of the target. However, further examination of the recovered projectiles was not performed. Regardless, these results show the influence of material strength when replacing these frontal layers.

While high-performance ballistic fabric systems show excellent resistance against ballistic impact, cut- and stab-resistance is another major requirement of these body armors [95], since these damage modes remain a viable threat to users of these armor systems. The feasibility of replacing the frontal material with a more stab-resistant material as well as knowing the fraction to which these high-performance fabrics can be replaced will no doubt be of great use in designing an efficient armor system. As mentioned, the amount of high-performance fabric material that can be replaced and the effects on the ballistic performance has yet to be fully quantified. The current work therefore focuses on 1) the systematic study of varying frontal material properties, and 2) the amount of frontal material that can be replaced without affecting the overall ballistic performance of the hybrid armor system.

6.2 Experimental procedure

6.2.1 Gas gun setup

Projectiles were shot with a single-stage smooth-bore light-gas gun with an inner bore diameter of 9.80 mm and barrel length of 3.66 m. In order to improve accuracy and reduce trajectory instability due to drag on the RCC projectiles, the target is

located approximately 0.4 m from the tip of the barrel. Alignment was performed to ensure perpendicularity of the target panel to the shot axis. A steel safety chamber was placed behind the target panel mount to retrieve any exiting projectiles using either terry cloth rags or 10% by weight porcine skin ballistic gelatin (temperatures permitting).

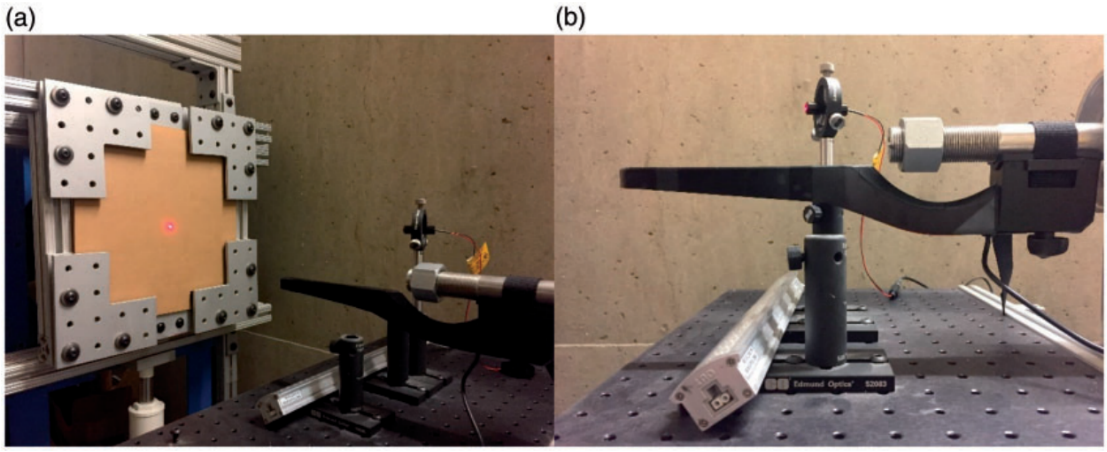

Figure 6.2. Front and side views of (a) target panel mount and (b) velocity-measurement device on gas gun setup. A point laser was used to ensure accuracy of the RCC shot on the target panel.

Target panels were clamped on all four corners using L-brackets with inner Neoprene rubber linings (50A Durometer) of 25.4 mm (1") width and 1/8-inch thickness to grip the target panel firmly, leaving an exposed surface area of 0.229 × 0.229 m^2 (9" × 9"). The L-brackets were secured using 12 flanged screws equally-spaced on all corners, and then tightened using a torque wrench to a maximum torque of 2.8 N-m (25 in-lb). Velocity measurements were made using a magnetic chronograph (MagnetoSpeed® Sporter) due to space limitations. The magnetic chronograph measurements have been compared with existing instrumentation such as a laser diode system and an optical chronograph to ensure that measured velocities were accurate to within 3.05 m/s (10 ft/s).

6.2.2 Target materials

The base Twaron® fabric samples (840 denier yarns) were obtained from Barrday and manufactured in 2015, with an areal density of 0.215 kg/m^2 per ply and 4.732 kg/m^2 for 22 plies. The hybrid target panel materials were selected for flexibility and to have a variety of shear strengths, namely Makrolon® film, cotton, and 120×120 grid size 304 stainless steel mesh (single-ply Ad 0.1585, 0.2720, and 0.4736 kg/m2 respectively). The shoot packs were designed and tested in various combinations as listed in Table 1, with the system areal densities kept relatively similar to the 22 plies (A25-22T) and 14 plies (B33-14T) of Twaron®. The percentage deviation of each system areal density from the full fabric pack is also calculated. The number of backing Twaron® plies were chosen for inelastic energy analysis, as will be detailed in the next section.

The fabric materials were cut to sample sizes of 0.305 × 0.305 m^2 (12“ × 12“), and subsequently edge-stitched three times together with a 25.4 mm (1-inch) margin from the edges for easier handling. Due to the loose stitching and stitch spacing, the edge-stitching does not significantly alter the ballistic performance. Since stitching is not possible for the stronger target materials (e.g. Makrolon® and 304 stainless steel mesh), these non-fabric layers were first attached at the edges with tape. For consistency, all panels were then heat-shrunk in a PVC bag with negligible areal density and thickness (0.051 mm). Panels were kept in storage in an air-tight container with clay desiccant packets for at least 12 hours prior to shooting to absorb any moisture that may be present due to transportation.

6.2.3 Projectiles

O1 tool steel right-circular cylinder (RCC) pieces were cut and faced from 9 mm rod stock to make the RCC projectiles. A nominal diameter of 9 mm was chosen as part of a larger study that was ongoing concurrently. Diameters and lengths of the RCC projectiles were measured to be within 9.01±0.01 mm (0.1% deviation) and

Table 6.1. Target panel materials and properties used in study (T = Twaron®, C = cotton, S = 304 stainless steel, M = Makrolon® polycarbonate).

	Panel material				
Panel No.	Front	Twaron®	Sys. A_d $[kg/m^2]$	Mat'l	% Dev.
A25-22T	-	22	4.732	0	0.0
A18-2C-19T	2 cotton	19	4.631	12	2.1
A32-2S-18T	2 steel	18	4.819	20	1.8
A29-5M-18T	5 Makrolon	18	4.664	17	1.4
A34-6C-14T	6 cotton	14	4.643	35	1.9
A27-4S-14T	4 steel	14	4.906	39	3.7
A35-11M-14T	11 Makrolon	14	4.755	37	0.5
A36-10C-9T	10 cotton	9	4.656	58	1.6
A30-6S-9T	6 steel	9	4.778	59	1.0
A37-18M-9T	18 Makrolon	9	4.789	60	1.2
A31-8S-4T	8 steel	4	4.649	81	1.8
B33-14T	-	14	3.011	0	0.0
B40-2S-9T	2 steel	9	2.883	33	4.3
B39-7M-9T	7 Makrolon	9	3.045	36	1.1
B38-8C-4T	8 cotton	4	3.036	72	0.8
B41-14M-4T	14 Makrolon	4	3.079	72	2.3

a nominal mass of 4.48 g. Due to the slightly over-sized bore diameter compared to the RCCs, Lyman copper gas checks were lightly attached using a thin layer of petroleum jelly to the non-impact end of the RCC to form a better gas seal for higher gun efficiency and higher exit velocities. The gas checks weigh approximately 0.4 g, and this weight is taken into consideration for effective density calculations. Prior to shooting, the rear non-impact end of these RCCs were marked using permanent ink to distinguish the impact end for post-mortem analysis.

The corners of the RCC projectiles were examined using scanning electron microscopy (FEI Nova NanoSEM 200) to verify the effect of target strength on any potential blunting of the corners which may affect the ballistic performance during perforation. The pre-shot cylinders have a corner radius of approximately 125 μm (Fig. 6.3a). Pre-shot projectile surfaces appear to be relatively smooth with minimal damage except for microscopic residual grooves due to machining processes (Fig. 6.3b).

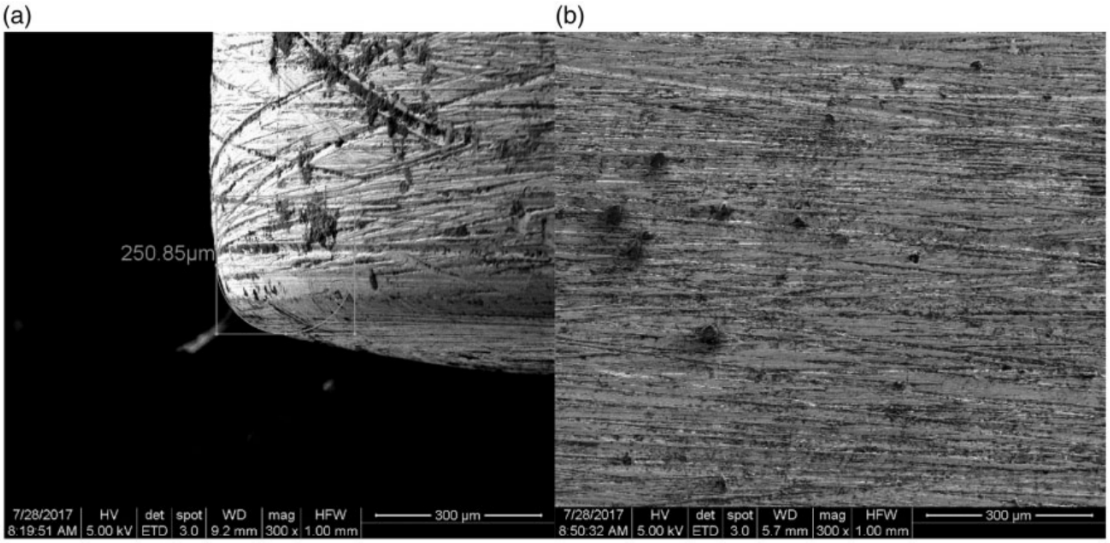

Figure 6.3. Micrographs of O1 tool steel RCCs prior to shooting, with measured corner radius of approximately 250 μm (a) and microscopic grooved surfaces due to machining (b).

6.2.4 Shooting procedure

A total of 12 shots were performed to determine the ballistic limit using the bracketing method as detailed in NIJ-0101.0615. Shot locations were pre-determined and marked using a template such that the shots were located 25.4 mm (1 inch) from the panel stitching, at least 50.8 mm (2 inches) apart from each other, and (as much as possible) that the principal yarns do not overlap. For uniformity in testing, pre-and post-test temperatures and humidity levels were also recorded to ensure that testing conditions do not vary significantly.

As the test chamber and targets are not exactly the same as detailed in the NIJ-0101.06 [70] standard, the methodology was slightly modified. The first shot is fired at a desired velocity of 304.8 m/s (1000 ft/s) – this velocity was referenced and estimated with respect to the manufacturer's datasheet for a 9 mm FMJ projectile impact. If the shot outcome is a partial penetration, a shot outcome of '0' is assigned to the shot number and the subsequent desired shot velocity is increased by 30.5 m/s (100 ft/s); if the shot outcome is a complete penetration, a shot outcome of '1' is assigned to the shot number and the subsequent desired shot velocity is decreased by 304.8 m/s (1000 ft/s). In the case of an unacceptable shot e.g. inaccurate shot location or large deviation of actual striking velocity from desired shot velocity of more than 3.05 m/s (10 ft/s), the shot is repeated.

The process is repeated till the first shot outcome 'reversal' i.e. from partial to complete penetration or vice versa. At this point, the change in desired velocity is lowered to 22.9 m/s (75 ft/s). Similarly, if the shot outcome is a partial penetration, a shot outcome of '0' is assigned to the shot number and the subsequent desired shot velocity is increased by 22.9 m/s (75 ft/s); if the shot outcome is a complete penetration, a shot outcome of '1' is assigned to the shot number and the subsequent desired shot velocity is decreased by 22.9 m/s (75 ft/s).

Again, this process is repeated till the next shot outcome 'reversal', where desired velocity step is further lowered to 15.2 m/s (50 ft/s). If the shot outcome is a partial

penetration, a shot outcome of '0' is assigned to the shot number and the subsequent desired shot velocity is increased by 15.2 m/s (50 ft/s); if the shot outcome is a complete penetration, a shot outcome of '1' is assigned to the shot number and the subsequent desired shot velocity is decreased by 15.2 m/s (50 ft/s). The procedure is then repeated till a total of 12 acceptable shots are completed, up to a total of 16 possible shots per target panel if necessary in the case of unacceptable shots.

6.3 Results & Discussion

Recorded pre- and post-testing temperatures and relative humidity levels were between 17.0-20.0°C and 34-41% respectively. Tests were typically completed within 5 hours of test commencement. For the 14-ply Twaron®-equivalent Series B targets, high-speed images were taking using a Shimadzu HPV-X2 (high-speed imaging capabilities were not available during the shooting phase for Series A panels). These images were used to ensure normal trajectory of the projectile without any significant yaw or pitch during flight (Fig. 6.4).

The image sequences revealed a particularly interesting phenomenon whereby a brief flash of light occurred at the time of impact, and seemingly appears only where the projectile initially contacts the fabric target. The flash only occurs very briefly for a maximum duration (estimated from frame rate and exposure) of about 5 μs. At $t = 0$, a small region around the right side of the impact site of the RCC lights up, and this corresponds with yarn movement in the fabric around the impact site. This is more apparent at $t = 2.5\mu s$, where the engaged principal yarns running vertically are being strained — the flash looks to be the brightest at this area as well.

A similar phenomenon was previously observed for ultra-high molecular weight polyethylene (UHMWPE) by Chocron *et al.* [87] when impacting Dyneema® HB80 laminates with a polyurethane matrix, and recently by Yang and Chen [88] when impacting Dyneema® SB71 UD laminates. Their images obtained were from the back, and it is only inferred that the flash happens on impact, although there is no

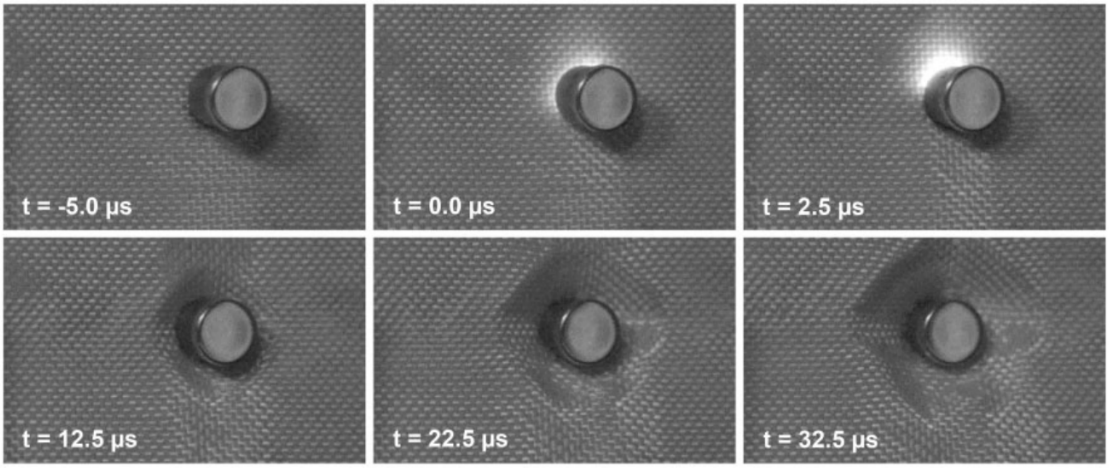

Figure 6.4. High-speed image sequence captured of the projectile impacting the fabric target at 339 m/s, with a frame rate of 400 kHz and 200 ns exposure. A brief flash occurs at the time and site of impact ($t = 0$). Note that image corrections of +20% brightness and + 20% contrast were applied to improve image clarity.

direct visual evidence. Chocron *et al.* attribute this to isentropic shock loading of the polyurethane matrix upon impact, and the flash is a result of an "autoignition effect" from the shock, resulting in localized melting of either the UHMWPE fibers or the polyurethane matrix, or both. As far as the authors are aware, there are currently no prior reports of similar phenomena occurring for aramid fibers, but it is possible that this flash is related to extremely localized deformation/damage.

6.3.1 Ballistic limit results

The outcome of each shot was assigned a value of '0' for non-perforated (or partial penetration) shots, and a value of '1' for perforated (or complete penetration) shots. Perforation of the panel was verified visually during the test, and via post-mortem for confirmation. Two different methods of estimating the V_{50} ballistic limit are given by the guidelines detailed in NIJ-0101.06 [70] and MIL-STD-662F [77], and these two

methods were compared and averaged. The former uses a regression for a logistical S-curve to determine two different regression constants. The shot outcomes (either '1' or '0') were plotted against their respective striking velocities.

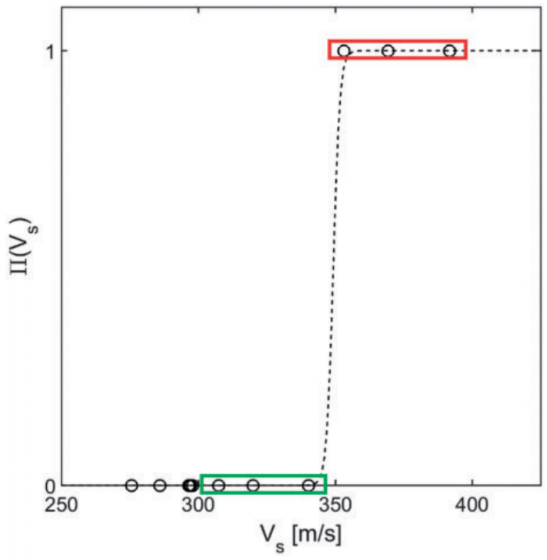

Figure 6.5. Typical plot of penetration probability against striking velocity for a target panel. Shown here are the shot outcomes for Panel A27-4S-14T.

The data points were curve-fitted using a Levenberg-Marquardt algorithm to obtain two curve-fit parameters, β_0 and β_1, as in Fig. 6.5. The ballistic limit is then calculated, with the regression curve given as

$$\Pi(V_s) = \frac{e^{\beta_0+\beta_1 V_s}}{1+e^{\beta_0+\beta_1 V_s}} \tag{6.5}$$

$$V_{50} = -\frac{\beta_0}{\beta_1} \tag{6.6}$$

In Equation 6.5, V_s is the striking velocity and $\Pi(V_s)$ is the probability of penetration at that particular striking velocity, as defined previously by either partial penetration or complete penetration. The V_{50} is then calculated using Equation 6.6.

Using Panel A27-4S-14T as an example, β_0 and β_1 are fitted as -287.5 and 0.8294 respectively, giving a calculated V_{50} via this method as 346.6 m/s.

In view of some of the possible uncertainties in calculating the V_{50} using just one method, the MIL-STD-662F [77] method of calculating the V_{50} was also employed. This method uses the arithmetic mean of the same number of lowest complete penetration velocities and highest partial penetration velocities. Acceptable velocities are selected within a range of 125 ft/s, and at least three points from each group have to be selected. As an example, in Fig. 6.5, the lowest complete penetration points used in calculation are highlighted in red, and the highest partial penetration points are highlighted in green. Using this method, the V_{50} calculated is 347.0 m/s. The V50s calculated using both methods are averaged and presented in Table 6.2. Although there are slight differences in areal densities of the target systems, this slight difference of up to 3.7% is not expected to contribute significantly to the differences in ballistic performance between panels. The results are all given in Table 6.2.

The V_{50} values were then plotted against the percentage of frontal material, as per Fig. 6.6. A Weibull-type fitting was used with the equation

$$V_{50} = V_{50f} exp\left(-f_s^{\alpha}\right) \tag{6.7}$$

where V_{50f} is the V_50 ballistic limit of a full fabric target system of equivalent areal density, f_s is the sacrificial material percentage, and α is a regression coefficient for the curve fit. The coefficient α has a value of 5.176 for Series A shots and 8.472 for Series B shots. The darker dashed line in Fig. 6.6 represents the Weibull curve-fit and the lighter dashed lines represent one standard deviation from the curve-fit.

The ballistic performance for all different frontal materials in Series A is not significantly altered up to 40%. Past this point, the ballistic limit begins to fall, even though the areal density is the same. The same effect is observed for Series B panels. After penetrating this frontal material, the residual velocity must exceed the V_{50} of the remaining Twaron® – the overall performance is therefore dependent on their elastic

Table 6.2. Experimental V_{50} results for Series A and B panels.

	Panel material			V_{50} [m/s]			
Panel	Front Matl.	Twaron®	% Front	NIJ	662F	Ave.	% Diff.
A25-22T	-	22	0	331.8	339.0	335.4	-
A18-2C-19T	2 cotton	19	12	331.4	332.6	332.0	-1.0
A32-2S-18T	2 steel	18	20	346.0	349.7	347.9	+2.8
A29-5M-18T	5 Makrolon	18	17	341.8	339.9	340.9	+0.7
A34-6C-14T	6 cotton	14	35	339.9	332.0	336.0	-0.7
A27-4S-14T	4 steel	14	39	346.6	347.0	346.8	+2.5
A35-11M-14T	11 Makrolon	14	37	315.5	314.9	315.2	-6.8
A36-10C-9T	10 cotton	9	58	293.0	309.5	301.2	-11.0
A30-6S-9T	6 steel	9	59	295.1	289.9	292.5	-13.6
A37-18M-9T	18 Makrolon	9	60	322.6	315.9	319.2	-5.7
A31-8S-4T	8 steel	4	81	263.7	265.2	264.5	-21.8
B33-14T	-	14	0	300.6	298.7	299.7	-
B40-2S-9T	2 steel	9	33	298.7	299.7	299.2	-0.2
B39-7M-9T	7 Makrolon	9	36	302.7	302.1	302.4	+0.9
B38-8C-4T	8 cotton	4	72	280.5	279.0	279.7	-7.7
B41-14M-4T	14 Makrolon	4	72	286.3	282.6	284.5	-5.1

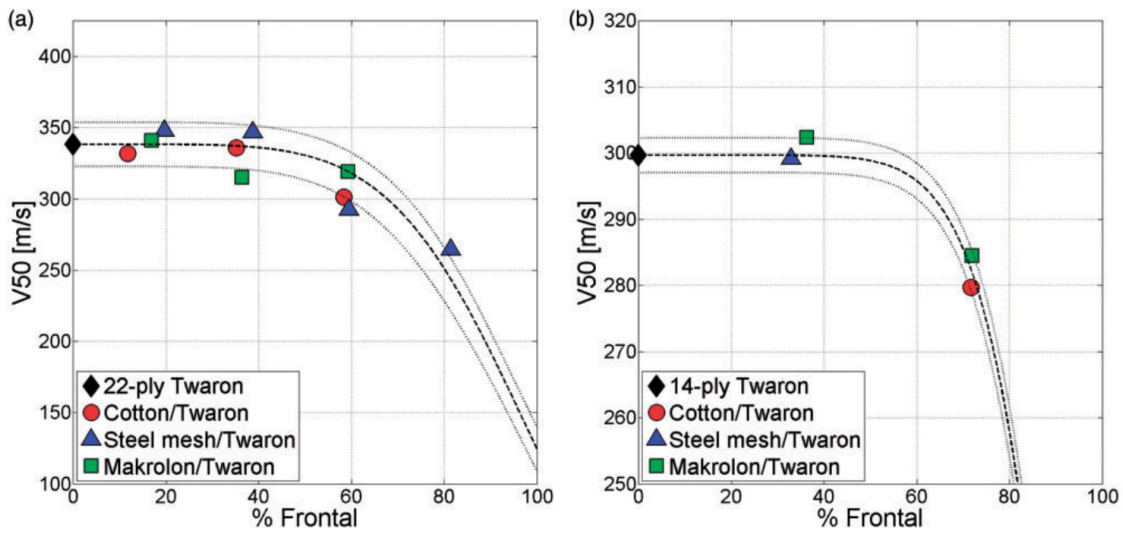

Figure 6.6. Plotted ballistic limits against frontal material ratio for the respective materials for (a) Series A and (b) Series B target panels.

properties. This is where the excellent mechanical behavior of high-performance fibers comes into play. At lower frontal material ratios, the high-performance Twaron® fabric still absorbs an appreciable amount of impacting energy from the RCC. However, with higher frontal material ratios (at the same areal density), the percentage of high-performance material decreases. The V_{50} with respect to the same RCC projectile then becomes low enough that the overall performance suffers.

Interestingly, even though cotton has a much lower strength than either steel or Makrolon® polycarbonate, there appears to be little to no discernible difference in ballistic performance for a given frontal material percentage, even at large ratios. These results only serve to reinforce the efficacy of using ballistic fibers as protective gear, as they still achieve the best performance at this given areal density ratio. A superficial understanding of the results seems to suggest that the effect of target strength does not seem to play a huge role in performance. However, to imply that the ballistic performance is only dependent on the areal density of the target is not entirely true, as this also means that the layering order of the target material and

fabric is not important. This has been shown not to be the case, as Cunniff [9] demonstrated a distinct difference in performance by a factor of about two when changing the order of Kevlar and Spectra single-ply layers.

This drastic difference in ballistic performance was easily demonstrated by shooting a hybrid panel Twaron® fabric face first and steel mesh first, i.e. a 4/14 steel mesh/Twaron® hybrid panel (Panel A-4S-14T) and a 14/4 Twaron®/steel mesh panel respectively, in this case (Fig. 6.7). Both panels were shot at approximately 300 m/s. For Panel A27-4S-14T, the 304-stainless steel mesh frontal layers sheared off before the projectile was stopped by the Twaron® backing material without even punching through the first layer. On the other hand, for the 14/4 Twaron®/steel mesh hybrid panel (Panel 14T-4S, not listed in Tables 6.1 or 6.2), the front 14 layers of Twaron® were perforated, but the steel mesh backing material failed critically after just one shot (Fig. 6.7).

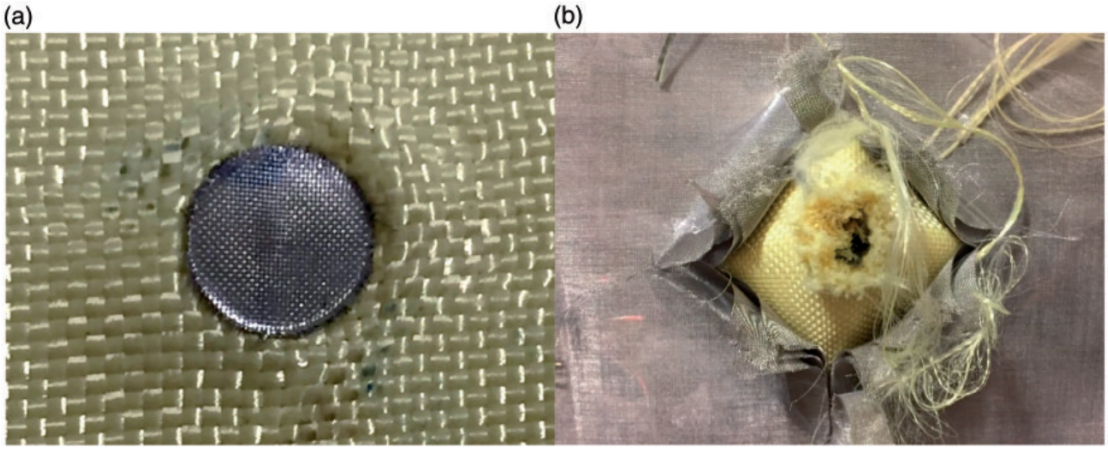

Figure 6.7. Post-impact images of 4/14 steel/Twaron® panel A27-4S-14T (left) and 14/4 Twaron®/steel hybrid panel 14T-4S (right).

For Panel A27, the frontal steel mesh obviously failed locally, resulting in a very well-defined shear plug. The residual velocity of the RCC after punching out the steel shear plug was insufficient to cause localized damage in the Twaron® fabric,

and so this absorbed energy gets somewhat dissipated around the impact site, as can be observed from the resulting tent shape.

6.3.2 Target post-mortem analysis

Target panels were analyzed post-mortem for different modes of damage and deformation near the impact site (Fig. 6.8). For cotton, stainless-steel mesh, and Makrolon® sheets, shear plugs were consistently formed for each shot regardless of the outcome. For Twaron®, formation of such a shear plug only occurred once out of all the impacted panels and their constituent plies, indicating the extreme unlikelihood of such an event. Instead, even though the initial few plies of Twaron® experience an impact velocity much higher than their individual ballistic limits, they often fail halfway along the circumference of the RCC to form a semi-circular tab rather than punching out the material fully (Fig. 6.8). The failure of the Twaron® fabric appears to be similarly localized, as observed from optical microscope images (Fig. 6.9).

The measured diameters of the recovered shear plugs are 8.60 mm, 9.01 mm, 8.11 mm, and 8.94 mm for Twaron®, stainless steel mesh, Makrolon®, and cotton respectively, reflecting the extremely localized inelastic failure of the initial plies via shearing/cutting or stress concentration-induced localized tensile failure. This indicates again that this is possibly where their respective failure strengths may become significant.

6.3.3 Energy analysis

The decoupled through-thickness ballistic response of a target armor system allows for a somewhat uncommon method of energy analysis to investigate the effects of the frontal material strength on the inelastic impact response. From the experimental results in Table 6.2 and Fig. 6.6, it is observed that the V_{50} limit does not drop significantly up to a frontal material ratio of 40%, which includes all of the Series

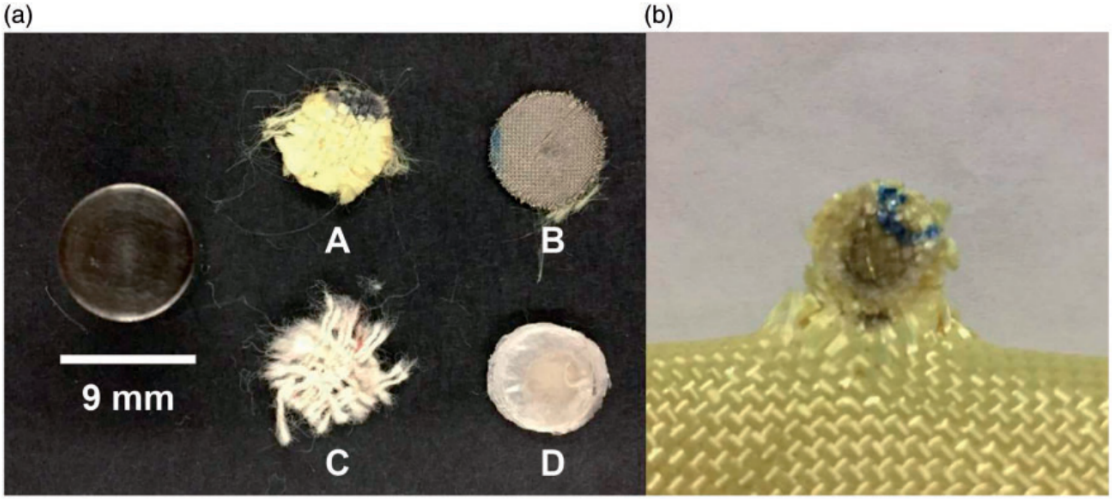

Figure 6.8. On left: recovered post-impact target "shear plugs": Twaron® (A), 304 stainless-steel mesh (B), cotton (C), and Makrolon® polycarbonate (D), with O1 tool steel RCC for reference. On right: typical semi-circular tab formation of initial plies of Twaron®.

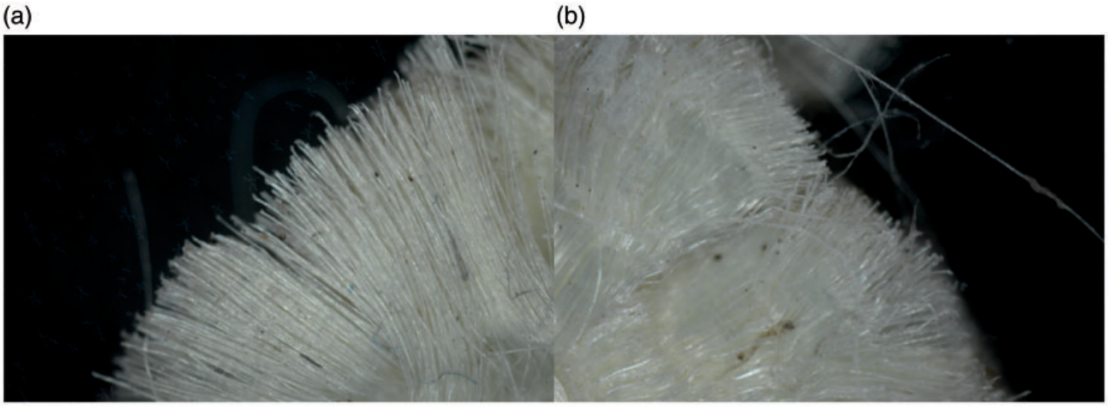

Figure 6.9. Optical microscope images of Twaron® shear plug edges at 12.5x magnification. Fiber and yarn failure appear to be extremely localized.

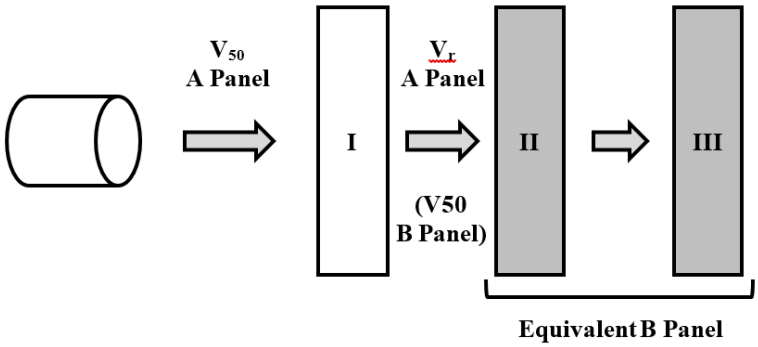

Figure 6.10. Schematic of decoupled response for Series A-14T panels into three subsystems and equivalent Series B panel on backing plies.

A-XX-14T panels (i.e. all panels with 14 plies of Twaron® as backing material). Series B comprises panels of areal densities equivalent to 14 plies of Twaron® fabric. In other words, at the V_{50} ballistic limit of the entire Series A-14T armor system, the residual velocity of the RCC after penetrating the frontal layer is sufficiently high to defeat a system of equivalent areal density to Series B. We first partition the overall system into three constituent subsystems I, II, and III, each with a certain percentage by mass of the overall system areal density. Subsystems II and III, when combined, will form an equivalent Series B panel, as in Table 6.3. The percentage by mass of each subsystem is similar for all panels, and Subsystem III for all panels consists of nine Twaron® plies.

Panel A25-22T is included because this panel can be considered a 14-layer Twaron® fabric with a frontal eight layers of Twaron®. Since the V_{50} is obtained statistically, we make the necessary assumption that at this velocity, the RCC fully penetrates the panel but exits with negligible residual velocity. Equation 6.4 gives the inelastic energy absorption as the difference between the projectile striking and residual kinetic energies – in this case, the residual kinetic energy of the initial subsystem I for Series A-14T panels is the V_{50} kinetic energy of the backing 14 plies of Twaron® i.e. V_{50}

for B33-14T. This difference in projectile kinetic energy is given in Table 4 under the column ΔKE.

From the third term in Equation 6.3, the kinetic energy of an assumed fabric "shear plug" of mass $A_d A_p$ moving at the residual velocity after penetrating Subsystem I (i.e. V_{50} velocity of the equivalent Series B panel) was also calculated under column KE_{plug}. Since recovered "shear plugs" were approximately the same diameter as the impacting RCC (Fig. 6.8), we assume that $\eta = 1$; a typical value of η for a Kevlar 29 fabric system is given as 1.36. At striking velocities much higher than the ballistic limit, the difference in kinetic energy ΔKE should be approximately equal to the plug kinetic energy, since the E_{shear} in Equation 6.3 remains constant. Again, it is stressed that for ballistic fabric material, this inelastic "shear energy" more than likely refers to localized failure around the impact site rather than a physical shear plug, as the latter has not been observed experimentally in existing literature or in this study.

Table 6.3. Series A-XX-14T and equivalent Series B panels for backing material behind Subsystem I.

A Series Panel		Subsystem I		Subsystem II		Subsystem III		Equivalent B Panel
No.	A_d [kg/m^2]	Mat'l	% A_d	Mat'l	% A_d	Mat'l	% A_d	
A25-22T	4.732	8 T	36.4	5 T	22.7	9 T	40.9	B33-14T
A34-6C-14T	4.643	6 C	35.1	5 T	23.2	9 T	41.7	B33-14T
A27-4S-14T	4.900	4 S	38.7	5 T	21.8	9 T	39.5	B33-14T
A35-11M-14T	4.755	11 M	36.4	5 T	22.9	9 T	40.7	B33-14T
A30-6S-9T	4.778	4 S	39.6	2 S	19.9	9 T	40.5	B40-2S-9T
A37-18M-9T	4.789	11 M	36.2	7 M	23.4	9 T	40.4	B39-7M-9T

Table 6.4. Series A-14T and Series B panels for 14-ply Twaron® equivalent backing material.

A Panel		Subsystem			Equivalent B Panel				
No.	V_{50} KE [J]	I	II	III	No.	V_{50} KE [J]	Δ KE [J]	KE_{plug} [J]	E_{shear} [J]
A25	279	8 T	5 T	9 T	B33	219	60.3	4.92	55.3
A34	275	6 C	5 T	9 T	B33	219	56.3	4.65	51.7
A27	293	4 S	5 T	9 T	B33	219	74.3	5.42	68.9
A35	242	11 M	5 T	9 T	B33	219	23.3	4.94	18.3
A30	209	4 S	2 S	9 T	B40	218	-9.67	5.39	-15.1
A37	249	11 M	7 M	9 T	B39	223	25.5	5.04	20.4

From the calculated energy values, we find that this shear plug kinetic energy far exceeds the change in kinetic energy of the projectile. Recall that the A-14T series panels have similar Subsystem I areal densities, implying that the energy dissipated due to inelastic mass collision must be similar regardless of material. This unaccounted deficit must therefore be related to some strength property inherent to the frontal material in Subsystem I. At this moment, the authors have yet to find a definitive correlation to the shear strength as per Equation 6.2, mainly due to the difficulties in obtaining an effective shear strength and thickness value for meshes and fabrics.

Although included as examples of subsystem energy partition, panels A30 and A37 do not have 14 plies of Twaron® as backing material and are therefore excluded in the above analysis. It is noted that comparing panel A30 to A27 numerically gives the change in energy absorption if the middle five layers of Twaron® were replaced by two layers of steel mesh; the same can be said by comparing panel A37 to A35, which numerically gives us the change by replacing the five Twaron® layers with Makrolon®. This conclusion is incorrect, as the impacting velocity on these middle layers may not actually be sufficiently fast to result in inelastic impact, and the energy partitioning analysis breaks down.

6.3.4 Projectile post-mortem analysis

The post-impact projectiles were recovered, and their dimensions were measured using calipers. Although projectiles were captured post-impact to the best of the authors' abilities, some projectiles unexpectedly yawed excessively after exiting the target and subsequently became damaged upon hitting the safety chamber – these projectile dimensions were not included. Measured projectiles were 9.01±0.01 mm in diameter and 9.00±0.02 mm in length, indicating negligible macro-scale deformation for O1 tool steel RCC impact at these striking velocities.

This brings us back to the initial hypothesis that projectile deformation during impact results in a different ballistic limit despite having the same areal density for the whole system. A quick look at the formulation of the areal density ratio suggests that a system can deform the projectiles either via mass loss or via 'mushrooming' of the projectile's impact end, both of which would increase η and consequently the ballistic limit. For this study, the macro-scale deformation was negligible and so η did not change significantly regardless of the outcome of the shot, implying that any deformation must happen at the micro-scale. To investigate this micro-scale deformation, the projectiles were subsequently examined using a scanning electron microscope. Figures 6.11- 6.14 show the micrographs for a variety of frontal material strengths and ratios, and impact velocities. Some tilt when mounting the projectiles may result in a spuriously large radius, and attempts were made to minimize any sample tilt under the microscope.

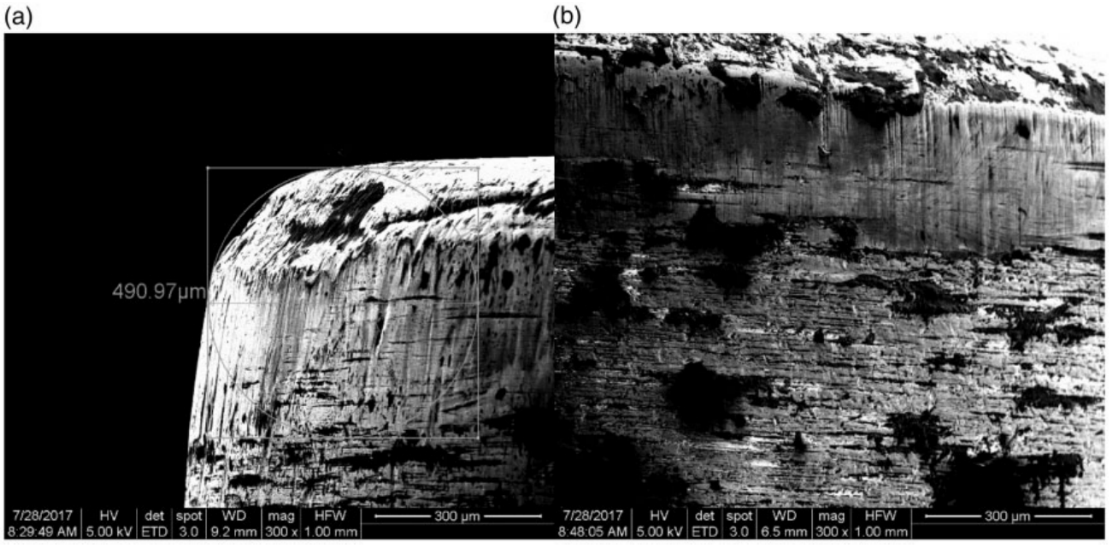

Figure 6.11. Micrographs of post-impact O1 steel RCC (a) corner and (b) impact end circumferential surface (right) for Panel A32-2S-18T Shot 1, partial penetration at 311 m/s.

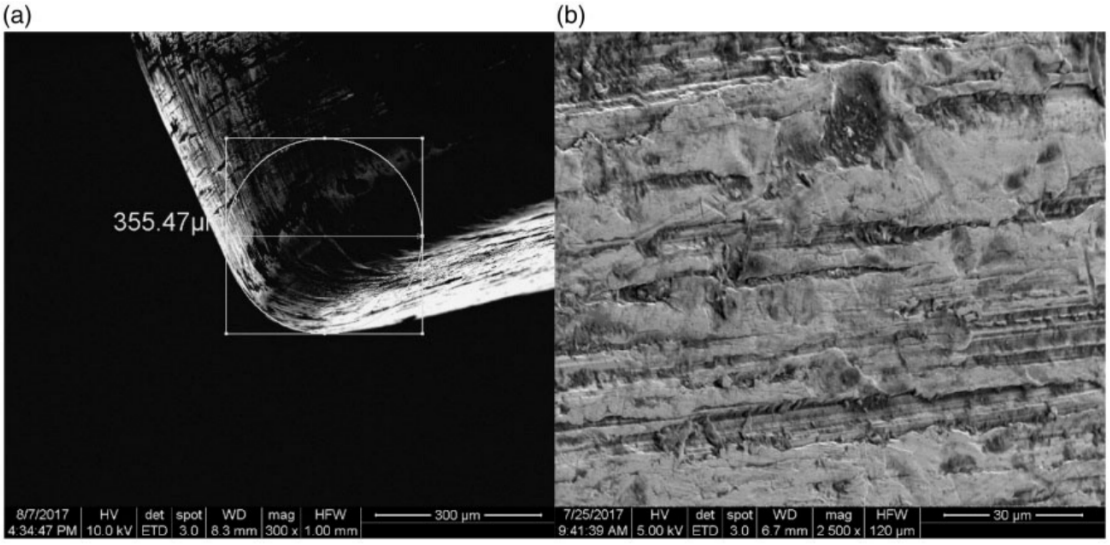

Figure 6.12. Micrographs of post-impact O1 steel RCC (a) corner and (b) impact end circumferential surface (right) for Panel A36-10C-9T Shot 2, partial penetration at 251 m/s.

Surface marring around the circumference of the cylinder impact end was apparent for all projectiles, presumably due to the high-performance fabric. Typical post-impact corner radii deformation for all impacted projectiles varied between approximately 150-250 μm from an original radius of about 125 μm, with no significant correlation between the deformation in radii and the impact velocity, frontal material strength, and frontal material ratio. On the other hand, there appears to be a slight correlation between the amount of Twaron® backing material and the change in corner sharpness. For example, for Panel A-10C-9T Shot 6 (nine Twaron® layers), the corner radius increased to 190 μm, while Shot 1 of Panel A32-2S-18T (18 Twaron® layers) increased its corner radius to 245 μm, even though they were fired at similar striking velocities. While the radius deformation is orders of magnitude smaller than the projectile radius, the constituent Twaron® fibers/yarns may be failing due to stress concentrations at the RCC corner. Single fibers and yarns have been shown to

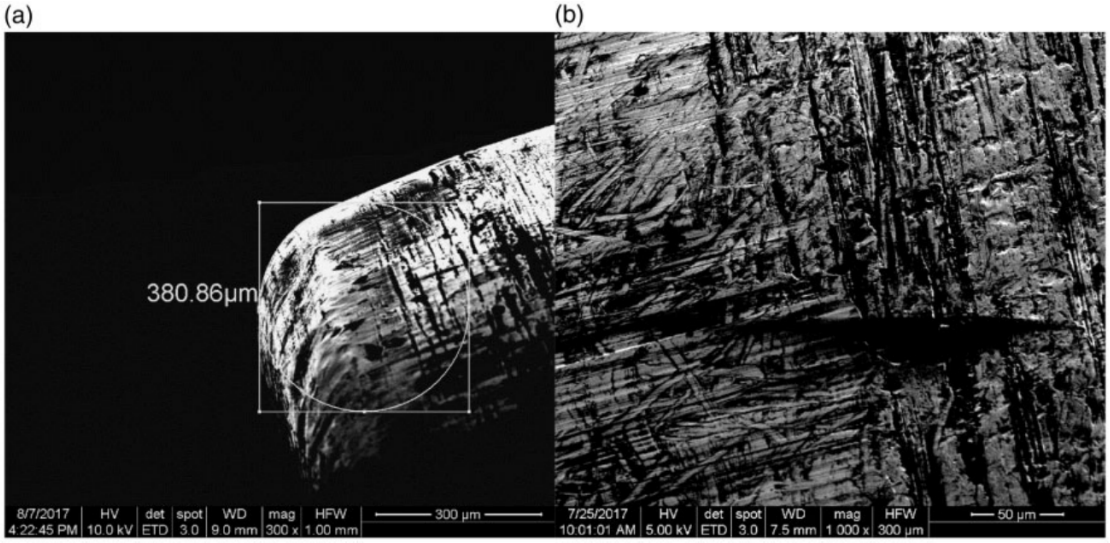

Figure 6.13. Micrographs of post-impact O1 steel RCC (a) corner and (b) impact end circumferential surface (right) for Panel A36-10C-9T Shot 6, complete penetration at 313 m/s.

fail at lower than theoretical critical velocities due to local variations in stress states, off-axis or otherwise [29–31, 61, 75, 96, 97]. Despite the multitude of studies on off-axis stress states during the transverse loading of yarns and fibers, these results have not been directly translated to a full fabric system due to its complexity. The micro-scale deformation of the RCCs in this study suggest that the efficiency of high-performance fabric systems (or in fact any frontal material that may be used in place) is somewhat dependent on their ability to "round off" these corners, thereby reducing the effects of stress concentration and consequently any localized failure.

6.3.5 Comparison of results with previous works

As previously mentioned, Alesi shot 17 grain T37 FSPs on three different hybrid target panels: window glass/12-ply nylon fabric, A-110AT titanium alloy/8-ply nylon fabric, and PMMA/5-layer PVB, as well as nylon and PVB of equivalent areal densi-

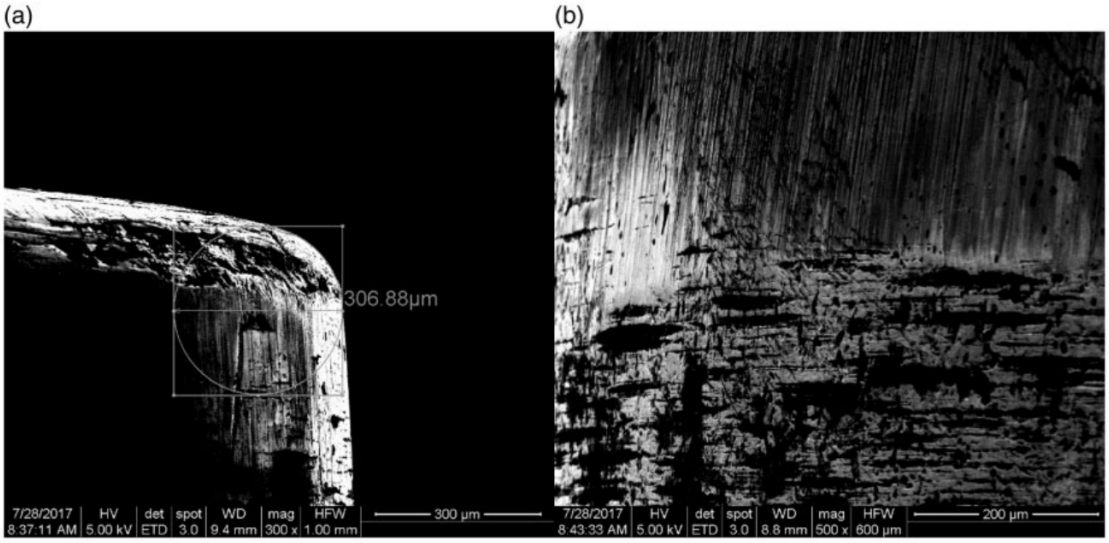

Figure 6.14. Micrographs of post-impact O1 steel RCC (a) corner and (b) impact end circumferential surface for Panel A35-11M-14T Shot 10, partial penetration at 300 m/s.

ties (i.e. 100% high performance material). In that study, the frontal material ratios and areal density ratios were not kept constant. Cunniff shot 2-, 4-, and 16-grain RCCs on 0.13-inch borosilicate glass/12-ply Kevlar® KM2 fabric as well as KM2 fabric panel of equivalent areal density, keeping the frontal material ratio constant but varying the areal density ratio. The frontal material ratios and areal density ratios were calculated, and the comparison of V_{50} limits is given as well. The check mark signifies that the panel resulted in a higher V50.

Table 6.5. Comparison of hybrid and 100% high performance backing material V50s from different studies.

	Materials				Higher V50	
Study	Front	Backing	% Front	100η	Hybrid	100% Fabric
Alesi, 1957	Glass	Nylon fabric	55	28.4	Similar	
	A-110AT	Nylon fabric	66	25.0	✓	
	PMMA	PVB[a]	84	28.8	✓	
Cunniff, 1999	Pyrex	KM2 fabric	73	23.9		✓
	Pyrex	KM2 fabric	73	37.9	✓	
	Pyrex	KM2 fabric	73	47.8	✓	
Current study	Varied	Twaron fabric	Varied	6.17		✓
	Varied	Twaron fabric	Varied	3.93		✓

[a]PVB: polyvinyl butyral

It appears from previous studies and the current dataset that the performance of a hybrid panel compared to a 100% high performance backing material of equivalent areal density is determined largely by the areal density ratio η. To re-iterate Cunniff's argument, lower areal density RCCs (2- and 4-grain) deformed when impacting the harder borosilicate glass frontal layer, whereas they do not deform during fabric armor impact. Similarly, since the larger 16-grain projectiles did not deform enough to affect the presented area significantly, the fabric armor behaves as expected, and the performance surpasses that of the hybrid panel. The transition seems to occur around a η value of 0.25-0.30.

6.4 Conclusions

In this study, the effects of replacing different amounts of high-performance Twaron® fabric with stainless steel mesh, Makrolon® polycarbonate, and cotton were studied as a possibility of replacing initial layers of high-performance material in an armor system with a lower-cost alternative, or some material with more desirable characteristics. These target panels were designed to have about 15%, 33%, 60%, and 75% frontal "sacrificial" material for two different areal densities at 4.732 and 3.011 kg/m2 (Series A and B respectively), and were impacted with an O1 tool steel right circular cylinder projectile. It was found that the ballistic performance of the system was maintained up to approximately 40% when using a Weibull-type curve-fit. Non-high performance frontal materials exhibited extremely localized failure and formed shear plugs consistently via a shearing/cutting mechanism, while the initial plies of Twaron® fabric exhibited a semi-circular tab at the impact site instead, although the failure mode appeared to be similarly localized or sheared. Since the ballistic response is decoupled, energy comparisons were made by partitioning a Series A armor system into three subsystems, and then comparing the striking energy at the ballistic limit with Series B panels. Deductions again showed the possibility of further energy absorption via inelastic "shear plug" formation related to transverse mechani-

cal properties. Scanning electron microscopy of post-impact projectiles showed slight deformation of the RCC corners, thereby reducing any stress concentration effects.

The design of a hybrid armor system therefore must meet two requirements: the high-performance material portion at any frontal material ratio must still have a ballistic limit high enough to maintain the same performance as a full fabric armor system 4, and that any frontal material used should be able to reduce the effects of stress concentration sufficiently for any improvement in ballistic performance. The frontal materials used in this study may not deform the corners significantly compared to the Twaron® fabric, but this is most likely where target frontal material strengths come into play, although further studies are recommended.

7. A SEMI-EMPIRICAL DESIGN PARAMETER FOR DETERMINING THE INELASTIC STRIKE-FACE FRACTION

Chapter adapted from prior published work. Z. Guo, W. Chen, J. Zheng, A semi-empirical design parameter for determining the inelastic strike-face mass fraction of soft armor targets, Int. J. Impact Eng. 125(2019): 83–92. doi:10.1016/j.ijimpeng.2018.10.007.

Abstract

At the ballistic limit velocity of a soft armor target pack, the impact response was shown to be decoupled in the thickness direction, with the initial few plies behaving in an inelastic fashion while the remaining plies dissipate energy via elastic strain modes. Since these initial plies only contribute to energy absorption via inelastic kinetic energy transfer, these plies may be replaced with another material with desirable properties, such as low costs or high shear strengths. The behavior of these diphasic armors has been shown in previous works to be varied depending on the type and the amount of strike face material that was replaced. However, there is a limited amount of published literature investigating this phenomenon. In this study, a framework is proposed to estimate the inelastic strike-face mass ratio as a function of the overall system areal density ratio to provide a preliminary design tool for diphasic armors.

7.1 Introduction

The significance and importance of soft body armors for personnel protection cannot be understated, and their usage has only increased multiple-fold over the decades

since their first conception. The impact and energy absorption mechanisms during the ballistic penetration of soft armor systems have long been a subject of extensive studies. The exact underlying physics behind the impact and failure phenomena is still not fully understood and still largely depends on empirical data from extensive ballistic tests. Earlier studies attempted to quantify the ballistic performance of target panels by measuring the projectile striking velocity and the projectile velocity after target perforation, i.e., residual velocity. A surprising amount of information on target failure mechanisms can be gleamed from post-impact residual velocity-striking velocity curves, such as that for a Kevlar® KM2 fabric system in Fig. 7.1.

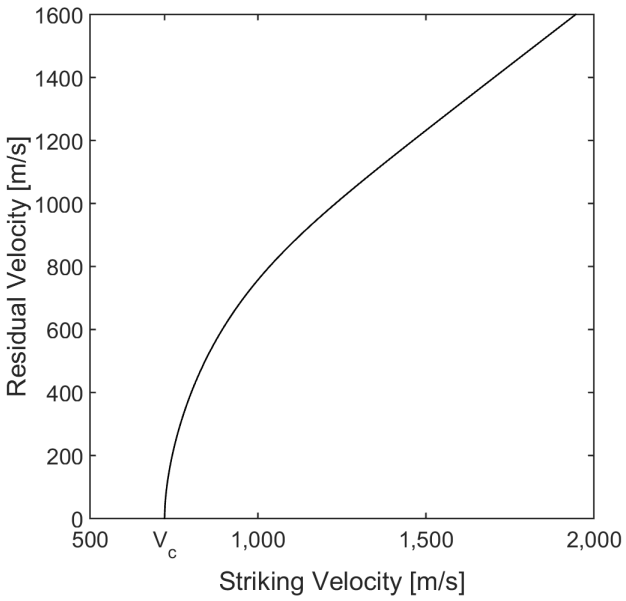

Figure 7.1. Typical residual velocity-striking velocity curve for Kevlar® KM2 fabric system.

Below the ballistic limit V_c, residual velocity is zero since penetration does not occur. As the impact velocity increases past the ballistic limit, the residual velocity transitions to a largely constant fraction of the impact velocity. Cunniff proposed that the total energy absorption E_{abs} of an armor system as the sum of two main

energy-absorption mechanisms [10, 12]: an elastic strain energy function Ω, typically dominant at velocities near the system's ballistic limit; and an inelastic impact function ξ, largely dominant at velocities past the ballistic limit. In this high impact velocity regime, the amount of striking kinetic energy absorbed via the fabric strain energy mechanism is assumed to be a decreasing function of striking velocity. The semi-empirical equations are given below

$$E_{abs} = \frac{1}{2} m_p \left(V_s^2 - V_r^2 \right) = \Omega + \xi \tag{7.1}$$

$$\Omega_c = \frac{1}{2} m_p V_c^2 \quad \text{for} \quad V_s = V_c \tag{7.2a}$$

$$\Omega = \frac{1}{2} m_p V_c^2 exp \left[-X_3 \left(\frac{V_s}{V_c} - 1 \right)^{X_4} \right] \quad \text{for} \quad V_s \geq V_c \tag{7.2b}$$

$$\xi = \frac{1}{2} X_2 A_d A_p V_{r,high}^2 \quad \text{for} \quad V_s \gg V_c \tag{7.3}$$

Note that Equation 7.3 differs slightly from Ref. [10] in that the latter provides the equation with an angle of obliquity via a *sec* θ term while the current analysis focuses on normal obliquity i.e. *sec* $\theta = 1$. In the above equations, V_c is defined as a critical velocity such that it is the highest striking velocity that results in no complete penetration, V_r is the residual velocity, $A_d A_p$ is the mass of a fabric plug immediately ahead of the projectile, and X_n are regression coefficients. At the instance of critical velocity impact, all the energy absorbed by the target is all in the form of strain energy (Equation 7.2a). The strain energy absorption function then exponentially decays with a further increase in striking velocity above the critical limit (Equation 7.2b) and eventually becomes negligible. Based on previous extensive studies [8,9,26,92,98], it was shown that at high striking velocities past the ballistic limit of the respective target panel, the measured residual velocity is essentially a linear function of the striking velocity. Consequently, the energy absorbed is also a fixed fraction of the striking kinetic energy (Equation 7.3). As such, we denote $V_{r,high}$ as the residual

velocity for high impact velocities past the ballistic limit for ease of discussion in later sections. Cunniff [9] describes this kinetic energy exchange mechanism as similar to that of impact with a theoretical shear plug with a mass equivalent to the target areal density multiplied by the projectile presented area. To the authors' knowledge, a shear plug has never been observed in-situ experimentally for fabric targets, only via inference by post-mortem analyses by other authors [92, 99]. However, this is conceptually identical to the inelastic impact shear plug model first proposed by Recht and Ipson [5] for impact on monolithic plates.

This energy partition and shear plug model has proven extremely useful and effective for soft armor design by providing a basis for predicting the ballistic performance via regression analysis. The critical velocity V_c is a function of the dimensionless areal density ratio $\eta = \frac{A_d A_p}{m_p}$ [8, 9], given by the equation

$$V_c = X_8 exp\left(X_6 \eta^{X_7}\right) \tag{7.4}$$

Combining Equations 7.1-7.3, the residual velocity of the armor system can be stated explicitly as [11]

$$V_r^2 = \frac{V_s^2 - V_c^2 exp\left[-X_3(\frac{V_s}{V_c} - 1)^{X_4}\right]}{1 + X_2\eta} \tag{7.5}$$

$$V_{r,high}^2 = \frac{V_s^2}{1 + X_2\eta} \quad \text{for} \quad V_s \gg V_c \tag{7.6}$$

Again, in Equations 7.4-7.6, the impact angle is assumed to be normal. It was found experimentally that the impact response of a soft armor panel is decoupled in the through-thickness direction. The strike-face plies of a multiple-ply armor system respond as if they were not backed by the remaining plies of the system [12]. At the critical velocity V_c of the entire armor system, the impact velocity of the projectile on these initial few plies is much higher than their respective critical velocities, i.e., $V_s \geq V_c$ locally, and therefore they fail inelastically before absorbing any significant

amount of strain energy. In this regime, the main energy absorption mechanism is via kinetic energy transfer and the areal density of the target is the critical parameter.

In this respect, the experimental observation of a two-stage (or in some literature, three-stage) penetration process corroborates the idea of a decoupled response, especially when impacting composite panels. In most of these composite panels, the two failure mode regimes are rather well-defined [15–20]. The initial transverse shear mode is easily observed via sectioned views, and in this regime, they often exhibit localized failure or fiber fracture. The subsequent onset of elastic energy dissipation at the rear side is demarcated by the presence of composite delamination, where the remaining target material exhibits a pyramidal tent, and failure modes tend to be tensile. Ćwik *et al.* [20,21] performed 20 mm FSP shots on Dyneema® HB26 and explicitly defined a First Major Delamination (FMD) within a composite target panel upon ballistic impact as the boundary between the frontal inelastic portion of the panel and the rear elastic membrane portion. Interestingly, at low striking velocities, the FMD occurs approximately 1/3 of the panel thickness from the strike face, but with higher striking velocities, the FMD gradually moves to about two-thirds of the thickness. Karthikeyan & Russell [18] investigated the impact response of steel spheres on Dyneema® HB26 composite panels and proposed the idea of a proximal (or strike-face) and distal region. In the proximal strike-face region, fiber fracture (i.e. localized failure) was shown to be one of the dominant failure mechanisms; in the distal region, membrane stretching, delamination, pull-out etc. were dominant features, indicating responses related to elastic properties. Although the terms "proximal mass" and "distal mass" were mentioned, they were not quantified.

In other recent works, Heisserer *et al.* [22] studied the depth of penetration into thin and thick Dyneema® HB26 ultra-high molecular weight polyethylene (UHMWPE) composite panels with hardened steel spheres and demonstrated a distinct impact response behavior difference in the specific energy absorption per ply. Zhang *et al.* [23] provided CT-scans of post-impact HB80 panels under ballistic impact, which reveal the obvious two-stage decoupled response in the thickness direction. Yang &

Chen [24, 25] investigated the energy absorption mechanism and failure mode of each constituent layer in a soft armor panel and determined the number of frontal perforated layers to be consistent regardless of panel thickness, although their impact velocities were not necessarily at the panel's ballistic limit.

Despite the ubiquity of ballistic materials and the extensive number of experiments performed on them, the actual fraction of inelastic strike-face material has never been explicitly investigated as a design tool. Previous works do seem to somewhat suggest some dependence on the target areal density. Cunniff highlighted the improved performance of a ceramic/composite diphasic target panel when using a thin ceramic frontal layer compared to a thick one, although values were not explicitly provided [100]. To the authors' best knowledge, the only study thus far that has experimentally quantified the specific amount of inelastic mass fraction as a ratio of the total areal density was by Nguyen *et al.* [19]. Dyneema® HB26 composite panels of various thicknesses were impacted with 12.7 mm and 20 mm fragment simulating projectiles (FSPs). In their work, thin panels were observed to fail in a single-stage elastic fashion via bulging and transverse deflection at their ballistic limit. The thicker panels, on the other hand, were observed to undergo a two-stage penetration process: first by localized shear plug formation at the strike face for a certain thickness, followed by elastic strain energy absorption for the remaining plies. The number of plies that failed via shearing in the thickness direction was measured and quantified, before being fitted with a power-law curve.

The decoupled impact response and the fact that the strike face material only contribute to energy dissipation via kinetic energy transfer means that the strike face material may be replaced with another material to produce a diphasic armor with other desirable properties. For example, Pyrex® borosilicate glass/KM2 fabric [12] and A-110AT titanium alloy/nylon fabric [26] hybrids have shown to improve the ballistic performance of the target panel over the full fabric panel equivalent due to the superior properties of the strike face material, but this improvement is not always sustained across different strike face ratios. A quasi-diphasic armor based on these

principles can also be designed. In a recent advancement in composite technology, the X-hybrid panel architecture [32] produced by the Army Research Laboratory (ARL) consisted of a 75% by panel net weight strike face in a typical [0°/90°] cross-ply fashion. The remaining 25% of the plies comprised a quasi-isotropic layup in which every two succeeding plies are laid in a [0°/22.5°/45°/67.5°/90°] fashion. Presumably, this takes advantage of the inelastic failure modes on the panel strike face to dissipate the initial striking kinetic energy. This is followed by dissipating energy via elastic strain energy, in which case the rotated plies provide a greater advantage by involving more armor material.

Indeed, a thorough knowledge of the fraction of strike face material that behaves in an inelastic manner is crucial in the design of diphasic armors, and it is the current focus of the study to elucidate the underlying mechanisms of the impact process in a semi-analytical fashion. Using observable trends in the $V_r - V_s$ curves, Cunniff's regression coefficients were slightly modified to present the inelastic strike-face mass ratio as a function of the system's areal density ratio. Results were compared to experimental data presented in existing literature by Cunniff [12], Alesi [26], Nguyen *et al.* [19], and Guo, Chen & Zheng [76], as well as a comparative analysis on some of the current soft armor design systems.

7.1.1 Purely Inelastic Impact Velocity V_ξ

The critical velocity of a target panel with a particular areal density ratio is calculated using Equation 7.4, and the residual velocity for a series of impact velocities is calculated using Equation 5. The resulting curve, along with the idealized fully inelastic impact given in Equation 7.6, is plotted in Fig. 7.2 below.

A few important points on the $V_r - V_s$ curve should be noted, and it may be prudent to define the necessary terms now to facilitate subsequent discussion. In Fig. 7.2, V_c is the critical velocity as previously described, and according to Equation 7.5, the residual velocity should be zero. If a hypothetical, purely inelastic impact

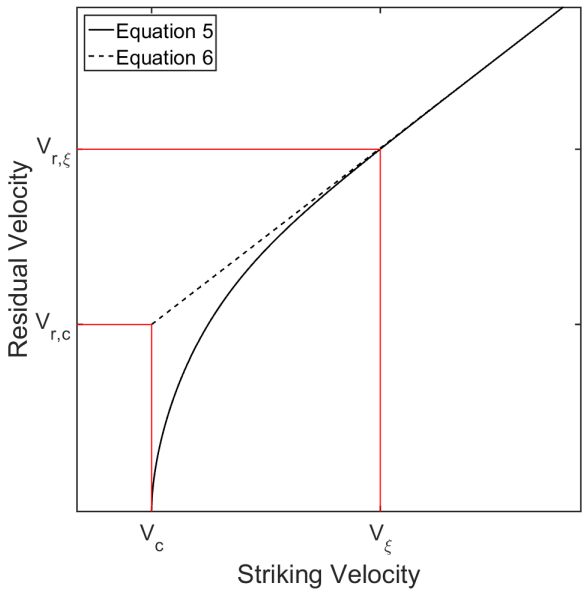

Figure 7.2. Theoretical $V_r - V_s$ curve for ballistic fabric impact.

response is assumed at V_c, the residual velocity will be given by Equation 7.6 as $V_{r,c}$. Physically, $V_{r,c}$ is the improvement in ballistic performance due to the elastic strain energy absorption of the fabric panel, compared to an inelastic collision energy-based absorption mechanism. This implies that, for a homogeneous soft armor target, the elastic strain energy mechanism at the ballistic limit will be more effective at energy-dissipation compared to an inelastic mechanism regardless of the initial areal density ratio, since the same impact velocity results in a residual velocity for the inelastic impact case. The same case was made by Nguyen *et al.* [101], who suggested that for the same target mass, the membrane tension mechanism (i.e. elastic mechanism) is significantly more efficient than the shear plugging mechanism (i.e. inelastic impact).

V_ξ is a theoretical striking velocity where the response of the full armor panel first becomes purely inelastic, and with this impact velocity, the residual velocity is denoted as $V_{r,\xi}$ (the subscript ξ from here on refers to a purely inelastic term). The V_ξ for each areal density ratio η can then be obtained using Equations 5 and 6. Calculating the V_c and V_ξ at each η, it can be verified that the ratio V_ξ/V_c is practically constant for each target material type (Fig. 7.3). This V_ξ/V_c ratio is henceforth termed X_{10} to be in line with Cunniff's regression coefficient nomenclature, with $X_{10} \geq 1$.

7.1.2 Tolerance ε

Since $V_{r,\xi}$ is dependent on the V_ξ point, it is imperative that a suitable method be used to determine this V_ξ value. The V_ξ at each areal density ratio can be theoretically calculated by setting Equations 5 and 6 to be equal. Doing this, however, imposes the following condition which approaches zero asymptotically

$$e^{-X_3\left(\frac{V_\xi}{V_c}-1\right)^{X_4}} = e^{-X_3(X_{10}-1)^{X_4}} \to 0 \tag{7.7}$$

This results in a mathematically infinite value of X_{10}. It is therefore necessary and (given the empirical nature of the regression analyses) more sensible to specify an allowable tolerance ε such that

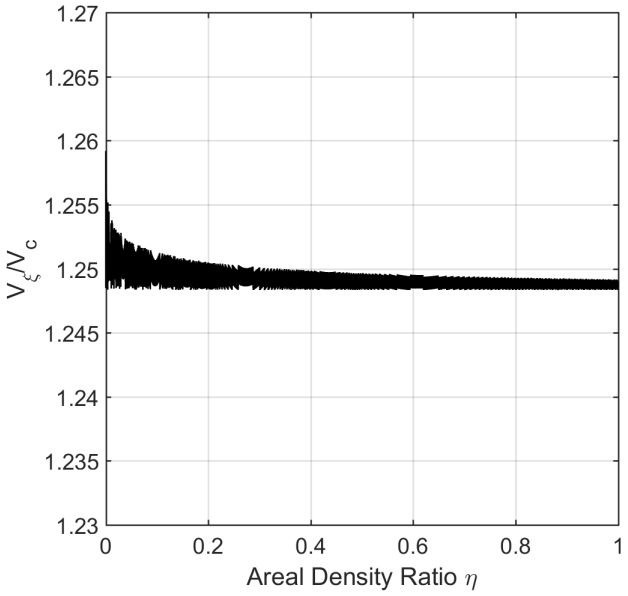

Figure 7.3. Ratio of $X_{10} = V_\xi/V_c$ against areal density ratio η for Kevlar® KM2 fabric.

$$\frac{V_r^2}{V_{r,high}^2} = 1 - \varepsilon = 1 - \frac{1}{X_{10}^2} e^{-X_3(X_{10}-1)^{X_4}} \tag{7.8a}$$

$$\therefore \varepsilon = \frac{1}{X_{10}^2} e^{-X_3(X_{10}-1)^{X_4}} \tag{7.8b}$$

with $\varepsilon \to 0$. Physically, this represents a transition from a strain-energy dominated absorption term from Equation 7.5 to a fully-inelastic absorption mode with the residual kinetic energy term from Equation 7.6. The transition curve is plotted in Fig. 7.4 below and shows a rapid change in energy absorption mechanism in the regime near the ballistic limit.

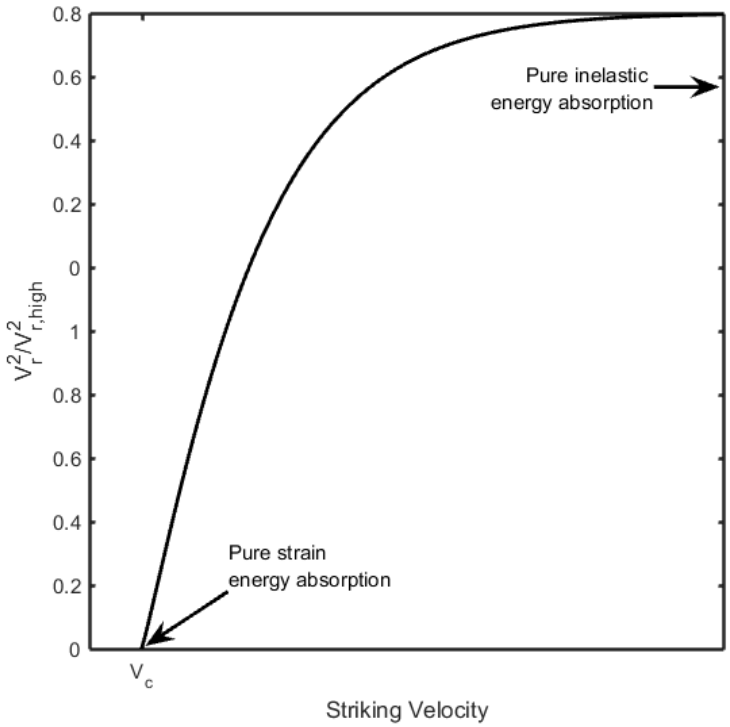

Figure 7.4. Ratio of mixed elastic-inelastic residual kinetic energy to fully inelastic energy absorption mode with increase in striking velocity. At high impact velocities, the ratio tends towards unity.

With a specified tolerance, the parameter X_{10} can then be obtained via iterative procedures, or by solving Equation 7.8b. The former method is more practical due to the complexity of the equation. It is also worth noting that Fig. 7.4 and Equation 7.8b are in fact the cumulative distribution function of a modified Weibull distribution. Referring to Equations 7.1- 7.3, the strain energy function Ω is dominant at or near the ballistic limit V_c, with the residual kinetic energy given as a function of V_r^2. As the striking velocity (and hence striking kinetic energy) increases, the strain energy function decreases exponentially and diminishes to zero, at which point the inelastic kinetic energy function ξ is dominant and the residual kinetic energy is a function of $V_{r,high}^2$. The ratio $V_r^2/V_{r,high}^2$ therefore indicates the degree of inelastic energy absorption, from a value of '0' at V_c indicating pure strain energy absorption to a value of '1' at high impact velocities indicating a purely inelastic kinetic energy mechanism. In a sense, Equation 7.8a gives an idea of how much "inelastic" localized failure the target panel can take before it is fully damaged in the impact zone. By obtaining the inelastic impact velocity V_ξ for each areal density ratio η, a curve similar to the V_c-η curve is obtained, as per Fig. 7.5.

In Fig. 7.5, the subscript *sf* refers to the strike-face fraction which responds inelastically, and the subscript *sys* refers to the full target system – the same nomenclature will be used for subsequent discussion. For a projectile-target pair with a system areal density ratio η_{sys}, the system critical velocity $V_{c,sys}$ (Point A) is calculated using Equation 7.4. At $V_{c,sys}$, this striking velocity initiates a fully-inelastic response for some strike-face fraction η_{sf} that is yet unknown. This inelastic strike-face fraction is obtained from the point at which the V_ξ-η curve has a value equivalent to the system critical velocity i.e. $V_{\xi,sf} = V_{c,sys}$ (Point B). Without prior regression analysis, η_{sf} cannot be computed directly from the V_ξ-η curve. However, we know that for this strike-face mass fraction, the areal density ratio is η_{sf}, and this strike-face fraction has a standalone critical velocity $V_{c,sf}$ (Point C). It must be noted that the strike-face critical velocity $V_{c,sf}$ is used purely as an intermediate step to obtaining η_{sf} in terms of $V_{c,sys}$ and should not be taken at face value. Using the previously-calculated

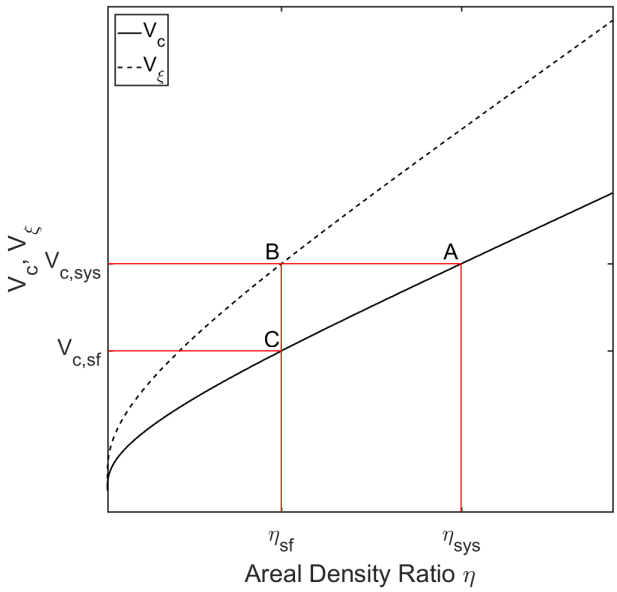

Figure 7.5. V_ξ and V_c plotted against areal density ratio η for comparison.

parameter X_{10}, we can obtain this strike-face fraction's critical velocity in terms of the system's critical velocity i.e. $V_{c,sf} = V_{\xi,sf}/X_{10} = V_{c,sys}/X_{10}$. Now, all the necessary parameters are given in terms of the system regression coefficients, which are known. Rearranging Equation 7.4 gives us, for a general projectile-target pair with areal density ratio η,

$$\eta = \left[\frac{1}{X_6} ln\left(\frac{V_c}{X_8}\right)\right]^{1/X_7} \tag{7.9a}$$

And specifically, for η_{sf},

$$\eta_{sf} = \left[\frac{1}{X_6} ln\left(\frac{V_{c,sf}}{X_8}\right)\right]^{1/X_7} = \left[\frac{1}{X_6} ln\left(\frac{V_{c,sys}/X_{10}}{X_8}\right)\right]^{1/X_7} \tag{7.9b}$$

It may be more useful as a design tool to have the inelastic strike-face mass fraction as a function of the system mass. This can be easily achieved by combining Equations 7.9a and 7.9b and rearranging logarithmic terms to give

$$k = \frac{\eta_{sf}}{\eta_{sys}} = \left[\frac{lnV_{c,sys} - lnX_8X_{10}}{lnV_{c,sys} - lnX_8}\right]^{1/X_7} \tag{7.10}$$

Finally, substituting for the system's critical velocity $V_{c,sys}$ as a function of the areal density ratio η (Equation 7.4), the inelastic mass ratio k as a function of η can be explicitly written as

$$k = \left[1 - \frac{1}{X_6}\left(\eta_{sys}^{-X_7}\right) lnX_{10}\right]^{1/X_7} \tag{7.11}$$

From the above set of equations, the parameter k can be obtained using regression coefficients X_3, X_4, X_6, and X_7 from Ref. [10]. Using available data, the relevant coefficients for tolerance values of 3, 5, 7, and 10% were calculated and tabulated in Table 7.1 below. A range of tolerance values was chosen because experimentally, system effects within the target would mean that there is no clear demarcation of

what defines localized inelastic failure e.g. localized tearing, yarn slippage, projectile nose-through etc. These mechanisms may result in localized defeat of the fabric with significantly reduced resistance [34, 78], but with no "shear plug" formation. These values were then used to generate a series of k-η curves at 3% ε tolerance for materials where the regression coefficients were available, as in Fig. 7.6. In the following sections, it can be shown that a tolerance value of 3-5% produces sufficiently accurate results. The generated curves for 5, 7, and 10% tolerances are given in Appendix A. It must be noted that due to the logarithmic and root functions in Equation 7.11, complex numbers may arise during iteration – these parts were truncated from the plots.

Table 7.1. Regression coefficients and calculated constants from Equation 7.11.

Target	X_3	X_4	X_6	X_7	X_{10}			
					3%	5%	7%	10%
Nylon fabric	2.1311	1.8422	1.9414	0.4074	1.4268	1.3561	1.3085	1.2577
Kevlar® KM2 fabric	4.1871	1.2768	2.7104	0.2728	1.2486	1.2047	1.1766	1.1461
Kevlar® 29 fabric	1.6266	0.3578	2.9068	0.7586	1.4376	1.3407	1.2816	1.2232
E-Glass/polyester comp.	0.5644	3.3177	5.1837	0.2658	1.6590	1.5339	1.4488	1.3593
Kevlar® 29/PVB comp.	2.2095	1.3151	2.8198	0.5692	1.3496	1.2853	1.2438	1.2008
Nylon comp.	0.7807	1.1385	4.3318	0.2145	1.4945	1.3902	1.3258	1.2613
Dyneema® HB26 comp.	1.9150	1.0180	7.8840	0.1145	1.3196	1.2537	1.2126	1.1711
Dyneema® HB26 comp.*	-	-	2.9090	0.5248	1.3080			

*data from direct fit of Equation 7.11

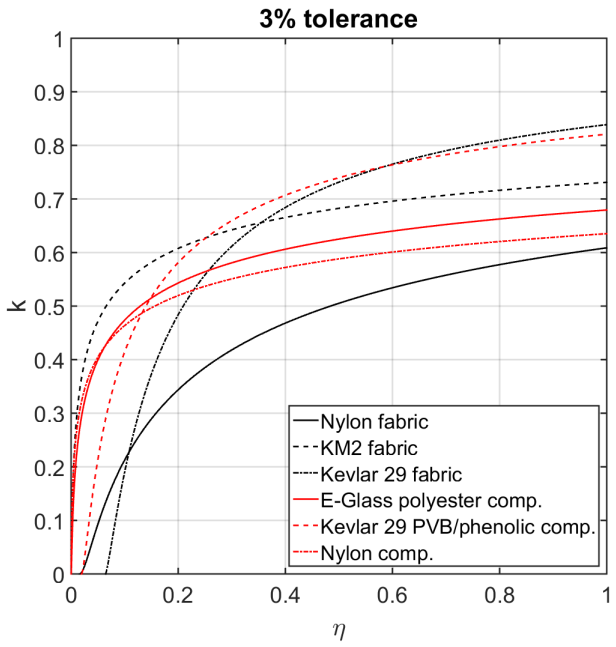

Figure 7.6. k-η curves at 3% ε tolerance values for all targets in Table 7.1.

7.2 Theoretical considerations

Although the curves differ slightly, they generally seem to tend towards a k value of about 70% inelastic mass fraction at a system areal density ratio η above 0.4. Conversely, if we consider the effects of a worst-case scenario i.e. a low η ratio projectile/target pair due to large projectile impact, the entire panel behaves elastically even if the target panel is considered nominally thick. This worst-case scenario results in a sub-optimal target performance if any of the plies are replaced. The same response behavior was noted by Cunniff [12] in that the percentage of material responding elastically would increase as the areal density ratio decreases, since the impact velocity at the V_{50} essentially becomes sufficiently low relative to the critical velocity of a single fabric ply – this effect is now explicitly demonstrated as in Fig. 7.6. Nguyen *et al.* [19] defined a critical areal density ratio η_t of 0.08 as the transition point from single-stage

perforation for thin targets to a two-stage shear/bulging perforation for thick targets using a power-law curve-fit, although it appears that this point was defined mostly as a matter of convenience to fit empirical data and may not be the result of anything physical. Due to lack of further experimental data, this thin/thick-target transition was not taken into consideration. In reality, such a value may be necessary for some targets.

Several models have been previously developed to rigorous degrees by Walker [93, 94] and Phoenix & Porwal [90, 102] to analyze the transverse deformation and localized strain development within the Kevlar® 29 fabric target upon impact. In Phoenix & Porwal's work on formulating 1-D string vs. a 2-D membrane model for soft armor targets, the normalized critical velocities of these targets were calculated as a function of the system's areal density ratio in a closed-form fashion. For η ratios below approximately 0.20-0.30, the system's 2-D critical velocity falls below the 1-D string's critical velocity [90], indicating that in this η regime, the longer duration of transverse cone growth allows much of the projectile's striking kinetic energy to be dissipated via strain energy. With a thicker target i.e. larger η ratios above 0.20, this cone growth duration is significantly reduced, meaning that near-immediate perforation occurs at their respective critical velocities without significant strain energy absorption by the frontal layers. The same behavior as determined by Phoenix & Porwal is observed in the system's k-η behavior in Fig. 7.6 showing a fundamental difference at low and high η ratios, with the transition zone around 0.15-0.30 depending on material.

This transitional behavior is further corroborated by results from a later study by Porwal & Phoenix [102], who applied the same analysis to model ballistic impact into multi-layered soft armor targets. The presented computational model used a step-wise integration scheme to calculate parameters such as cone-wave growth and localized strains as the RCC projectile sequentially contacts each layer, thereby allowing for a deeper examination of the system effects of multi-ply soft armor. This study explicitly calculated and showed that, all other parameters being constant, the transverse cone-

wave growth increases almost exponentially as the system areal density ratio decreases i.e. target thickness becomes thinner.

In particular, the strain development of an 8-ply spaced system (V_c 338 m/s) at several different projectile striking velocities were examined. At a striking velocity of 230 m/s, far below the system critical velocity, the striking kinetic energy is fully absorbed via elastic strain energy since none of the individual layers reach the failure strain. When the striking velocity is increased to 335 m/s (at or slightly below the system critical velocity), a total of six layers reach their failure strain, but two of these frontal layers (25% of the target areal density, or $k = 0.25$) fail immediately before the next layer is activated. Subsequent layers fail while being engaged, contributing partly to strain energy absorption. Further increasing the striking velocity to 350 m/s results in similar immediate failure of the frontal three layers (37.5% of target areal density, or $k = 0.375$), but the entire target system is perforated with a residual velocity Vr of 181 m/s. Using Equation 11 for Kevlar® 29, for an η ratio of 0.115 and ε tolerance of 3%, the k value is 0.2561, which is close to their numerically-obtained value of 0.25 by Porwal & Phoenix. Granted, the effects of equally-spaced inter-layer gaps were included in their calculated value – minimizing or modifying this gap in their model would most likely result in a different k value. However, they do suggest that for effective decoupling of the target system for a diphasic response, the inter-layer spacing may be asymmetrically-designed with zero gap in the frontal layers so that they may be engaged together. In this manner, the frontal portion retards the projectile sufficiently for the remaining plies to be activated without failing too early. Their in-depth analysis of multi-ply soft armor systems lends more credence to the concepts presented in this study.

The following sections provide a comparative analysis of previously-published ballistic data using the k-η curves, although certain factors have to be considered. Firstly, these k-η curves act as preliminary design tools which only explicitly state the minimum through-thickness fraction of localized inelastic failure at the strike face. At the interface of the inelastic/elastic modes of energy absorption, the failure mode is

not expected to abruptly change, but rather, a non-monotonic transition is expected (see Fig. 7.4). For example, if a diphasic armor is constructed as a monolithic target rather than simply layered and clamped together in sequence, a larger band of uncertainty may be expected. In this respect, this non-monotonic transition may be more pronounced in a composite target panel due to more through-thickness interaction compared to stacked plies in a fabric system. Secondly, due to the different methods of fabric clamping and testing across the different studies, boundary conditions and other testing parameters will no doubt play a role in the ballistic responses of the target panels [103]. Finally, the difference in definitions of a target ballistic limit using V_c (as given by Cunniff) compared to the more typical V_{50} (50% statistical chance of perforation) for some of the studies may cause slight deviations in the predictive capabilities of the k-η curve. Moreover, the V_{50} limits obtained by some authors were not based on existing ballistic limit determination standards. These issues may be assumed to be captured by the tolerance parameter ε.

7.2.1 Comparison with existing data -– Twaron® CT2040 fabric panel

In a previous work, Guo *et al.* [76] impacted Twaron® CT2040 fabric panels using O1 tool steel RCC projectiles of 9 mm nominal diameter to explicitly study the effects of replacing strike-face materials with varying strengths and varying ratios. Fabric panels had overall areal densities of 4.732 and 3.011kg/m^2, giving η values of approximately 0.0617 and 0.0313 respectively. These fabric panels were constructed with thin Makrolon® polycarbonate sheets, 304 stainless steel mesh (120×120 mesh size) layers, and greige cotton plies as strike-face materials, and constructed with varying strike-face mass fractions of about 15, 35, 60, and 75%. A hybrid panel strike-face material ratio of up to 40% (regardless of material) was shown to maintain the ballistic performance relatively well with respect to a full-fabric panel of equivalent areal density. The k-η values of the experimental results are plotted in Fig. 7.7 below. A hybrid target panel is considered to have similar performance if its ballistic limit

is at least 95% of the V_{50} for a full fabric panel of equivalent areal density. Since Twaron® CT2040 ballistic data was not readily available, ballistic data for two other similar para-aramids i.e. Kevlar® KM2 and Kevlar® 29 fabric were plotted instead, for corresponding tolerance values of 3%.

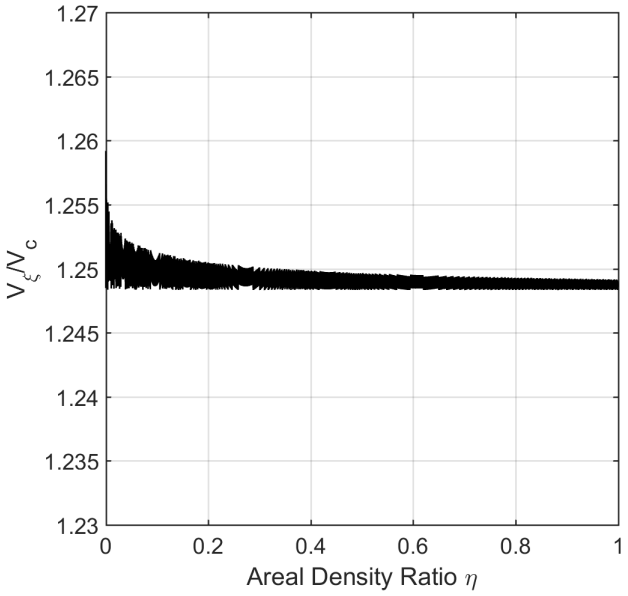

Figure 7.7. Twaron® CT2040 ballistic data and KM2/Kevlar® 29 k-η curves at 3% tolerance values for comparison [76].

An outlier, the only white circle below the k-η curve (i.e. poorer hybrid performance), is seen at a k value of approximately 37%. The actual ballistic limit of the hybrid was about 94.3% of the full fabric panel, which indicates that the performance is still relatively unaffected, though for consistency in analysis it was determined to under-perform. The areal density ratios tested in Ref. [76] are not commonly found in existing literature, and thus provide a good basis for testing the current inelastic mass fraction analysis. In general, the performance of the target panel is maintained if the strike-face mass fraction is under the allowable k-η curve. For the same areal density ratio, if the strike-face mass is increased further past the k-η curve, the rela-

tive ballistic performance decreases. For k fractions of 60%, the ballistic performance was about 90% of the full-fabric equivalent; for k fractions of 70% and above, this ballistic performance rapidly falls to less than 80% of the full-fabric equivalent.

7.2.2 Comparison with existing data – Dyneema® HB26 composite panel

Existing data detailing the inelastic mass ratio k are sparse, with one of the few direct measurements from Nguyen *et al.* [19] for Dyneema® HB26 composite panels using 12- and 20-mm FSPs. The ballistic limit was obtained as a function of areal density ratio for a series of various projectiles. Since regression analysis was not performed for this dataset, a Levenberg-Marquardt fitting algorithm was employed to obtain the regression coefficients X_6 to X_8 as per Equation 7.4 for the V_c-η curve, giving values of 7.884, 0.1145, and 1.232 respectively. Coefficients X_2 to X_4 were then fitted to the $V_r - V_s$ data for a 20 mm FSP impact on a 10 mm thick panel as detailed by Langston [104] to give values of 1.838, 1.915, and 1.018 respectively. The same procedure detailed previously was then performed to obtain the k-η curve for a 3% tolerance. These fitted regression values lie within the same order of magnitude as the other Cunniff regression constants in Table 7.1, indicating relative consistency with this methodology. The abovementioned results are plotted in Fig. 7.8.

The experimental k-η curve (dashed line) follows the data points well at higher η ratios, though not as well as a direct experimental curve-fit. These deviations from the power-law fit are due to the constraining dependence on the other regression coefficients X_3 to X_7 that were used to fit the ballistic limit velocity, thereby leading to a more restrictive range of possible regression values for X_{10}. A lack of more extensive experimental ballistic limit and residual velocity data is presumed to be the cause of the poorer fit at lower η ratios. A direct fit (dash-dot line) of Equation 11 to the experimental data was therefore performed as a comparison to both methods, giving X_6, X_7, and X_{10} values of 2.909, 0.5248, and 1.308 respectively, and an R2

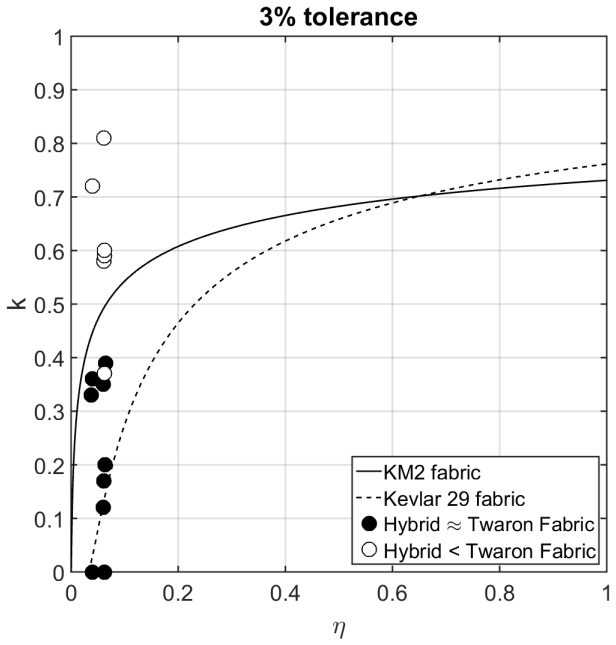

Figure 7.8. k-η curve for Dyneema HB26 composite panels, with shot data and shear plug thickness data from Nguyen *et al.* [19].

value of 0.9088. This direct fit tends to overestimate the k fraction at higher areal density ratios compared to the other two fits.

Comparing the power law fit and the experimental k-η curve, the inelastic mass fraction for UHMWPE composite panels increases rapidly over a short range of system areal densities, before levelling off at a k fraction of approximately 74%. In other words, past an η_{sys} value of about 0.4, the amount of material at the strike face that fails inelastically, either through shear plugging or some other form of localized failure mode, remains relatively constant. It may also be noted that below a certain η ratio, any inelastic form of energy dissipation i.e. shear plugging is practically non-existent at the system's ballistic limit. Specifically, for Fig. 7.8, the transition η ratio where shear plugging was first observed is 0.08. An analytical model recently developed by Langston [104] for UHMWPE composite panels explicitly calculated the shear failure distance within the target for Nguyen *et al.*'s data. At the ballistic limit for a 10 mm target panel impacted by a 20 mm FSP, the shear failure distance levelled off at 13 mm during the penetration process, indicating a 65% inelastic failure mass fraction at the strike face.

Ćwik *et al.* [20] impacted Dyneema® HB26 composite panels using 20 mm steel FSPs (mass 53.1 g) with a thickness of 24.02 mm, giving an areal density ratio of 0.1225. Using regression coefficients for Nguyen's ballistic data, the V_{50} for an η of 0.1225 is approximately 664 m/s. They noted the occurrence of the First Major Delamination (or FMD), explaining that it demarcates the boundary between the inelastic strike-face portion and the rear elastic membrane portion. The distance from the strike face to the FMD was measured for a range of impact velocities, and was determined to be approximately 11.6 mm, giving a k fraction of 0.48. This point is plotted as a white square in Fig. 7.8, and is seen to lie near both direct curve fits.

Interestingly, it may not be coincidental that this steady value of 74% appears to be at the same strike face mass of 75% in the ARL X hybrid composite panel architecture designed by Vargas *et al.* [32], although any inelastic failure thickness was not measured. In the study, 17-grain .22-caliber FSPs were used to impact 7.8

kg/m^2 UHMWPE composite panels, giving a system η ratio of 0.174. Based on the experimental k-η curve in Fig. 7.8 (dashed line), the inelastic mass ratio at $\eta = 0.17$ is approximately 70%. This point is plotted as a grey triangle in Fig. 7.8, and lies slightly above the theoretical k-η curve. It is unknown if the 75% fraction value was obtained as an exact value or a result of large experimental intervals e.g. if the strike face mass fraction was tested at intervals of 25%, but it lies relatively close to all three curves. Nonetheless, both the architecture panel layup ratio and stacking order were experimentally determined to be the most optimal in terms of retaining the ballistic performance and reducing the backface deformation [32]. For all the above studies, FSPs rather than RCCs were used, which may result in slight deviations from theoretical curves and regression constants determined from RCC shot data.

7.2.3 Comparison with existing data – KM2 fabric and Pyrex®/KM2 fabric hybrid

The k-η curves for KM2 are plotted for ε tolerance values of 3, 5, and 7%, as in Table 7.1. In one of Cunniff's works detailing the decoupled response of an armor system [12], the V_{50} ballistic performance of a Pyrex glass/KM2 hybrid was evaluated in comparison to a full KM2 fabric of the same areal density (approx. 10.1 kg/m^2) when impacted by 2-, 4-, and 16-grain projectiles (η values of 0.239, 0.379, and 0.478 respectively). The Pyrex® borosilicate glass had a thickness of 0.13 inches, giving a strike-face material areal density of 7.36 kg/m^2, or a strike-face material ratio of 73% for all hybrid systems. The k-η curve for KM2 fabric was plotted along with the data points given in Ref. [12] for a k value of 73% (Fig. 7.9).

The full KM2 fabric system slightly outperformed the hybrid Pyrex®/KM2 system when impacted by the larger mass projectile (i.e. $\eta = 0.239$). As previously discussed, when the strike face material ratio of the physical system exceeds the allowable k value, the remaining mass of the system is then rendered sub-optimal, since elastic energy dissipation is always more effective than inelastic energy dissipation. Due

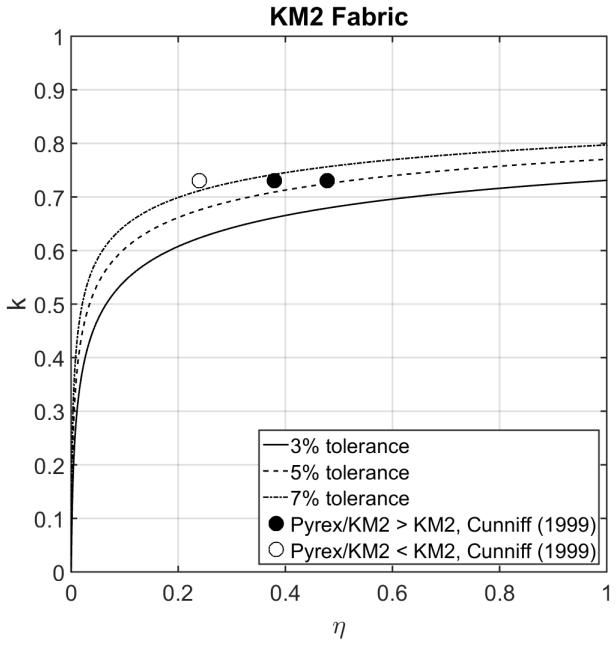

Figure 7.9. k-η curve of KM2 fabric with data points from Ref. [12].

to the proximity to the optimal k-η curve, the decrease in performance was not significantly large (-7%). Deviation is expected to be due to projectile deformation.

7.2.4 Comparison with existing data – Carbon fiber-Epoxy/KM2-PVB-phenolic hybrid composite

In the same study as the Pyrex®/KM2 panels discussed above, Cunniff also impacted carbon fiber-epoxy/KM2-PVB-phenolic hybrid composite panels [12]. These target panels were constructed with different frontal mass fractions of 20, 30, and 60% carbon fiber/epoxy, and then backed with Kevlar® KM2/PVB-phenolic resin composites. The full treatment and preparation process is detailed in Ref. [12] and therefore left out for brevity. Panels were impacted with 2-, 4-, 16-, and 64-grain projectiles, giving projectile-target system η ratios between 0.05-0.45. The V_{50} results were compared to a full panel of KM2/PVB-phenolic resin composite with equivalent areal density ratios. Although Ref. [10] provides regression coefficient values for KM2 PVB/phenolic composite panels for X5 to X8, it does not provide values for X_2 to X_4, which are necessary for the calculation of X_{10}. The values used for X_{10} in this case were averaged across all materials in Table 7.1 for an ε tolerance of 3%, giving a value of 1.4360. Kevlar® 29 PVB/phenolic composite and Kevlar® KM2 fabric k-η curves are also plotted in Fig. 7.10 for comparison.

Similarly, the k-η curve for KM2 PVB/phenolic composite shows that the ballistic performance is somewhat maintained if the frontal mass fraction lies below the design curve. The curve fits the data arguably well considering the lack of more ballistic data and the relevant regression coefficients. The presence of more outliers in this case may be due to several factors. Firstly, at higher areal density ratios i.e. smaller projectiles, synergistic effects as observed on the Pyrex®/KM2 hybrid may come into play via projectile deformation. On the other hand, at low areal density ratios i.e. larger projectiles or thinner panels, the impact may have resulted in a much larger fraction of the panel to behave in an elastic fashion. In this case, the inelastic mass

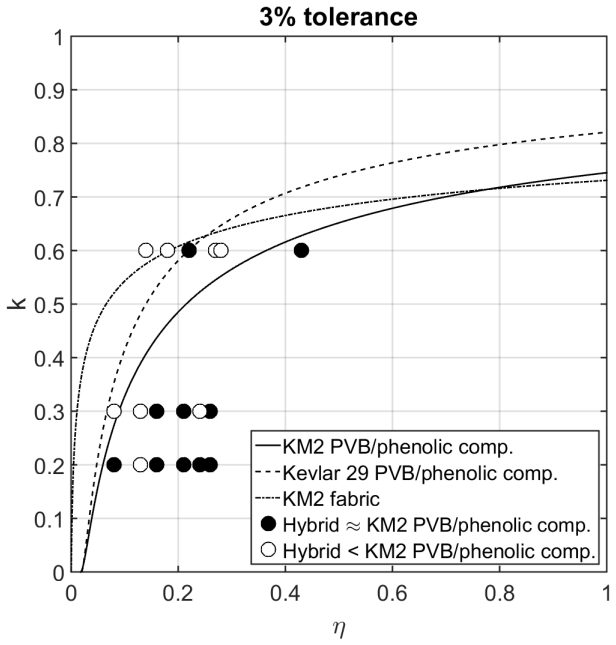

Figure 7.10. k-η curves at 3% tolerance for three different materials, with experimental data points from Cunniff [12].

fraction analysis may not be as accurate, especially for a stiffer composite panel. A generalized determination of this "thin-panel" transition ratio is not discussed here.

7.2.5 Comparison with existing data – Nylon fabric diphasic hybrid

As a final comparison with existing experimental data, Alesi's study presents a particularly interesting choice of material [26]. In this study, he impacted a series of various fabric and hybrid panels, namely a window glass/nylon fabric hybrid, A-110AT titanium alloy/nylon fabric hybrid, and a PMMA/PVB hybrid. Projectiles used were 17-grain T37 FSPs. Due to lack of published experimental ballistic data for PMMA and PVB materials, only the first two are discussed in this study. The window glass/nylon fabric hybrid (and the full nylon fabric equivalent) had an areal density of 12.73 kg/m^2, giving an η value of 0.278. Both systems had practically equivalent ballistic limits of 533 and 539 m/s respectively. The strike face material ratio was 55% for the hybrid system. The titanium alloy/nylon fabric hybrid and its full fabric equivalent had areal densities of 11.26 kg/m^2, giving calculated η values of 0.250. The strike face material ratio was 66% for the hybrid, and the ballistic limits were 558 and 511 m/s respectively, indicating slightly superior hybrid performance over the full fabric equivalent by approximately 9%. The respective curves and experimental data points are plotted in Fig. 7.11.

The strike face material ratios for both target panels lie under the optimal k-η curve, meaning that the strike face material was responding in an inelastic fashion. A synergistic effect in the hybrid may be observed for the A-110AT titanium alloy/nylon fabric hybrid, which is slightly atypical compared to the previous results presented. Even though the Ti alloy/nylon hybrid panel lies within the k-η curve tolerance bands, the hybrid panel outperformed the full nylon panel – this may be attributed to the superior strength of the A-110AT alloy as a standalone target. While an improvement of 9% may not appear to be significant, these results nonetheless show that is possible

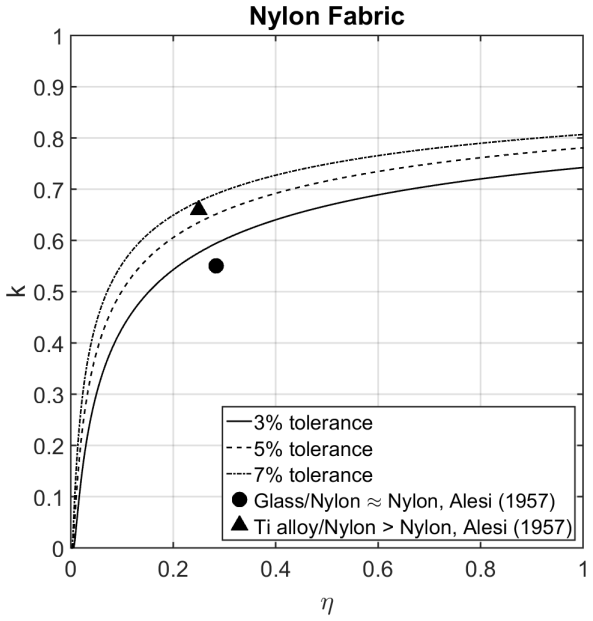

Figure 7.11. k-η curves for nylon fabric, with hybrid panel data points from Alesi [26]

to design a diphasic armor with a maximum k ratio while the overall performance can be further improved via careful selection of materials with relevant properties.

7.3 Conclusions

By using Cunniff's regression analysis to estimate a characteristic velocity V_ξ at which a fully inelastic impact response is initiated at the strike face, a proposed X_{10} parameter was used to determine the amount of material k at the armor panel strike face which fails inelastically at the corresponding ballistic limit of the target system for each areal density ratio η. This inelastic mass fraction k was further computed as a function of the system areal density ratio to produce k-η curves for a series of target materials. Overall, these k-η curves provide a preliminary design tool for an armor panel. Comparison with existing literature demonstrated that the k-η curves may be used as a preliminary design tool to determine the amount of material at the strike face that can be replaced without sacrificing the ballistic performance.

Since a fraction k at the strike face does not absorb significant strain energy, it is possible to replace this k portion with a material of similar areal density and keep the ballistic performance of this diphasic armor relatively unchanged. It is possible to design a diphasic armor with proper selection criteria for frontal material such that the overall performance is maintained or even improved, and the design and material selection will have to be within these constraints presented. For a percentage of alternative strike face material above the k-value at a particular system areal density were replaced, the portion up to k fails inelastically. Within this regime, for the same areal density of strike face material, other off-axis material properties such as target transverse shear strength would help with the total striking energy absorption. However, since subsequent plies will need to absorb significant strain energy, the elastic energy absorption mechanism dominates, and further replacement of the frontal material would lead to a decrease in performance. This is due to the greater advantage in absorption efficiency of an elastic mechanism compared to an

inelastic mechanism. For some of the inelastic mass portion above the k-η curve to offset some of the decrease in elastic energy absorption efficiency, a proper frontal material must be carefully selected within the constraints presented in the current study.

7.4 Appendix

Appendix A: Generated curves for 3, 7, and 10% tolerance values for materials in Table 7.1

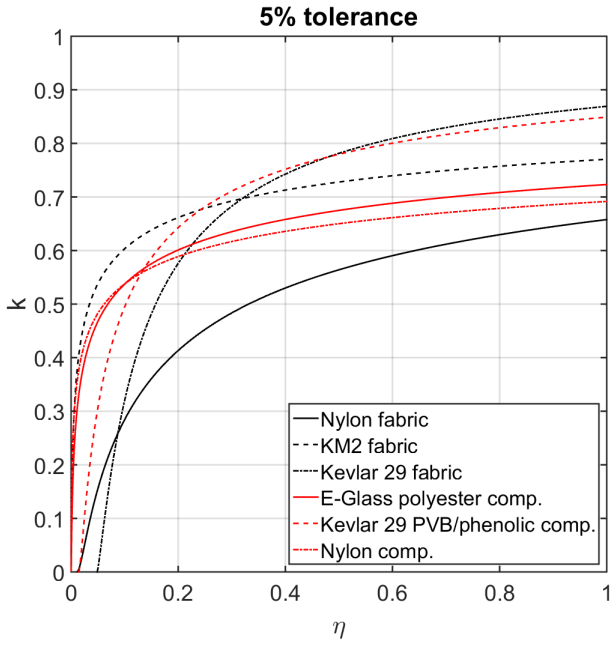

Figure 7.12. k-η curves at 5% ε tolerance values for all targets in Table 7.1.

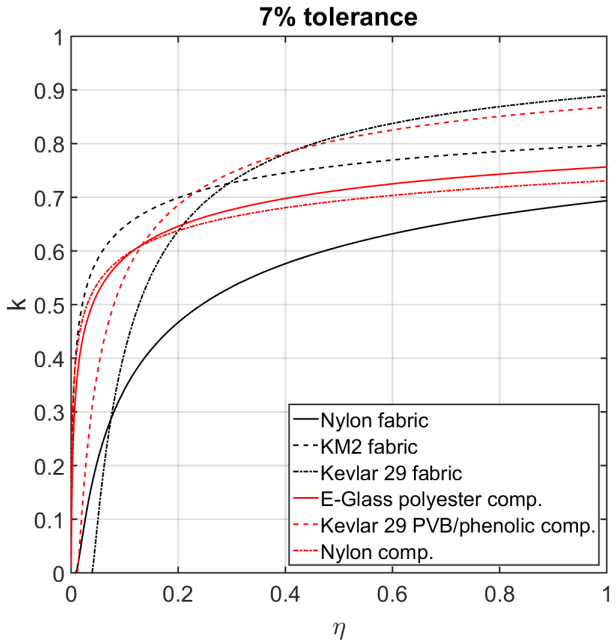

Figure 7.13. k-η curves at 7% ε tolerance values for all targets in Table 7.1.

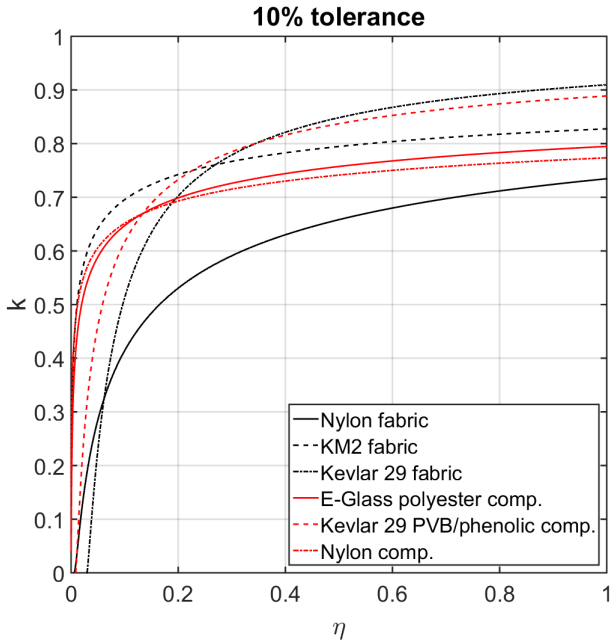

Figure 7.14. k-η curves at 10% ε tolerance values for all targets in Table 7.1.

8. CUNNIFF VELOCITY AS A MERIT PARAMETER TO DETERMINE THE STACKING ORDER OF MATERIALS

Chapter adapted from prior published work. Z. Guo, W. Chen, A merit parameter to determine the stacking order of heterogeneous diphasic soft armor systems, J. Comp. Struct. (2020). (In review).

Abstract

The effects of stacking order on the ballistic performance may be detrimental if the order is improperly chosen. When the frontal material is constrained transversely by the rear material, it results in sub-optimal performance compared to the alternate configuration where both layers can freely deform. In this study, we examine the possibility of using the Cunniff velocity as a merit parameter in determining the optimal stacking order of heterogeneous diphasic soft armor systems by reviewing the results from previous studies. Experiments were performed on heterogeneous systems comprising ballistic-grade polyurea, Twaron® fabric, and Dyneema® UD laminate plies. Results show that the two constituent materials should be ordered such that the material with a higher Cunniff velocity is placed at the rear to minimize interference. The use of the merit parameter is then analyzed via existing models to examine the effects of changing various parameters. We further discuss the idea of "ballistically-thin" materials in relation to the concept of membrane strain energy dissipation efficiency of a soft armor target.

8.1 Introduction

In a series of works studying the ballistic impact response and failure of soft armor systems, Cunniff observed a stacking order effect [14] when testing a heterogeneous two-layer 1000 denier Kevlar® 29/Spectra® 1000 (A/B configuration) target in efforts to investigate the synergistic effects on the system's performance. This A/B system had a ballistic limit of 269 m/s. Reversing the order of the plies (B/A configuration) was found to be extremely detrimental to the ballistic performance in comparison to the first system, as the reversed order gave a ballistic limit of 114 m/s. However, when a two-ply system comprising two mechanically-similar materials 1000 denier Kevlar® 29/1040 denier Kevlar® 49 was tested in both A/B and B/A configurations, the ballistic performance was relatively unaffected in comparison.

Such bi-material soft armor systems and the effects of stacking order have since been further experimentally-investigated on various combinations of materials [20, 21, 88, 105–110]. While material stacking configurations are limitless, the current study focuses on the simplest configuration: bi-material heterogeneous diphasic systems i.e. one material at the strike face and the other at the rear. Larsson *et al.* [105] investigated a broad range of different materials and configurations, but focused on carbon fiber fabric comprising Torayca® T300 fibers and Dyneema® SK66 UD fabric impacted by 5.46 mm fragment-simulating projectiles (FSPs) at different mass fractions of either material. In all cases, it was shown that a Dyneema® SK66 backing layer always has a higher ballistic limit velocity than the other configuration with Dyneema® SK66 at the strike face. Muhi *et al.* [108] investigated the effects of hybridized plain-woven E-glass/Kevlar® 29 target panels impacted by flat-, hemispherical-, and conical-nosed projectiles of the same mass and measured the respective energy absorption E_{abs}. Interestingly, the ballistic results showed that a Kevlar® 29 backing layer provides optimal energy absorption compared to other stacking configurations, regardless of projectile nose-shape or number of material phases. Similarly, Hazell *et al.* [110] examined the energy-absorption levels of carbon-

fiber reinforced polymers (CFRPs) backed by 6061 aluminum and Kevlar® 29 fabric. With this combination of atypical materials, it was found that having the CFRP laminates placed at the strike face provided better energy absorption compared to the reverse stacking order, although the CFRP/Kevlar® 29 system resulted in the best ballistic performance among all the configurations by far. In a broad series of similar works by Chen, Zhou, and Yang *et al.* [88, 106, 107, 111], the ballistic performance of various weaves and configurations of para-aramid fabrics, Dyneema® UD laminate plies, and plain-woven Dyneema® SK75 fabrics were tested using 5.5-mm right circular cylinders (RCCs) as projectiles. The ballistic performance was evaluated using the specific energy absorption values i.e. energy absorbed divided by areal density as well as backface deformation (BFD). It was found that a Kevlar® 29/Dyneema® system performed better than the reverse configuration, but more interestingly, a woven Dyneema® SK75 fabric/Dyneema® UD hybrid system will outperform its reverse configuration [107], even if the constituent fiber properties are relatively similar. In one of their more recent studies detailing their analytical model for fabric systems [111], they noted that the UD panels allowed for more transverse deflection than a woven fabric of the same material, resulting in a constraining effect if the woven fabric were placed at the rear.

In his work, Cunniff initially attributed this phenomenon to the longitudinal moduli of the constituent fibers, commenting that, as with the Kevlar® 29/Spectra® 1000 system, the higher modulus of the Kevlar® 49 should have resulted in similar degradation in performance of the hybrid panel, which was shown not to be the case. This diphasic stacking order phenomenon was further investigated analytically by Phoenix & Porwal *et al.* [102, 112, 113], who modeled the inter-layer interference to determine the stacking order and its effects on the overall ballistic performance. Upon projectile impact, the material in both layers move at the same transverse velocity at the impact site. In both layers, a tensile wave propagates outwards at the longitudinal wave speed, pulling in material that feeds into the transverse tent/cone forming behind this

tensile wave. This transverse cone wave speed (in the Lagrangian frame of reference) as the projectile deforms the target is calculated by [90]

$$V_{cone} \approx 1.23c \left(\frac{V}{c\sqrt{2}} \right)^{2/3} \tag{8.1}$$

where c is the tensile wave speed and V is the instantaneous projectile velocity (which decreases as the projectile progressively perforates the target panel). In a bi-material diphasic soft armor system, the relative cone wave velocities become important. When the transverse cone of the rear layer grows faster than that of the front layer, both materials are able to maximize their energy dissipation capabilities. However, in the case of a faster-growing cone wave in the front layer, the slower-growing rear material hinders the frontal layer's deflection, resulting in sub-optimal performance. This transverse deflection appears to be the determinant factor in stacking order effects, a sentiment echoed by several later works [106, 107, 114] involving experiments and numerical simulations.

In their work, Porwal & Phoenix [112] demonstrated the same effect of stacking order and solved this problem analytically for the Kevlar® 29/Spectra® 1000 heterogeneous system. A cursory look at Equation 8.1 seems to imply that the transverse cone wave velocity should be determined simply by the tensile wave speed c of the constituent fibers. This would explain the results for the Kevlar® 29/Spectra® 1000 system, since Kevlar® 29 has a tensile wave speed of 7.4 km/s and Spectra® 1000 at about 11.1 km/s. A Spectra® 1000/Kevlar® 29 stacking order would therefore result in the Spectra® fabric being constrained transversely by the slower-moving Kevlar® 29 fabric (disregarding any local heating/melting effects of the Spectra® system). However, this does not adequately explain the Kevlar® 29/Kevlar® 49 results, since Kevlar® 49 has a wave speed of 9.1 km/s, a difference large enough to warrant significant synergistic effects. These two materials were not modeled by Porwal & Phoenix to explain the discrepancy.

Clearly, with these results in mind, there is a need for a merit parameter that sufficiently captures these differences but still maintain the dependence of results on the constituent material and mechanical properties. Although the aforementioned studies have reported similar synergistic or deleterious effects for diphasic systems, obtaining these results necessitated a large amount of experimentation and/or computational analysis. While Porwal & Phoenix do provide explicit equations for the solution of the cone wave speed in the laboratory reference frame, the set of equations require iterative solutions that make it difficult to extract a merit parameter. A merit parameter to determine the optimal stacking order would be useful as a preliminary design tool to screen out diphasic stacking configurations that would prove to be sub-optimal.

8.1.1 Cunniff velocity as merit parameter

In one of his earlier works, Cunniff proposed two non-dimensional parameters [11] whereby the ballistic performance of a target panel could be well-predicted using the mechanical properties of its constituent fibers. The first parameter is an areal mass ratio of the target to the projectile given as

$$\eta = \frac{A_d A_p}{m_p} \tag{8.2}$$

where A_d is the areal density of the target panel, A_p is the presented area of the projectile, and m_p is the projectile mass. The second parameter is a dimensionless ballistic limit velocity $V_{50}/\Omega^{1/3}$, where Ω is given as

$$\Omega = \frac{\frac{1}{2}\sigma_f \varepsilon_f}{\rho} \cdot c \quad \Rightarrow \quad \sqrt[3]{\Omega} = \left(\frac{\frac{1}{2}\sigma_f \varepsilon_f}{\rho} \cdot c \right)^{1/3} \tag{8.3}$$

It is important to mention at this point that the mechanical properties being input into the calculation of the Cunniff velocity are mostly derived from quasi-static experiments [11]. Since these fibers exhibit linear-elastic stress-strain response at

quasi-static rates, we can rearrange Equation 8.3 to give an alternate form of $\sqrt[3]{\Omega}$ that is only dependent on two parameters.

$$\Omega = \frac{1}{2}\varepsilon^2 c^3 \quad \Rightarrow \quad \sqrt[3]{\Omega} = \left(\frac{\varepsilon_f}{\sqrt{2}}\right)^{2/3} \cdot c \tag{8.4}$$

In Equations 8.3 and 8.4, σ_f and ε_f are the failure stress and strain of the constituent fibers within the armor, and ρ is the fiber density. Conceptually, the Cunniff velocity $\sqrt[3]{\Omega}$ may be thought of as a material's ability per unit mass to transport the impact kinetic energy away from the impact site at the inherent longitudinal wave speed of the constituent fiber material. Since the calculation of $\sqrt[3]{\Omega}$ only depends on elastic mechanical properties, it inherently assumes that the target material is isotropic and dissipates the absorbed impact energy as membrane strain energy (via elastic properties). In a sense, $\sqrt[3]{\Omega}$ gives an idea of the panel's membrane strain energy dissipation efficiency of the target panel.

Using the dimensionless ballistic limit velocity V50/$\sqrt[3]{\Omega}$, the ballistic performance of different soft armor target systems could be collapsed onto a single master curve. The elegance of Equations 8.2 and 8.3 lie in the fact that the system's macro-scale ballistic performance may be expressed as a function of the constituent fiber's quasi-static properties at the micro-scale using two dimensionless parameters. Going back to the Kevlar® 29/Spectra® 1000 and Kevlar® 29/Kevlar® 49 systems, the η values are 621 for Kevlar® 29, 801 for Spectra® 1000, and 612 for Kevlar® 49. Note that in Ref. [14], the Kevlar® 49 denier is reported as 1040 while the $\sqrt[3]{\Omega}$ value of 612 is reported for 1140 denier Kevlar® 49 in Ref. [11], but the Cunniff velocity does not seem particularly dependent on the yarn denier in any case.

8.1.2 Comparison with existing literature

In a survey of existing literature on diphasic soft armor experimental testing, we found 9 different studies explicitly investigating bi-material systems [14, 20, 21,

88, 105–110], of which only 30 sets of forward/reverse-type configuration test results were reported. Comparison with existing ballistic testing results from previous works are shown in Tables 8.1 and 8.2 to demonstrate the use of the Cunniff velocity as a preliminary parameter for material choice. In these tables, the ratio of the rear to frontal Ω velocities are calculated.

As several different metrics of ballistic performance were used across different studies, a direct quantitative comparison of forward-reverse stacking order testing results would not be possible. Therefore, in Tables 8.1 and 8.2, we compare the relative performance difference between A/B and B/A panels by obtaining a secondary comparison metric by calculating the primary metric as a ratio of the mean of the A/B and B/A results. For example, for the Kevlar® 29/Spectra 100 (A/B) two-ply system tested by Cunniff, the comparison V_{50} metric for the A/B system was 269 m/s, while the mean of the A/B and B/A test results was 191.5 m/s. The relative performance of the A/B system is therefore $269/191.5 = 1.40$ while that for the B/A system is 0.60. This method allows us to compare the relative performances of the stacking order with respect to the back/front η ratios (also given in Tables 8.1 and 8.2). For the V_{50} and energy-absorption E_{abs} metrics used, a comparison metric greater than 1 implies better performance than the alternate stacking order; for BFD values, since a larger value (i.e. deeper deformation depth) is related to poorer energy-dissipation, the comparison metric is calculated by using the result from the alternate configuration instead to keep the trend consistent with the V_{50} and E_{abs} comparison metric values.

Table 8.1. Ballistic testing of forward/reverse systems with V_{50} as primary metric.

Ref.	Mat'l	$\sqrt[3]{\Omega}$	η	Config.	% by A_d	V_{50} [m/s]	$\sqrt[3]{\Omega}$ ratio	Comp.
Cunniff [14]	1000d Kevlar® 29 (A)	621	0.0105	A/B	61.7/38.3	269	1.291	1.40
	375d Spectra® (B)	802		B/A	38.3/61.7	114	0.774	0.60
	1000d Kevlar® 29 (A)	621	0.0135	A/B	47.9/52.1	N/A	0.988	∼1
	1040d Kevlar® 49 (B)	614		B/A	52.1/47.9	N/A	1.012	∼1
Larsson *et al.* [105]	Carbon fiber T300 (A)	555	0.1725	A/B	26.7/73.3	313	1.532	1.11
				B/A	73.3/26.7	251	0.653	0.89
			0.1580	A/B	52.2/47.8	324	1.532	1.09
				B/A	47.8/52.2	268	0.653	0.91
	Dyneema® SK66 (B)	850	0.1473	A/B	76.6/23.4	334	1.532	1.10
				B/A	23.4/76.6	271	0.653	0.90

Table 8.2. Ballistic testing of forward/reverse systems with E_{abs} as primary metric.

Ref.	Mat'l	$\sqrt[3]{\Omega}$	η	Config.	% by Ad	E_{abs} [J]	$\sqrt[3]{\Omega}$ ratio	Comp.
Zhou *et al.* [106]	Kevlar® 49 (A)	486	0.0114	A/B	50/50	0.0192	1.921	1.07
				B/A	50/50	0.0167	0.521	0.93
			0.0228	A/B	50/50	0.0442	1.921	1.06
				B/A	50/50	0.0393	0.521	0.94
	Woven Dyneema® SK75 (B)	933	0.0342	A/B	50/50	0.0684	1.921	1.11
				B/A	50/50	0.0547	0.521	0.89
Muhi *et al.* [108]	Kevlar® 29 (A)	621	0.0112	A/B	30.6/69.4	25.8	0.776	0.94
				B/A	69.4/30.6	29.3	1.289	1.06
			0.0112	A/B	30.6/69.4	21.7	0.776	0.89
				B/A	69.4/30.6	26.8	1.289	1.11
	Woven E-glass (B)	482	0.0112	A/B	30.6/69.4	16.0	0.776	0.84
				B/A	69.4/30.6	22.3	1.289	1.16

Hazell *et al.* [110]	CFRP (A)	375	0.1712	A/B	74.3/25.7	223	1.184	1.03
	Al 6061-T6 (B)[a]	∼444		B/A	25.7/74.3	210	0.845	0.97
	CFRP (A)	375	0.1712	A/B	74.3/25.7	399	1.668	1.34
	Kevlar® 29 1500d (B)	625		B/A	25.7/74.3	198	0.600	0.66
Yang *et al.* [88]	Twaron® fabric (A)	641	0.0081	A/B	45.4/54.6	0.1180	1.442	1.09
				B/A	54.6/45.4	0.0995	0.694	0.91
	Dyneema® SB71 (B)	924	0.0244	A/B	45.4/54.6	0.3872	1.442	1.11
				B/A	54.6/45.4	0.3096	0.694	0.89

[a]note that unlike polymer fibers, Al6061 does not exhibit linear-elastic response. $\sqrt[3]{\Omega}$ for Al6061 was therefore estimated using toughness calculated via stress-strain curves.

Table 8.3. Ballistic testing of forward/reverse systems with BFD as primary metric.

Ref.	Mat'l	$\sqrt[3]{\Omega}$	η	Config.	% by Ad	BFD [mm]	$\sqrt[3]{\Omega}$ ratio	Comp.
Yang *et al.* [88]	Twaron (A)	641	0.1006	A/B	29.4/70.6	9.80	1.442	1.11
	Dyneema® SB71 (B)	924		B/A	70.6/29.4	12.0	0.694	0.89
Chen *et al.* [107]	Woven Dyneema® SK75 (A)	886 (626)	0.1376	A/B	24.9/75.1	6.27	1.415	1.16
				B/A	75.1/24.9	8.74	0.707	0.84
			0.1373	A/B	49.8/50.2	8.51	1.415	1.08
				B/A	50.2/49.8	9.99	0.707	0.92
	Dyneema® SB21 (B)	886	0.1371	A/B	74.9/25.1	11.0	1.415	1.11
				B/A	25.1/74.9	13.8	0.707	0.89

We note that for all the target panels tested, the areal density ratio η lies between 0.01 (single-ply) to about 0.18 – these η values may be described as "ballistically-thin" targets with respect to the impinging projectile. This concept is elaborated upon in later sections. As mentioned previously, a special case needs to be made for the results obtained by Chen *et al.* [107] for a woven Dyneema® SK75 fabric/Dyneema® SB21 UD hybrid system, since it is technically bi-material not in terms of the constituent fibers, but because of architecture. Due to the crimp in the woven fabric, the high modulus of the Dyneema® fibers is not fully taken advantage of, resulting in a slower transverse cone wave speed for the woven fabrics than for the UD plies. Phoenix & Porwal [90] suggest that the effective longitudinal wave speed for a fabric is about 30% slower (exactly $1/\sqrt{2}$ times) than the fiber's wave speed. Substituting for this effective fabric wave speed into Equation 8.4, we see that the effective Cunniff velocity is equivalently scaled down. As such, this assumed effective Cunniff velocity of 626 m/s for the woven Dyneema® SK75 is also listed Table 8.3. In general, from the results listed in Tables 8.1 to 8.3, when a hybrid armor panel has a higher Cunniff velocity η ratio of the rear to the front material, the ballistic performance always outperforms the corresponding B/A configuration in 100% of all tested cases reported, regardless of materials chosen for testing. For the Kevlar® 29/Kevlar® 49 system, Cunniff noted that the A/B and B/A system ballistic limits were extremely close, although exact values were not given. From their Cunniff velocities, the two fibers have similar "strain energy-dissipating" properties, resulting in similar ballistic performance.

In efforts to further ascertain this use of the Cunniff parameter, experiments were performed by keeping the areal densities and thicknesses of both materials in a diphasic armor target the same. In most of the prior works listed, the areal densities of the individual materials were not of particular focus i.e. both materials have different areal densities and thicknesses, which may affect the performance of their respective stacking order. In this study, we aim to keep the target panel as balanced as possible i.e. similar areal densities and similar thicknesses of the front and rear material. Experiments were performed using Twaron® CT709 fabric, Dyneema®

SB31 UD laminates extracted from soft armor vests, and a ballistic-grade polyurea XS-350 manufactured by Line-X®. Additionally, in a previous study by Guo, Chen, & Zheng [115], the amount of strike-face mass that responds in an inelastic fashion was determined semi-empirically. For Twaron® CT709 fabric, the optimal areal density ratio η for a 50/50 by mass bi-material diphasic soft armor target panel is approximately 0.062.

8.2 Experimental

8.2.1 Projectiles

Standard .30-cal skirted fragment-simulating projectiles (mass 2.85 g) were used to impact the targets. The 30-cal FSPs were fired using a universal receiver with a rifled barrel having a twist rate of 1:12. This system was used as preliminary testing showed reliable velocities and accuracy of the projectiles fired compared to a smooth barrel system.

8.2.2 Target materials

The base soft armor material is plain-woven balanced-weave Twaron® CT709, a commonly-used para-aramid fiber with similar properties as Kevlar®. The Twaron® CT709 yarn are made up of CT2040 fibers. Secondary panel materials chosen are XS-350 polyurea (manufactured by Line-X) and Dyneema® SB31 $[0°/90°]_2$ laminate plies extracted from existing soft armor vests. Since the full properties of the constituent fibers of Dyneema® SB31 are not readily available, we assume them to be Dyneema® SK76 (or a fiber with similar properties) as they are the most commonly-used in ballistic applications.

Hybrid target systems consist of the secondary frontal material and the Twaron® fabric material in the rear (A/B configuration), and the same materials in reverse order i.e. Twaron® at front (B/A configuration). Target panels measure 152 $\times$

Table 8.4. Properties of constituent materials.

Mat'l	σ_f [GPa]	ε_f [%]	E [GPa]	ρ [kg/m^3]	c [km/s]	$\sqrt[3]{\Omega}$ [m/s]
Twaron® CT2040	3.3	3.30	90	1440	7.9	668
XS-350 polyurea [116]	0.0192	48.0	0.1	1072 [117]	0.3	109
Dyneema® SK76[a]	3.8	3.51	132	980	11.6	923
Dyneema® SK76[b]	2.55	6.26	N/A	970	6.48	698
Dyneema® SK76[c]	N/A	2.8	120	980	11.1	810

[a]From Nguyen *et al.* [19]

[b]From Russell, Karthikeyan, Deshpande *et al.* [118]

[c]From van der Werff and Heisserer [119]

152 mm^2 (6 $\times$ 6 sq. in.) and secured on all four edges with Dyneema® composite tape. In order to reduce the effects of the inelastic strike-face fraction coming into play when switching the stacking order, primary Twaron® material and secondary material areal masses and thicknesses are chosen to be approximately equal as far as possible. Combinations of materials and their respective areal masses are given in Table 8.5. The Dyneema® SB31/Twaron® CT709 hybrid panels are of more interest due to their use in soft armor vests, therefore further experiments were performed on their individual components (e.g. 15-ply Dyneema® SB31 and 10-ply Twaron® CT709).

Table 8.5. Target panel system properties. T = Twaron®, D = Dyneema® SB31, PXX = XS-350 polyurea of thickness XX mil.

	Twaron®			Secondary			Total			% Twaron	
Set	Mat'l	Ad [kg/m^2]	Thick. [mm]	Mat'l	Ad [kg/m^2]	Thick. [mm]	Ad [kg/m^2]	Thick. [mm]	η	By Ad	By Thick.
1	10T	1.98	2.48	3P25	2.18	2.20	4.05	4.68	0.062	49	53
2	10T	1.98	2.48	15D	1.89	2.53	3.88	5.01	0.062	51	50
3	20T	3.96	4.95	3P50	4.35	4.39	8.31	9.34	0.126	48	53
4	20T	3.96	4.95	30D	3.79	5.05	7.75	10.00	0.121	51	50
5	10T	1.98	2.48	—	—	—	1.98	2.48	0.031	—	—
6	20T	3.96	4.95	—	—	—	3.96	4.95	0.062	—	—
7	—	—	—	15D	1.89	2.70	1.89	2.70	0.030	—	—
8	—	—	—	30D	3.79	5.40	3.79	5.40	0.059	—	—

8.2.3 Testing procedure

Target panels were edge-clamped to give an active area of 102 × 102 mm^2 for projectile impact. Each material pair in Table 8.5 was tested at different striking velocities to measure the residual velocities. Impact velocities were measured with an in-house laser diode system and residual velocities were measured using a series of break screens (Whithner Graphic Solutions, Inc.) located 140 mm apart. Panels were removed as carefully as possible to preserve the failure modes for post-mortem analysis.

8.3 Results & Discussion

The critical ballistic limit velocity was obtained by curve-fitting the V_r-V_s data with Cunniff's equation given in Equation 8.5 using a Levenberg-Marquardt algorithm. The results of the experiments and curve-fits are given in Table 8.6. As with data from existing literature given in Tables 8.1-8.3, the diphasic panel performs better with a higher Cunniff velocity placed in the rear.

$$V_r^2 = \frac{V_s^2}{1 + X_2\eta} - \frac{V_c^2}{1 + X_2\eta}\left\{\exp\left[-X_3\left(\frac{V_s}{V_c} - 1\right)^{X_4}\right]\right\} \tag{8.5}$$

Table 8.6. Ballistic impact results with curve-fit parameters.

Mat'l	$\sqrt[3]{\Omega}$	η	Config.	% by Ad	X_2	X_3	X_4	V_{bl} [m/s]	$\sqrt[3]{\Omega}$ ratio	Comp.
XS-350 polyurea (A)	109	0.062	A/B	51/49	1.931	1.982	1.308	388	6.128	1.014
Twaron® CT709 (B)	668		B/A	49/51				377	0.163	0.986
XS-350 polyurea (A)	109	0.126	A/B	52/48				581	6.128	1.113
Twaron® CT709 (B)	668		B/A	48/52				462	0.163	0.887
Dyneema® SB31 (A)	698	0.060	A/B	49/51	3.047	3.958	0.865	470	0.957	0.988
Twaron® CT709 (B)	668		B/A	51/49				481	1.045	1.012
Dyneema® SB31 (A)	698	0.121	A/B	49/51				607	0.957	0.971
Twaron® CT709 (B)	668		B/A	51/49				643	1.045	1.029

8.3.1 XS-350 polyurea/Twaron® ballistic results

V_r-V_s data points for the .30-cal FSP impact on the Dyneema®/Twaron® targets are given in Figure 8.1 below. Curve-fits using Equation 8.5 are also plotted in their respective figures. At the "optimal" areal density ratio of about 0.062, Figure 8.1a for the thinner targets show minimal difference in performance between the A/B (Twaron® at rear) and B/A configurations, although the A/B configuration did result in a slightly higher ballistic limit velocity. With the system areal density ratio doubled at about 0.126 while still keeping the fraction of Twaron® at 50% and the thicknesses of both materials relatively the same, the ballistic limit velocities are drastically different. The A/B configuration shown in white circles had a much higher ballistic performance of about 580 m/s compared to the B/A configuration ballistic limit of about 460 m/s.

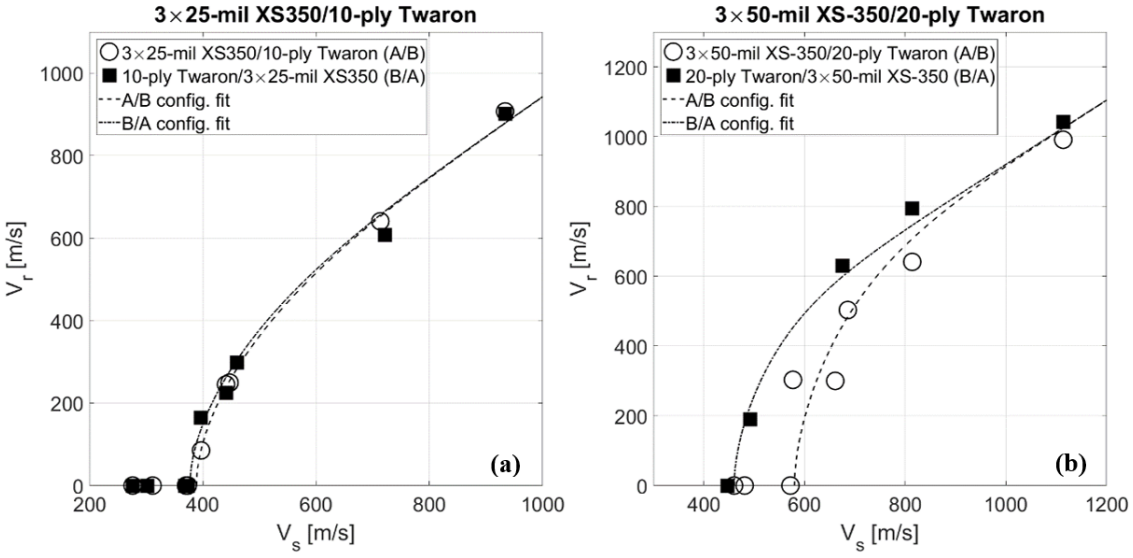

Figure 8.1. V_r-V_s curves for both A-B and B-A configurations for XS-350 polyurea/Twaron® CT709 impacted by .30-cal FSP, areal density ratios $\eta = 0.063$ (a) and 0.126 (b).

As predicted by Porwal & Phoenix [112], the more compliant Twaron® CT709 fabric at the rear was able to dissipate more energy by deforming in the transverse direction. The B configuration restricted the transverse cone wave of the frontal Twaron®, resulting in diminished performance of the entire system. Post-mortem examination of the targets (Figures 8.2a and b) shows that the Twaron® rear material in the A/B configuration was able to dissipate the projectile's impact kinetic energy via strain energy through the formation of a transverse cone. This transverse cone formation is restricted in the B/A configuration and the projectile exits with a neat hole through the polyurea rear panel.

Figure 8.2. Post-mortem images showing localized rear material deformation and failure of (a) 3P50/20T and (b) 20T/3P50 configurations at $V_s \approx 450$ m/s.

8.3.2 Dyneema® SB31/Twaron® ballistic results

Since the Dyneema® SB31/Twaron® hybrid panels are of more interest due to their use in soft armor vests, we examine the experimental results more in-depth compared to the XS-350/Twaron® CT709 hybrid panels. As with the polyurea/Twaron® systems, the difference in performance is not significant at lower areal density ratios.

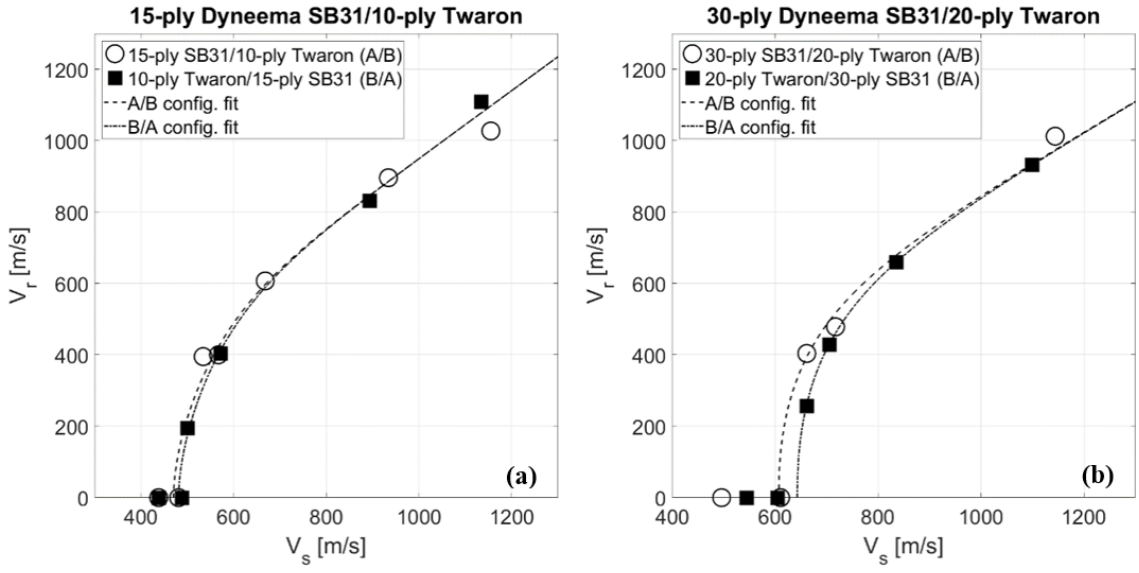

Figure 8.3. V_r-V_s curves for both A/B and B/A configurations for Dyneema® SB31/Twaron® CT709 impacted by .30-cal FSP, areal density ratios η = (a) 0.062 and (b) 0.124.

At the "optimal" areal density ratio of about 0.062 (Figure 8.3a), the thinner targets show no significant difference between the A/B and B/A configurations (470 and 481 m/s, respectively). The energy-absorption modes of the targets in both configurations at this areal density ratio do not seem particularly dependent on the stacking order. With the areal density ratio at about 0.124 while keeping the fraction of Twaron® still at 50% and the thicknesses of both materials relatively similar, the ballistic limit velocities start to deviate. The A/B configuration shown in white circles had a lower ballistic performance of about 607 m/s compared to the B/A configuration ballistic limit of about 643 m/s. Again, as predicted by Porwal & Phoenix [112,113], the more compliant Dyneema® SB31 plies at the rear were able to dissipate more energy by deforming in the transverse direction. The A/B configuration restricted the transverse cone wave of the frontal Dyneema®, resulting in slightly-diminished performance of the entire system. It should be mentioned that in Figure 8.3a, the B/A fit could have given a V_{bl} value much closer to the A/B fit, indicating negligible improvement – this could be a result of the smaller active area of the sample limiting the transverse deflection and in-plane of the Dyneema® SB31 rear panel. This effect has been previously observed by Cunniff [14] when testing 1-, 4-, and 8-inch holders, noting that the ballistic performance is strongly affected by the aperture size. However, we expect all the sample panels to be equally affected by the aperture size effect, which should still reflect a difference in ballistic performance between A/B and B/A configurations. The ballistic performance results of the respective mono-material target panels are given in Table 8.7 for comparison. Alesi [26] discusses a sum-of-squares method used in prior literature (though not fully referenced) to estimate the ballistic performance of a bi-material diphasic armor, and subsequently used this method in his work to predict the performance of nylon-based diphasic armors. The equation is given as

$$V_{50,sys} = \sqrt{V_{50,1}^2 + V_{50,2}^2} \tag{8.6}$$

Table 8.7. Ballistic results of Dyneema® SB31/Twaron® CT709 hybrid and constituent materials, $\eta = 0.060$ and 0.121.

Target	A_d [kg/m^2]	V_{bl} [m/s]
15-ply Dyneema® SB31	1.894	339
10-ply Twaron® CT709	1.981	395
15-ply SB31/10-ply CT709, predicted	3.875	521
15-ply SB31/10-ply CT709, experimental	3.875	470
10-ply CT709/15-ply SB31, experimental	3.875	481
30-ply Dyneema® SB31	3.789	488
20-ply Twaron® CT709	3.961	496
30-ply SB31/20-ply CT709, predicted	7.750	696
30-ply SB31/20-ply CT709, experimental	7.750	607
20-ply CT709/30-ply SB31, experimental	7.750	643

with $V_{50,1}$ and $V_{50,2}$ being the respective ballistic limit velocities of the constituent panels. Equation 8.6 basically assumes optimal energy-absorption via complete strain-energy dissipation of the constituent panels, which has been shown by Cunniff [12] to overestimate the performance of soft armor systems. Moreover, the form given in Equation 8.6 does not include the effects of stacking order. Nonetheless, these predicted values have been included for comparison as well.

As expected, the predicted ballistic limit velocity using Equation 8.6 based on the constituent panels far overestimates the actual ballistic performance of either stacking order. This is due to the sub-optimal energy-absorption of the strike face material at the system's ballistic limit velocity where the material fails prematurely before the cone wave can sufficiently propagate and dissipate energy. We note that the 10-ply Twaron® CT709 panel has a significantly higher ballistic limit than 15-ply SB31 (395 vs. 339 m/s), but the 10T/15D system outperforms the 15D/10T system.

This is likely due to the thermal softening effect that has been previously discussed in prior works [11, 112]. The comparison metrics in Tables 8.1-8.3 and 8.7 are plotted against the Cunniff velocity ratios in Figure 8.4. The general trend indicates that a rear material with a higher Cunniff velocity results in a better ballistic performance regardless of performance metric. However, there exists no clear correlation between the value of the Cunniff velocity ratio and the performance metric, understandably due to the complexities of soft armor ballistic response in general. Nonetheless, these data points strongly suggest that the Cunniff velocity is useful as a preliminary design tool to select the optimal stacking order in the design of bi-material diphasic armors.

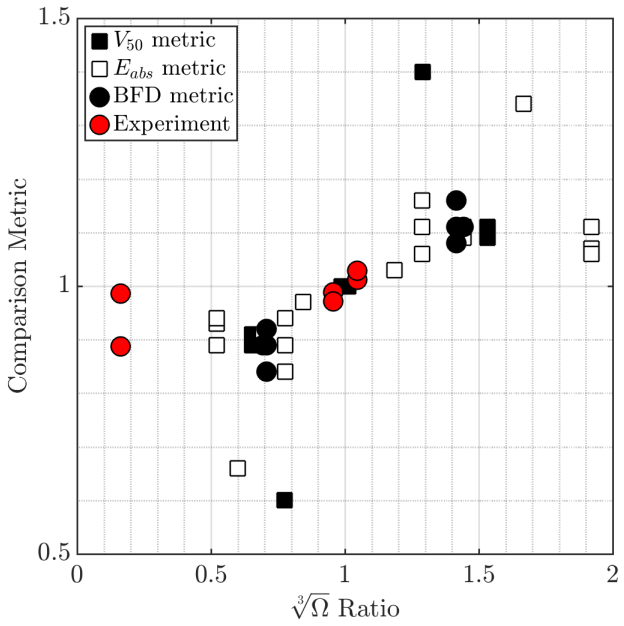

Figure 8.4. V_r-V_s curves for both A/B and B/A configurations for Dyneema® SB31/Twaron® CT709 impacted by .30-cal FSP, areal density ratios η = (a) 0.062 and (b) 0.124.

8.3.3 Analysis of interference using Phoenix & Porwal's bi-layer membrane model

To gain some insight into the stacking order effects, we examine the problem using Porwal & Phoenix's bi-layer membrane model [90, 112]. For brevity, the entire set of equations is not given here. The reader is instead directed to these references for a more complete derivation of their model. The extensive system of equations was numerically solved using MATLAB to obtain the projectile velocity V_p and the transverse cone edge displacement x_{cone} against the projectile transverse displacement δ. Figure 8.5 gives the results for a two-layered hybrid system consisting of 0.235 kg/m^2 generic Kevlar® (E = 73 GPa, ρ = 1440 kg/m^3, ε_f = 3.6%) at the strike face and 0.245 kg/m^2 Spectra® (E = 120 GPa, ρ = 970 kg/m^3, ε_f = 4.5%) at the rear. These areal densities are typical of single-ply targets. The behavior of the impact process may be inferred from the plots. When impacted by a 16-grain (approx. 1 g) RCC projectile (radius Rp = 2.76 mm) at a striking velocity of 200 m/s, the cone edge x_{cone} of the Spectra® layer is observed to travel faster than the Kevlar® layer i.e. this arrangement is non-interfering since both layers can freely travel and deform without restraint from the other material. The Kevlar® layer fails first at a normalized transverse displacement of about 0.9. The rear Spectra® layer cone wave continues propagating and dissipating kinetic energy before eventually failing at δ/R_p = 1.6 and a normalized cone edge displacement of 5.6. The residual velocity V_r (i.e. V_p when both layers fail) is approximately 156 m/s. These results compare well with prior results obtained in Ref. [112]. Note that we have only used the non-interfering versions of the model to demonstrate qualitative trends rather than explicitly calculating for numerical results. As such, the interfering/non-interfering models will yield the same cone edge displacement values. Some results may qualitatively exhibit interference based on cone wave propagation, but the actual ballistic response of the interference is not numerically calculated as it requires an alternate formulation of the model and is not the current focus of the study. With the verification of the numerical model, four

further cases are presented to explain and demonstrate how the Cunniff velocity may be used as a merit parameter for determining the optimal stacking order of bi-layered, bi-material soft armor targets.

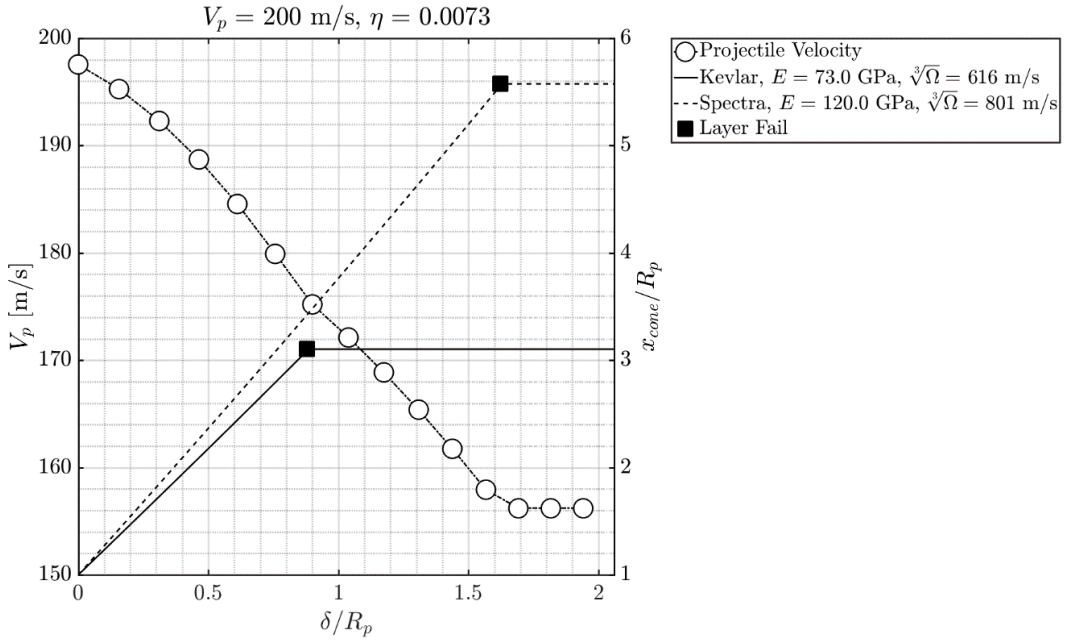

Figure 8.5. Evolution of normalized cone edge displacement x_{cone}/R_p (solid and dashed lines) and projectile velocity (white circles) against normalized projectile displacement δ/R_p for a bi-material Kevlar®/Spectra® target. Black squares indicate point of failure of layer when local projectile edge strain reaches the material's failure strain.

8.3.4 Case 1: Kevlar® 29/Kevlar® 49 systems with different areal densities.

Cunniff first noted a lack of performance difference between a frontal 1000 denier Kevlar® 29 (E = 78.8 GPa, $\rho = 1440$ kg/m^3, $\varepsilon_f = 3.25\%$ [11]) layer and a rear Kevlar® 49 ($E = 120$ GPa, $\rho = 1440$ kg/m^3, $\varepsilon_f = 2.55\%$ [11]) and the corresponding reverse configuration, even though the mismatch between the elastic moduli is the

same as Kevlar®/Spectra® bi-layer system. Figures 8.6a-c give the evolution of the cone wave displacement and projectile velocities for total areal densities of 0.940, 9.40, and 94.0 kg/m^2, with both constituent materials each making up 50% of the total system areal mass. From Figures 8.6a, despite the much larger elastic modulus of the Kevlar® 49, it fails at the same time as the Kevlar® 29. Since the non-interfering model gives the same cone edge displacement regardless of stacking order, we see that switching the stacking order would only result in minimal interference. In contrast to Figures 8.5 for Kevlar®/Spectra®, switching the order would deleteriously constrain the Spectra® layer and result in sub-optimal performance. This similarity in ballistic performance persists across different magnitudes of areal density ratio η, although care must be taken when using such results for η above 0.25. For $\eta = 0.73$ (equivalent to about 200 plies total), the performance difference is practically insignificant.

The form of the Cunniff velocity in Equation 8.4 explains these results. The Kevlar® 49 with a superior elastic modulus (and consequently, elastic wave speed) allows the layer to propagate slightly faster than Kevlar® 29, resulting in minimal interference. However, what it makes up for in rate of dissipation, it severely lacks in failure strain compared to Kevlar® 29. Before the Kevlar® 49 layer can propagate energy sufficiently like the Spectra® layer did, it fails when it reaches its lower failure strain value. If we hold the Cunniff velocity in Equation 8.4 constant, we see that a decrease in elastic wave speed must be compensated for with a much higher increase in failure strain for the materials to behave similarly. In the next two cases, we examine these effects more closely using a fictive Kevlar® analog material.

8.3.5 Case 2: Kevlar® 29/fictive Kevlar® analog system with decreased modulus E

For all results in this case, the striking velocity V_s was held constant at 200 m/s, the total areal density held constant at 0.47 kg/m^2 (same as the Kevlar®/Spectra® case in Figure 8.5) and both layers at 50%/50% mass fraction. The fiber density and

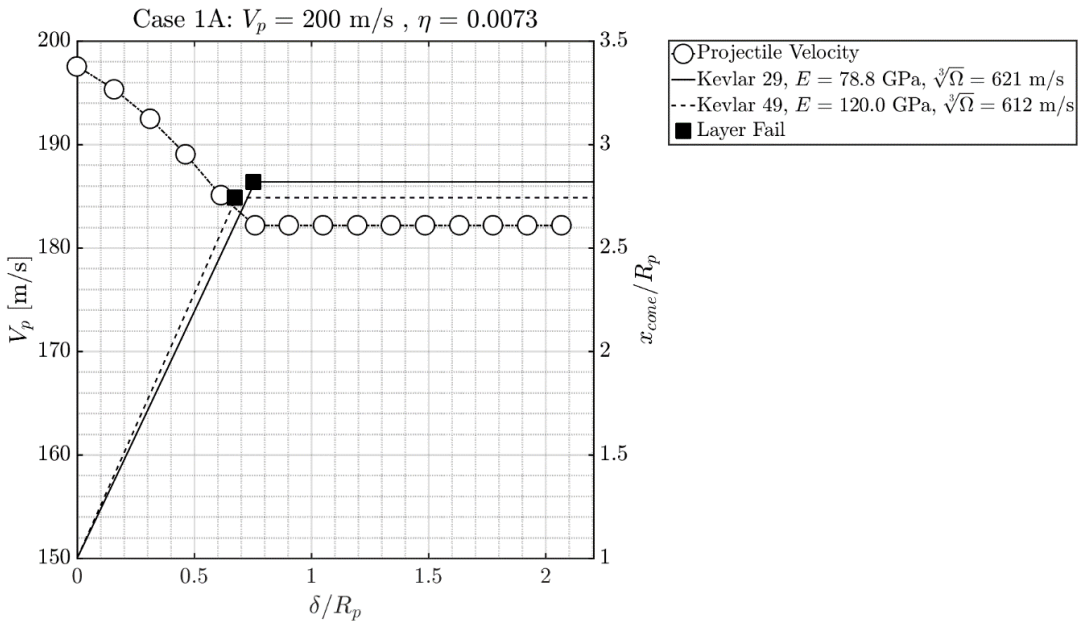
Case 1A: $V_p = 200$ m/s , $\eta = 0.0073$
Projectile Velocity
Kevlar 29, $E = 78.8$ GPa, $\sqrt[3]{\Omega} = 621$ m/s
Kevlar 49, $E = 120.0$ GPa, $\sqrt[3]{\Omega} = 612$ m/s
Layer Fail
V_p [m/s]
x_{cone}/R_p
δ/R_p

(a)

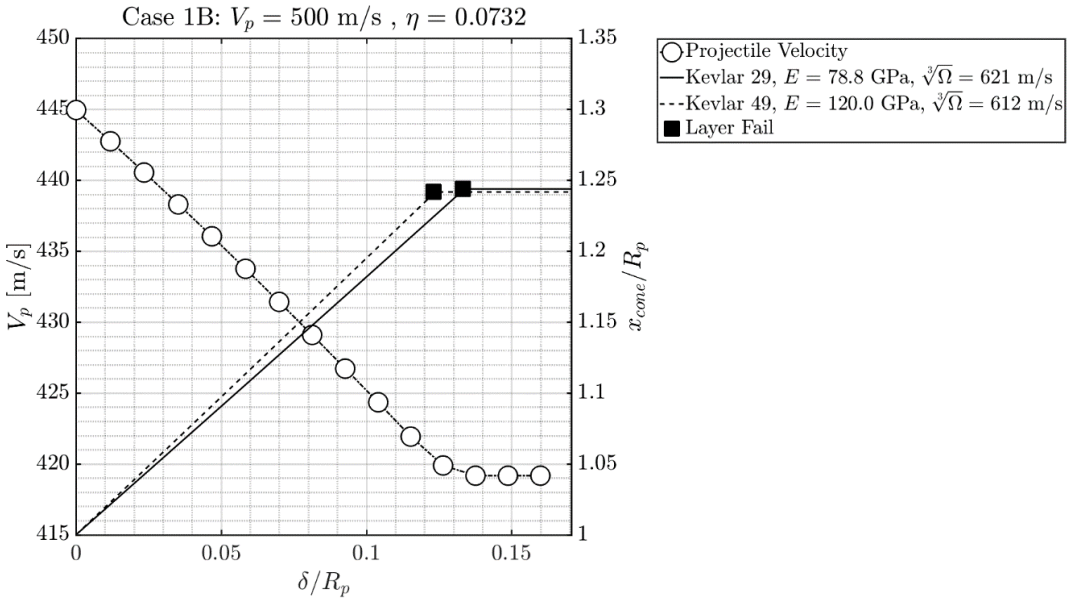
Case 1B: $V_p = 500$ m/s , $\eta = 0.0732$
Projectile Velocity
Kevlar 29, $E = 78.8$ GPa, $\sqrt[3]{\Omega} = 621$ m/s
Kevlar 49, $E = 120.0$ GPa, $\sqrt[3]{\Omega} = 612$ m/s
Layer Fail
V_p [m/s]
x_{cone}/R_p
δ/R_p

(b)

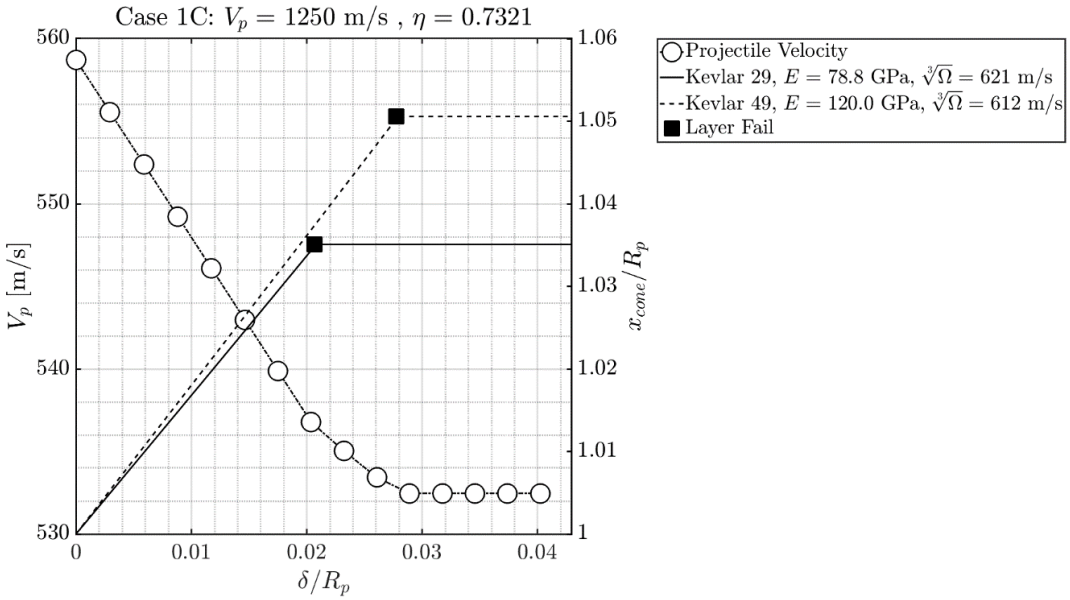

(c)

Figure 8.6. Evolution of normalized cone edge displacement x_{cone}/R_p (solid and dashed lines) and projectile velocity (white circles) against normalized projectile displacement δ/R_p for a bi-layered Kevlar® 29/Kevlar® 49 target, with system areal densities of (a) 0.94 kg/m^2, (b) 9.40 kg/m^2, and (c) 94.0 kg/m^2.

failure strain were held constant at 1440 kg/m^3 and 3.6% respectively. The impact response of a baseline Kevlar®/Kevlar® bi-layer with the same material and system properties is shown in Figures 8.7. As expected, both layers behave in the exact same manner, since the model was formulated with the assumption that the constituent material layers are membranes. Due to the lack of improved energy dissipation by a Spectra® layer, the residual velocity of the Kevlar®/Kevlar® system is much higher at 179 m/s i.e. poorer energy absorption.

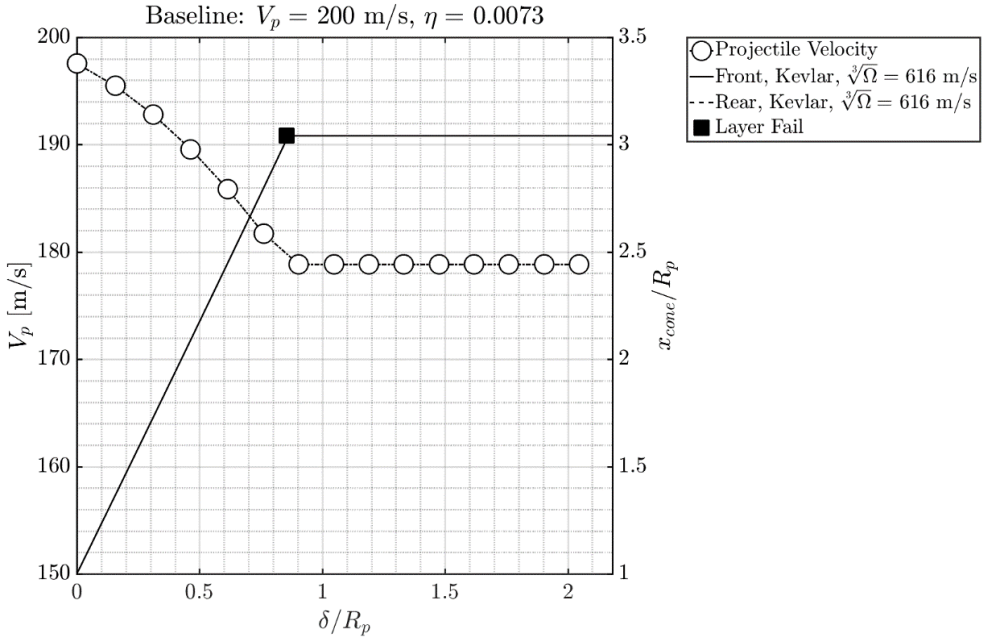

Figure 8.7. Evolution of normalized cone edge displacement x_{cone}/R_p (solid and dashed lines) and projectile velocity (white circles) against normalized projectile displacement δ/R_p for a bi-layered Kevlar®/Kevlar® target, system areal density 0.94 kg/m^2 and impact velocity 200 m/s.

In Case 2A (Figure 8.8a), the elastic modulus of the frontal Kevlar® is 73 GPa, but the modulus of the rear fictive material is lowered by 85% while keeping all else constant. With density being held the same, this results in a lowered elastic wave speed, and so the layer does not propagate sufficiently before reaching its failure strain.

Interestingly, there is some interference between layers as evidenced by the frontal cone overtaking the rear cone, but this interference is on the order of a hundredth of the actual cone displacement and may be considered negligible. This configuration results in a residual velocity of about 181 m/s compared to the Kevlar®/Kevlar® result in Figure 8.7. For Case 2B (Figure 8.8b), the failure strain is adjusted so that the resulting Cunniff velocities of both layers are the same, and consequently these two layers deform and fail together at the same time, as with the effect observed for Kevlar® 29/Kevlar® 49. When the fictive Kevlar® failure strain is further increased such that its modulus remains 85% of the frontal Kevlar® while the Cunniff velocity of the fictive Kevlar® exceeds that of the frontal material, the rear portion fails much later, resulting in improved energy absorption.

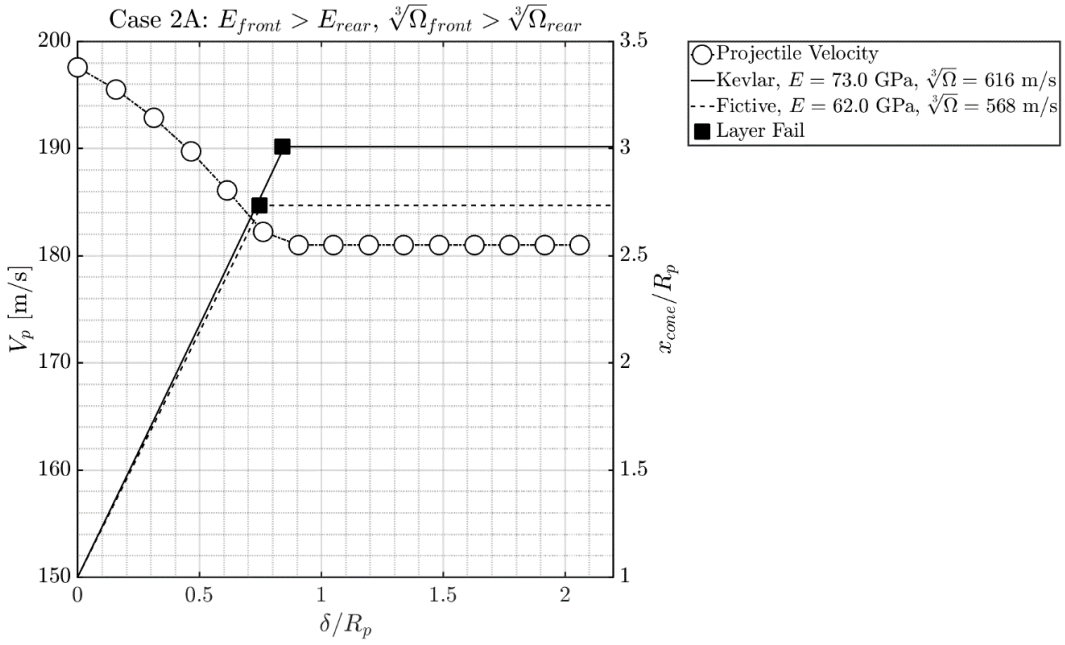

(a)

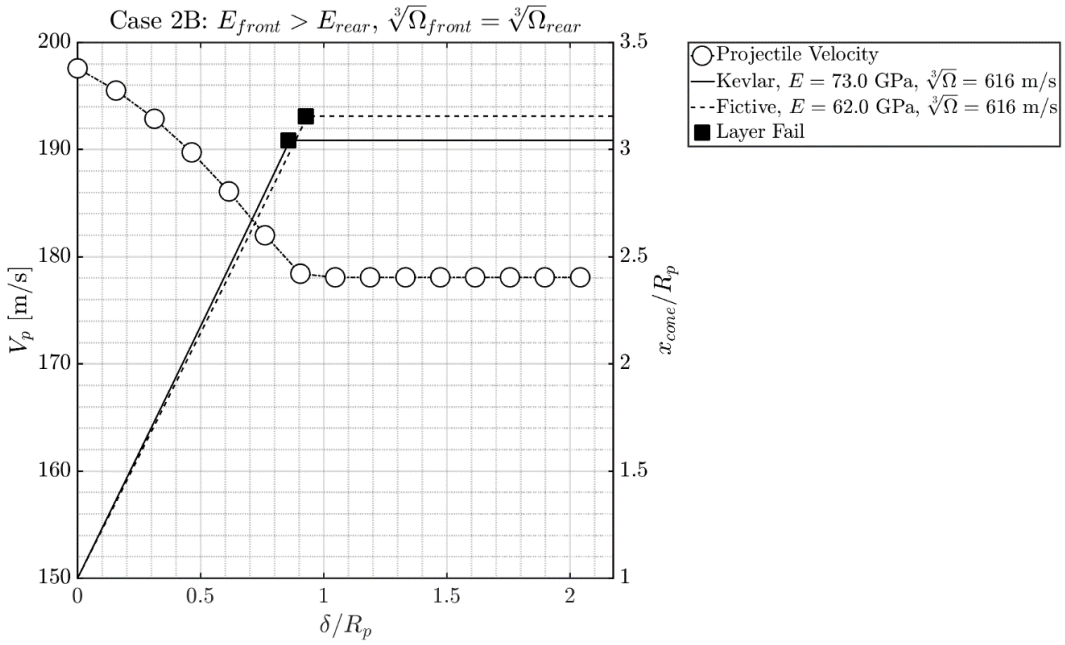
Case 2B: $E_{front} > E_{rear}$, $\sqrt[3]{\Omega}_{front} = \sqrt[3]{\Omega}_{rear}$
200
190
180
170
160
150
V_p [m/s]
0
0.5
1
1.5
2
δ/R_p
3.5
3
2.5
2
1.5
1
x_{cone}/R_p
Projectile Velocity
Kevlar, $E = 73.0$ GPa, $\sqrt[3]{\Omega} = 616$ m/s
Fictive, $E = 62.0$ GPa, $\sqrt[3]{\Omega} = 616$ m/s
Layer Fail

(b)

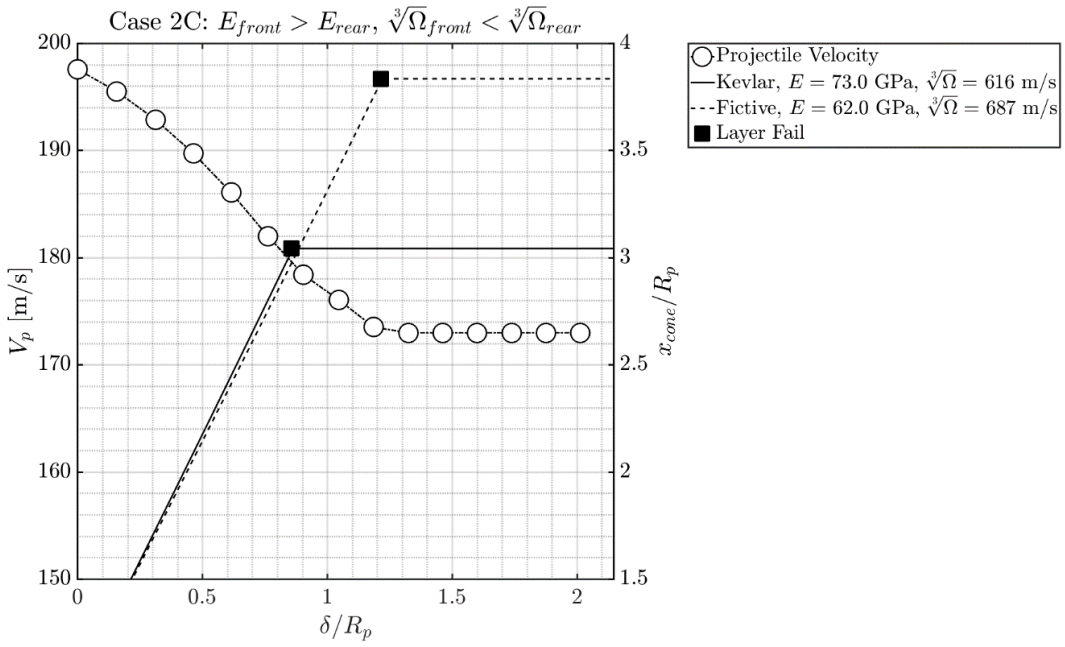

(c)

Figure 8.8. Evolution of normalized cone edge displacement x_{cone}/R_p (solid and dashed lines) and projectile velocity (white circles) against normalized projectile displacement δ/R_p for a bi-layered Kevlar®/fictive Kevlar® target with lowered modulus, system areal density 0.94 kg/m^2 and impact velocity 200 m/s.

8.3.6 Case 3: Kevlar® 29/fictive Kevlar® analog system with decreased failure strain ε_f

For all results in this case, the striking velocity V_s was held constant at 200 m/s, the total areal density held constant at 0.47 kg/m^2 (same as the Kevlar®/Spectra® case in Figure 8.5) and both layers at 50%/50% mass fraction. The failure strain of the fictive Kevlar® was set at 85% of Kevlar®. At the fiber level, the density was held constant at 1440 kg/m^3, which means that the parameter to be adjusted is the elastic modulus E, and indirectly, the elastic wave speed. Again, the results show the same trend whereby the ballistic performance of the system may be sustained or even improved as long as the other parameters are adjusted accordingly (Figures 8.9a-c). The small magnitude of residual velocity differences in the cases so far are likely due to the targets being single plies —- in the next case, we look at these effects on thicker targets with more realistic system areal densities

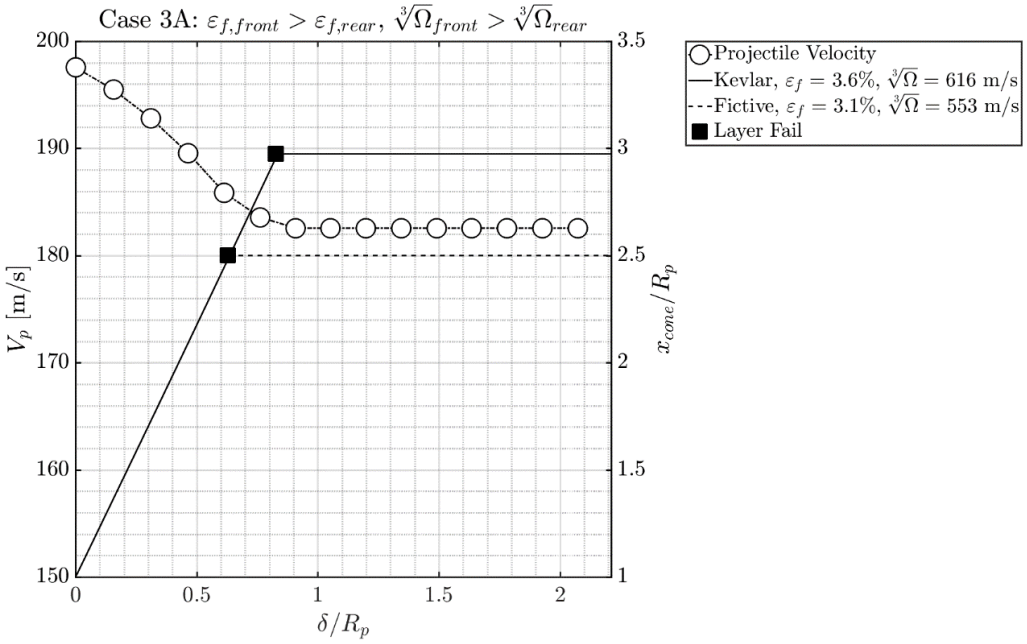

(a)

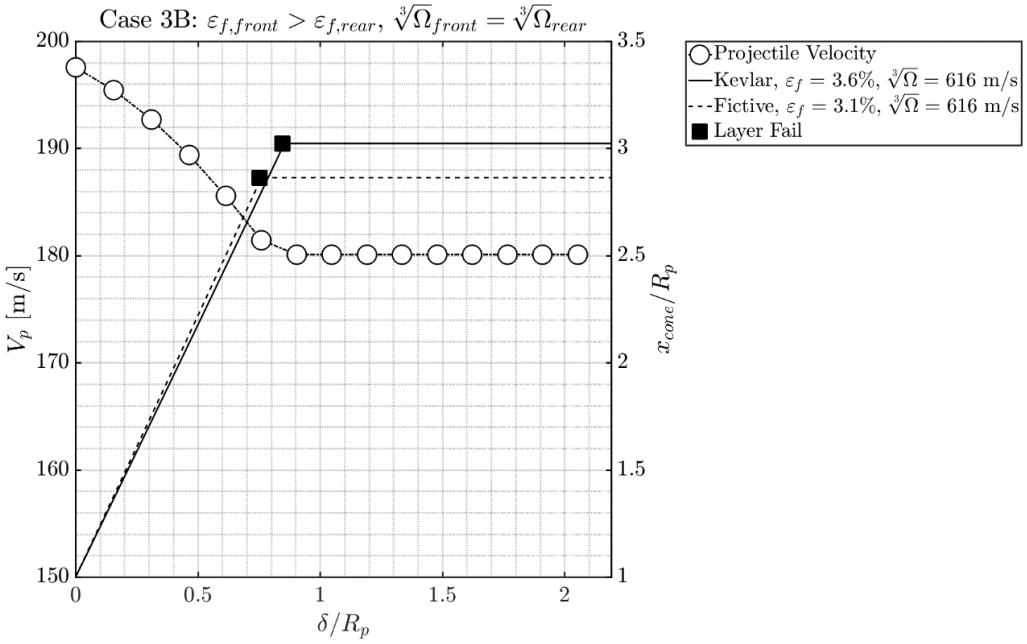
Case 3B: $\varepsilon_{f,front} > \varepsilon_{f,rear}$, $\sqrt[3]{\Omega}_{front} = \sqrt[3]{\Omega}_{rear}$
V_p [m/s]
x_{cone}/R_p
δ/R_p
200
190
180
170
160
150
3.5
3
2.5
2
1.5
1
0
0.5
1
1.5
2
Projectile Velocity
Kevlar, $\varepsilon_f = 3.6\%$, $\sqrt[3]{\Omega} = 616$ m/s
Fictive, $\varepsilon_f = 3.1\%$, $\sqrt[3]{\Omega} = 616$ m/s
Layer Fail

(b)

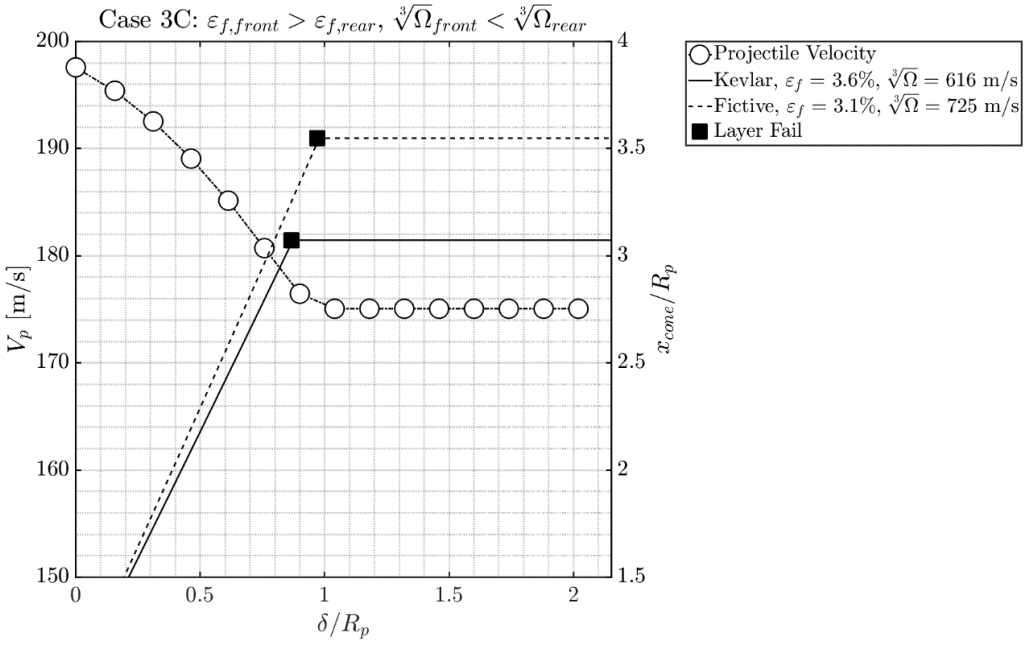

(c)

Figure 8.9. Evolution of normalized cone edge displacement x_{cone}/R_p (solid and dashed lines) and projectile velocity (white circles) against normalized projectile displacement δ/R_p for a bi-layered Kevlar®/fictive Kevlar® target, system areal density 0.94 kg/m^2 and impact velocity 200 m/s.

8.3.7 Case 4: Thicker Kevlar® 29/fictive Kevlar® analog system with decreased modulus E

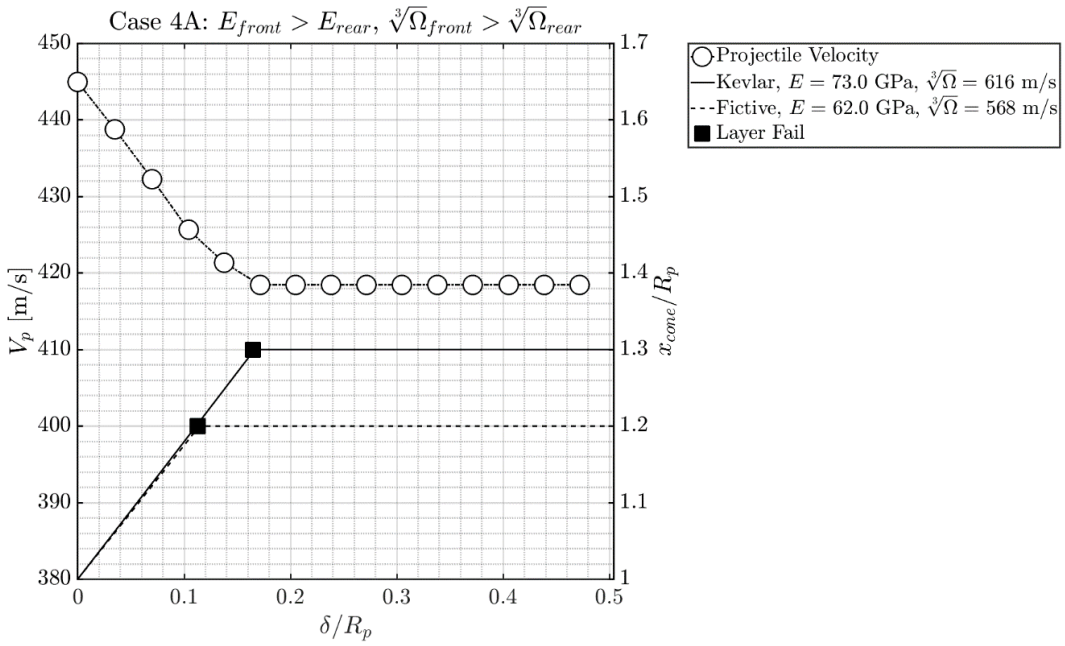

(a)

For Cases 4A-C, the system areal densities modelled were 9.40 kg/m^2, or an areal density ratio η of 0.073 for impact by a standard 16-grain RCC. This areal density range corresponds to approximately 20 plies of Kevlar®, which is similar to the systems tested experimentally in this study. The results given in Figures 8.10a-c show the same trend with the rest of the cases, but the residual velocities of 418, 408, and 392 m/s respectively for each case exhibit a much larger difference than the single-ply targets in Cases 2 and 3. However, despite the trends presented in this section (such as in Case 1C for the extremely thick targets), care should be taken when applying the Cunniff velocity as a merit parameter to thicker bi-material targets. The models formulated by Phoenix *et al.* and presented herein were based largely on membrane assumptions, which tend to maximize the in-plane energy-dissipation efficiency of the target materials. Although the models have shown great accuracy in predicting the trends and target response observed experimentally, these assumptions

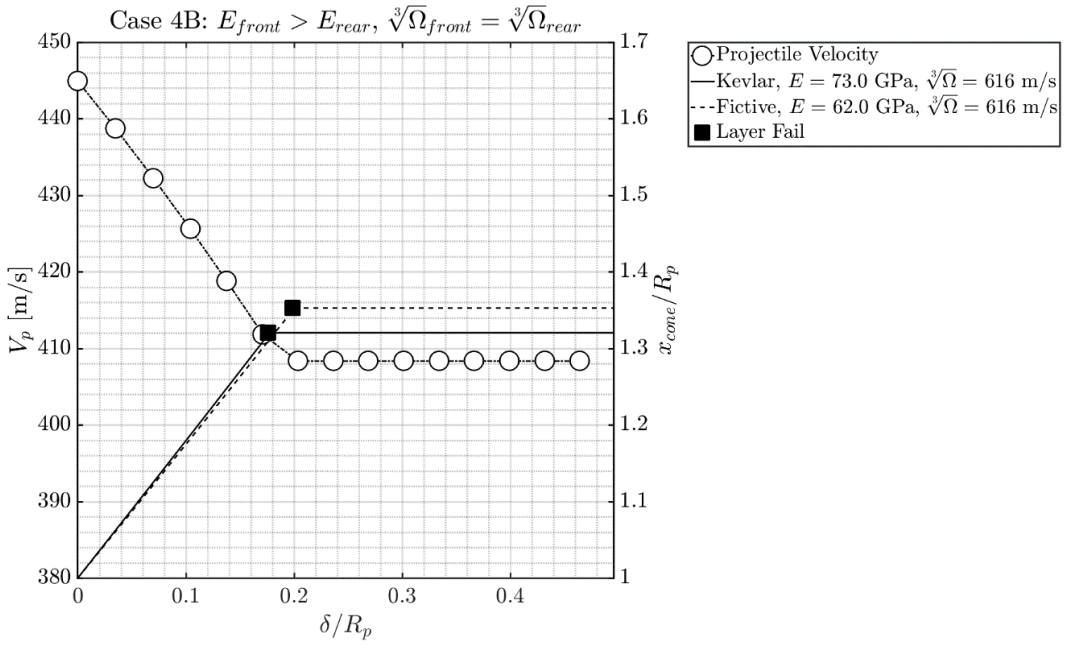
Case 4B: $E_{front} > E_{rear}$, $\sqrt[3]{\Omega}_{front} = \sqrt[3]{\Omega}_{rear}$
V_p [m/s]
x_{cone}/R_p
δ/R_p
450
440
430
420
410
400
390
380
1.7
1.6
1.5
1.4
1.3
1.2
1.1
1
0
0.1
0.2
0.3
0.4
Projectile Velocity
Kevlar, $E = 73.0$ GPa, $\sqrt[3]{\Omega} = 616$ m/s
Fictive, $E = 62.0$ GPa, $\sqrt[3]{\Omega} = 616$ m/s
Layer Fail

(b)

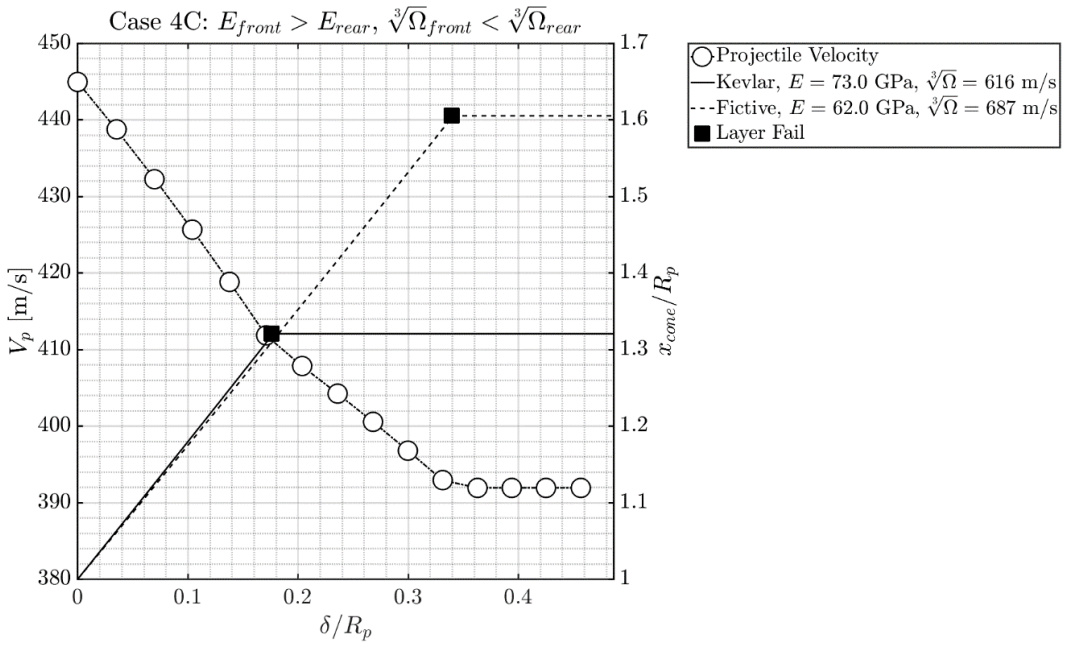

(c)

Figure 8.10. Evolution of normalized cone edge displacement x_{cone}/R_p (solid and dashed lines) and projectile velocity (white circles) against normalized projectile displacement δ/R_p for a bi-layered Kevlar®/fictive Kevlar® target, system areal density 9.40 kg/m^2 and impact velocity 500 m/s.

may not physically hold true in real-world applications, thus we find it necessary to discuss these limitations via the concept of "ballistically-thin" targets.

8.3.8 "Ballistically-thin" targets and their relation to $\sqrt[3]{\Omega}$ as a merit parameter

In earlier sections, the areal density ratio η of listed experiments were observed to be between 0.01 and approximately 0.20. This range of η values may be described as "mechanically-thin" with respect to the impinging projectile. We provide justification for this description by referring to prior works from Phoenix & Porwal [90, 102], who used a 1D strip/2D membrane model to analyze the dynamics of projectile impact. Figure 8.11a replots two specific curves from Figure 8.5a from Ref. [90] showing the dimensionless ballistic limit velocity $V_{50}/\sqrt[3]{\Omega}$ against the areal density ratio η for a 1D strip model and a 2D membrane. For η values up to about 0.25, the behavior of the 2D membrane is drastically different from a 1D strip (which always has a higher theoretical critical velocity). This drastic change in behavior is shown in Figure 8.11b where the critical velocities in Figure 8.11a are plotted as a ratio against η. Phoenix & Porwal explain that, for this low η regime, the 2D membrane is not instantly perforated, but rather the transverse cone must grow while the strain begins to build up and reaches its critical failure strain value. This cone growth process in the target does work to decelerate the projectile, and in fact, the lower the η, the longer the strain takes to reach critical value, allowing more kinetic energy to be dissipated via membrane strain before perforation occurs. Porwal & Phoenix further expounded [102] this idea in looking at multi-ply system effects under ballistic impact. With an increase in the areal density ratio η, progressive strain build-up from layer to layer becomes more rapid, which in turn adversely affects the transverse cone wave growth. Although further increases in target areal density still contributes to projectile deceleration via momentum exchange, the high impinging velocities at the strike face result in rapid failure of the frontal layers. Therefore, the resultant increase

in ballistic performance with an increase in mass is offset by this rapid strain build-up and failure through the frontal layers, which reduces the armor panel's overall efficiency in strain energy propagation.

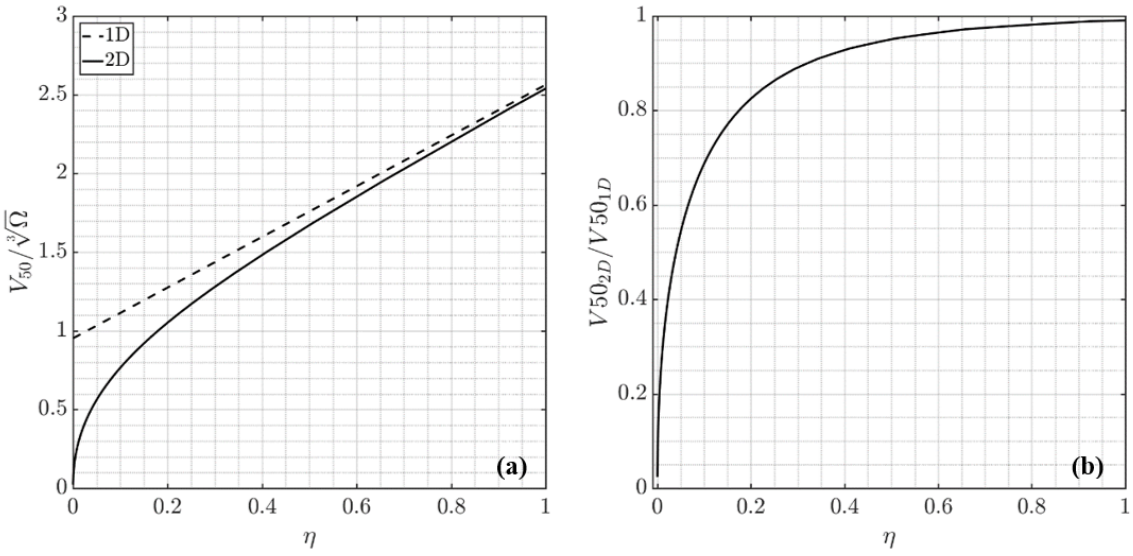

Figure 8.11. Comparison of non-dimensional ballistic velocities for 1D and 2D models at different areal density ratios

In summary, when impacted at their critical velocities, the target panels in the lower η regime (below approx. 0.25) tend to behave more like a membrane, with this membrane behavior being more pronounced the lower the η. Similar concepts from prior works by Ben-Dor *et al.* [120] and Guo *et al.* [115] are explored in Appendix 8.6. Going back to the original observation that the target panels in the listed studies have η values ranging between 0.01-0.20, we can relate this to the Cunniff parameter since it describes elegantly, albeit conceptually, the efficiency of these soft armor panels in dissipating the striking kinetic energy via membrane-like mechanisms. This would explain why the Cunniff velocity works as a merit parameter to determine the stacking order for these ballistically-thin targets listed. Putting it in physical quantities, an η of 0.25 translates to approximately 40 plies of Twaron® CT709 or 60 plies of Dyneema® SB31 for a .30-cal FSP, which is a reasonable quantity for

soft armor targets. On the other hand, thicker targets tend to exhibit inelastic or extremely localized failure modes at the strike face. In this larger η regime, the high striking velocity of the projectile results in rapid failure upon impact, which persists through the layers of the target. This rapid strain to failure inhibits transverse cone growth, which minimizes membrane strain energy dissipation. Moreover, off-axis failure modes such as transverse shear or even bending may occur, which the Cunniff velocity is unable to capture. As such, using $\sqrt[3]{\Omega}$ as a merit parameter for thick targets may be tenuous at best.

8.4 Conclusions

In this study, we investigated the possibility of using the Cunniff velocity $\sqrt[3]{\Omega}$ as a merit parameter in determining the optimal stacking order of heterogeneous diphasic soft armor systems. Existing literature examined this phenomenon by evaluating performance metrics such as the V_{50} ballistic limit, energy absorbed, and the back-face deformation. Due to the different metrics used, a secondary comparison metric was calculated to objectively compare the performance of the diphasic panel in both forward and reverse configurations. Results show that the two constituent materials should be ordered such that the material with a higher $\sqrt[3]{\Omega}$ velocity is placed at the rear to minimize material interference during transverse cone growth.

To further test this atypical use of the Cunniff velocity, experiments were performed by impacting .30-cal FSPs on heterogeneous systems comprising ballistic-grade XS-350 polyurea, Twaron® fabric, and Dyneema® UD laminate plies. The target panels were designed to have each material near-equivalent in areal mass and panel thickness, giving areal density ratios around 0.060 and 0.120. For the XS-350/Twaron® CT709 and Dyneema® SB31/Twaron® CT709 hybrid panels, we only observe a slight difference in ballistic performance for $\eta = 0.060$; at double the areal density ratio, the ballistic performance is more pronounced. In both cases, the configuration where the material with higher $\sqrt[3]{\Omega}$ is placed at the rear gives superior

performance, providing further justification for its use as a preliminary design tool. We further discuss the idea of "ballistically-thin" soft armor materials in relation to the concept of $\sqrt[3]{\Omega}$ as a parameter that describes the target's dissipation efficiency via membrane strain mechanisms. At lower η ratios below 0.25, target panels behave in a more "membrane-like" fashion, which allows for $\sqrt[3]{\Omega}$ to be a suitable merit parameter for determining the stacking order. This concept may not be applicable at higher η ratios where strain energy dissipation is sub-optimal due to constrained transverse cone growth, and high projectile impinging velocities result in localized failure without significant membrane strain development.

8.5 Acknowledgments

The authors would like to thank the U.S. Army, P.M. Soldier Protection and Individual Equipment, Technical Management Directorate for their support during this project. The authors would also like to thank Stephenie Martinez-Morales for her help with sample preparation and ballistic experiments.

8.6 Appendix A: Further discussion on "ballistically-thin" targets

The concept of "ballistically-thin" targets was briefly discussed in previous sections to describe a regime of areal density ratios whereby the target behaves somewhat membrane-like. Although not formally named, and Guo *et al.* [115] and Ben-Dor *et al.* [120] have previously observed this phenomenon as well. In the former work, Guo *et al.* proposed a framework to determine the inelastic strike-face fraction of the target panel i.e. the amount of strike-face material that exhibits sub-optimal strain energy absorption at the entire system's ballistic limit. The proposed design parameter is based heavily on Cunniff's regression analysis to obtain a family of curves presenting this optimal inelastic strike-face fraction k as a function of the areal density ratio η. The equation is given without derivation as

$$k_{opt} = \left[1 - \frac{1}{X_6}\left(\eta_{sys}^{-X_7}\right)\ln X_{10}\right]^{1/X_7} \tag{8.7}$$

In Equation 8.7, X_n are regression coefficients detailed in Refs. [10] and [115]. Figure 8.12 shows an example of such a curve for Kevlar® 29 fabric. At low η values, the k fraction is small, indicating that a large fraction of the targets behaves elastically i.e. absorption via membrane strain energy dissipation dominates. The fraction of the target exhibiting inelastic impact response rapidly increases with an increase in η before leveling off at around $\eta = 0.20$. This k-η curve exhibits features similar to Phoenix & Porwal's curve in Figure 8.5b, namely that the system behaves mostly as an elastic membrane at low η values i.e. "ballistically-thin" targets.

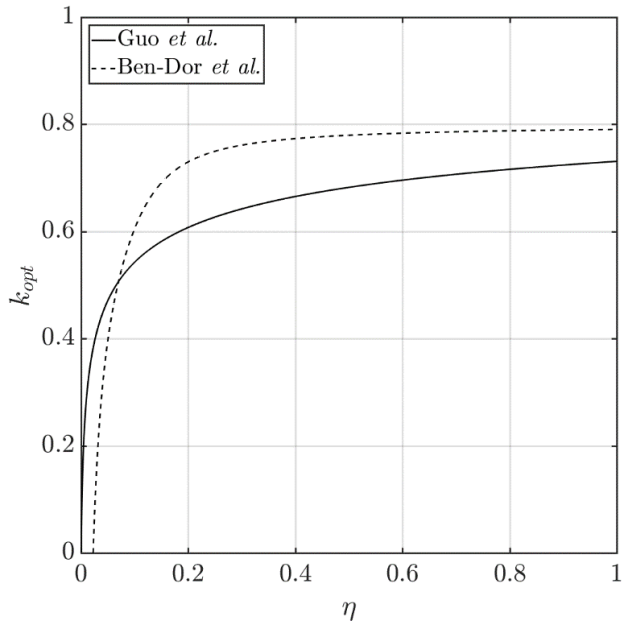

Figure 8.12. Inelastic strike-face fraction k_{opt} against areal density ratio η, as derived by Guo *et al.* [115] and Ben-Dor *et al.* [120]

Ben-Dor, Dubinsky, and Elperin [120] sought a closed-form solution to optimize the design of a two-component composite armor to determine the optimal fraction

k_{opt} of the ceramic material in the system such that the ballistic limit velocity is maximized. While their derivation focused solely on optimizing ceramic-faced soft armor systems, the input parameters may be modified to use the material and mechanical properties of a soft armor target, although certain assumptions have to be made. For brevity, the entire derivation from their work is not included, but the set of pertinent equations is given as

$$c_3 k_{opt}^3 + c_2 k_{opt}^2 + c_1 k_{opt} + c_0 = 0 \tag{8.8}$$

$$\beta = 4\frac{\rho_p}{\rho_t}\eta \tag{8.9}$$

$$c_0 = \eta\,(4\beta - 1) + 2\beta - 1 \tag{8.10}$$

$$c_1 = \eta\beta\,(8\beta - 7) - 3\beta \tag{8.11}$$

$$c_2 = \eta\beta^2\,(4\beta - 11) \tag{8.12}$$

$$c_3 = -5\eta\beta^3 \tag{8.13}$$

In Equation 8.13, ρ_p is the projectile density and ρ_t is the target density. We assume that the projectile is a steel RCC of density 7830 kg/m^3 and the "ceramic" in this case has a density of 1440 kg/m^3, equivalent to Kevlar® 29. Solving for Equation 8.8 gives the optimal fraction of the strike-face that fails without significant strain energy absorption as plotted in Figure 8.12. Again, we see the characteristic curve shape that drops to rapidly zero below an η value of about 0.25-0.3, indicating that the dominant energy absorption mode is via membrane strain in this low η regime. Based on the results shown in this section, the concept of a "ballistically-thin" target is justified, and this regime appears to lie within the range of η values below 0.25.

9. SIMPLE ANALYTICAL MODELS FOR INVESTIGATING RELATIVE TIMESCALES OF IMPACT

The diphasic response of fibrous soft armor targets was more closely analyzed in prior chapters. It was shown that these targets exhibit an inelastic response at the strike face i.e. localized failure upon initial impact. Once the projectile has slowed down sufficiently, the rear portion responds in an elastic membrane-like fashion, deforming in the transverse direction and dissipating energy away from the impact site. The areal mass of the target strike-face material that responds inelastically can be calculated via the parameter k. This k fraction may be replaced with a cheaper material with the same areal mass and still maintain the ballistic performance, but it has been shown that replacement of the material with a stronger transverse response may actually improve the overall ballistic performance. For example, Cunniff [12] showed that replacement of a certain strike face portion with Pyrex® glass improved the overall hybrid system's performance significantly (provided the areal density ratio η is not too low). The same effect was shown for Alesi's work [26], where the frontal portion of a nylon fabric system was replaced with a titanium alloy. However, these frontal material choices are not ideal for personal body armor systems, where flexibility is of utmost importance.

In this regard, a soft armor material is a suitable choice to maintain flexibility while maintaining the ballistic performance of the overall system. The difficulty in selecting a suitable constituent fiber for such a soft armor frontal system is a lack of further work in existing work bridging the micro-scale with the macro-scale. When looking at the system-level design optimization of these soft armor targets, it is imperative to first look at why they respond differently in the through-thickness direction and

how the micro-scale properties of the constituent material contribute to the overall structural impact response.

The structural impact response further poses another level of complexity. In quasi-static analysis of plates and membranes, the condition that the thickness direction be smaller than the in-plane directions may be easily satisfied in a rudimentary fashion with geometric ratios of thickness/length much smaller than 1 in both directions. For an isotropic material, the quasi-static loading response has been analyzed in-depth in prior literature [121–124]. Orthotropic plates pose a slightly more complex problem, but solutions have nonetheless been similarly provided in existing literature. In the dynamic analysis of orthotropic plates, it is insufficient to consider the loading response purely based on the geometries of the problem.

In this chapter, the experimentally-obtained micro-scale fiber properties are homogenized to give macro-scale structural parameters. Some simplified loading models via nonlinear ordinary differential equations are implemented to give an idea of the change in behavior of the target under impact when micro-scale material properties are modified. Given the many aspects of simplification and homogenization of the system, the results presented are by no means quantitatively accurate, but merely serve as a trend study.

9.1 Propagation of different waves during impact

The mechanical response of the target may be broadly categorized into several regimes based on the relative time scales of wave propagation in their respective directions. At the early onset of projectile impact, several waves propagate from the impact site outwards towards the boundaries of the target panel. At early time scales before this dilational wave gets reflected at the boundary i.e. the rear surface, the response of the target plate is dominated by three-dimensional wave propagation, since the information has not reflected from the boundary yet. Within this regime, the response is dominated by contact indentation.

9.1.1 Through-thickness wave propagation

The through-thickness wave propagation response may be well-approximated with the dilational wave speed $c_t = \sqrt{E_{33}/\rho}$, and the transit time is calculated for a plate of thickness h in Equation 9.1.

$$t_{dil} = \frac{h}{\sqrt{E_{33}/\rho}} \tag{9.1}$$

9.1.2 Bending wave propagation

Flexural wave propagation in plates is not as straightforward as the other wave speeds discussed prior to this section. Firstly, flexural waves tend to be dissipative, with higher frequencies travelling faster than lower frequencies [125]. Without *a priori* knowledge of the loading history of the impactor-plate system, it is hard to deduce the actual flexural wave speeds of the problem. Olsson et al. [126, 127] provided a simplified method of calculating the propagation velocity of the flexural wavefront via a similarity analyses. The equation is given as

$$a_{jk} = 2\sqrt{\pi}\left(\frac{D_{11}}{A_d}\right)^{1/4}\left[2\left(A+1\right)\right]^{1/8}\left(jk\right)^{1/4}\sqrt{t_{bend}}, \quad A \equiv \frac{D_{12}+2D_{66}}{\sqrt{D_{11}D_{22}}} \tag{9.2}$$

where j and k are the mode numbers in the x- and y-directions respectively. For this analysis, since the flexural waves are closed i.e. near-elliptical, we only consider modes where $j \equiv k$. The above equation assumes calculations based on a 3D orthotropic solid. In prior sections, the membrane model proposed by Phoenix [90] assumes a transverse cone wave front that is only dependent on in-plane tensile properties rather than flexural properties. This cone wave velocity is approximated by Equation 8.1, and this lateral transit time based on axial tensile cone assumptions is given by Equation 9.3. Note that this equation is given in material coordinates — the Eulerian

wave speed is slightly slower, but the Lagrangian wave speed provides a good first order approximation.

$$t_{cone} \approx \frac{a/2}{1.23c_0(V_p/c_0\sqrt{2})^{2/3}} \tag{9.3}$$

Additionally, we include the transit time based on the Cunniff velocity (Equation 8.4) and for a 1D yarn based on the Smith velocity [128]. These parameters are based on the constituent fiber properties and not of the system as a whole.

$$t_{Cunniff} \approx \frac{a/2}{c_0 \cdot \left(\varepsilon_f/\sqrt{2}\right)^{2/3}} \tag{9.4}$$

$$t_{Smith} \approx \frac{a/2}{c_0 \cdot \sqrt{2\varepsilon_f\sqrt{\varepsilon_f}}} \tag{9.5}$$

9.1.3 Transverse wave propagation

In different targets with certain symmetry planes i.e. isotropic and orthotropic materials, the upper bound on transverse wave propagation is determined by the Rayleigh wave speed. The actual value is usually hard to calculate, and typically becomes even more complex for non-isotropic materials with varying properties in the through-thickness direction. The transit time for a transverse wave front to reach the target boundary was therefore estimated using the transverse shear wave speed $c_{lat} = \sqrt{G_{13}/\rho}$. It must be noted, however, that the shear wave speed c_{lat} tends to be slightly slower than the Rayleigh wave speed, giving a slightly lower upper bound of transverse wave velocity. Although this transverse shear wave speed is not entirely necessary since the bending wave is always slower, we present it nonetheless for comparison.

$$t_{lat} \approx \frac{a/2}{\sqrt{G_{rz}/\rho}} \tag{9.6}$$

9.1.4 Global deformation

When the contact duration is longer than the time it takes for several transverse wave reflections to occur off the plate edge boundaries, the response is dominated by global deformation response such as bending and membrane stretching at large deformations. In such cases, the response is analytically similar to that of a quasi-static loading case. Although Lin & Fatt [129] further investigated the quantitative values of plate resistance to impact loading, the complexities involved with fabric impact are likely to result in large numerical inaccuracies. Moreover, the ballistic velocities typically occur on much longer timescales and as such are not of particular interest in this section.

9.2 Load analysis on projectile

9.2.1 Contact indentation load P_{con}

The contact load P_{con} is calculated via contact analysis with the following set of equations. A subscript *1* refers to the indenter and *2* refers to the target.

$$
\begin{aligned}
P_{con}(\delta) &= k_c \cdot \delta^m \\
k_c &= \begin{cases} \frac{4}{3} E^* \sqrt{R_{eff}} & \text{, round} \\ 2E^* R_{eff} & \text{, flat cylinder} \end{cases} \\
m &= \begin{cases} 3/2 & \text{, round} \\ 1 & \text{, flat cylinder} \end{cases}
\end{aligned}
\tag{9.7}
$$

The necessary contact parameters are given as [130]

$$\begin{aligned}
\frac{1}{R_{eff}} &= \frac{1}{R_1} + \frac{1}{R_2} \\
E^* &= \frac{1}{n_1 + n_2} \\
n_1 &= \frac{1 - \nu_1^2}{E_1} \\
n_2 &= \frac{\sqrt{B_{11}}\left[(\sqrt{B_{11}B_{22}} + G_{rz})^2 - (B_{12} - G_{rz})^2\right]}{2\sqrt{G_{rz}}(B_{11}B_{22} - B_{12}^2)}
\end{aligned} \tag{9.8}$$

We note that the indenter is assumed to be isotropic (hence the form of n_1) and that the target plane has an infinite radius of curvature R_2, hence R_{eff} reduces to simply R_1. The equations based on material properties involved are given as [130]

$$\begin{aligned}
B_{11} &= E_z(1 - \nu_r)\beta \\
B_{22} &= E_r\beta \cdot \frac{1 - \nu_{zr}^2\alpha}{1 + \nu_r} \\
B_{12} &= E_r\nu_{zr}\beta \\
\beta &= \frac{1}{1 - \nu_r - 2\nu_{zr}^2\alpha} \\
\alpha &= E_r/E_z
\end{aligned} \tag{9.9}$$

9.2.2 Bending load P_{bend}

Plate bending loads become significant for targets with lower aspect ratios i.e. thicker panels. Lin & Fatt [129] provide the relevant equations as

$$\begin{aligned}
P_{bend} &= K_b \cdot w_t^3 \\
K_b(a) &= \frac{64}{45a^2}\left[9(D_{11} + D_{22}) + 10D_{12} + 80D_{66}\right]
\end{aligned} \tag{9.10}$$

D_{ij} are the bending stiffness matrix terms expressed as

$$\begin{bmatrix} M_{xx} \\ M_{yy} \\ M_{xy} \end{bmatrix} = \begin{bmatrix} D_{11} & D_{12} & D_{16} \\ D_{12} & D_{22} & D_{26} \\ D_{16} & D_{26} & D_{66} \end{bmatrix} \begin{bmatrix} \kappa_x \\ \kappa_y \\ \kappa_{xy} \end{bmatrix} \tag{9.11}$$

9.2.3 Membrane stretching load P_{mem}

For large deflections, strain energy via membrane stretching becomes significant. Lin & Fatt [129] provide the relevant equations as

$$\begin{aligned} P_{mem} &= K_m \cdot w_t \\ K_m(a) &= \frac{128}{45a^2}\left[49(A_{11} + A_{22}) + 90A_{12} + 180A_{66}\right] \end{aligned} \tag{9.12}$$

where A_{ij} are the in-plane laminate matrix terms expressed as

$$\begin{bmatrix} N_{xx} \\ N_{yy} \\ N_{xy} \end{bmatrix} = \begin{bmatrix} A_{11} & A_{12} & A_{16} \\ A_{12} & A_{22} & A_{26} \\ A_{16} & A_{26} & A_{66} \end{bmatrix} \begin{bmatrix} \varepsilon_x \\ \varepsilon_y \\ \varepsilon_{xy} \end{bmatrix} \tag{9.13}$$

9.3 Homogenization of fiber properties

Thus far, the actual link between the macro-scale structural properties and micro-scale fiber mechanical properties have not yet been fully established, which is necessary to obtain contact parameters. We see in prior sections that these properties are related in the A_{ij} and D_{ij} matrices, but the actual derivation of these matrices still proves to be a complex issue. Classical Laminate Plate Theory (CLPT) allows for well-studied laminates to be modelled and homogenized, but for woven fabrics, problem of obtaining these matrices are compounded by their meso-scale properties such as weave and yarn dimensions. To obtained these values, a combination of TexGen and SwiftComp® were used for homogenization of these properties.

TexGen is an open source software developed by the University of Nottingham's Textile Composites Research Group, and is widely used to create complex textile models for finite element simulations. SwiftComp is a multiscale composite simulation code that allows for complex structural problems to be effectively homogenized and subsequently analyzed with simpler engineering models. For the Swiftcomp homogenization runs, the model was output with 10 voxels per yarn width and 20 voxels in the z-direction i.e. thickness direction. Domain was kept exactly the same size as the yarn model i.e. no increase in domain. Convergence tests for 1-, 2-, 5-, 10-, and 20-ply Twaron® CT709 fabric systems showed no dependence of any homogenized properties on the thickness, which is expected. No significant differences were observed for stiffness matrices obtained via the 3D Solid model and the Mindlin-Reissner models, and so the 3D Solid model was output instead.

Twaron® CT709 fabric

The Twaron® CT709 fabric used in experiments are balanced plain-woven with an areal density per ply of 200 g/m^2 and a ply thickness of 0.3 mm. Warp and weft densities were 105 ends/picks per 10 cm and the yarn spacing was set to 0.935 mm. The constitutive yarns are comprised of 1000 Twaron® CT2040 fibers with diameter approximately 12 μm and linear density 93 mg/m. Isotropic matrix properties were set as 0 MPa for the elastic modulus and 0.3 for the local yarn Poisson's ratio. The Twaron® CT2040 material properties are listed below.

$$
\begin{aligned}
E_x &= 90.00 \text{ GPa} \\
E_y = E_z &= 1.168 \text{ GPa} \\
G_{xy} = G_{xz} &= 24.40 \text{ GPa} \\
G_{yz} &= 0.471 \text{ GPa} \\
\nu_{xy} = \nu_{xz} &= 0.6 \text{ [57]} \\
\nu_{yz} &= 0.24 \text{ [57]}
\end{aligned}
$$

The homogenized elastic constants are given as

$$
\begin{aligned}
E_r = E_{11} = E_{22} &= 23.79 \text{ GPa} \\
E_z = E_{33} &= 1.954 \text{ GPa} \\
G_r = G_{12} &= 11.67 \text{ GPa} \\
G_{rz} = G_{13} = G_{23} &= 1.718 \text{ GPa} \\
\nu_r = \nu_{12} &= 0.138 \\
\nu_{rz} = \nu_{13} = \nu_{23} &= 0.596
\end{aligned}
$$

From there, the effective stiffness matrix for a 1 layer Twaron® CT709 fabric is calculated as

$$
C = \begin{bmatrix}
25.25 & 4.35 & 1.45 & 0 & 0 & 0 \\
4.35 & 25.25 & 1.45 & 0 & 0 & 0 \\
1.45 & 1.45 & 2.10 & 0 & 0 & 0 \\
0 & 0 & 0 & 1.72 & 0 & 0 \\
0 & 0 & 0 & 0 & 1.72 & 0 \\
0 & 0 & 0 & 0 & 0 & 11.67
\end{bmatrix} \text{ GPa}
$$

From there, the Q matrix can be calculated via

$$[Q] = [C_e] - [C_{et}][C_t]^{-1}[C_{et}]^T = \begin{bmatrix} Q_{11} & Q_{12} & 0 \\ Q_{12} & Q_{22} & 0 \\ 0 & 0 & Q_{66} \end{bmatrix} \tag{9.14}$$

For the homogenized Twaron® CT709 fabric ply, the C_e, C_{et}, and C_t matrices are defined below. Note that C_{et} is not symmetric.

$$C_e = \begin{bmatrix} C_{11} & C_{12} & C_{16} \\ & C_{22} & C_{26} \\ & & C_{66} \end{bmatrix} \tag{9.15}$$

$$C_t = \begin{bmatrix} C_{33} & C_{34} & C_{35} \\ & C_{44} & C_{45} \\ & & C_{55} \end{bmatrix} \tag{9.16}$$

$$C_{et} = \begin{bmatrix} C_{13} & C_{14} & C_{15} \\ C_{23} & C_{24} & C_{25} \\ C_{36} & C_{46} & C_{56} \end{bmatrix} \tag{9.17}$$

From the above, Q matrix is calculated as

$$[Q] = \begin{bmatrix} 24.25 & 4.35 & 0 \\ 4.35 & 25.25 & 0 \\ 0 & 0 & 11.67 \end{bmatrix} \text{GPa}$$

Since all the fabric plies have the same properties, the ABD matrices are defined as follows, with h as the thickness of the entire fabric target panel.

$$[A] = [Q] \cdot h, \quad [B] = 0, \quad [D] = [Q] \cdot \frac{h^3}{12} \tag{9.18}$$

At this point, the one crucial point that should be noted is that, regardless of homogenization scheme, the effective plate bending stiffness from Equation 9.23 is

inherently dependent on the plate thickness as per Equations 9.18 for the ABD matrices. This coupling makes it difficult to obtain a purely material-based comparison between woven structures of different constituent fibers. However, since all components of the D_{ij} matrix are obtained by multiplying the Q_{ij} matrix by the same factor $h^3/12$. This can be factored out from Equation 9.23 to give a effective parameter Q^* instead, which is calculated as

$$Q^* = \frac{1}{2}\left[Q_{12} + 2Q_{66} + \sqrt{Q_{11}Q_{22}}\right] \tag{9.19}$$

This Q^* can be obtained directly from the stiffness matrix and is independent of the plate thickness, which makes it a simple parameter to relate the macro-scale structural properties to the micro-scale fiber properties. For a Twaron® CT709 fabric comprising CT2040 fibers, Q^* is calculated as 26.22 GPa.

S-2® Glass fiber composite

S-2® Glass fiber composites are typically used for damage mitigation at the strike face. The elastic constants are given by the manufacturer as [60]

$$\begin{aligned} E_r &= 53 - 59 \text{ GPa} \\ E_z &= 16 - 20 \text{ GPa} \\ G_{rz} &= 6 - 9 \text{ GPa} \\ \nu_{rz} &= 0.26 - 0.28 \end{aligned}$$

For a transversely isotropic material, the compliance matrix is given by

$$\begin{bmatrix} \varepsilon_{xx} \\ \varepsilon_{yy} \\ \varepsilon_{zz} \\ \varepsilon_{yz} \\ \varepsilon_{zx} \\ \varepsilon_{xy} \end{bmatrix} = \begin{bmatrix} \frac{1}{E_r} & -\frac{\nu_r}{E_r} & -\frac{\nu_{zr}}{E_z} & 0 & 0 & 0 \\ -\frac{\nu_r}{E_r} & \frac{1}{E_r} & -\frac{\nu_{zr}}{E_z} & 0 & 0 & 0 \\ -\frac{\nu_{rz}}{E_r} & -\frac{\nu_{rz}}{E_r} & \frac{1}{E_z} & 0 & 0 & 0 \\ 0 & 0 & 0 & \frac{1}{2G_{zr}} & 0 & 0 \\ 0 & 0 & 0 & 0 & \frac{1}{2G_{zr}} & 0 \\ 0 & 0 & 0 & 0 & 0 & \frac{1+\nu_r}{E_r} \end{bmatrix} \begin{bmatrix} \sigma_{xx} \\ \sigma_{yy} \\ \sigma_{zz} \\ \sigma_{yz} \\ \sigma_{zx} \\ \sigma_{xy} \end{bmatrix}$$

where $\nu_{rz}/E_r = \nu_{zr}/E_z$. ν_r is assumed to be that of a single fiber in the axial direction and have a value of 0.27. Inverting the compliance matrix to get the stiffness matrix, we can proceed as with the prior materials.

$$C = \begin{bmatrix} 63.03 & 18.94 & 7.11 & 0 & 0 & 0 \\ 18.94 & 63.03 & 7.11 & 0 & 0 & 0 \\ 7.11 & 7.11 & 19.23 & 0 & 0 & 0 \\ 0 & 0 & 0 & 15.00 & 0 & 0 \\ 0 & 0 & 0 & 0 & 15.00 & 0 \\ 0 & 0 & 0 & 0 & 0 & 44.09 \end{bmatrix} \text{GPa}$$

$$Q = \begin{bmatrix} 60.40 & 18.94 & 0 \\ 18.94 & 63.03 & 0 \\ 0 & 0 & 44.09 \end{bmatrix} \text{GPa}$$

Similarly, the corresponding ABD matrix is dependent on ply thickness as per Equation 9.18. The Q^* is calculated as 84.4 GPa.

Fictive CT709 fabric with S2 Glass fibers

To examine the effects of fiber properties on the macro-scale homogenized properties, a fictive fabric with isotropic fibers was modeled in TexGen4SC. Fabric plies are balanced plain-woven with an areal density per ply of 200 g/m^2 and a ply thickness of

0.3 mm. Warp and weft densities were 105 ends/picks per 10 cm and the yarn spacing was set to 0.935 mm. The constitutive yarns are assumed to comprise of 1000 fibers with diameters approximately 12 μm and linear density 93 mg/m. Isotropic matrix properties were set as 0 MPa for the elastic modulus and 0.3 for the Poisson's ratio. The S-2 glass fibers in this case are assumed to have the same mass as the longitudinal fiber properties of Twaron® CT2040. The Q^* value calculated is 50.53 GPa.

$$\begin{aligned} E &= 90.00 \text{ GPa} \\ G &= 34.6 \text{ GPa} \\ \nu &= 0.3 \end{aligned}$$

The elastic constants are then calculated as

$$\begin{aligned} E_r &= 54.27 \text{ GPa} \\ E_z &= 7.668 \text{ GPa} \\ G_r &= 19.29 \text{ GPa} \\ G_{rz} &= 2.956 \text{ GPa} \\ \nu_r &= 0.274 \\ \nu_{rz} &= 0.241 \end{aligned}$$

The effective stiffness matrix for a single layer of isotropic fiber fabric is given by

$$C = \begin{bmatrix} 59.54 & 16.93 & 2.61 & 0 & 0 & 0 \\ 16.93 & 59.54 & 2.61 & 0 & 0 & 0 \\ 2.61 & 2.61 & 7.85 & 0 & 0 & 0 \\ 0 & 0 & 0 & 2.96 & 0 & 0 \\ 0 & 0 & 0 & 0 & 2.96 & 0 \\ 0 & 0 & 0 & 0 & 0 & 19.29 \end{bmatrix} \text{GPa}$$

$$Q = \begin{bmatrix} 58.67 & 16.93 & 0 \\ 16.93 & 59.54 & 0 \\ 0 & 0 & 19.29 \end{bmatrix} \text{GPa}$$

The corresponding ABD matrix is then calculated (depending on ply thickness as per Equation 9.18. The Q^* value for this fictive isotropic fiber woven as a Twaron® CT709 fabric is calculated as 50.53 GPa.

Using these homogenized properties, the nonlinear ODE analysis may now be performed to investigate the material properties of these fibers and the relation to the macro-scale structural properties. It should be noted that the projectile/target behavior considered thus far has been purely elastic, which means that any effects of impact plasticity or target failure have not been considered.

9.4 Two Degree-of-Freedom Model

Shivakumar [130] first proposed a two degree-of-freedom model to investigate the dynamics of the projectile and of the plate's midplane movement. The two DOF system allows for the individual masses to be tracked over the duration of projectile impact. Olsson [126, 127] and Lin & Fatt [129] further modified the model to analyze wave-controlled impact dynamics. In said work, the contact duration is first estimated by assuming that the target is a half-space, and the following equation is solved

$$\begin{aligned} m_p \ddot{\delta} &= -P_{con}(\delta) \\ \delta(0) = 0, \quad \dot{\delta}(0) &= V_p \end{aligned} \tag{9.20}$$

It is then assumed that the total load acting on the target are a combination of the bending load P_{bend}, in-plane membrane stretching P_{mem}, and contact force P_{con}. In reality, many other complicated mechanisms for a multi-ply system are involved, such as transverse shear, in-plane shear, matrix delamination and cracking etc.

$$
\begin{aligned}
m_p \ddot{w}_p &= -P_{con}(\delta) \\
m_t \ddot{w}_p &= -P_{bend}(w_t) - P_{mem}(w_t) + P_{con}(\delta) \\
\ddot{\delta} &= \ddot{w}_p - \ddot{w}_t \\
w_p(0) = w_t(0) = \dot{w}_t(0) = 0, &\quad \dot{w}_p(0) = V_p
\end{aligned}
\tag{9.21}
$$

The selection of loading criteria depends on the duration of contact with respect to the through-thickness propagation duration t_{thru} and the transverse shear wave t_{lat}.

9.4.1 Results of 2DoF model

The through-thickness and through-k fraction thickness durations are also plotted along with the load history curve. For a thin target e.g. a 5-ply Twaron® CT709 fabric 9.1, the contact load duration persists past the through-thickness wave propagation duration, resulting in a transverse wave propagation away from the impact site. During this contact duration, the membrane mode resistive load increases rapidly due to large plate displacements.

At larger η ratios of about 0.3 (corresponding to a 75-ply Twaron® C709 fabric system as in Figure 9.1), the contact duration (approx. 25 μs) lies within both the through-thickness and through-k fraction duration, with a peak contact load of approximately 275 kN. Bending and contact loads are more dominant while the membrane modes do not kick in during the projectile load history due to the thickness. The transverse deflection is small, as evidenced by the normalized plate displacement plot.

In Figure 9.3, for a similar thickness fictive S-Glass fabric (Q^* 50.53 GPa), the contact duration (approx. 14 μs) is slightly longer than the through-thickness duration, but the peak contact load of about 590 kN lies within the though-thickness duration. Bending and contact loads are more dominant while the membrane modes

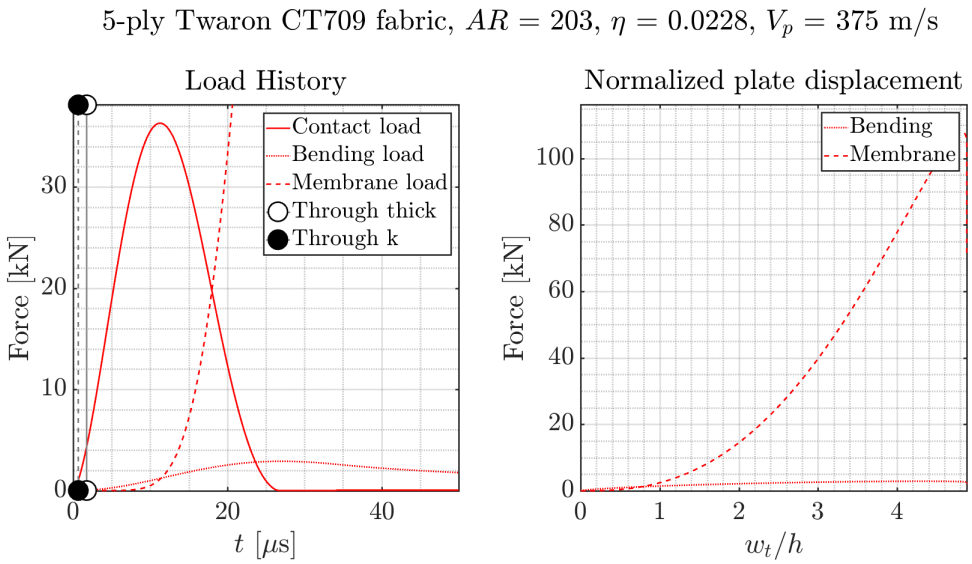

Figure 9.1. Load history of spherical and cylindrical projectile impacting 5-ply Twaron® CT709 fabric.

do not kick in during the projectile load history due to the thickness. The transverse deflection is small, as again evidenced by the normalized plate displacement plot.

The results via the two degree-of-freedom model reveal two observations: firstly, the low areal density ratio systems e.g. 5-ply Twaron® CT709 lie within the "ballistically-thin" regime, where the k-fractions are small and the entire target system behaves as a membrane. On the other hand, past the previously-discussed "ballistically-thin" regime, the target strike-face transverse displacements are small and the contact/bending loads are maximized, resulting in an inelastic response without significant membrane-like response. These effects are now demonstrated by the two degree-of-freedom model.

Secondly, the Q^* values for the fictive S2-glass (50.53 GPa) is about double that of the Twaron® CT2040 systems (26.22 GPa), which may appear to correspond to the contact peak load being approximately doubled for the fictive glass fabric compared to the CT2040 fabric. In contrast, the contact duration is halved, meaning that the

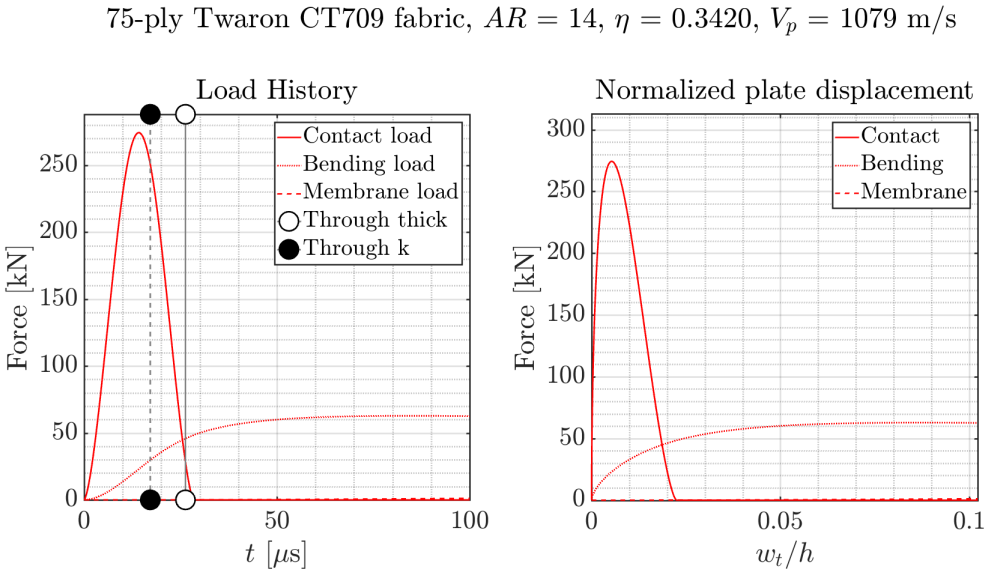

Figure 9.2. Load history of spherical projectile impacting 75-ply Twaron® CT709 fabric.

impulse imparted to the plate is approximately the same in both cases. A better metric of relating the energy-absorption via contact/bending is likely necessary to relate them to the Q^* values.

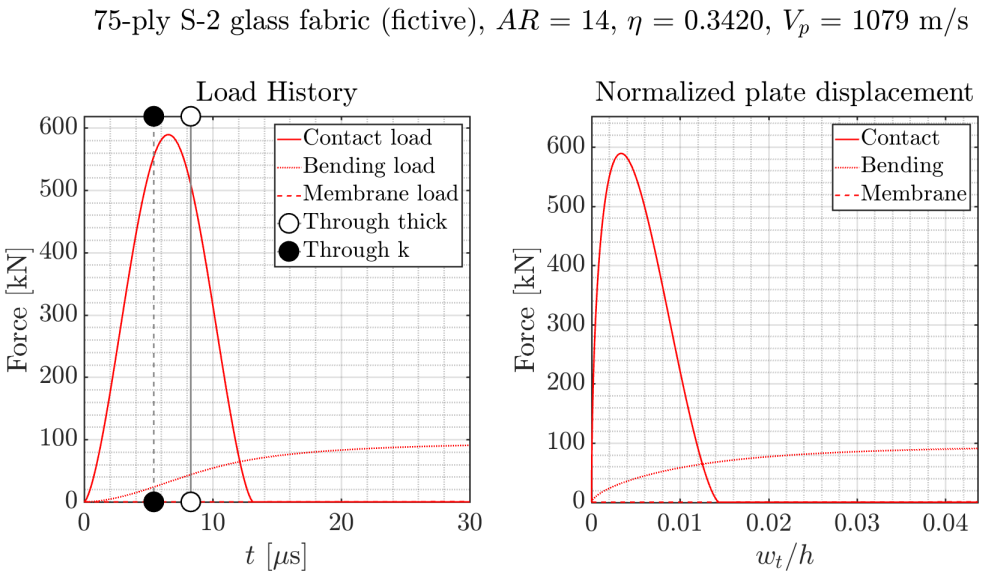

Figure 9.3. Load history of spherical projectile impacting 75-ply S2 Glass fabric.

9.5 Doyle's Single Degree-of-Freedom Model

We note in Lin & Fatt's work [129] that the appropriate loading conditions i.e. P_{con}, P_{mem}, P_{bend} were chosen depending on the contact duration with respect to the propagation duration of different waves as given in Section 9.1. In view of the actual dynamics of the problem, the model may be appropriately simplified to a 1DoF model as proposed by Doyle [131] when considering some simplifying assumptions.

The assumptions put forth are best exemplified by first examining the structural impact response of a Dyneema® HB26 composite panel via post-mortem (Figure 9.4). Firstly, the strike-face k fraction is typically much smaller in the thickness dimension compared to the in-plane dimensions. With this in mind, the strike-face may be modeled as a thin plate. Therefore, loads due to bending shear may be considered negligible as the target may be modeled as a Kirchoff-Love plate.

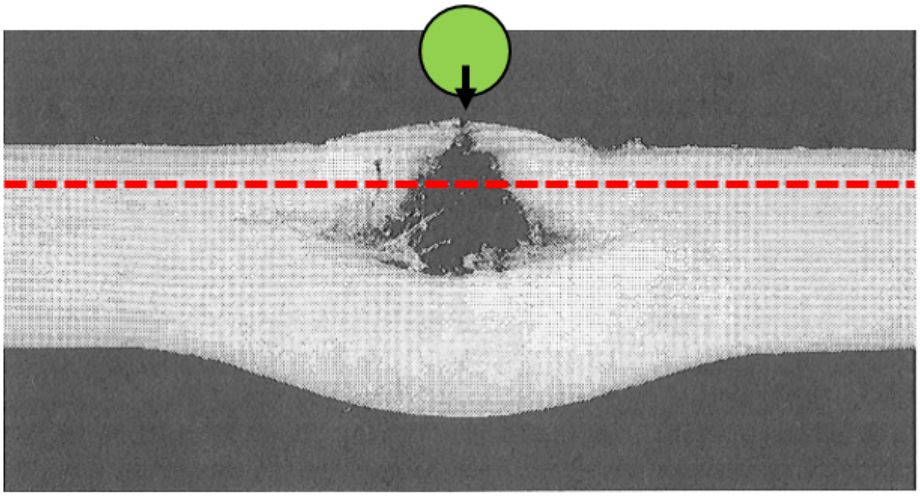

Figure 9.4. Post-mortem cross-sectioning of HB26 composite impacted by FSP [15]. Red dashed line denotes approximate mid-plane of frontal strike-face section.

Secondly, we note that the strike face does not deform significantly in the transverse direction, as evidenced by the approximate midplane. As such, the loads acting on the projectile can be assumed to be just due to projectile-target contact and plate bending, since in-plane membrane loads require large transverse out-of-plane deflections.

Finally, we assume that the entire strike-face k fraction behaves as a monolithic piece i.e. no progressive layer-wise failure. Failure modes may be appropriately employed to better elucidate the over ballistic performance dependence on microstructure properties, but it is out of the scope of the current chapter as a rudimentary analysis on the mechanics and dynamics of the strike-face when being impacted.

$$\begin{gathered} \ddot{w_p} = \ddot{w_t} \\ \ddot{w_p} = -\frac{P_{con}}{m_p}, \quad \ddot{w_t} = \frac{1}{8\sqrt{\rho h D^*}} \dot{P}_{con}(w_t) \\ w_p(0) = 0, \quad \dot{w_p}(0) = V_p \end{gathered} \tag{9.22}$$

In the above equations, ρ is the target density, h is the target thickness, and D^* is the effective plate flexural rigidity defined as

$$D^* = \frac{1}{2}\left[D_{12} + 2D_{66} + \sqrt{D_{11}D_{22}}\right] \tag{9.23}$$

The components D_{ij} are plate bending stiffness matrix components as given in Equation 9.11. For an isotropic plate, D^* reduces to $D = Eh^3/12(1-\nu^2)$. Solving the above set of differential equations gives

$$P(t) = V_p m_p \cdot \mu e^{-\mu t}, \quad w_p(t) = w_t(t) = \frac{V_p}{\mu}\left[1 - e^{-\mu t}\right], \quad \mu \equiv \frac{8\sqrt{\rho h D^*}}{m_p} \tag{9.24}$$

Depending on the parameters of the problem, the equation may be suitably modified to include contact effects. When contact indentation is considered, $\delta = w_p - w_t$ becomes nonzero and the contact load P_{con} is calculated based on the indentation depth and the geometries involved, as will be discussed in subsequent sections. Combining the above equations, we obtain a nonlinear differential equation that can be solved to obtain the behavior of the projectile and the target.

$$\begin{gathered}
\dot{w}_t = \frac{1}{8\sqrt{\rho h D^*}}\dot{P}_{con}(\delta) \Longrightarrow \ddot{w}_t = \frac{1}{8\sqrt{\rho h D^*}}\frac{dP_{con}}{d\delta}\dot{\delta} \\
m_p\ddot{\delta} + P_{con}(\delta) + \frac{1}{8\sqrt{\rho h D^*}}\dot{P}_{con}(\delta) = 0 \\
\Longrightarrow \ddot{\delta} = -\frac{1}{m_p}\cdot k_c \cdot \delta^m - \frac{1}{8\sqrt{\rho h D^*}}\left[k_c \cdot m\delta^{m-1}\right]\dot{\delta} \\
\delta(0) = 0, \quad \dot{\delta}(0) = V_p
\end{gathered} \tag{9.25}$$

In Equation 9.25, the contact response of the plate is governed by $P(\delta)$ and the bending response governed by $\dot{P}(\delta)/(8\sqrt{\rho h D^*})$. These two responses are seen to be coupled in the bending response term. It should be re-iterated that this formulation only works for cases where the plate's transverse displacement is not large enough to initiate in-plane membrane stretching within the target.

9.5.1 Variation of impactor radius of curvature

We first examine the loading trends as the impactor's radius of curvature increases while keeping the impactor mass constant. The behavior of the solutions should transition from being a sphere to being more like a flat cylinder (with radius $R_1 = \infty$). From Figure 9.5, we indeed observe that with an increase in radius, the solution tends towards that of a flat cylinder impacting a plate (as per Equation 9.24). Based on these trends, it suffices to simplify the analyses by looking mainly at the trends of a sphere on plate solution rather than explicitly solving for all the other solutions.

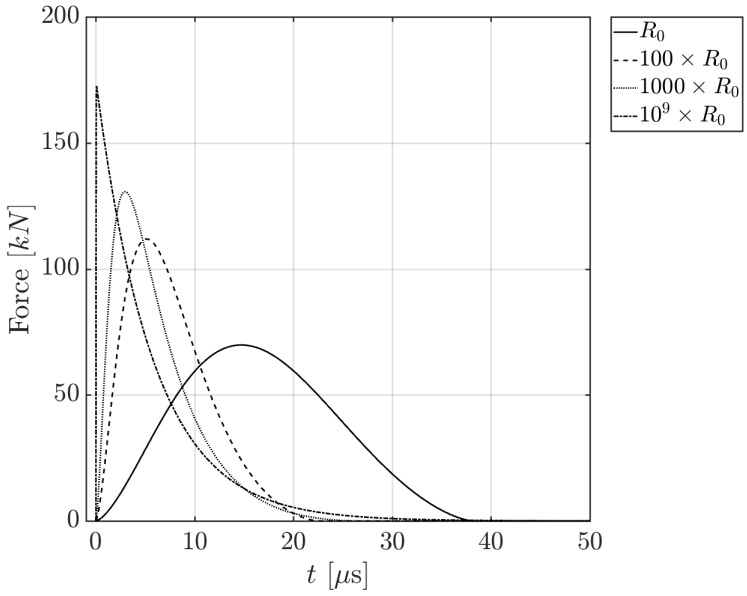

Figure 9.5. Effect of increasing impactor radius while keeping mass constant. The solution converges to that of a cylinder impacting a plate.

9.5.2 Variation of plate properties

From Equation 9.25, the plate bending properties are governed by the coefficient $1/8\sqrt{\rho h D^*}$. With the thin plate assumption, the target plate thickness h cannot be

varied drastically, leaving only plate stiffness D^* as the only parameter that can be easily varied without violating the assumptions. With an increase in target bending stiffness, the normalized contact load P_{con}/P_0 converges to the solution of a sphere impacting a solid half-space; on the other hand, as the target bending stiffness is drastically decreased, the contact load acting on the projectile decreases as well.

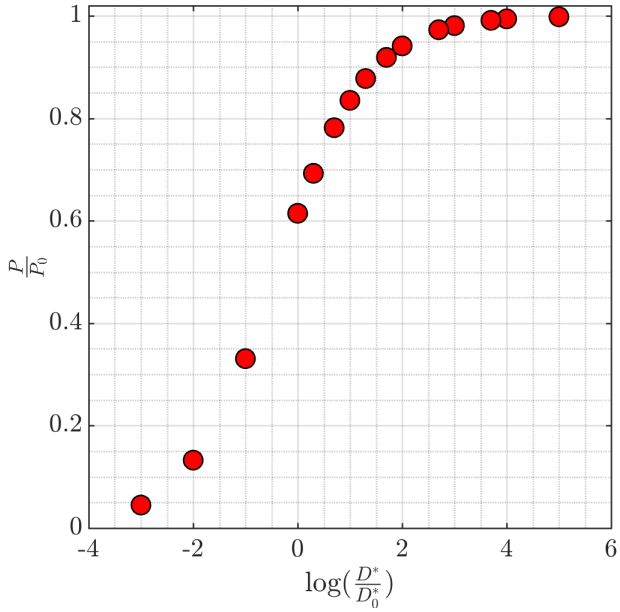

Figure 9.6. Variation of normalized contact load P_{con}/P_0 with D^*.

Although the plate thickness cannot be varied significantly in order to preserve the thin plate assumptions, the dependence of the coefficient $1/8\sqrt{\rho h D^*}$ on the thickness h is the same as the dependence on the plate stiffness D^*. As the thickness goes to infinity, the contact load converges to that of a half-space indentation; as the thickness goes to zero, the contact load effectively goes to zero due to the load being carried mainly via plate deflections (almost like a membrane). Granted, different formulations are required for membrane and thick plate bending, but the trends still correspond nonetheless to physical observations.

9.5.3 Results of 1DoF model

Although it was previously shown that modeling a sphere impacting a plate suffices for a trend study, the results for a flat cylinder impacting a plate has also been included in the calculations as a comparison to show that the projectile load histories are extremely similar. The energy over the entire contact duration may be approximated by Equation 9.26. The nonlinearity of the contact load and plate deflection require the total energy to be step-wise integrated via MATLAB® .

$$E_{con} = P_{con}(\delta) \cdot w_t, \quad w_t = \frac{1}{8\sqrt{\rho h D^*}} P_{con}(\delta) \tag{9.26}$$

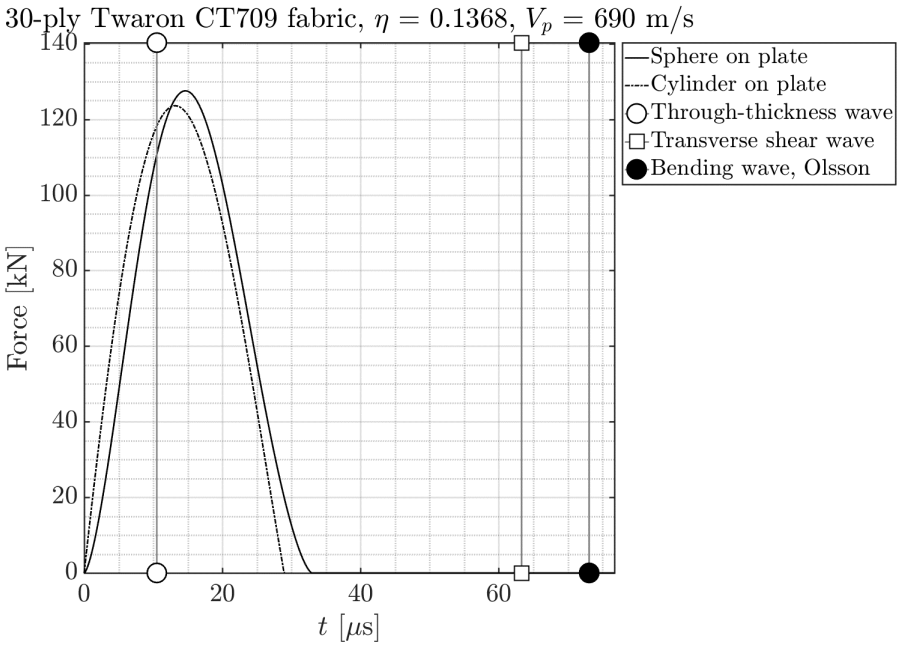

Figure 9.7. Load history of spherical and cylindrical projectile impacting 30-ply Twaron® CT709 fabric.

When comparing two systems of the same areal density impacted by a spherical projectile with a V_p of 690 m/s, the peak loads for a 30-ply Twaron® CT709 fabric

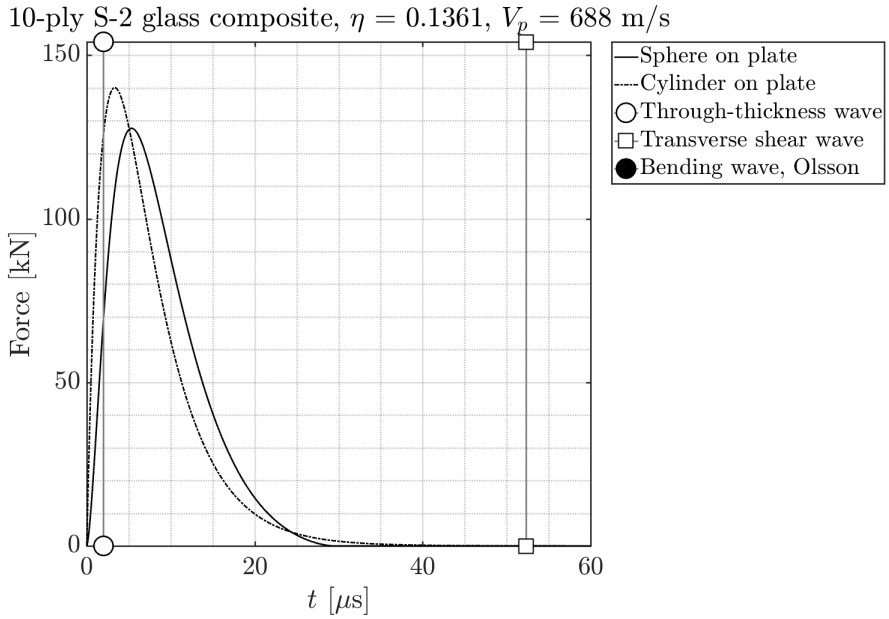

Figure 9.8. Load history of spherical and cylindrical projectile impacting 10-ply S2 Glass fabric.

(Q^* 26.22 GPa) and a 10-ply S2 glass composite (Q^* 84.42 GPa) are similar at about 125 kN. However, the 10-ply glass composite results in a longer contact duration due to a thinner target. The impinging kinetic energy is approximately 475 J for both systems; the plate bending energies are approximately 280 J and 187 J for the 30-ply Twaron® and 10-ply S-2 glass composite respectively.

In comparison to the 30ply Twaron® CT709 fabric, a 30-ply fictive comprising S2-glass fibers (Q^* 50.53 GPa) exhibits a contact response with half the contact duration (15 μs) but exactly double the load (250 kN), which means that the total impulse imparted to the plate is the same. However, the fictive fabric gives a total contact energy of 354 J for the same striking kinetic energy.

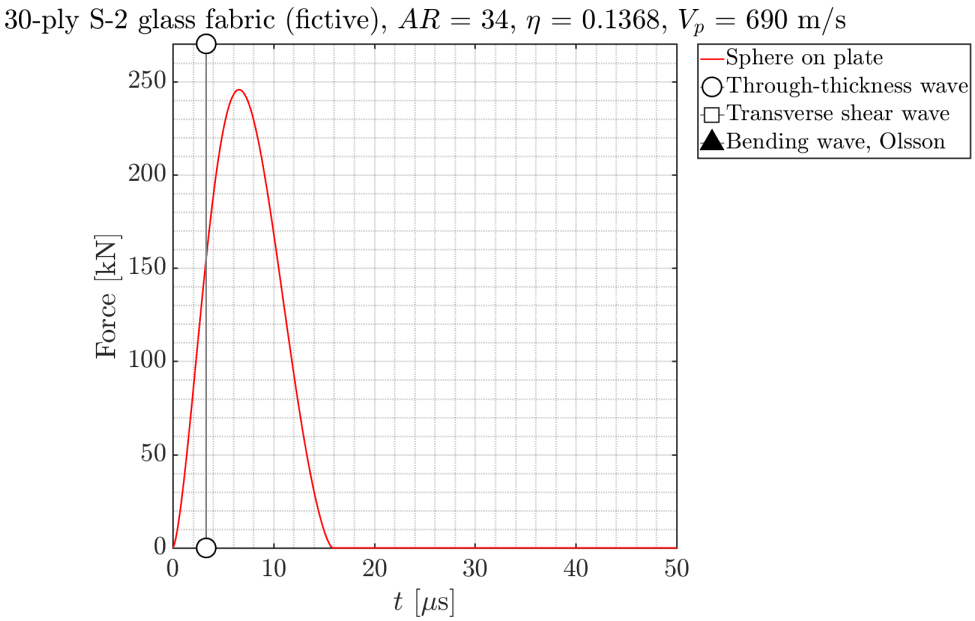

Figure 9.9. Load history of spherical projectile impacting 30-ply fictive S-2 glass fabric.

9.6 Conclusions

In this chapter, we took a more analytical approach via solution of a nonlinear ODE and further examining the timescales of impact response. At the initial time of impact before through-thickness waves have reflected off the rear surface, the load response is dominated by contact indentation by the projectile. At longer timescales when the through-thickness waves have reflected several times, transverse waves and bending waves begin propagating towards the boundary of the target plate. It is during this regime that projectile kinetic energy is dissipated more effectively away from the impact site. At much longer timescales when the bending/transverse waves have reflected several times off the boundary, the plate response is effectively quasi-static.

To investigate the relationship between micro-scale fiber properties and macro-scale structural properties, constituent fiber properties were homogenized via Tex-

Gen4SC to obtain equivalent ABD matrices for the fabric plies. Transverse properties of the fibers were obtained via previous transverse compression experiments. Preliminary results show that a transversely stiffer constituent fiber results in a higher overall plate bending stiffness. The main effect of this stiffer plate is to increase the contact force acting on the projectile, and to sufficiently slow down the projectile before it reaches the rear portion. A higher transverse stiffness also results in a faster through-thickness wave speed, and so the contact indentation response is not as dominant. The plate response, instead, is dominated by transverse waves propagating away from the impact site, which more effectively dissipates the impact energy. Understanding the relation between the micro-scale fiber properties and macro-scale structural properties allows us to gain a better understanding of optimizing the material choice for the target strike-face.

10. PUTTING IT ALL TOGETHER: EXAMINING THE CONSTRUCTION OF COMPOSITE ARMOR SYSTEMS

In this chapter, we examine how the design concepts discussed in prior chapters are exemplified in two composite armor constructions: the ARL X Hybrid [32] and a typical bi-material bullet-resistant vest.

10.1 Level IIIA bullet-resistant vests

This section examines the construction of a bi-material Type IIIA bullet-resistant vest. This type of construction is typical of some of the vests that were sent to us by different law enforcement agencies such as the Federal Bureau of Investigation and police departments. The construction of an NIJ-0101.08 [70] Level IIIA bullet-resistant vest incorporates a frontal aramid portion backed by a portion of UHMWPE UD laminate plies.

Figure 10.1. Level IIIA vest (without ceramic insert) manufactured by Custom Armor.

Frontal portion

The frontal portion of a Level IIIA system is made of a woven fibrous Kevlar® KM2/aramid system. The areal density of this fibrous woven portion is 3.297 kg/m^2 and stitched together in the z-direction (i.e. through-thickness) to increase its bending stiffness. This portion also improves resistance against spinning bullets via entanglement and engagement of the fibrous material at the strike face.

Rear portion

The rear portion comprises 21 Dyneema® SB31 plies, each ply being a $[0°/90°]_2$ laminate. The total areal density of the rear portion is 2.764 kg/m^2. The smooth laminates are unstitched in the z-direction to reduce bending stiffness and promote more membrane-like in-plane movement to improve energy dissipation via strain energy.

System-level construction

Some typical threats that Level IIIA vests face are 44-cal Magnum Semi-Jacketed Hollow Point (SJHP) bullets and 9-mm Full Metal Jacket (FMJ) bullets. Bullet masses are 15.5 and 8.0 g. Based on the total estimated areal density of the vest, the η ratio is 0.036 and 0.048 for the .44 Magnum SJHP and 9 mm FMJ respectively.

Dyneema® is placed at the rear because of its higher Cunniff velocity of 801 m/s compared to Kevlar® KM2 of about 682 m/s. This stacking order reduces interference between the two phases in order to optimize the ballistic performance of the system with regards to the ballistic limit velocity and backface deformation. The higher Cunniff velocity of the rear Dyneema® portion also promotes more efficient strain energy dissipation from the impact site compared to the aramid front portion.

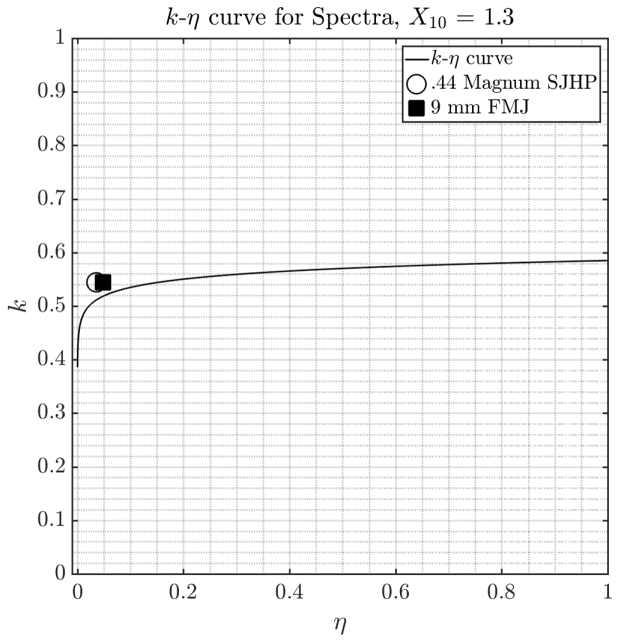

Figure 10.2. k-η curve for Spectra with Level IIIA vest data points plotted.

Based on the areal masses of both phases, the k fraction of the Custom Armor vest is 0.544. Calculating the k-η curve for UHMWPE shows that the actual vest k

value falls close to the k value predicted by the curve. Note that Spectra® is used in Figure 10.2 due to lack of ballistic data for Dyneema® SB31.

10.2 ARL X Hybrid

Construction & testing

The ARL X Hybrid [32] architecture incorporates two separate constructions of Dyneema® HB26 UD laminates. The frontal strike face is a 75% by areal mass layer of cross-ply ([0°/90°]) laminates. The remaining 25% of the rear consists of a quasi-isotropic layup, with every two succeeding plies rotated 22.5°clockwise with respect to the previous orientation ([0°/22.5°/45°/67.5°/90°]). All panels were constructed with a nominal areal density of 7.8 kg/m^2. For V50 ballistic limit determination, panels were impacted by .22-cal 17-grain FSPs; for BFD measurements, panels were impacted by 124-grain 9 mm FMJ rounds.

Frontal portion compressive strength

O'Masta et al. [132] found that the compressive strength of cross-ply laminates is much higher for [0°/90°] cross-ply laminates compared to laminates rotated at a smaller angle each ply, resulting in a higher overall compressive toughness (Figure 10.3). This compressive strength is directly correlated to the their resistance to ballistic penetration.

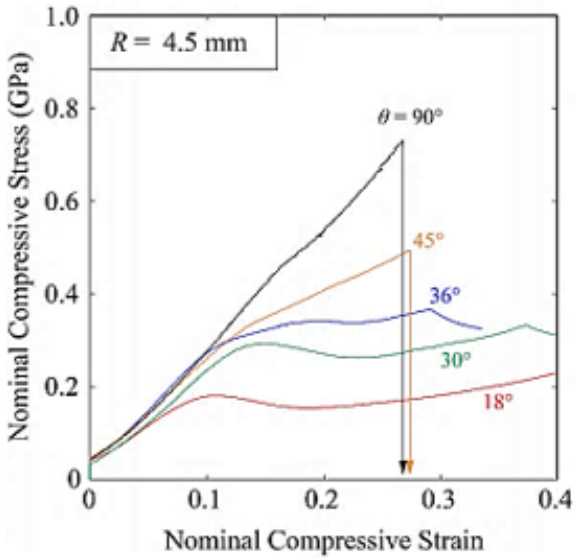

Figure 10.3. Transverse compressive strength of Dyneema® HB26 composites with different layup angles [132].

Rear portion strain energy dissipation

Wang et al. [133, 134] showed experimentally and numerically that rotated plies result in better energy absorption of the system. This statement was similarly echoed by O'Masta et al. [132] in a later work, who stated that "fiber-reinforced laminates with an inter-ply angle $\theta < 90°$are of interest for ballistic resistance due to their reduced back face deflections when transversely impacted in comparison to traditionally implemented cross-ply ($\theta = 90°$) laminates."

This was verified for the X Hybrid architecture via DIC performed on the rear surface of the target system [135] (Figure 10.5). Vargas-Gonzalez explained that in a [0°/90°] construction, the principal directions carry most of the load, as the DIC images show that strain energy along these directions is maximal. With the ply orientations changing every few plies, the construction is effectively quasi-isotropic (Figure 10.5), and the strain energy is spread out over a larger area rather than only along the principal 0°/90°directions.

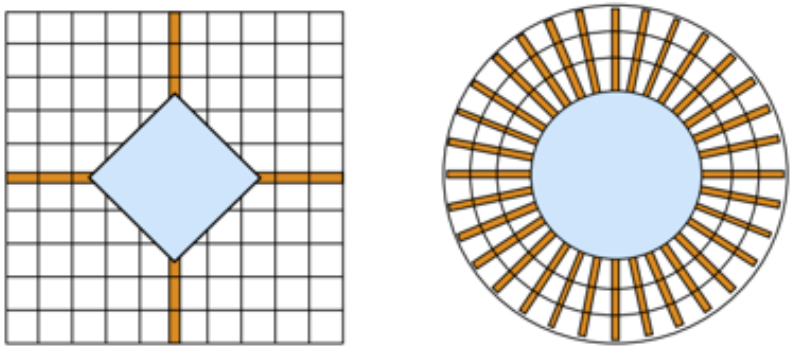

Figure 10.4. Schematic of effect of ply orientation on rear portion deformation field [134].

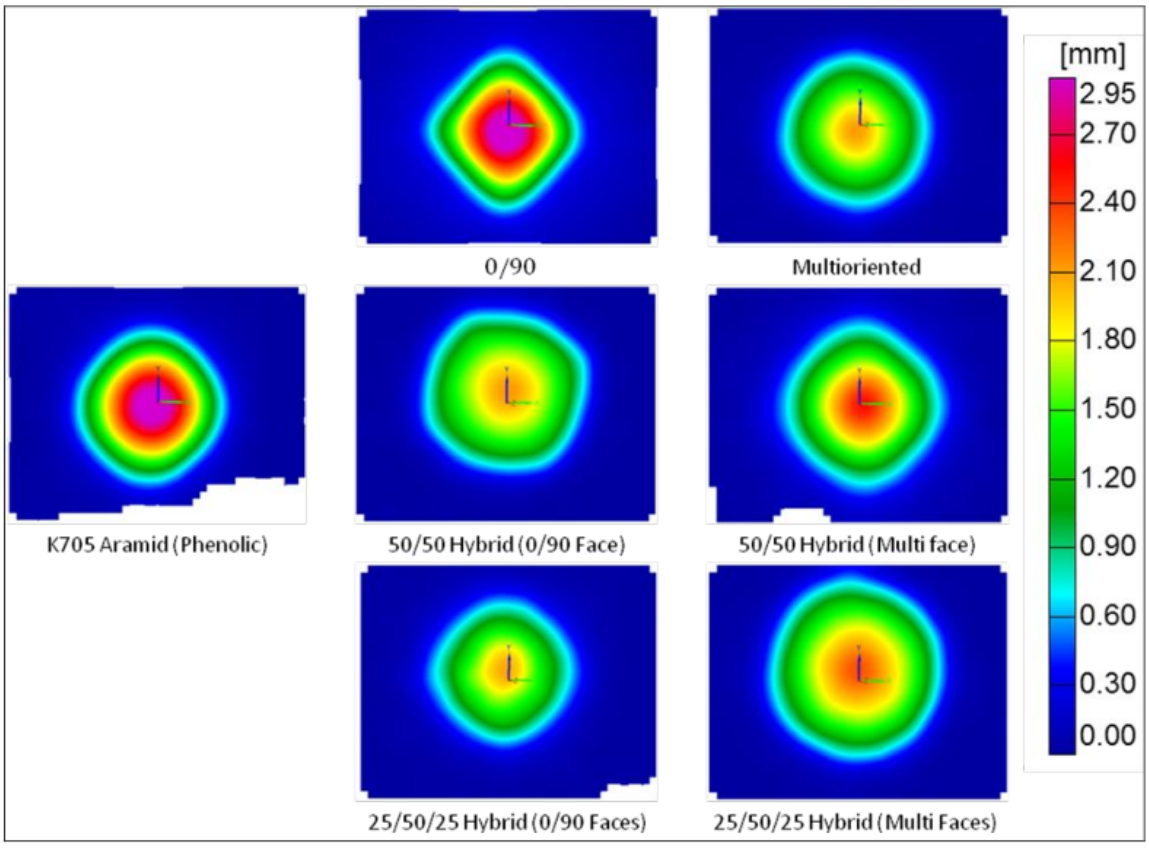

Figure 10.5. Rear face deformation in hybrid target samples obtained using DIC [135].

System-level construction

The η fraction of the 7.8 kg/m^2 system impacted by a 17-grain .22-cal FSP is 0.18. The k-fraction is assumed to be 0.75 based on the construction of the strike and rear phases of the armor system. This k-η point lies close to the optimal curve obtained in Chapter 7 for Dyneema® HB26.

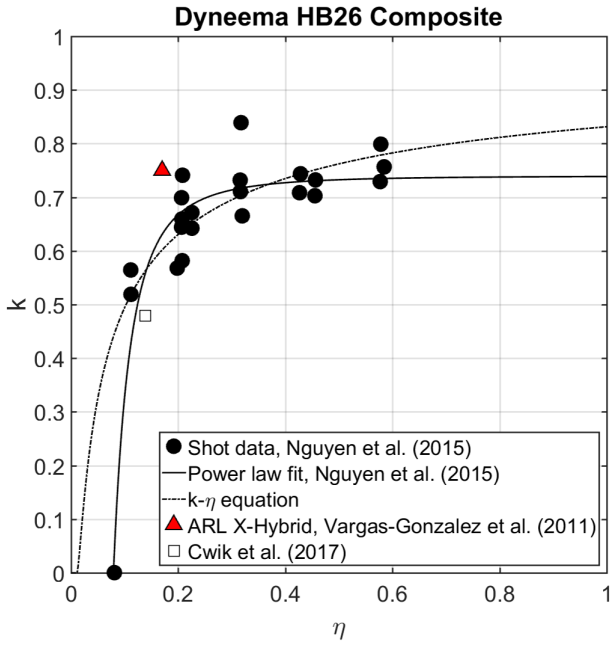

Figure 10.6. $k - \eta$ curve of Dyneema® HB26 composites.

System ballistic performance

Vargas-Gonzalez [32] et al. showed that this X Hybrid construction exhibits the optimal ballistic performance with regards to the ballistic limit performance (V50) and the backface deformation (BFD), as in Figure 10.7.

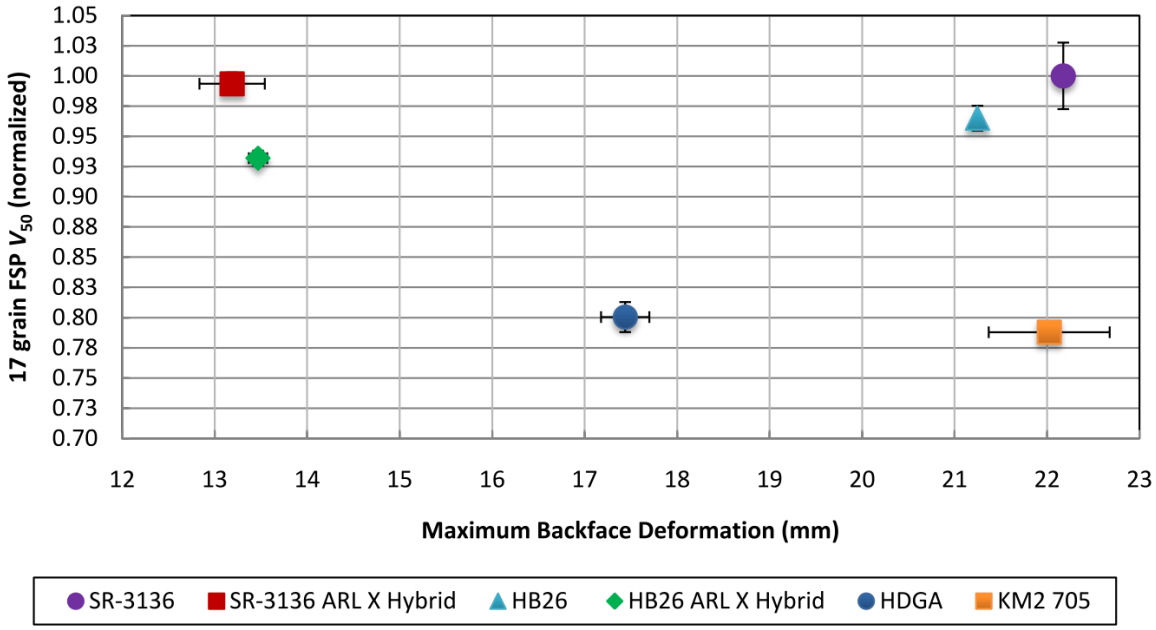

Figure 10.7. Ballistic performance of ARL X-hybrid comparing V50 and BFD metrics across different configurations [32].

10.3 Conclusions

This chapter qualitatively discusses at the concepts from prior sections by examining the construction of two different armor systems: a Custom Armor Level IIIA bullet-resistant armor system (sans ceramic insert) and the ARL X Hybrid architecture typically used in helmet construction. The stacking order, inelastic strike face fraction k, and the strike face design and constituent material choice were briefly discussed.

Experiments on ballistic impact of other materials

This part is a collection of the works stemming both directly and indirectly from the experimental studies performed on the materials detailed in the prior volume. In the pursuit of determining the criteria and parameters that optimize the ballistic performance of soft body armors, alternative materials and interesting phenomena were further investigated.

Prior chapters noted the occurrence of a particularly interesting phenomenon where a transient flash occurs when a steel cylinder impacts Twaron® aramid fabric. This flash has been previously observed by other authors when impacting UHMWPE laminates [87], and was attributed to the shock response of the polyurethane matrix.

11. USING MECHANOLUMINESCENCE AS A LOW-COST, NON-DESTRUCTIVE DIAGNOSTIC METHOD FOR IMPACT PROCESSES

Chapter adapted from prior published work. Z. Guo and W. Chen, Using mechanoluminescence as a low-cost, non-destructive diagnostic method for transient polymer impact processes, J. Meas. doi:10.1016/j.measurement.2019.107173.

Abstract

At ballistic velocities, certain polymers such as nylon and polyethylene have been shown to exhibit mechanoluminescence (ML) upon impact. This ML event results in the emission of photons in the visible wavelength spectrum and may occur on transient timescales as short as a sub-microsecond. In this study, we take advantage of this ML phenomenon to design a low-cost diagnostic tool by recording the ML emissions. The design consists of photodiodes of spectral range in the near-infrared to visible spectrum located radially in order to record the luminescence emissions around the circumference of the ML footprint during impact. Ultra-high molecular weight polyethylene rods were fired at velocities between 200-450 m/s as preliminary proof of concept experiments. Recorded signals were post-processed to yield information such as the projectile's time-of-arrival, approximate impact location, and approximate attitude during initial impact. The experimental setup, measurement and post-processing techniques, and reconstruction results are detailed and discussed in this work.

11.1 Introduction

The deformation of certain solids may result in the emission of particles such as electrons [136–138], positive ions (PIE), or photons. Since the 1980s, Dickinson *et al.* have published a large volume of work examining the fracto-emission of polymers under various conditions [139–146]. Weak electron and photon emissions were observed during the onset of material plastic yielding, indicating that inter-chain bond-breakage is occurring due to the polymer chains sliding over and past one another. Mechanoluminescence refers to a specific type of emission where photons in the visible range of the electromagnetic spectrum are produced when certain solids undergo deformation. In this study, we take advantage of this mechanoluminescence phenomenon to design an auxiliary experimental setup for obtaining information such as time-of-arrival and impact attitudes using an emission-based setup. With this setup, external systems could be reliably triggered to within tens of nanoseconds. In this particular work, the emission intensity signal was used to trigger high-speed imaging equipment in order to capture the impact event at relatively high frame rates of 10 million frames per second (10 MHz). Furthermore, since high-speed cameras only offer a two-dimensional image from one direction, projectile impact characteristics such as compound yaw and shot location in the plane of impact are not easily observed. The compound yaw and shot location of projectile impact may be verified by using additional cameras or mirrors placed orthogonally. However, the former tends to be an expensive investment, and mirrors may not be viable due to factors such as limited space. In the current work, we present a non-destructive, non-interfering method to obtain information on transient impact processes. While other robust and precise diagnostic methods do exist, the attractiveness of this setup lies in its extremely low cost, modular versatility, and ease of use.

A previous study by Bonora *et al.* [147] showed that impacting nylon rods on a steel anvil under ambient conditions produced luminescence of high intensity. Similarly, we focus on Taylor impact experiments of polymer rods in the current work as a proof of

concept to demonstrate some of the capabilities that this setup offers. The emission intensity signals were post-processed to yield a statistical map to give an idea of the impact location and characteristics. Although experiments were limited to Taylor impact tests in this work as they were the most straightforward to perform, this setup may be used for any other experiments where luminescence emissions may be expected. Previous studies have shown that mechanoluminescence is emitted when polymer targets such as Kevlar® fabric [76] and Dyneema® UHMWPE (ultra-high molecular-weight polyethylene) composite targets [20, 87, 88] were impacted at ballistic velocities.

11.2 Materials & Methods

11.2.1 Luminescence intensity measurement

For luminescence measurement, PIN photodiodes (Osram SFH 213) were used for their low cost and ease of availability. Photodiodes with a spectral wavelength range of 400-1100 nm were used as near-infrared (NIR) emissions were expected, but the versatility of this setup allows for the user to choose appropriate photodiodes and sensitivity values based on their respective experimental parameters. The photodiodes have a rise time of 5 ns, active area of 1 mm^2, and a half-angle of 10°. Due to low signal-to-noise ratios when using just a photodiode/resistor circuit, a variable DC power supply (Tektronix PWS2185) set to 9 V and an NPN transistor (2N2222) were used to amplify the output signal, which was captured using a Tektronix MDO3014 oscilloscope at a sampling rate of 2.5 GHz. The circuit diagram is given in Figure 11.1. The resistors R1 and R2 in Figure 11.1 have values of 1 kΩ and 560 Ω respectively, but quantities and specifications may be changed as individual experimental conditions dictate. Although not used in this study, phototransistors may also be used instead for faster response time with sufficient resolution to resolve any small peaks, as well as reduce the number of components.

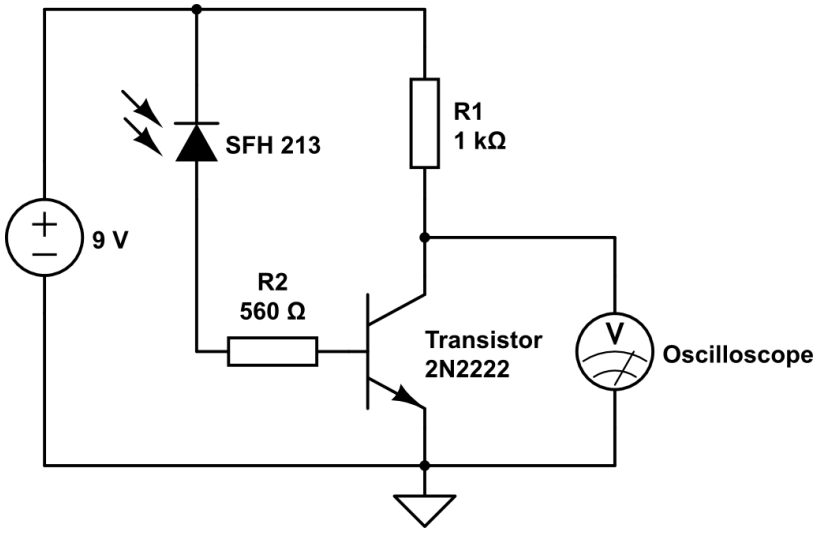

Figure 11.1. Schematic of photodiode circuit with NPN transistor and oscilloscope output. Schematic drawn using CircuitLab.

Several diodes are required to measure the luminescence around the whole circumference of the impacting rod. In the current set of experiments with smaller rod diameters, we find that three photodiodes were sufficient to capture the luminescence intensity around the entire circumference of the rod during impact (Figure 11.2). To achieve this, custom diode mounts made from Delrin® acetal were used to hold the photodiodes. Through-holes were drilled through the Delrin® screws and the diodes slotted and secured with epoxy within the hole. Threaded through-holes were then positioned in an equiangular fashion of 120° spacing around a steel shaft collar of inner diameter 50.4 mm (2 in.). To protect the diodes and the camera lens from impact debris, a thin polycarbonate sleeve of thickness 1.5 mm was slotted within the shaft collar. This modular system allows for easy replacement of the diodes and polycarbonate sleeve, which was especially prudent considering that the setup is placed at the impact site.

The shaft collar assembly was then fixed on a rotary optic mount (Edmund Optics) to allow for minute angular adjustments so that the diodes were positioned at the 0°, 120°, and 240° positions in line with the polar axis. Although not used in this

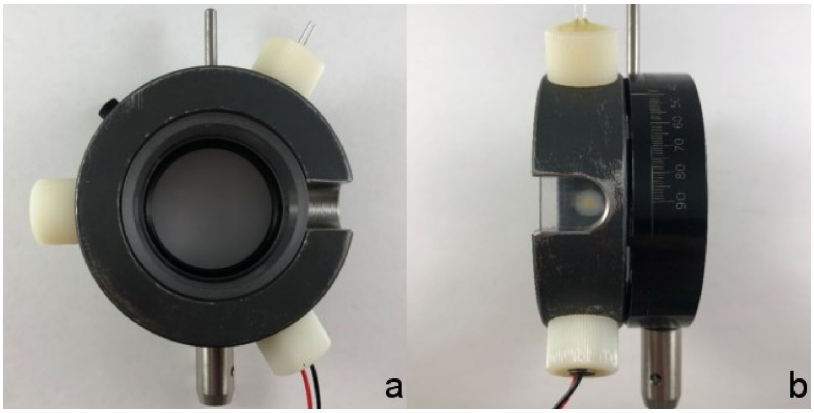

Figure 11.2. (a) Rear view of setup showing Delrin® diode mounts at various stages of connection; and (b) side view of setup looking through the viewport.

particular study, a channel half the width of the shaft collar was slotted to act as a viewport for high-speed imaging from the perpendicular axis, if desired. The rotary mount therefore also allows the shot axis to be fully visible through the viewport. The entire setup was then secured on an optical post via the base of rotary optic mount and the shaft collar was positioned flush with the target block. The height of the setup was accurately aligned with collimated lasers to ensure concentricity of the shaft collar assembly with the shot axis. Prior to experimentation, an LED located at the center of the diode mounting ring was used to ensure that the diodes collect the same amount of information given the same concentric source.

11.2.2 Ballistic impact setup

UHMWPE polymer rods of 50.4-mm (2.0 in.) length were cut and faced from 6.35-mm (0.25 in.) diameter rod stock. A single-stage smooth-bore light-gas gun was used to propel the polymer rods using helium at striking velocities between 200-420 m/s. Striking velocities were measured using a series of in-house laser diodes. High-speed images were recorded with a Shimadzu HPV-X2 camera placed perpendicular to the shot axis at the impact location. To verify the impact attitude of the polymer rods in

relation to the diode signals, a series of experiments were done with a 25.4-mm thick Makrolon® polycarbonate block in place of a rigid target block that is more typical of Taylor impact experiments. The high-speed camera was then mounted behind the polycarbonate block to observe the evolution of luminescence at the impact face.

It should also be noted that the specifications (viz. spectral response) of the camera's FTCMOS2 detector are likely proprietary and therefore not completely available. Without prior knowledge of the spectral response, it is assumed to be at least within the typical visible range of about 380-740 nm, which is well within the spectral range of the SFH 213 diodes (400-1100 nm). Therefore, any emissions captured by the camera's detector will also show up on the diode signals, except in the unlikely case where high energy violet/ultraviolet photons are emitted during impact. Nonetheless, camera parameters and settings were kept the same shot to shot for consistency.

11.3 Results & Discussion

In all impact experiments, visible light emission was observed to initiate from the impact end of the polymer rods (Figure 11.3), which was captured by the high-speed camera showing an emission duration range of up to 5 μs. Previous experiments by Bonora *et al.* [12] captured the luminescence of nylon with a framerate of 40 kHz; in the current work, the ML phenomenon was recorded at 10 MHz unless stated otherwise.

In this study, three diodes were sufficient to capture the emission of photons around the circumference. As the projectile impacts the rigid target, the emitted luminescence is captured by the photodiodes and the corresponding signal is recorded by the oscilloscope, as in Figure 11.4. The luminescence intensity signal rises rapidly to a peak before decaying exponentially over a longer period of time [148]. In the current work, the absolute peak magnitudes in relation to the impact parameters are not studied, as they are better left to a future work focusing on this aspect of ML.

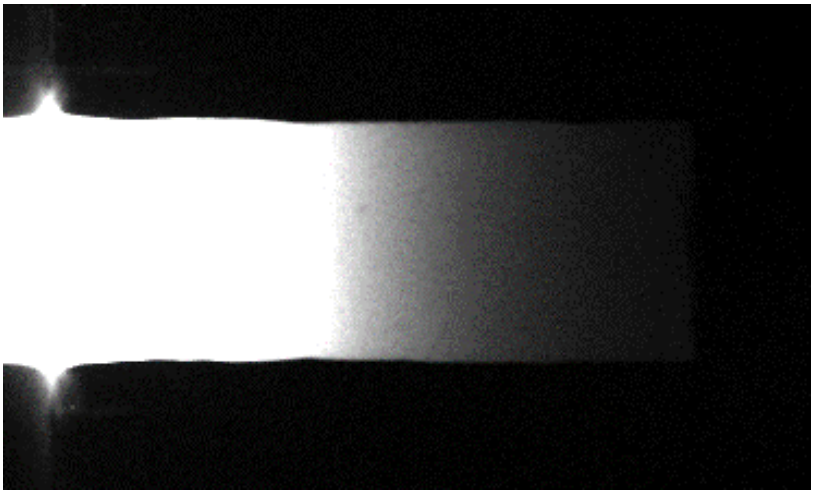

Figure 11.3. Image of ML phenomenon occurring in UHMWPE rod during the initial phase of Taylor impact, impact velocity 272 m/s and 200 kHz framerate. ML is observed to initiate at the impact end of the rod and propagating towards the rear end.

This rise in the intensity signal may be used to trigger an external system — in this case, a high-speed imaging system.

11.3.1 Time-of-Arrival (TOA) determination

The high-speed camera records a fixed number of frames, which means that the total recording time is dependent on the frame rate. At a relatively low frame rate of 1 kHz (1,000 frames per second), the total recording time is 256 ms; at the maximum frame rate of 10 MHz (10 million frames per second), the total recording time is a mere 25.6 μs. This extremely short duration of recording requires a precise method of triggering. Prior to the setup described in the current study, the output signal from the laser diodes for velocity measurement were also used as a trigger signal for the camera. This previous method is only fairly reliable for lower recording frame rates due to longer recording durations to ensure that the impact event is captured. Moreover, since the laser diodes are located a certain distance away from the anvil, triggering the camera off the laser signal requires recalculation of trigger delay times

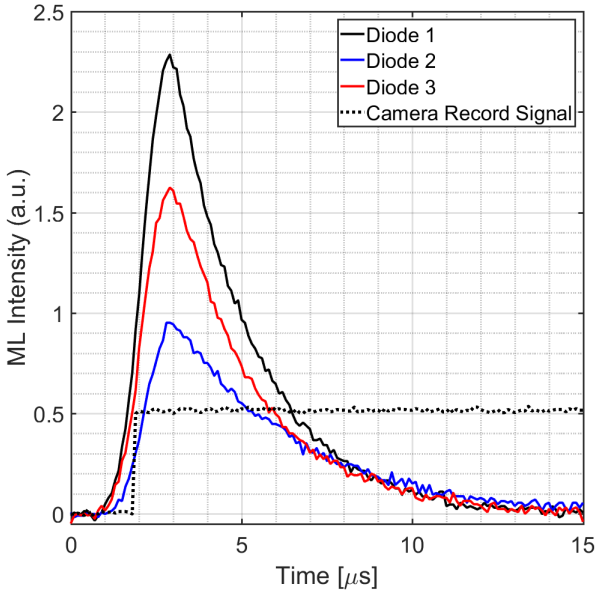

Figure 11.4. Mechanoluminescence intensity signals from the three photodiodes during the transient luminescence process. High-speed camera was triggered using photodiode signals.

based on projectile velocity. The uncertainties in actual projectile arrival are further compounded by drag forces acting on the projectile, which are again dependent on striking velocity and minor perturbations during flight.

By contrast, using the current technique of triggering the camera off luminescence emissions, high-speed images could be recorded reliably without the need for guesswork in setting camera trigger delays. Furthermore, since the impact luminescence occurs at the instance of impact, the luminescence peak measured by the diode would give the time of arrival of the projectile with the target accurate to within the rise time of the diodes being used (5 ns in this case). This diode luminescence signal was output to the oscilloscope, which subsequently triggers the HPV-X2 camera for recording. High-speed images were captured reliably at 10 MHz via this method. If only an auxiliary triggering method is desired, a single diode instead of a full circular array may be used, further lowering the cost of experimentation.

11.3.2 Obtaining approximate impact location and attitude from luminescence signal

To verify the impact location of the projectile with respect to the diodes, high-speed images were captured from behind the clear target block in line with the shot axis. However, the low exposure time of 50 ns at 10 MHz framerate typically resulted in under-exposed image sequences, with only sufficient exposure time to capture the impact flashing phenomenon as it occurs (Figure 11.5a). External light sources may be used to illuminate the impact site, but the luminescence footprint would be washed out due to over-exposure, and the photodiode signal would be inadvertently skewed as well. To overcome this issue, a static shot of the diode ring setup captured using longer exposure times (Figure 11.5b) was overlaid on the luminescence image to create a composite image, as in Figure 11.5c. This allowed for a comparison of the captured images with the recorded diode signals.

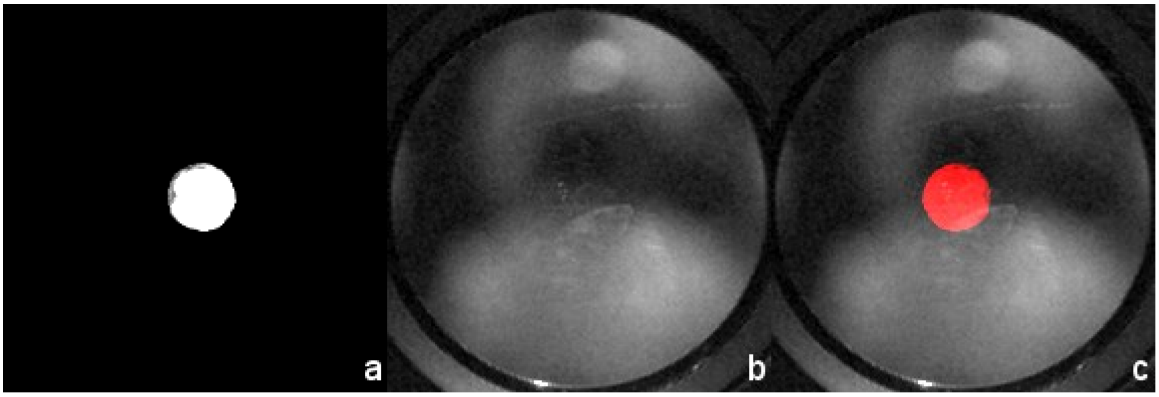

Figure 11.5. (a) High-speed camera image still of luminescence upon impact, and (b) static shot of diode setup at impact end with external lighting. Both images were merged together in ImageJ to create a composite image (c) to allow for determination of actual projectile shot location and impact attitude.

The captured luminescence peak magnitudes and their relative times give an approximate indication of the accuracy and attitude of the projectile upon impact.

Consider an ideal rod impact with zero yaw and perfect concentricity with the shot axis: at the time of impact, the luminescence profile of the impact footprint would resemble a perfect circle throughout the whole process, since the entire circular face of the rod impacts the block. This luminescence signal would then be captured by the photodiodes at the exact same time with the exact same magnitude, giving three diode signals that would lie on top of each other.

In the case of a zero-yaw off-axis (i.e. non-concentric) impact, the luminescence should occur at the exact same time since the impact profile is still perfectly circular. However, due to the differences in relative distances from the three diodes, the signal peaks would have differing magnitudes depending on the shot location. An example of such a case is shown in Figure 11.4. On the other hand, a yawed projectile with perfect shot accuracy would have its tilted edge impacting the target first before the rest of the strike face catches up, resulting in a crescent-shaped initial luminescence profile along the impacted edge that gradually evolves to a slight ellipse in the plane of yaw. In this compound yaw case, the photodiode signal peaks would occur at slightly different times but with similar magnitudes.

The relative strengths of the photodiode signals may be represented graphically to give a clearer picture of the impact process. Electrical noise from the intensity signals were first filtered using a Fast Fourier Transform to more clearly discern the actual intensity signal. The intensity signal values at each point in time were then plotted on a complex Cartesian grid with respect to each diode's angular location (i.e. 0°, 120°, and 240°) centered at the origin. The centroid of the three points was then calculated using the following equations

$$x_{c,k} + i \cdot y_{c,k} = \frac{1}{3}[V_1 \quad V_2 \quad V_3]_k \cdot \left(\cos \begin{bmatrix} 0^\circ \\ 120^\circ \\ 240^\circ \end{bmatrix} + i \cdot \sin \begin{bmatrix} 0^\circ \\ 120^\circ \\ 240^\circ \end{bmatrix} \right) \tag{11.1}$$

$$r_k = \sqrt{x_{c,k}^2 + y_{c,k}^2} \tag{11.2}$$

$$\overline{r}_k = \frac{r_k}{max(r)} \tag{11.3}$$

$$\theta_k = tan^{-1}\left(\frac{y_{c,k}}{x_{c,k}}\right) \tag{11.4}$$

where x_c and y_c are the Cartesian coordinates of the centroid, V_1-V_3 are the signal values for diodes 1-3, and the subscript k denotes the instantaneous value at a particular point in time. Equation 11.3 normalizes the centroid radial coordinates by the absolute maximal diode signal value obtained through the whole process. This was necessary to eliminate the dependence of the centroid radial values on the striking velocity of the polymer rod, as it is not the focus of the current study. The normalized centroid polar coordinates were then plotted on a polar scatter plot using MATLAB, with the time history of the luminescence process denoted by the color of the data points. It must be noted that this method does not claim to yield exact values of instantaneous impact location and attitude, but rather, it provides a good statistical approximation by observing the time history of the calculated 'cloud' of centroids.

Off-axis shot with minimal compound yaw

To demonstrate, Figure 11.6 shows a series of high-speed images of the UHMWPE projectile impacting the clear target block with a striking velocity of 342 m/s, along with the corresponding centroid cloud at the timestamp calculated using Equations 11.1-11.4. Each point in the centroid cloud represents the instantaneous centroid location. The camera was triggered with the diode signal and captured the event at a framerate of 10 MHz i.e. image sequence frames are 0.1 μs apart. The luminescence footprint is observed to grow rapidly to a near perfect circle within 0.4 μs, indicating minimal compound yaw. However, the impact location is observed to be located slightly towards the upper-left corner at 124° from the polar axis as measured using ImageJ, indicating off-axis impact. As abovementioned, for an off-axis shot with zero com-

pound yaw, the centroid of the initial shot location is located away from the origin, but the centroid cloud should be located around this initial impact site. The complete time history of the centroid cloud evolution for the duration of the observable luminescence is given in Figure 11.7.

The centroid cloud starts growing at about 120° from the polar axis, which corresponds well with the observed luminescence footprint. A circular footprint is developed very early on at about $t = 0.3$ μs after impact and maintains its shape and intensity till about $t = 1.0$ μs. From this point onwards, the centroid cloud begins shifting back to the origin as the intensity peaks start to decay to zero. For brevity, only the final centroid cloud time history polar plot is given for subsequent examples. The durations of the intensity signal time histories have been truncated down to the duration of the luminescence visibility as seen from the high-speed image sequence. Again, it must be mentioned that the size of the centroid cloud is by no means an indication of the intensity of the emitted luminescence, as the centroid locations have been normalized as per Equation 11.3.

Centered shot with slight compound yaw

This shot shows an example of a yawed projectile which impacted near the center of the diode ring. From the initial impact location calculated in Figure 11.9, the shot is relatively centered, although slightly skewed to the right. This corresponds to the composite image sequence in Figure 11.8, where the shot is elongated at $t = 0.6$ μs, resulting in a slightly right-skewed initial impact point. The elongated footprint is due to the top edge of the rod striking the target block first. Depending on the magnitude and persistence of the luminescence emitted, the footprint would gradually grow to its maximum size as the oblique strike face completely impacts the target block. At $t = 1.8$ μs, the luminescence footprint is observed as a full circle almost perfectly centered within the diode ring. From the time history of the centroid cloud, at about $t = 1.6$-1.8 μs the cloud is centered at the origin. At $t = 2.4$ μs, the

upper portion of the footprint that struck the target first begins to gradually decay in luminescence intensity, eventually leaving a small spot centered towards the bottom left of the concentric shot location where the oblique strike face impacted last. This is again reflected in the centroid cloud time history at about t = 2.5-3.0 μs. Finally, the centroid cloud starts drifting back towards the origin as the intensity signals start to decay to zero.

Off-axis shot with severe compound yaw

For this shot, the projectile inaccurately impacted the target with a severe angle of compound yaw. The resulting luminescence footprint is characteristic of such a shot as exhibited in the composite image sequence in Figure 11.10, which shows a thin luminescence streak moving in the yaw direction over time. As with the previous section, the compound yaw caused the oblique strike face to luminesce at different points in time. However, due to the lower striking velocity of 220 m/s for this shot, the luminescence emission does not persist long enough for the entire oblique strike face to show up in a single frame. This results in the streaking behavior over time due to the rapid decay in emission intensity.

At t = 0 μs, a small luminescence streak is observed towards the top of the shot axis when the edge first contacts the polycarbonate block. This streak grows till t = 2.0 μs, where the semicircular footprint appears to indicate that the other edge has contacted the target block towards the top left of the shot axis. The footprint finally decays nearly fully at $t = 2.5\mu s$, with the luminescent spot located at about 140° as measured using ImageJ. This result corresponds well with the centroid cloud time history in Figure 11.11 at t = 2.5 μs.

11.4 Conclusions

A low-cost, modular, non-destructive method of using mechanoluminescence as a diagnostic tool was developed as an auxiliary technique of obtaining information

during impact. This proof of concept was tested via Taylor impact of UHMWPE rods at ballistic velocities between 250-400 m/s. The design uses a series of equiangularly-spaced photodiodes located radially around the shot axis detect emissions upon projectile impact, and the signals were subsequently amplified using an external circuit to increase the signal peak intensity. These amplified diode signals may then be used as a triggering method for external systems as well as provide determination of the projectile time of arrival accurate to the order of nanoseconds. Post-processing of the diode signals via calculation of the centroids yields a statistical "centroid cloud" approximation of the shot location and time history of the impact attitude of the polymer rods. In the case of projectiles undergoing non-ideal impact attitudes, the time evolution of the centroid cloud was able to track the compound yaw using the mechanoluminescence produced during impact. In general, results using the centroid cloud method show relatively good agreement with the experimental high-speed images captured of the luminescence footprint, and further improvements on this design may prove useful in other fields of study requiring such diagnostic and triggering methods.

11.5 Acknowledgments

The authors would like to thank Stephenie Martinez-Morales for her tremendous help with sample preparation and ballistic testing.

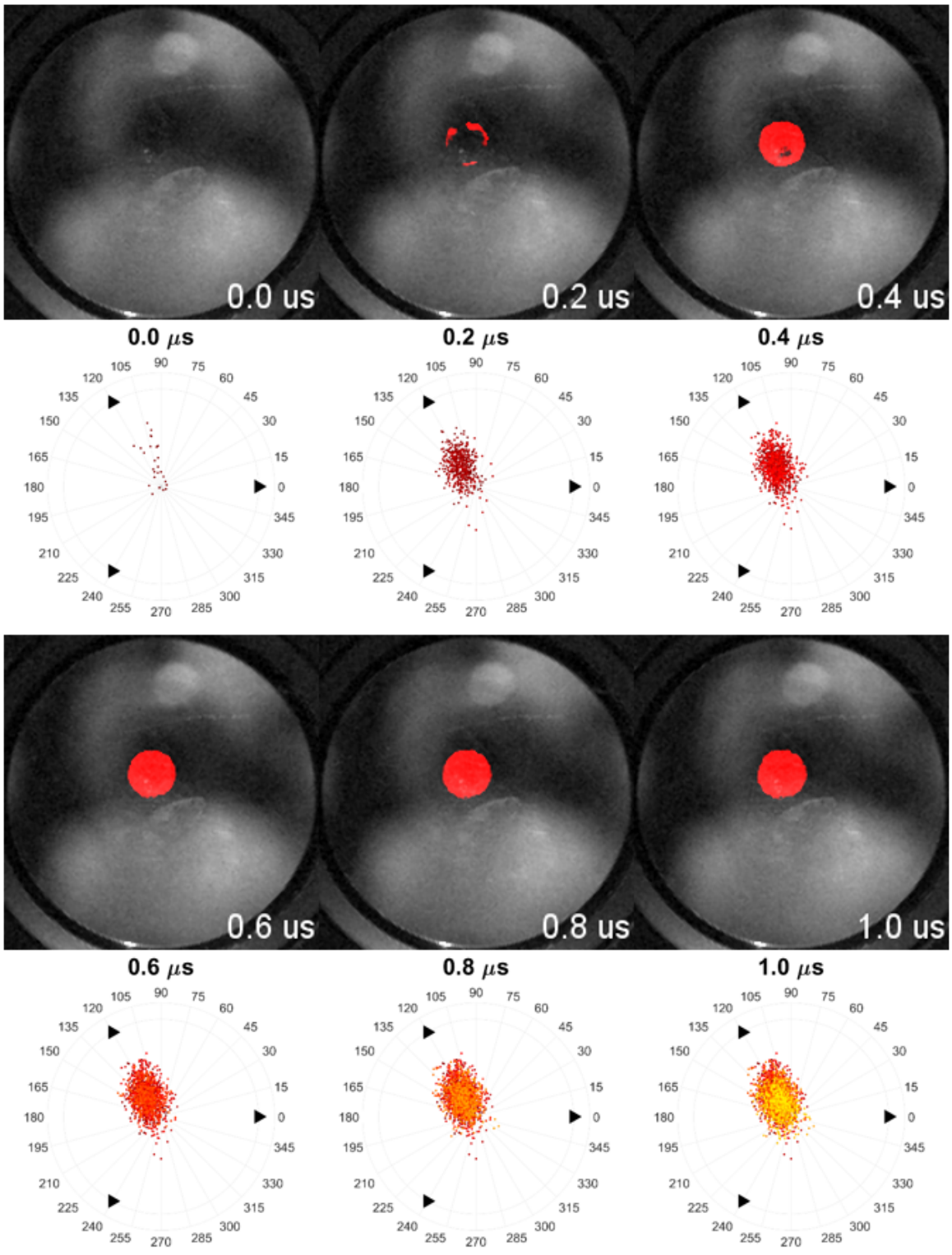

Figure 11.6. Composite image sequence of transient impact ML, striking velocity 342 m/s. The time evolution of the reconstructed centroid cloud is given at the corresponding timestamp.

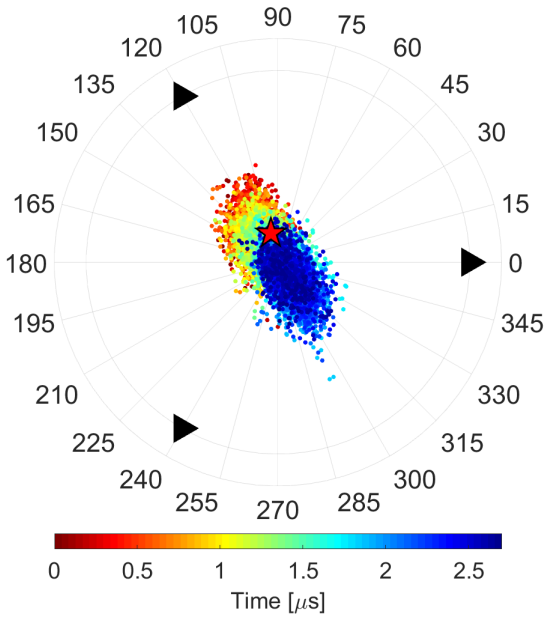

Figure 11.7. Time history of diode signal centroid cloud, striking velocity 342 m/s. The red star denotes the approximate impact location as calculated using the initial centroid values. As the luminescence signal starts to decay, the centroid cloud gradually moves back to the origin.

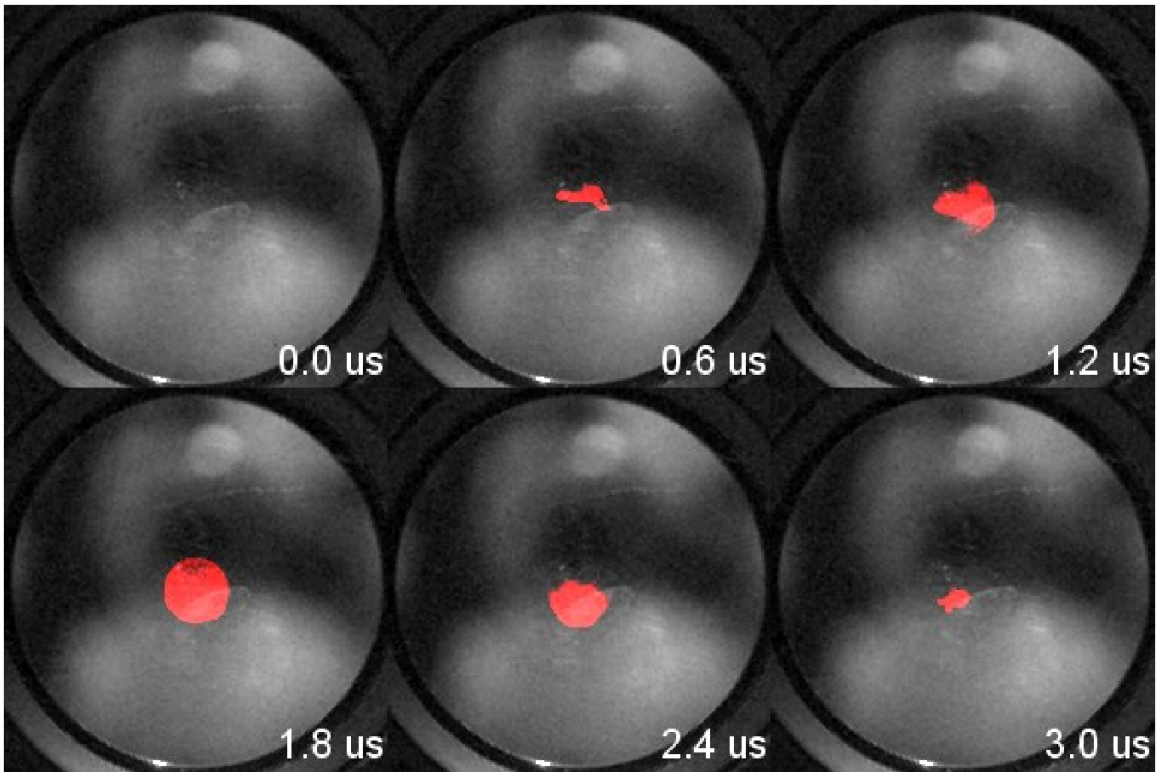

Figure 11.8. Composite image sequence of transient impact ML, striking velocity approximately 275 m/s. Luminescence shows up as a moving streak, indicating slight yaw downwards.

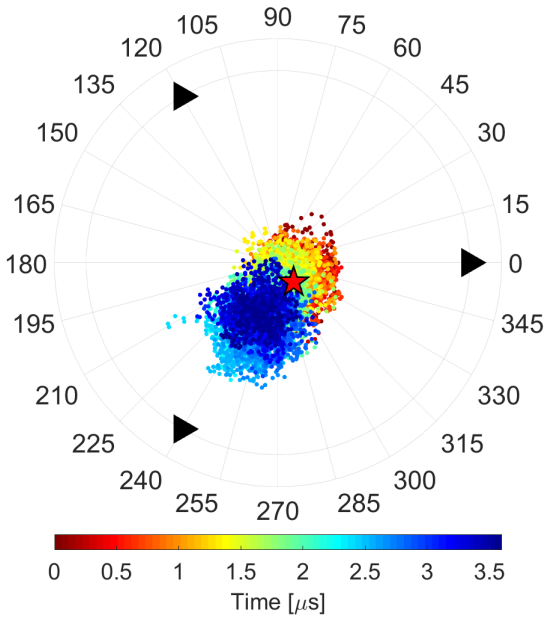

Figure 11.9. Time history of diode signal centroid cloud, striking velocity approximately 275 m/s. The red star indicates the impact location as calculated using the initial centroid values.

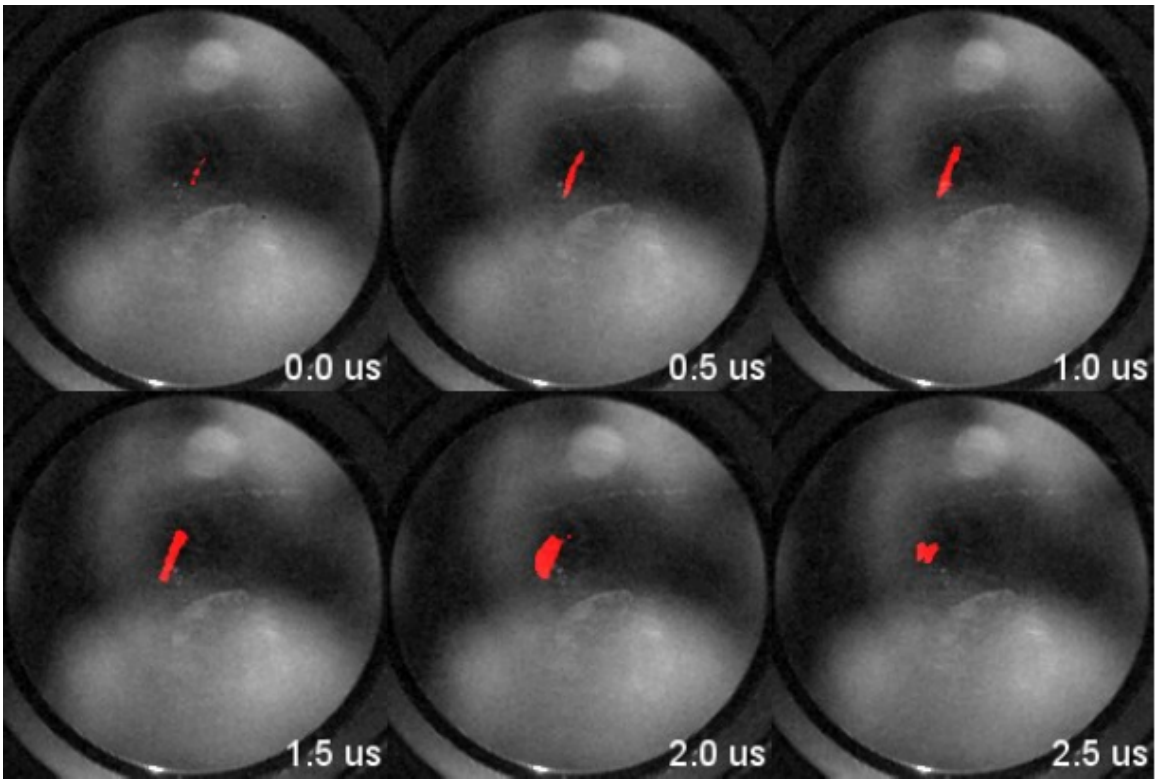

Figure 11.10. Composite image sequence of transient impact ML, striking velocity approximately 220 m/s. Luminescence shows up as a thin moving streak, indicating severe yaw towards the left.

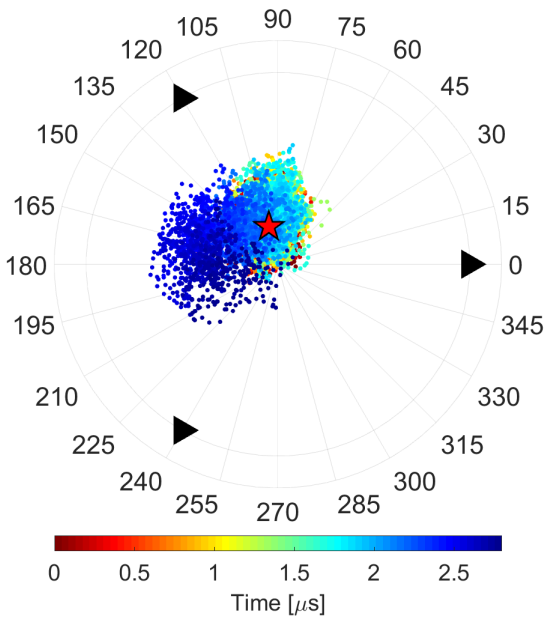

Figure 11.11. Time history of diode signal centroid cloud. Impact velocity approximately 220 m/s. The red star indicates the impact location as calculated using the initial centroid values. As the luminescence signal starts to decay, the centroid cloud gradually moves back to the origin.

12. PERFORATION OF ALUMINUM ARMOR PLATES WITH FRAGMENT-SIMULATING PROJECTILES

Chapter adapted from prior published work. Z. Guo, M.J. Forrestal, S. Martinez-Morales, W. Chen, Perforation of Aluminum Armor Plates with Fragment-Simulating Projectiles, J. Dyn. Behav. Mater. (2019) 2–8. doi:10.1007/s40870-019-00200-3.

Abstract

Experiments with fragment-simulating projectiles (FSP) and aluminum plates are conducted to evaluate the performance of various aluminum alloys and plate thicknesses to resist perforation against fragments. Ballistic-limit velocity data for several aluminum alloys and plate thicknesses are presented in several US Army Research Laboratory (ARL) reports. In this study, we present additional ballistic-limit data for plates thinner than the plates reported by ARL. In addition, we present an equation that predicts the ballistic-limit velocity for fragment-simulating projectiles (FSP) that perforate aluminum armor plates. The ballistic-limit equation is presented in terms of dimensionless parameters so that the geometric and material problem scales are identified. Predictions and data from two different fragment-simulating projectiles and two different strength aluminum alloys show the range of plate thicknesses for reasonable model predictions.

12.1 Introduction

As discussed in [149], the fragment-simulating projectiles (FSP) shown in Figure 12.1 are used in material evaluations to simulate the performance of aluminum

armor plates against fragments. Ballistic-limit velocity data from experiments conducted at the US Army Research Laboratory (ARL) are reported for 6055-T651 [149], 6061-T651 [150], and 2139-T8 [151] aluminum alloys. To extend the ARL data range, we conducted additional experiments with 6061-T651 plates with smaller thicknesses than that presented in [150]. We will compare our model with these data.

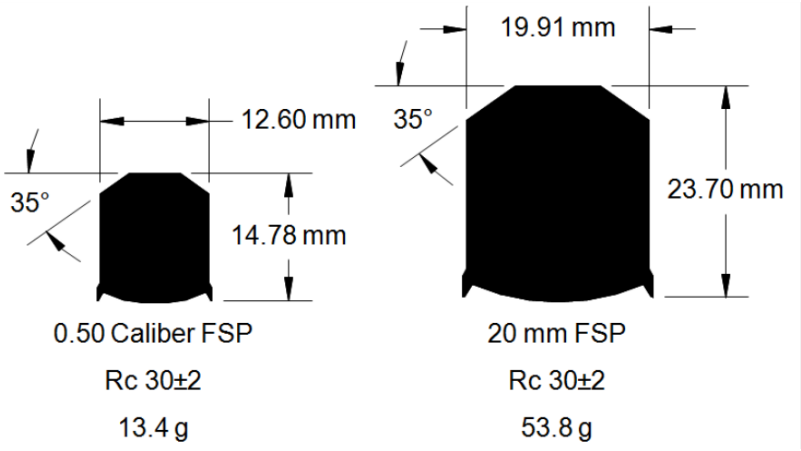

Figure 12.1. Fragment-simulating projectiles (FSPs) made from 4340 Rc 30 steel. The 0.50-cal FSP has mass 13.4 grams and the 20-mm FSP has mass 53.8 grams.

We present a model that predicts the ballistic-limit velocity for the FSPs shown in Figure 12.1 against aluminum armor plates. The model approximates the FSP geometries as flat-nosed, right circular cylinders with length L and diameter D. Recht and Ipson [5] give an empirical model for this projectile geometry. They present an equation for the residual velocity V_r in terms of the ballistic-limit velocity V_{bl} that must be determined from experimental data. By contrast, our model predicts both V_{bl} and V_r. The ballistic-limit equation is presented in terms of dimensionless parameters so that the geometric and material problem scales are identified. Predictions and data from the two different projectiles and two different strength aluminum alloys show the range of plate thicknesses for reasonable model predictions.

12.2 Model

Figures 12.2a and 12.2b show the problem geometry and assumed perforation mechanism. The model projectile impacts the target plate with striking velocity V_s, perforates the plate, and the projectile and plug exit the plate at velocity V_r. Both the projectile and plug are taken as rigid bodies. We further assume that the plate does not move during the perforation process and that the projectile is only resisted by the shear stress on the plug surface in contact with the plate.

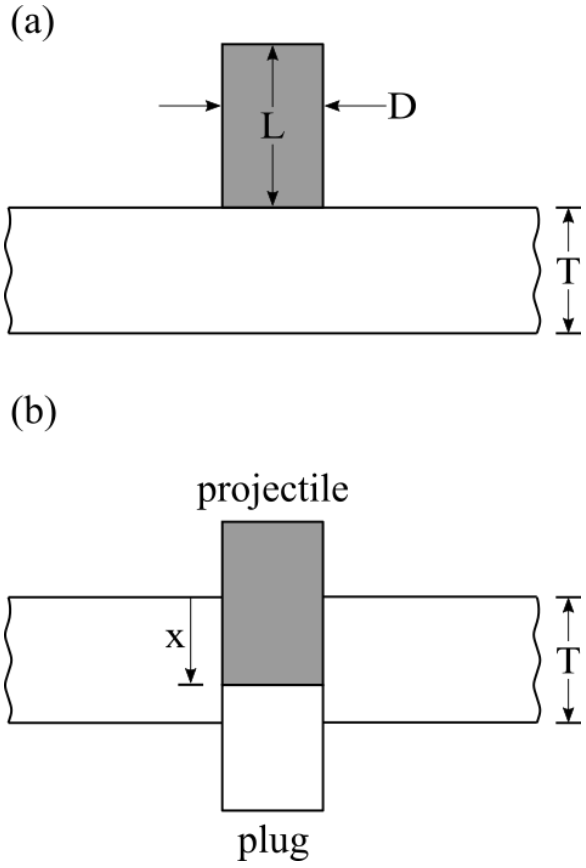

Figure 12.2. Problem geometry (a) before impact, and (b) during perforation.

Recht and Ipson [5] give an energy balance analysis for this problem and present an equation for the residual velocity V_r that contains the work done due to the shear stress on plug-plate interface. This work term contains the ballistic-limit velocity V_{bl} that must be found from experimental data. By contrast, we derive an expression

for the work term and then present predictive equations for V_r and the ballistic-limit velocity V_{bl}. First consider the initial impact by the projectile and the projectile-plug response. Since we assume the projectile and plug are rigid bodies, conservation of momentum gives

$$MV_s = (M + m)V_i \tag{12.1}$$

where V_s is the striking velocity, V_i is the projectile-plug velocity after impact that starts the perforation process, M is the projectile mass, and m is the plug mass. The kinetic energy lost during initial impact is

$$E_i = \left(\frac{m}{M+m}\right)\frac{MV_s^2}{2} \tag{12.2}$$

Then, an energy balance for kinetic energy and work done by the shear stress on the plug surface W gives

$$\frac{MV_s^2}{2} = E_i + \left(\frac{M+m}{2}\right)V_r^2 + W \tag{12.3}$$

The minimum striking velocity required to perforate the plate is the ballistic-limit velocity V_{bl}, so $V_s = V_{bl}$ when $V_r = 0$. From Equation 12.3

$$W = \left(\frac{M}{M+m}\right)\frac{MV_{bl}^2}{2} \tag{12.4}$$

From Equations 12.2, 12.3, and 12.4, the residual velocity is given by

$$V_r = \frac{M}{M+m}\left(V_s^2 - V_{bl}^2\right)^{\frac{1}{2}} \tag{12.5}$$

For the model presented by Recht and Ipson [5], V_{bl} is determined experimentally and then V_r can be calculated from Equation 12.5. Now, we derive an equation for the

work done by the shear stress τ on the plate-plug interface shown in Figure 12.2b. The incremental work is related to the incremental plug movement by

$$dW = Fdx, \quad F = \pi D\tau(T - x) \tag{12.6}$$

An integration gives

$$W = \frac{\pi DT^2\tau}{2} \tag{12.7}$$

The constant shear stress τ can be related to the uniaxial yield stress σ_0 through the von Mises yield criteria. From [152, 153], $\tau = \sigma_0/\sqrt{3}$. Then, Equation 12.7 becomes

$$W = \frac{\pi DT^2\sigma_0}{2\sqrt{3}} \tag{12.8}$$

Next, we define the projectile and plug masses as

$$M = \rho_p \left(\frac{D}{2}\right)^2 \pi L, \quad m = \rho_t \left(\frac{D}{2}\right)^2 \pi T \tag{12.9}$$

From Equations 12.4, 12.8, and 12.9, we obtain dimensionless equations for V_{bl} that can be written in two forms. Thus,

$$\frac{V_{bl}}{(\sigma_0/\rho_p)^{\frac{1}{2}}} = \left\{ \frac{4}{\sqrt{3}} \left(\frac{T}{D}\right) \left(\frac{T}{L}\right) \left[1 + \frac{T}{L}\frac{\rho_t}{\rho_p}\right] \right\}^{\frac{1}{2}} \tag{12.10a}$$

$$\frac{V_{bl}}{(\sigma_0/\rho_p)^{\frac{1}{2}}} = \left\{ \frac{4}{\sqrt{3}} \left(\frac{L}{D}\right) \left(\frac{T}{L}\right)^2 \left[1 + \frac{T}{L}\frac{\rho_t}{\rho_p}\right] \right\}^{\frac{1}{2}} \tag{12.10b}$$

The equation for V_r is

$$V_r = \frac{1}{1 + \frac{T}{L}\frac{\rho_t}{\rho_p}} \left(V_s^2 - V_{bl}^2\right)^{\frac{1}{2}} \tag{12.11}$$

Thus, these equations for the ballistic-limit and residual velocities are predictive. For the special case of the projectiles shown in Figure 12.1, $(L/D) = 1.19$ for the 20-mm FSP and $(L/D) = 1.17$ for the 0.50-in. FSP. In our numerical study, we let $(L/D) = 1.18$ for both projectiles and from Equation (10b) we obtain

$$\frac{V_{bl}}{(\sigma_0/\rho_p)^{\frac{1}{2}}} = \left\{ 2.73 \left(\frac{T}{L}\right)^2 \left[1 + \frac{T}{L}\frac{\rho_t}{\rho_p}\right] \right\}^{\frac{1}{2}} \tag{12.12}$$

Equation 12.12 shows the geometric and material scales for this problem.

12.3 Experiments

In our study, we compare our model with existing ARL data. We also conducted additional experiments with 6061-T651 plates with smaller thicknesses than those presented in [150].

12.3.1 ARL Data

Gallardy [149] describes the experimental procedures for the tests conducted at the US Army Research Laboratory. Ballistic-limit data for the 20-mm FSP are reported for 6055-T651 [149], 6061-T651 [150], and 2139-T8 [151] plates with nominal thicknesses of 25.4, 38.1, and 50.8 mm. Data are reported for the 0.50-in. caliber FSP for 6055-T651 plates with nominal thicknesses of 19.05 and 25.4 mm. Data tables for the ballistic-limit velocities V_{bl} versus plate thicknesses T are given in [149] and [151]. For the plots shown in [150], the data points are $T = 25.7$ mm, $V_{bl} = 442$ m/s; $T = 38.8$ mm, $V_{bl} = 762$ m/s; and $T = 51.2$ mm, $V_{bl} = 1218$ m/s.

12.3.2 Purdue Experiments

We conducted ballistic experiments at the Purdue University Impact Science Laboratory with a 20-mm caliber, smooth-bore powder gun. The 20-mm FSP projectiles

were launched to striking velocities V_s = 120-500 m/s. Three sets of experiments were conducted with 6061-T651 aluminum plates with thicknesses of T = 19.1, 12.7, and 6.35 mm. The square target plates had a width of 152 mm and were clamped on all four edges leaving an active width of 102 mm. FSP striking velocities V_s were measured with a series of laser diodes and residual velocities V_r were measured with a break-wire system, both systems with an accuracy within 3 m/s. Figures 12.3, 12.4, and 12.5 show data and curve-fits for the T = 19.1, 12.7, and 6.35 mm-thick plates. These data were curve-fit with the least squares method and the empirical equation

$$V_r = \frac{1}{1 + \frac{T}{L}\frac{\rho_t}{\rho_p}} \left(V_s^p - V_{bl}^p\right)^{1/p} \tag{12.13}$$

where p is an empirical constant. Thus, we determine the experimental values of V_{bl} from this data-fit. For T = 19.1 mm, p = 2.88 and V_{bl} = 338 m/s; for T = 12.7 mm, p = 2.03 and V_{bl} = 218 m/s; for T = 6.35 mm, p = 3.47 and V_{bl} = 162 m/s.

In Figure 12.6, we show post-impact images of a sectioned, T = 19.1-mm-thick plate and the shear plug ejected from the target plate. For these images, V_s = 432 m/s and the residual velocity was V_r = 266 m/s. The nominal shear plug length was nearly equal to the plate thickness. Figure 12.7 shows a post-test image for a T = 19.1-mm-thick plate with a striking velocity of 341 m/s, which is close to the ballistic-limit velocity. In Figure 12.8, we show a post-impact image of a sectioned 6.35- mm-thick plate and a shear plug that is nearly ejected from the target plate. For this image, V_s = 165 m/s. Figure 12.8 also shows severe target plate bending. By contrast, Figure 12.6a for the thicker 19.1-mm target plate shows no visible plate bending.

12.4 Results & Discussion

Figures 12.9, 12.10, and 12.11 present model predictions and data. Projectile and target densities are taken as 7830 kg/m^3 and 2710 kg/m^3, respectively The alloys

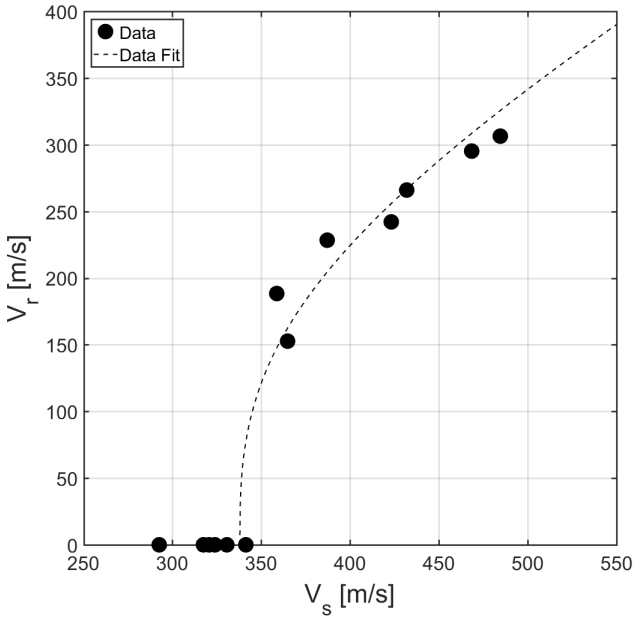

Figure 12.3. Residual velocity versus striking velocity for 20-mm FSPs impacting 19.1-mm thick 6061-T651 plates. V_{bl} = 338 m/s and p = 2.88.

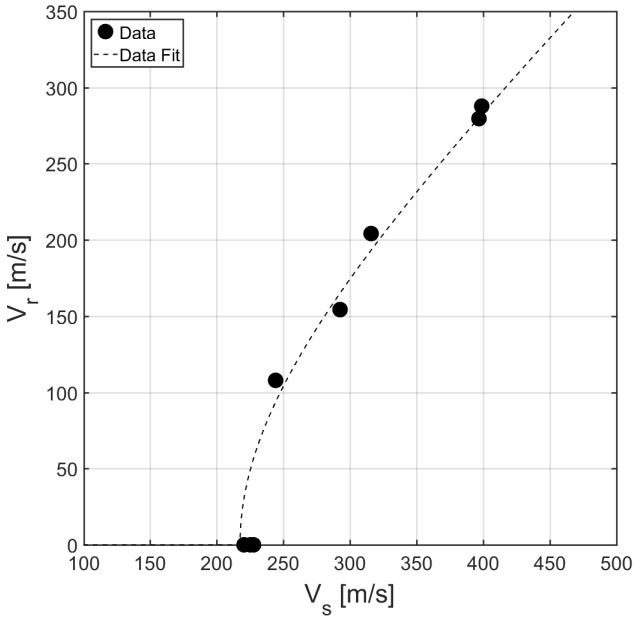

Figure 12.4. Residual velocity versus striking velocity for 20-mm FSPs impacting 12.7-mm thick 6061-T651 plates. V_{bl} = 218 m/s and p = 2.03.

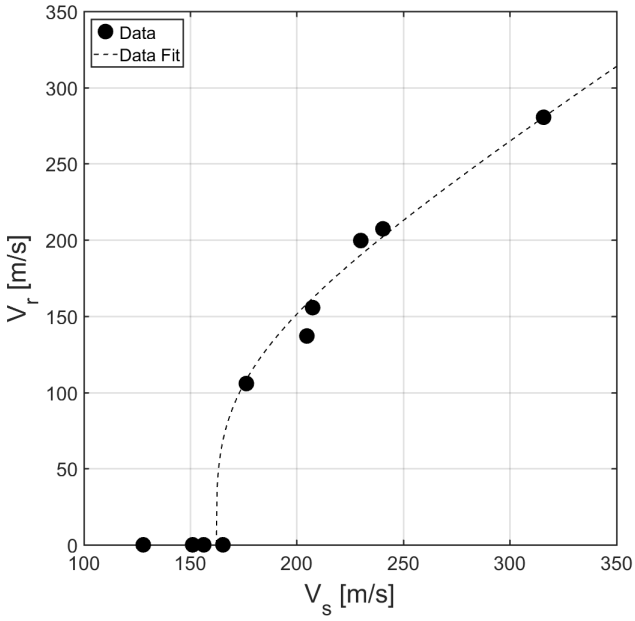

Figure 12.5. Residual velocity versus striking velocity for 20-mm FSPs impacting 6.35-mm thick 6061-T651 plates. V_{bl} = 162 m/s and p = 3.47.

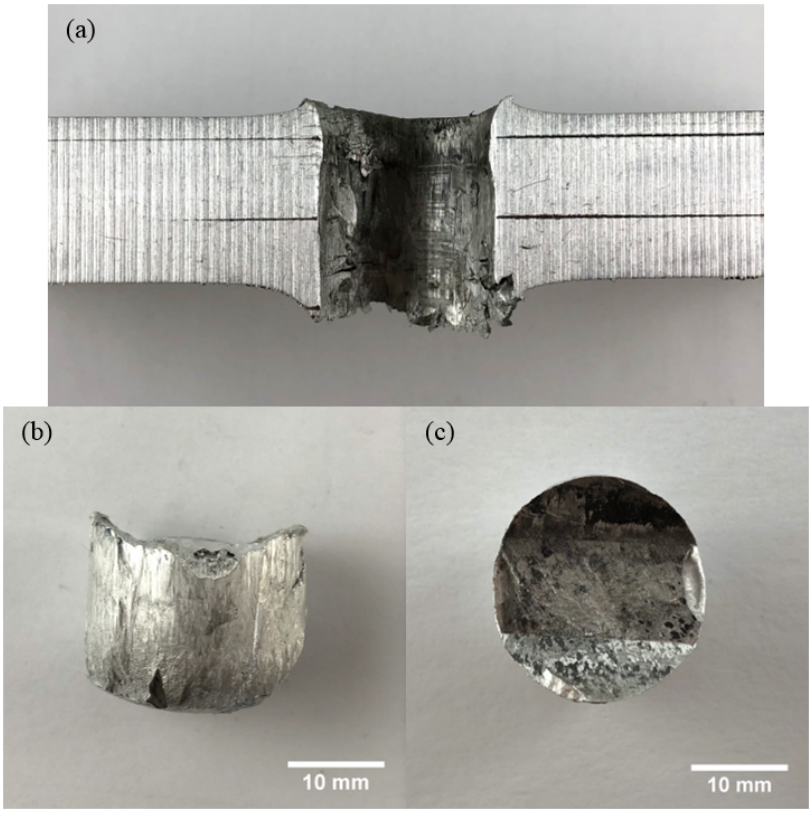

Figure 12.6. Post-impact images for a 19.1-mm plate. (a) Perforated plate cross-section, (b) side view of shear plug, and (c) top view of shear plug. $V_s = 432$ m/s.

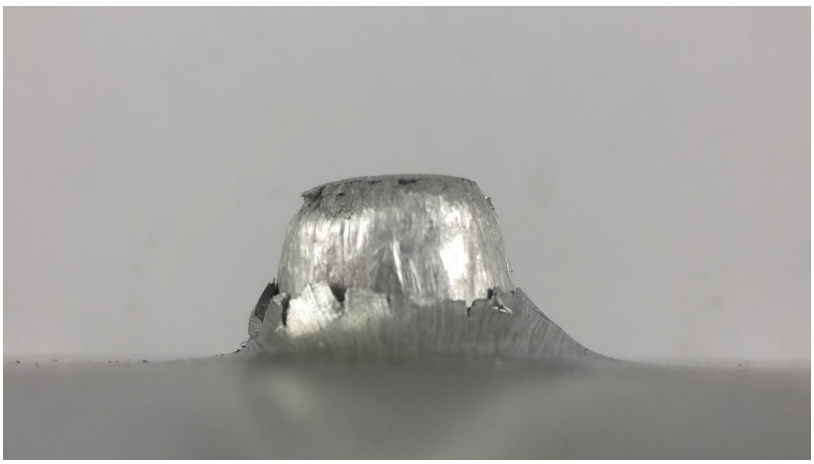

Figure 12.7. Side profile of a nearly-ejected shear plug for 19.1-mm plate. $V_s = 342$ m/s.

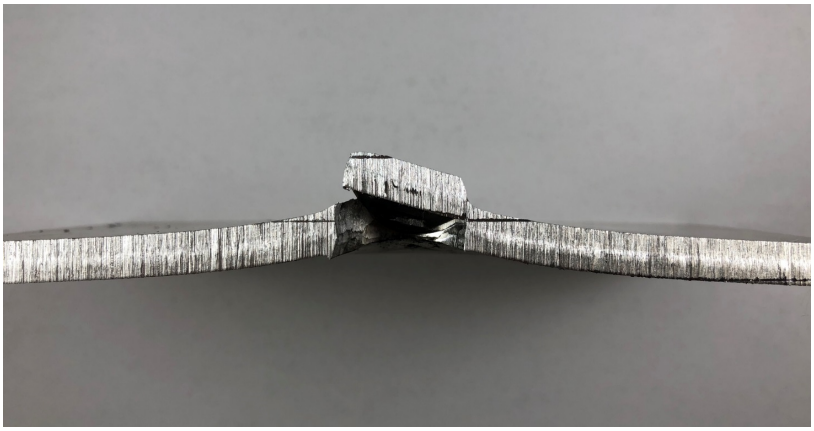

Figure 12.8. Side profile of nearly-ejected shear plug for a 6.35-mm thick plate. Plate exhibits severe bending. $V_s = 165.4$ m/s.

6055-T651 and 6061-T651 have compressive strengths [154] of 400 MPa, and the alloy 2139-T8 has a compressive strength [155] of 600 MPa. Figure 12.9 compares predictions and data for plates with compressive strengths of 400 MPa and 600 MPa. In Figure 12.10, we show dimensionless plots for two different FSP geometries with the same target strength. Figure 12.11 shows dimensionless plots for the 20-mm FSP and two different target strengths. The dimensionless plots show the geometric and material problem scales.

As shown in Figure 12.9, model predictions for the 20-mm FSPs are in good agreement with data for plate thicknesses up to $T = 38.1$ mm. For $T = 50.8$ mm, the model under predicts the data by about 10 percent. As the plate thickness increases to $T = 50.8$ mm, the problem approaches a penetration rather than a perforation problem and the perforation model becomes less accurate. The experiments conducted at Purdue with plate thicknesses of $T = 19.1$ mm and 12.7 mm are in excellent agreement with the model predictions. For $T = 19.1$ mm, the measured and predicted ballistic-limit velocities were 338 m/s and 339 m/s, respectively. For $T = 12.7$ mm, the measured and predicted ballistic limit velocities were 218 m/s and 217 m/s respectively. For the thinner target plates with $T = 6.35$ mm, the measured and predicted ballistic limit velocities were 162 m/s and 104 m/s respectively. Thus, the model does not predict accurately for the thinner $T = 6.35$-mm plates. Figure 12.8 shows severe plate bending for $T = 6.35$ mm, whereas Figure 12.6b shows no visible plate bending for the thicker $T = 19.1$ mm plate. Our model assumes no target plate bending and is not valid for the 6.35-mm plates. Therefore, we do not include data points for the 6.35-mm target plates in Figures 12.9 and 12.11.

12.5 Conclusions

We present a ballistic-limit equation for the FSP projectiles shown in Figure 12.1 that perforate aluminum armor plates with thicknesses between 6.35 mm and 50.8 mm. Model predictions are in good agreement with data for plate thicknesses between

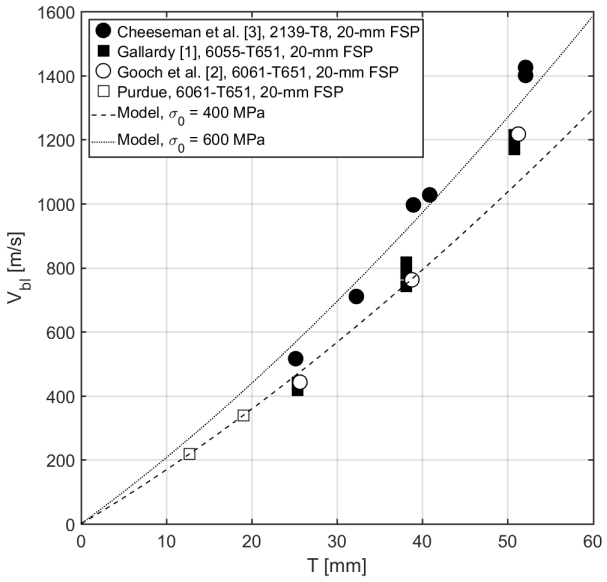

Figure 12.9. Model predictions and data for the ballistic-limit velocity versus plate thickness for 20-mm FSPs.

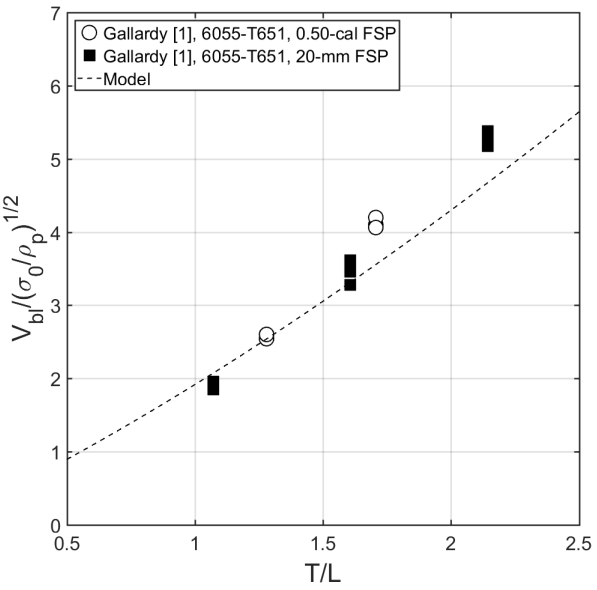

Figure 12.10. Dimensionless model predictions and data for the ballistic-limit velocity versus plate thickness for 0.50-cal and 20-mm FSPs.

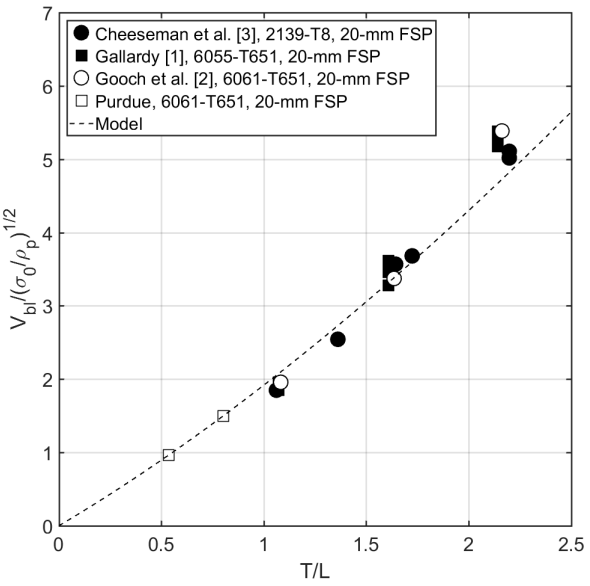

Figure 12.11. Dimensionless model predictions and data for the ballistic-limit velocity versus plate thickness for 20-mm FSPs and two aluminum alloy strengths.

12.7 mm and 38.1 mm. For the plate thickness of 50.8 mm, the model under predicts the data by about 10 percent. For the plate thickness of 6.35 mm, the model is no longer valid because of severe plate bending. The ballistic-limit equation is presented in terms of dimensionless parameters so that the geometric and material scales are identified. Predictions and data from two FSP projectiles and two different strength aluminum alloy plates show the scaling law to be accurate.

12.6 Acknowledgments

This material is based upon work supported in part by the U. S. Army Research Laboratory and the U. S. Army Research Office under grant number W911NF1710241. The authors would also like to thank Denver Gallardy of the U.S. Army Research Laboratory (Aberdeen Proving Ground, MD) for his comments and insightful discussions.

13. CONCLUSIONS

In the design of soft armor systems, especially systems for personnel protection, existing efforts in the design and evaluation of these systems have been largely empirical. Numerous analytical and computational efforts have been put forth by numerous authors, but it is usually in the interest of soft body armor manufacturers to be able to quickly distinguish and predict the ballistic performance of a particular system to save on time and cost. The current work aims to bridge this gap between detailed analyses of soft armor impact response present in the state-of-the-art and a quick way to discern an optimized system from a sub-optimal configuration. This is achieved by answering some of the existing questions and propose some preliminary parameters and considerations to guide future soft armor designs, and more specifically with regards to diphasic armor systems that are commonly-used in such applications.

For such a diphasic system, the three main questions that the current work aims to answer are: (1) how to select the most appropriate frontal and rear material; (2) how to best choose the frontal materials for optimal ballistic resistance; and (3) how much can actually be replaced. Given two materials, the first decision is to determine the best rear portion material, which can be decided using the Cunniff velocity calculated from the constituent fiber properties. Having a higher Cunniff velocity for the rear portion inherently results in minimal interference between the two layers, and this interference usually leads to premature failure of either portion.

The frontal material should then be chosen and designed for maximal projectile deformation and deceleration. For this strike face portion, a higher transverse stiffness is ideal since the failure mode at the strike face is localized and the striking energy is not sufficiently carried away from the impact site. In such a situation, a stiffer strike face would be useful in deforming the projectile and dissipating some of the kinetic energy via plastic deformation. Additionally, the mushrooming of the projectile due

to plastic deformation increases the amount of ballistic resistance from subsequent plies. The transverse stiffness may be maximized via the choice of constituent fiber which may be experimentally determined via fiber transverse compression tests, or by architecture as in the case of [0°/90°] composite layups for the ARL X-hybrid. From preliminary ballistic experiments, it appears that a fibrous woven material is a good strike face material choice as well, since most projectiles in real world applications have an added component of projectile spin for stability, and woven armors have shown to perform better against such spinning threats.

Finally, given the choice of material for the strike face and rear body portion, the amount of each material to use can then be decided using the $k - \eta$ curves for a given rear portion material. Based on existing ballistic data, the amount of replaceable strike-face material for maintaining the same ballistic limit velocity may be determined semi-empirically — this portion may in fact be replaced with a material with better material properties (as abovementioned) for improved ballistic performance.

14. RECOMMENDATIONS

The current work focuses on the optimization of soft armor systems based on proposed design guidelines, which were in turn based on the different types of failure modes and defeat mechanisms of the constituent fibrous material. From a design perspective, the macro-scale response and performance seem to indicate that the exact failure mode is not exactly crucial when considering the possibly minute differences in the magnitude of energy-dissipation. From a scientific point of view, however, the exact mechanisms of fiber failure is still a major gap in research.

Much effort by the Impact Science Laboratory group at Purdue University has been directed towards teasing out the failure mechanisms, specifically on whether these polymer fibers fail under localized tension or via transverse shear when under high velocity impact. A large portion of our group's work has been focused on elucidating these mechanisms, either via post-impact post-mortem analysis, or in more recent work, by observing the failure modes via in-situ tensile loading in a scanning electron microscope [156, 157]. These methods have given some cursory insight into the fiber failure modes under impact, but are still limited to inference via surface analysis.

Some preliminary work has been performed by the author at the Advanced Photon Source at Argonne National Laboratory. The transmission X-ray microscope (TXM) at Beamline 32-ID-C was used to observe the changes in microstructure of these fibers under off-axis loading. The main limitation with the experiments performed was the lack of contrast between the crystalline and amorphous phases. A modified method of osmium vapor staining these fibers has shown some limited success, with more work to be done in this area.

Finally, with the advent of computational methods, machine learning and neural networks have become prominent in many areas of research. Particularly in the field of

composites, Pidaparti & Palakal [158] were among the first to utilize neural networks to generate appropriate material models for cyclic fatigue loading predictions. Yu et al. [159–161] have continued extensive work in deep learning methods and extending the concepts to textile composites and their respective failure modes. It is expected that future directions in this field would trend largely towards machine learning for more efficient and accurate impact failure predictions.

REFERENCES

[1] José M. García, Félix C. García, Felipe Serna, and José L. de la Peña. High-performance aromatic polyamides. *Progress in Polymer Science*, 35(5):623–686, may 2010.

[2] Roelof Marissen. Design with Ultra Strong Polyethylene Fibers. *Materials Sciences and Applications*, 02(05):319–330, 2011.

[3] JB Donnet and RC Bansal. *Carbon fibers*. CRC Press, 1998.

[4] M Lewin and J Preston. High Technology Fibers: Part D. In Menachem Lewin and Jack Preston, editors, *Handbook of Fiber Science and Technology: Volume III*. 1996.

[5] R. F. Recht and T. W. Ipson. Ballistic Perforation Dynamics. *Journal of Applied Mechanics*, 30(3):384–390, 1963.

[6] W. Johnson, Collins C., and Kindred F. A Mathematical Model for Predicting Residual Velocities of Fragments After Perforating Helmets and Body Armor. Technical report, 1968.

[7] P. G. Morfogenis. A Learning Curve Type Equation Predicting Residual Velocity. Technical report, Ballistic Research Laboratories, 1975.

[8] D. Clark, L. Crow, and J. Sperrazza. A Weibull Model to Estimate Residual and Critical Velocities for Target Penetrations. Technical Report July, US Army Materiel Systems Analysis Activity, Aberdeen Proving Ground, Maryland, 1976.

[9] Philip M Cunniff. A semiempirical model for the ballistic impact performance of textile-based personnel armor. *Textile Research Journal*, 66(1):45–59, 1996.

[10] Philip M Cunniff. A Design Tool for the Development of Fragmentation Protective Body Armor. In *Proceedings of 18th International Symposium on Ballistics*, 1999.

[11] Philip M Cunniff. Dimensionless parameters for optimization of textile-based body armor systems. In *Proceedings of 18th International Symposium on Ballistics*, 1999.

[12] Philip M Cunniff. Decoupled Response of Textile Body Armor. In *Proceedings of 18th International Symposium on Ballistics*, pages 1–8, 1999.

[13] D. Roylance, A. Wilde, and G. Tocci. Ballistic Impact of Textile Structures. *Textile Research Journal*, 43(February):34–41, jan 1973.

[14] Philip M Cunniff. An analysis of the system effects in woven fabrics under ballistic impact. *Textile Research Journal*, 62(9):495–509, 1992.

[15] M. J. Iremonger and A. C. Went. Ballistic impact of fibre composite armours by fragment-simulating projectiles. *Composites Part A: Applied Science and Manufacturing*, 27(7 PART A):575–581, 1996.

[16] M. J. Iremonger and The International Ballistics Committee. Polyethylene Composites for Protection against High Velocity Small Arms Bullets. In *18th International Symposium on Ballistics*, volume 2, pages 946–953, 1999.

[17] B. R. Scott. The Penetration of Compliant Laminates by Compact Projectiles. In *Proceedings of 18th International Symposium on Ballistics*, pages 1184–1191, San Antonio, 1999.

[18] K. Karthikeyan and B.P. Russell. Polyethylene ballistic laminates: Failure mechanics and interface effect. *Materials & Design*, 63:115–125, nov 2014.

[19] Long H. Nguyen, Shannon Ryan, Stephen J. Cimpoeru, Adrian P. Mouritz, and Adrian C. Orifici. The effect of target thickness on the ballistic performance of ultra high molecular weight polyethylene composite. *International Journal of Impact Engineering*, 75:174–183, 2015.

[20] Tomasz K. Ćwik, Lorenzo Iannucci, Paul Curtis, and Dan Pope. Investigation of the ballistic performance of ultra high molecular weight polyethylene composite panels. *Composite Structures*, 149:197–212, 2016.

[21] Tomasz K. Ćwik, Lorenzo Iannucci, Paul Curtis, and Dan Pope. Design and Ballistic Performance of Hybrid Composite Laminates. *Applied Composite Materials*, 24(3):717–733, jun 2017.

[22] U Heisserer, H Van Der Werff, and J Hendrix. Ballistic Depth of Penetration Studies in Dyneema ® Composites. *27th international symposium, Germany*, (January 2016), 2013.

[23] Timothy G. Zhang, Sikhanda S. Satapathy, Lionel R. Vargas-Gonzalez, and Shawn M. Walsh. Ballistic impact response of Ultra-High-Molecular-Weight Polyethylene (UHMWPE). *Composite Structures*, 133:191–201, dec 2015.

[24] Yanfei Yang and Xiaogang Chen. Investigation of energy absorption mechanisms in a soft armor panel under ballistic impact. *Textile Research Journal*, page 004051751667112, 2016.

[25] Yanfei Yang and Xiaogang Chen. Investigation on energy absorption efficiency of each layer in ballistic armour panel for applications in hybrid design. *Composite Structures*, 164:1–9, mar 2017.

[26] Anthony L. Alesi. Composite Personnel Armor. Technical report, 1957.

[27] U.S. DoJ. Stab Resistance of Personal Body Armor, NIJ Standard-0115.00. Technical report, 2000.

[28] Philip M. Cunniff. Variability in Ballistic Impact Performance Due To Projectile Physical Properties and Dimensions. In *24th International Symposium on Ballistics*, 2008.

[29] Matthew Hudspeth, Dawei Li, Jennifer Spatola, Weinong Chen, and James Zheng. The effects of off-axis transverse deflection loading on the failure strain of various high-performance fibers. *Textile Research Journal*, 86(9):897–910, jun 2016.

[30] Matthew Hudspeth, Weinong Chen, and James Zheng. Why the Smith theory over-predicts instant rupture velocities during fiber transverse impact. *Textile Research Journal*, 86(7):743–754, may 2016.

[31] Matthew Hudspeth, Xu Nie, and Weinong Chen. Dynamic failure of Dyneema SK76 single fibers under biaxial shear/tension. *Polymer*, 53(24):5568–5574, nov 2012.

[32] L. R. Vargas-Gonzalez, S. M. Walsh, and J. C. Gurganus. Examining the Relationship Between Ballistic and Structural Properties of Lightweight Thermoplastic Unidirectional Composite Laminates. (August), 2011.

[33] Matthew Hudspeth, Apaar Agarwal, Beck Andrews, Ben Claus, Feng Hai, Curtis Funnell, James Zheng, and Weinong Chen. Degradation of yarns recovered from soft-armor targets subjected to multiple ballistic impacts. *Composites Part A: Applied Science and Manufacturing*, 58:98–106, mar 2014.

[34] M. Hockauf, L. W. Meyer, F. Pursche, and O. Diestel. Dynamic perforation and force measurement for lightweight materials by reverse ballistic impact. *Composites Part A: Applied Science and Manufacturing*, 38(3):849–857, 2007.

[35] T.G. Montgomery, P.L. Grady, and C. Tomasino. The Effects of Projectile Geometry on the Performance of Ballistic Fabrics. *Textile Research Journal*, 52(7):442–450, jul 1982.

[36] V.B.C Tan, C.T Lim, and C.H Cheong. Perforation of high-strength fabric by projectiles of different geometry. *International Journal of Impact Engineering*, 28(2):207–222, feb 2003.

[37] Zherui Guo, Jihye Hong, James Zheng, and Weinong Chen. Loading rate effects on dynamic out-of-plane yarn pull-out. *Textile Research Journal*, 84(16):1708–1719, oct 2014.

[38] Zherui Guo, Jihye Hong, James Zheng, and Weinong Chen. Out-of-plane effects on dynamic pull-out of p-phenylene terephthalamide yarns. *Textile Research Journal*, 85(2):140–149, jul 2015.

[39] Anthony F. Wilde. Photographic Investigation of High-Speed Missile Impact upon Nylon Fabric. Part II: Retarding Force on Missile and Transverse Critical Velocity. *Textile Research Journal*, pages 772–778, 1974.

[40] Y. Termonia. Impact Resistance of Woven Fabrics. *Textile Research Journal*, 74(8):723–729, aug 2004.

[41] IM Ward and PR Pinnock. The mechanical properties of solid polymers. *British Journal of Applied Physics*, 3, 1966.

[42] PR Pinnock, IM Ward, and JM Wolfe. The compression of anisotropic fibre monofilaments. II. *Proceedings of the Royal Society of London. Series A, Mathematical and Physical Sciences*, 291(1425):267–278, 1966.

[43] DW Hadley, PR Pinnock, and IM Ward. Anisotropy in oriented fibres from synthetic polymers. *Journal of Materials Science*, 4:152–165, 1969.

[44] S.L. Phoenix and J. Skelton. Transverse Compressive Moduli and Yield Behavior of Some Orthotropic, High-Modulus Filaments. *Textile Research Journal*, 44(12):934–940, dec 1974.

[45] S. Kawabata. Measurement of the transverse mechanical properties of high-performance fibres. *Journal of the Textile Institute*, 81(4):432–447, jan 1990.

[46] J Singletary and H Davis. The transverse compression of PPTA fibers Part I Single fiber transverse compression testing. *Journal of Materials Science*, 5:573–581, 2000.

[47] J Singletary, H Davis, Y Song, North Carolina, and W Knoff. The transverse compression of PPTA fibers Part II Fiber transverse structure. *Journal of Materials Science*, 5:583–592, 2000.

[48] Ming Cheng, Weinong Chen, and Tusit Weerasooriya. Experimental investigation of the transverse mechanical properties of a single Kevlar® KM2 fiber. *International Journal of Solids and Structures*, 41(22-23):6215–6232, nov 2004.

[49] Jaeyoung Lim, James Q. Zheng, Karl Masters, and Weinong W. Chen. Mechanical behavior of A265 single fibers. *Journal of Materials Science*, 45(3):652–661, oct 2009.

[50] S. Abdul Jawad and I. M. Ward. The transverse compression of oriented nylon and polyethylene extrudates. *Journal of Materials Science*, 13:1381–1387, 1978.

[51] Zherui Guo, Daniel Casem, Matthew Hudspeth, Xu Nie, Jianzhuo Sun, and Weinong Chen. Transverse compression of two high-performance ballistic fibers. *Textile Research Journal*, 86(5):502–511, mar 2016.

[52] Peter J. Walsh, Xianbo Hu, Philip Cunniff, and Alan J. Lesser. Environmental effects on poly-p-phenylenebenzobisoxazole fibers. I. Mechanisms of degradation. *Journal of Applied Polymer Science*, 102(4):3517–3525, 2006.

[53] Peter J. Walsh, Xianbo Hu, Philip Cunniff, and Alan J. Lesser. Environmental effects on poly-p-phenylenebenzobisoxazole fibers. II. Attempts at stabilization. *Journal of Applied Polymer Science*, 102(4):3819–3829, 2006.

[54] C Allan Gunnarsson, Tusit Weerasooriya, and Paul Moy. The Effect of Loading Rate on the Tensile Behavior of Single Zylon Fiber. volume 1 of *Conference Proceedings of the Society for Experimental Mechanics Series*, pages 195–204, New York, NY, 2011. Springer New York.

[55] S. Sockalingam, D. Casem, T. Weerasooriya, P. McDaniel, and J. Gillespie. Experimental Investigation of the High Strain Rate Transverse Compression Behavior of Ballistic Single Fibers. *Journal of Dynamic Behavior of Materials*, 3(3):474–484, 2017.

[56] DSM. Technical brochure: Dyneema in marine and industrial applications, 2008.

[57] Ming Cheng, Weinong Chen, and Tusit Weerasooriya. Mechanical Properties of Kevlar® KM2 Single Fiber. *Journal of Engineering Materials and Technology*, 127(2):197, 2005.

[58] CY Yue, GX Sui, and HC Looi. Effects of heat treatment on the mechanical properties of Kevlar-29 fibre. *Composites science and technology*, 60:421–427, 2000.

[59] J Lim, JQ Zheng, K Masters, and W Chen. Effects of Gage Length and Loading Rates on the Strength of PPTA Fibers. In *International Conference on Composite Materials*, pages 18–21, 2008.

[60] David Hartman, Mark E. Greenwood, and David M. Miller. High strength glass fibers. Technical report, 1996.

[61] J. Mayo and E. Wetzel. Cut resistance and failure of high-performance single fibers. *Textile Research Journal*, 84(12):1233–1246, 2014.

[62] Toyobo co. LTD. Zylon Technical Information. Technical report, 2005.

[63] Y Yamashita, S Kawabata, S Okada, and A Tanaka. Mechanical Characteristics of PBO Single Fiber. In *Proceedings of the 7th Asian Textile Conference*, pages 1–7, New Delhi, 2003.

[64] Roger J. Morgan, Cesar O. Pruneda, and Wayne J. Steele. The relationship between the physical structure and the microscopic deformation and failure processes of poly(p-phenylene terephthalamide) fibers. *Journal of Polymer Science: Polymer Physics Edition*, 21(9):1757–1783, sep 1983.

[65] M. G. Dobb and R. M. Robson. Structural characteristics of aramid fibre variants. *Journal of Materials Science*, 25(1):459–464, 1990.

[66] Kevin Golovin and Stuart Leigh Phoenix. Effects of extreme transverse deformation on the strength of UHMWPE single filaments for ballistic applications. *Journal of Materials Science*, 51(17):8075–8086, 2016.

[67] Kenneth E. Strawhecker and Daniel P. Cole. Morphological and local mechanical surface characterization of ballistic fibers via AFM. *Journal of Applied Polymer Science*, 131(19):n/a–n/a, oct 2014.

[68] R. J. Young, R. J. Day, and M. Zakikhani. The structure and deformation behaviour of poly (p-phenylene benzobisoxazole) fibres. *Journal of Materials Science*, 25:127–136, 1990.

[69] Tooru Kitagawa, Hiroki Murase, and Kazuyuki Yabuki. Morphological Study on Poly-p-phenylenebenzobisoxazole. *Journal of Polymer: Part B: Polymer Physics*, 36(January):39–48, 1997.

[70] U.S. DoJ. Ballistic Resistance of Personal Body Armor NIJ Standard–0101.06. Technical Report August, 2008.

[71] 758 ZenTron Product Information. Technical report.

[72] M Kinsella, D Murray, and D Crane. Mechanical properties of polymeric composites reinforced with high strength glass fibers. *International Sampe Technical Conference Series*, 33:1644–1657, 2001.

[73] Applications Branch, Standards Office, and Aberdeen Proving Ground. MIL-DTL-46593B. Technical Report July, 2006.

[74] J.P. Attwood, B.P. Russell, H.N.G. Wadley, and V.S. Deshpande. Mechanisms of the penetration of ultra-high molecular weight polyethylene composite beams. *International Journal of Impact Engineering*, 93:153–165, jul 2016.

[75] Matthew Hudspeth, Jou-mei Chu, Emily Jewell, BoonHim Lim, Ernest Ytuarte, Waterloo Tsutsui, Suzanne Horner, James Zheng, and Weinong Chen. Effect of projectile nose geometry on the critical velocity and failure of yarn subjected to transverse impact. *Textile Research Journal*, 87(8):953–972, may 2017.

[76] Zherui Guo, Weinong Chen, and James Zheng. Effect of replacement strike-face material on the ballistic performance of multi-ply soft armor targets. *Textile Research Journal*, 89(5):711–725, 2019.

[77] MIL-STD-662F. V50 Ballistic Test for Armor. Technical Report 18 December 1997, US Department of Defense, 1997.

[78] Zherui Guo, James Zheng, and Weinong Chen. Reverse ballistics penetration of Kevlar® fabric with different indenters at different loading rates. *Textile Research Journal*, 87(10):1165–1176, jun 2017.

[79] Rodney F. Recht. Taylor ballistic impact modelling applied to deformation and mass loss determinations. *International Journal of Engineering Science*, 16(11):809–827, jan 1978.

[80] R. S.J. Corran, P. J. Shadbolt, and C. Ruiz. Impact loading of plates - An experimental investigation. *International Journal of Impact Engineering*, 1(1):3–22, 1983.

[81] Matthew Calvin Hudspeth. *Multi-Axial Failure of High-Performance Fiber During Transverse Impact*. Ph.d. thesis, Purdue University, 2016.

[82] Hans Qvarnström. Technical Note: A mathematical formula for transformation between the steel hardness scales of Rockwell C and Vickers. *Journal of Heat Treating*, 7(1):65–67, mar 1989.

[83] E.J. Pavlina and C.J. Van Tyne. Correlation of Yield Strength and Tensile Strength with Hardness for Steels. *Journal of Materials Engineering and Performance*, 17(6):888–893, dec 2008.

[84] Uddeholm. AISI O1 Cold work tool steel. Technical report.

[85] Markus Knoerr, Kurt Lange, and Taylan Altan. Fatigue failure of cold forging tooling: causes and possible solutions through fatigue analysis. *Journal of Materials Processing Technology*, 46(1-2):57–71, oct 1994.

[86] Zherui Guo, Weinong Chen, and James Zheng. Localized impact stress concentrations in soft armors due to microscale projectile edge geometries. *Textile Research Journal*, page 004051751880905, oct 2018.

[87] Sidney Chocron, Nikki King, R. Bigger, James D. Walker, Ulrich Heisserer, and Harm van der Werff. Impacts and waves in Dyneema HB80 strips and laminates. *Journal of Applied Mechanics*, 80(3):031806, 2013.

[88] Yanfei Yang and Xiaogang Chen. Investigation of failure modes and influence on ballistic performance of Ultra-High Molecular Weight Polyethylene (UHMWPE) uni-directional laminate for hybrid design. *Composite Structures*, 174:233–243, aug 2017.

[89] W. Johnson. *Impact Strength of Materials*. Hodder Arnold, 1972.

[90] S. L. Phoenix and Pankaj K. Porwal. A new membrane model for the ballistic impact response and V50 performance of multi-ply fibrous systems. *International Journal of Solids and Structures*, 40(24):6723–6765, dec 2003.

[91] M. P. Flanagan, M. A. Zikry, J. W. Wall, and A. El-Shiekh. An Experimental Investigation of High Velocity Impact and Penetration Failure Modes in Textile Composites. *Journal of Composite Materials*, 33(12):1080–1103, jun 1999.

[92] A Prosser. Penetration of Nylon Ballistic Panels by Fragment-Simulating Projectiles Part I: A Linear Approximation to the Relationship between the Square of the V50 or Vc Striking Velocity and the Number of Layers of Cloth in the Ballistic Panel. *Textile Research Journal*, 58(3):61–85, 1988.

[93] J.D. Walker. Constitutive model for fabrics with explicit static solution and ballistic limit. In *18th International Symposium on Ballistics*, volume 2, pages 1231–1238, 1999.

[94] James D Walker. Ballistic Limit of Fabrics with Resin. In *19th International Symposium of Ballistics*, number May, pages 1409–1414, 2001.

[95] U.S. DoJ. Stab Resistance of Personal Body Armor, NIJ Standard-0115.00. Technical report, 2000.

[96] James D. Walker and Sidney Chocron. Why Impacted Yarns Break at Lower Speed Than Classical Theory Predicts. *Journal of Applied Mechanics*, 78(September 2011):051021, 2011.

[97] Jianzhuo Sun, Matthew Hudspeth, and Weinong Chen. Biaxial shear/tension failure behavior of Spectra single fibers. *Composites Part A: Applied Science and Manufacturing*, 88:286–294, 2016.

[98] L. C. Lin, A. Bhatnagar, and H. W. Chang. Ballistic Energy Absorption of Composites. In *22nd International SAMPE Technical Conference*, pages 1–13, Boston, Massachusetts, 1990.

[99] A Prosser. Penetration of Nylon Ballistic Panels by Fragment-Simulating Projectiles Part II: Mechanism of Penetration. (March):3–7, 1988.

[100] Philip M. Cunniff. Assessment of Small Arms (Ball Round) Body Armor Performance. In *Proceedings of 18th International Symposium on Ballistics*, pages 806–813, 1999.

[101] L. H. Nguyen, S. Ryan, S. J. Cimpoeru, A. P. Mouritz, and A. C. Orifici. The Efficiency of Ultra-High Molecular Weight Polyethylene Composite Against Fragment Impact. *Experimental Mechanics*, 56(4):595–605, apr 2016.

[102] Pankaj K. Porwal and S. Leigh Phoenix. Modeling system effects in ballistic impact into multi-layered fibrous materials for soft body armor. *International Journal of Fracture*, 135(1-4):217–249, 2005.

[103] James Singletary, Tom Steinruck, and Pat Fitzgerald. Effects of boundary conditions on V50 and zone of mixed results of fabric armor targets. In *23rd International Symposium on Ballistics*, pages 865–871, 2007.

[104] Tye Langston. An analytical model for the ballistic performance of ultra-high molecular weight polyethylene composites. *Composite Structures*, 179:245–257, nov 2017.

[105] Fritz Larsson and Lars Svensson. Carbon, polyethylene and PBO hybrid fibre composites for structural lightweight armour. *Composites - Part A: Applied Science and Manufacturing*, 33(2):221–231, 2002.

[106] Yi Zhou, Jun Hou, Xiaozhou Gong, and Dan Yang. Hybrid panels from woven Kevlar ® and Dyneema ® fabrics against ballistic impact with wearing flexibility. *The Journal of The Textile Institute*, 5000(December):1–8, 2017.

[107] Xiaogang Chen, Yi Zhou, and Garry Wells. Numerical and experimental investigations into ballistic performance of hybrid fabric panels. *Composites Part B: Engineering*, 58:35–42, 2014.

[108] R.J. Muhi, F. Najim, and M.F.S.F. de Moura. The effect of hybridization on the GFRP behavior under high velocity impact. *Composites Part B: Engineering*, 40(8):798–803, dec 2009.

[109] P. Rama Subba Reddy, T. Sreekantha Reddy, K. Mogulanna, I. Srikanth, V. Madhu, and K. Venkateswara Rao. Ballistic Impact Studies on Carbon and E-glass Fibre Based Hybrid Composite Laminates. *Procedia Engineering*, 173:293–298, 2017.

[110] P.J. Hazell and G. Appleby-Thomas. A study on the energy dissipation of several different CFRP-based targets completely penetrated by a high velocity projectile. *Composite Structures*, 91(1):103–109, nov 2009.

[111] Yanfei Yang and Xiaogang Chen. Determination of Materials for Hybrid Design of 3D Soft Body Armour Panels. *Applied Composite Materials*, 25(4):861–875, aug 2018.

[112] PK Porwal and SL Phoenix. Effects Of Layer Stacking Order on the V50 Velocity of a Two-Layered Hybrid Armor System. *Journal of Mechanics of Materials and Structures*, 3(April), 2008.

[113] S. Leigh Phoenix, A. Kadir Yavuz, and Pankaj K. Porwal. New Interference Approach for Ballistic Impact into Stacked Flexible Composite Body Armor. *AIAA Journal*, 48(2):490–501, 2010.

[114] Xiaogang Chen, Fuyou Zhu, and Garry Wells. An analytical model for ballistic impact on textile based body armour. *Composites Part B: Engineering*, 45(1):1508–1514, feb 2013.

[115] Zherui Guo, Weinong Chen, and James Zheng. A semi-empirical design parameter for determining the inelastic strike-face mass fraction of soft armor targets. *International Journal of Impact Engineering*, 125(March):83–92, mar 2019.

[116] Hao Wang, Ximin Deng, Haijun Wu, Aiguo Pi, Jinzhu Li, and Fenglei Huang. Investigating the dynamic mechanical behaviors of polyurea through experimentation and modeling. *Defence Technology*, (xxxx), 2019.

[117] Line-X® XS-350. Technical report, 2018.

[118] B.P. Russell, K. Karthikeyan, V.S. Deshpande, and N.A. Fleck. The high strain rate response of Ultra High Molecular-weight Polyethylene: From fibre to laminate. *International Journal of Impact Engineering*, 60:1–9, oct 2013.

[119] H. van der Werff and U. Heisserer. High-performance ballistic fibers. In *Advanced Fibrous Composite Materials for Ballistic Protection*, pages 71–107. Elsevier, 2016.

[120] G. Ben-Dor, A. Dubinsky, and T. Elperin. Optimization of two-component composite armor against ballistic impact. *Composite Structures*, 69(1):89–94, 2005.

[121] SP Timoshenko and S Woinowsky-Krieger. *Theory of plates and shells*. McGraw-hill, 1959.

[122] Raymond D. Mindlin. Influence of rotatory inertia and shear on flexural motions of isotropic, elastic plates,. 1951.

[123] Eric Reissner. The effect of transverse shear deformation on the bending of elastic plates. 1945.

[124] Eduard Ventsel and Theodor Krauthammer. *Thin Plates and Shells*. CRC Press, aug 2001.

[125] M. A. Medick. On Classical Plate Theory and Wave Propagation. *Journal of Applied Mechanics*, 28(2):223–228, jun 1961.

[126] Impact response of orthotropic composite plates predicted from a one-parameter differential equation. *AIAA Journal*, 30(6):1587–1596, 1992.

[127] R. Olsson. Mass criterion for wave controlled impact response of composite plates. *Composites Part A: Applied Science and Manufacturing*, 31(8):879–887, 2000.

[128] J. C. Smith, J. M. Blandford, and H. F. Schiefer. Stress-Strain Relationships. in Yarns Subjected to Rapid Impact Loading: Part VI: Velocities of Strain Waves Resulting from Impact. *Textile Research Journal*, 30(10):752–760, oct 1960.

[129] C Lin and Fatt MS. Perforation of composite plates and sandwich panels under quasi-static and projectile loading. *Journal of Composite Materials*, 40(20):1801–1840, 2006.

[130] K. N. Shivakumar, W. Elber, and W. Illg. Prediction of impact force and duration due to low-velocity impact on circular composite laminates. *Journal of Applied Mechanics, Transactions ASME*, 52(3):674–680, 1985.

[131] James F. Doyle. Constructing Simple Analytical Models. In *Guided Explorations of the Mechanics of Solids and Structures*, pages 376–438. Cambridge University Press, Cambridge.

[132] M.R. O'Masta, B.P. Russell, and W. Ronan. Inter-ply angle influence on the out-of-plane compressive response of polyethylene fibre laminates. *Composites Part A: Applied Science and Manufacturing*, 110:11–20, jul 2018.

[133] Ying Wang, Xiaogang Chen, Robert Young, Ian Kinloch, and Wells Garry. An experimental study of the effect of ply orientation on ballistic impact performance of multi-ply fabric panels. *Textile Research Journal*, 86(1):34–43, jan 2016.

[134] Ying Wang, Xiaogang Chen, Robert Young, Ian Kinloch, and Garry Wells. A numerical study of ply orientation on ballistic impact resistance of multi-ply fabric panels. *Composites Part B: Engineering*, 68:259–265, jan 2015.

[135] Lionel Vargas-Gonzalez, Shawn M. Walsh, and James Wolbert. Impact and Ballistic Response of Hybridized Thermoplastic Laminates. Technical report, 2011.

[136] AM Polyakov and NA Krotova. An investigation of mechanoelectron emission intensity when polymer films are torn off and deformed. *Dokl. Akad. Nauk SSSR*, 151(1):130–133, 1963.

[137] P.Yu. Butyagin, V.S. Yerofeyev, I.N. Musayelyan, G.A. Patrikeyev, A.N. Streletskii, and A.D. Shulyak. The luminescence accompanying mechanical deformation and rupture of polymers. *Polymer Science U.S.S.R.*, 12(2):330–342, jan 1970.

[138] V. A. Zakrevskii and V. A. Pakhotin. Mechanical emissions by polymers. *Polymer Science U.S.S.R.*, 17(3):653–657, 1975.

[139] J. T. Dickinson, L. C. Jensen, and A. Jahan-Latibari. Fracto-Emission from Filled and Unfilled Elastomers. *Rubber Chemistry and Technology*, 56(5):927–941, nov 1983.

[140] J T Dickinson, A Jahanlatibari, and L C Jensen. Fracto-Emission from Single Fibers of Kevlar. *Journal of Materials Science*, 20(5):1835–1841, 1985.

[141] J. T. Dickinson and L. C. Jensen. Fracto-emission from filled and unfilled polybutadiene. *Journal of Polymer Science: Polymer Physics Edition*, 23(5):873–888, may 1985.

[142] J Thomas Dickinson. Fracto-Emission from Polymers. Technical report, Washington State University, 1987.

[143] J T Dickinson. Particle Emission and Charging Effects Induced by Fracture. Technical report, 1991.

[144] S. C. Langford and J. T. Dickinson. Emission of Particles and Photons from the Fracture of Minerals and Inorganic Materials. pages 224–244. nov 1990.

[145] J. T. Dickinson, L. C. Jensen, and R. P. Dion. Fracto-emission from high density polyethylene: Bond breaking versus tribological stimulation. *Journal of Applied Physics*, 73(6):3047–3054, mar 1993.

[146] K. A. Zimmerman, S. C. Langford, J. T. Dickinson, and R. P. Dion. Electron and photon emission accompanying deformation and fracture of polycarbonate. *Journal of Polymer Science Part B: Polymer Physics*, 31(9):1229–1243, 1993.

[147] N Bonora, A Ruggiero, G Iannitti, C Abbate, F Iannuzzo, and G Busatto. Mechanoluminescence of nylon under high velocity impact. *J. Phys.: Conf. Ser.*, 500:182005, 2014.

[148] Ross S. Fontenot, William A. Hollerman, Mohan D. Aggarwal, Kamala N. Bhat, and Shawn M. Goedeke. A versatile low-cost laboratory apparatus for testing triboluminescent materials. *Measurement: Journal of the International Measurement Confederation*, 45(3):431–436, 2012.

[149] Denver Gallardy. Ballistic Evaluation of 6055 Aluminum. Technical Report September, US Army Research Laboratory, 2015.

[150] W. A. Gooch, M. S. Burkins, and R. J. Squillacioti. Ballistic Testing of Commercial Aluminum Alloys and Alternate Processing Techniques to Increase the Availability of Aluminum Armor. In *23rd International Symposium on Ballistics*, number April, pages 981–988, Tarragona, Spain, 2007.

[151] A Cheeseman, WA Gooch, and MS Burkins. Ballistic Evaluation of Aluminum 2139-T8. *Proceedings of the 24th international symposium on ballistics*, (September):651, 2008.

[152] R Hill. *The Mathematical Theory of Plasticity*. 1950.

[153] Norman Jones. *Structural Impact*. 1989.

[154] K. T. Ramesh. High Strain Rate and Impact Experiments. In *Handbook of Experimental Solid Mechanics*, chapter 33, page 874. Springer, 2008.

[155] B. Cao, M. Shaeffer, D. Cadel, K. T. Ramesh, and S. Prasad. An Analysis of Strengthening Mechanisms and Rate-Dependence in a High Strength Aluminum Alloy. *Journal of Dynamic Behavior of Materials*, 4(1):6–17, mar 2018.

[156] J. Gao, Y. Nie, B.H. Lim, N. Kedir, and W. Chen. A Microscopic Experimental Method Transversely Loading on Single High-Performance Fibers. *Experimental Mechanics*, 59(5):669–679, jun 2019.

[157] Jinling Gao, Yizhou Nie, Boon Him Lim, Xuedong Zhai, Nesredin Kedir, and Weinong Chen. In-situ observation of cutting-induced failure processes of single high-performance fibers inside a SEM. *Composites Part A: Applied Science and Manufacturing*, 131:105767, apr 2020.

[158] R. M. V. Pidaparti and M. J. Palakal. Material model for composites using neural networks. *AIAA Journal*, 31(8):1533–1535, aug 1993.

[159] Xin Liu, Wenbin Yu, Federico Gasco, and Johnathan Goodsell. A unified approach for thermoelastic constitutive modeling of composite structures. *Composites Part B: Engineering*, 172:649–659, sep 2019.

[160] Xin Liu, Fei Tao, and Wenbin Yu. A neural network enhanced system for learning nonlinear constitutive relation of fiber reinforced composites. In *AIAA Scitech 2020 Forum*, Reston, Virginia, jan 2020. American Institute of Aeronautics and Astronautics.

[161] Fei Tao, Xin Liu, Haodong Du, and Wenbin Yu. Physics-informed artificial neural network approach for axial compression buckling analysis of thin-walled cylinder. In *AIAA Scitech 2020 Forum*, Reston, Virginia, jan 2020. American Institute of Aeronautics and Astronautics.

VITA

Zherui Guo is a Ph.D. student under Professor Weinong Chen at Purdue University, School of Aeronautics and Astronautics since the Fall 2012 semester.

Zherui Guo was born in Singapore in 1986. He started his undergraduate studies at Purdue University's School of Aeronautics & Astronautics in 2007. During this time, he first started working for Prof. Weinong Chen as a SURF Summer Undergraduate Research Foundation) student on single-loading Kolsky bars in the summer of 2008. Upon completion of his Bachelor's degree, he started doing research under Prof. Weinong Chen on the transverse compression of ballistic polymer fibers, which eventually became the topic of his M.S. thesis. Most of Zherui's current work and publications focus on terminal ballistics phenomena and impact mechanical response of different materials, with specific focus on soft armor impact.